Multiplexed detection of chemical and biological analytes with microscale organic electrochemical transistor arrays

Von der Fakultät für Elektrotechnik und Informationstechnik der Rheinisch-Westfälischen Technischen Hochschule Aachen zur Erlangung des akademischen Grades einer Doktorin der Ingenieurwissenschaften genehmigte Dissertation

vorgelegt von

Chunling Li, M. Sc.

aus Weinan, Shaanxi, China

Berichter: Univ.-Professor Dr. rer. nat. Sven Ingebrandt

Univ.-Professor Dr. rer. nat. Patrick Wagner, KU Leuven, Belgien

Tag der mündlichen Prüfung: 18.11.2024

Diese Dissertation ist auf den Internetseiten der Universitätsbibliothek online verfügbar.

Abstract

Over the last ten years, there has been extensive research in the field of chemical and biological sensors on Poly(3,4-ethylenedioxythiophene) polystyrene sulfonate (PEDOT:PSS), which is a mixed ionomer capable of conducting positive and negative charges. PEDOT:PSS has been utilized in a wide range of applications due to its outstanding properties, such as high electrical conductivity, transparency and biocompatibility. PEDOT:PSS has been applied as a sensor material to detect and monitor the ion concentrations in sweat, enabling non-invasive and real-time health monitoring. Additionally, it has been used as a low-impedance electrode coating for stimulating and recording cells and tissues in bioelectric applications. It has been also utilized in flexible and wearable devices to monitor physiological parameters such as heart rate, skin temperature and muscle activity. The most common application of PEDOT:PSS is its use in organic electrochemical transistors (OECTs), where a thin PEDOT:PSS film functions as a channel material. In this configuration, PEDOT:PSS can be gated through the doping/de-doping process by cations from the electrolyte solution, causing a significant change in the electrical conductivity of the material and hence an electrochemical gating of the OECTs. This effect enables the OECTs to operate electronically similarly to p-doped silicon or thin film field-effect transistors and to provide further advantages including high sensitivity to ionic strength in liquid environments, biocompatibility, flexibility, cost-effectiveness, and scalability. Despite the wide applications of PEDOT:PSS, it is essential to further explore and enhance the functionality and performance of OECTs. This dissertation contains two main objectives: the first is the improvement and enhancement of the reliability, stability and electrochemical performance of OECTs for chemical and biosensing applications; the second is the development of sensors with high sensitivity and selectivity for the detection of ions and neurotransmitters, which can be applied for the sensing of sweat composition or in environment monitoring. To achieve these goals, the following developments and tasks were conducted: i) development of wafer-scale processing techniques for microscale OECT arrays; ii) investigation of various electrode materials and device structures, including the thickness variation of PEDOT:PSS; iii) optimization of the composition of the polymer; iv) integration of ion-selective membranes (ISMs) on the OECTs for selective detection of desired ions (Na^+ and K^+); v) development of a readout principle for the detection of the neurotransmitter dopamine (DA) with high sensitivity and selectivity; vi) demonstration of the sensor functionality for the real-time monitoring of various ions and DA concentrations in solution.

A microfabrication process which is reliable, reproducible and enabling high-throughput for manufacturing PEDOT:PSS OECT microarrays at 4-inch wafer scale was established by developing and optimizing cleanroom processes. The microfabrication process consisted of optical lithography, a lift-off process for interdigitated electrodes (IDEs) and reactive ion etching (RIE), spin-coating and lift-off process for patterning PEDOT:PSS to ensure ultra-thin polymer layers on wafer scale, as well as other steps. To ensure the reliable operation of OECTs in the liquid solution, silicon oxide was applied on the contact lines as a passivation layer. The utilization of spin-coating and subsequent lift-off techniques was developed to deposit the PEDOT:PSS on the IDE structures with the controlled thickness down to 30 nm.

Wire-bonding and encapsulation protocols were established for the electrical characterization experiments and for the different applications of the OECT microarrays described within this thesis. Furthermore, the integration of the OECTs into a microfluidic system was developed to facilitate real-time and reliable analyte detection. Compared to other materials (Au, Pt, TiN, ITO), iridium oxide (IrO_x) was found to exhibit the lowest contact resistance to PEDOT:PSS as electrode material in the IDEs. In addition to wafer-scale processes, PEDOT:PSS was successfully integrated into cotton yarn to create ion-selective textile sensors, showing its potential for flexible and wearable electronics in the future.

To realize the selective detection of the desired ion type using the OECT microarrays, an ISM is necessary to prevent undesired ions in the electrolyte solution from entering the PEDOT:PSS layer. In this thesis, ISMs for different ions were successfully integrated into the same OECT array with a spin-coating technique, enabling the multiplexed sensing for both Na^+ and K^+ ions. Additionally, the optimization of the spin-coating speeds and the composition of ISM solution enabled control of the thickness of ISMs down to 80 nm, which offered the high sensitivity while maintaining an excellent selectivity of the OECTs. An optimal composition and thickness of ISM has been achieved for the detection of Na^+ and K^+ ion concentrations. By integrating the OECTs into a microfluidic system, the multiplexed, real-time and reversible sensing for both ions in the applicable concentration range from 1 mM to 100 mM in different electrolyte solutions were possible.

Due to the low concentration of DA and the existence of interfering molecules such as ascorbate acid (AA) and uric acid (UA), the highly sensitive and selective detection of DA concentration is a significant challenge. A new platform has been developed for detecting DA using an OECT microarray in combination with a Pt gate electrode. This platform showed a good sensitivity to DA while maintaining a good selectivity against AA and UA. The OECT microarrays exhibited a reliable limit of detection as low as 1 nM, while a standard electrochemical setup with a 3-electrode configuration using the same Pt electrode only reached a detection limit of 1 µM. A surface modification of the Pt gate electrode with chitosan significantly improved the selective detection of the OECTs against UA and AA. Furthermore, the effect of the PEDOT:PSS film thickness on the sensitivity of DA detection was characterized, and the results indicated that the decrease of the film thickness from 108 nm to 45 nm led to an increased sensitivity of DA detection. The novel platform for DA detection showed the potential for various applications, such as real-time monitoring of neurotransmitters, in vivo applications, and neurological research.

In this thesis, significant scientific progress has been achieved by fabricating stable and reliable PEDOT:PSS OECT microarrays on a wafer scale for detecting the concentrations of ions and DA. Multiplexed sensing with high sensitivity and selectivity for both Na^+ and K^+ ions was successfully demonstrated using 16 channel PEDOT:PSS OECT microarrays integrated with ISMs. This enhanced technique and platform have the potential to be applied in various fields in the future, including environmental monitoring, modern healthcare applications, clinical diagnostics, and flexible and wearable electronics.

Zusammenfassung

In den letzten zehn Jahren wurden auf dem Gebiet der chemischen und biologischen Sensoren umfangreiche Forschungsarbeiten zu Poly(3,4-Ethylendioxythiophen)-Polystyrolsulfonat (PEDOT:PSS) durchgeführt, einem gemischten Ionomer, das positive und negative Ladungen leiten kann. PEDOT:PSS wird aufgrund seiner herausragenden Eigenschaften, wie hohe elektrische Leitfähigkeit, Transparenz und Biokompatibilität, in einer Vielzahl von Anwendungen eingesetzt. So wurde PEDOT:PSS beispielsweise als Sensormaterial zum Nachweis und zur Überwachung der Ionenkonzentration im Schweiß eingesetzt, was eine nicht-invasive Gesundheitsüberwachung in Echtzeit ermöglicht. Darüber hinaus wurde es als Elektrodenbeschichtung mit niedriger Impedanz für die Stimulation und Aufzeichnung von Zellen und Geweben in bioelektrischen Anwendungen eingesetzt. Es wurde auch in flexiblen und tragbaren Geräten zur Überwachung physiologischer Parameter wie Herzfrequenz, Hauttemperatur und Muskelaktivität verwendet. Die häufigste Anwendung von PEDOT:PSS ist der Einsatz in organischen elektrochemischen Transistoren (OECTs), bei denen ein dünner PEDOT:PSS-Film als Kanalmaterial dient. In dieser Konfiguration kann PEDOT:PSS durch den Dotierungs-/De-Dotierungsprozess durch Kationen aus der Elektrolytlösung gesteuert werden, was zu einer erheblichen Änderung der elektrischen Leitfähigkeit des Materials und damit zu einer elektrochemischen Steuerung der OECTs führt. Dieser Effekt ermöglicht es den OECTs, elektronisch ähnlich wie p-dotierte Silizium- oder Dünnfilm-Feldeffekttransistoren zu arbeiten und bietet weitere Vorteile wie hohe Empfindlichkeit gegenüber der Ionenstärke in flüssigen Umgebungen, Biokompatibilität, Flexibilität, Kosteneffizienz und Skalierbarkeit. Trotz der breiten Anwendungsmöglichkeiten von PEDOT:PSS ist es wichtig, die Funktionalität und Leistung von OECTs weiter zu erforschen und zu verbessern. Diese Dissertation verfolgt zwei Hauptziele: Das erste ist die Verbesserung und Steigerung der Zuverlässigkeit, Stabilität und elektrochemischen Leistung von OECTs für chemische und biologische Anwendungen; das zweite ist die Entwicklung von Sensoren mit hoher Empfindlichkeit und Selektivität für den Nachweis von Ionen und Neurotransmittern, die für die Messung der Schweißzusammensetzung oder die Umweltüberwachung eingesetzt werden können. Um diese Ziele zu erreichen, wurden die folgenden Entwicklungen und Aufgaben durchgeführt: i) Entwicklung von Verarbeitungstechniken im Wafermaßstab für mikroskalige OECT-Arrays; ii) Untersuchung verschiedener Elektrodenmaterialien und Bauelementstrukturen, einschließlich der Variation der Dicke von PEDOT: PSS; iii) Optimierung der Polymerzusammensetzung; iv) Integration ionenselektiver Membranen (ISMs) auf den OECTs zum selektiven Nachweis der gewünschten Ionen (Na^+ und K^+); v) Entwicklung eines Ausleseprinzips für den Nachweis des Neurotransmitters Dopamin (DA) mit hoher Empfindlichkeit und Selektivität; vi) Demonstration der Sensorfunktionalität für die Echtzeitüberwachung verschiedener Ionen und DA-Konzentrationen in Lösung.

Durch die Entwicklung und Optimierung von Reinraumprozessen wurde ein zuverlässiger und reproduzierbarer Mikroherstellungsprozess etabliert, der einen hohen Durchsatz für die Herstellung von PEDOT:PSS-OECT-Mikroarrays im 4-Zoll-Wafer-Maßstab ermöglicht. Der

Mikrofabrikationsprozess bestand aus optischer Lithographie, einem Lift-off-Prozess für interdigitale Elektroden (IDEs) und reaktivem Ionenätzen (RIE), Spin-Coating und Lift-off-Prozess für die Strukturierung von PEDOT:PSS, um ultradünne Polymerschichten im Wafermaßstab zu gewährleisten, sowie weiteren Schritten. Um den zuverlässigen Betrieb der OECTs in der flüssigen Lösung zu gewährleisten, wurde Siliziumoxid als Passivierungsschicht auf die Kontaktlinien aufgebracht. Es wurden Spin-Coating- und anschließende Lift-off-Techniken entwickelt, um PEDOT:PSS mit einer kontrollierten Dicke von bis zu 30 nm auf die IDE-Strukturen aufzubringen. Für die elektrischen Charakterisierungsexperimente und die verschiedenen in dieser Arbeit beschriebenen Anwendungen der OECT-Mikroarrays wurden Protokolle für das Drahtbonden und die Verkapselung erstellt. Darüber hinaus wurde die Integration der OECTs in ein mikrofluidisches System entwickelt, um eine zuverlässige Echtzeit-Detektion von Analyten zu ermöglichen. Im Vergleich zu anderen Materialien (Au, Pt, TiN, ITO) wurde festgestellt, dass Iridiumoxid (IrO_x) den geringsten Kontaktwiderstand zu PEDOT:PSS als Elektrodenmaterial in den IDEs aufweist. Zusätzlich zu den Prozessen im Wafer-Maßstab wurde PEDOT:PSS erfolgreich in Baumwollgarn integriert, um ionenselektive Textilsensoren herzustellen, was sein Potenzial für flexible und tragbare Elektronik in der Zukunft zeigt.

Um den selektiven Nachweis der gewünschten Ionenart mit Hilfe der OECT-Mikroarrays zu realisieren, ist ein ISM erforderlich, um zu verhindern, dass unerwünschte Ionen in der Elektrolytlösung in die PEDOT:PSS-Schicht gelangen. In dieser Arbeit wurden ISMs für verschiedene Ionen erfolgreich in dasselbe OECT-Array mit einer Spin-Coating-Technik integriert, was die Multiplex-Sensorik für Na^+ und K^+ Ionen ermöglicht. Darüber hinaus ermöglichte die Optimierung der Spin-Coating-Geschwindigkeiten und der Zusammensetzung der ISM-Lösung die Kontrolle der ISM-Dicke auf bis zu 80 nm, was eine hohe Empfindlichkeit bei gleichzeitiger Beibehaltung einer ausgezeichneten Selektivität der OECTs ermöglichte. Für den Nachweis von Na^+- und K^+-Ionenkonzentrationen wurde eine optimale Zusammensetzung und Dicke des ISM erreicht. Durch die Integration der OECTs in ein mikrofluidisches System war die multiplexe, Echtzeit- und reversible Erfassung beider Ionen im anwendbaren Konzentrationsbereich von 1 mM bis 100 mM in verschiedenen Elektrolytlösungen möglich.

Aufgrund der geringen Konzentration von DA und der Existenz störender Moleküle wie Ascorbatsäure (AA) und Harnsäure (UA) stellt der hochempfindliche und selektive Nachweis der DA-Konzentration eine große Herausforderung dar. Es wurde eine neue Plattform zum Nachweis von DA entwickelt, die ein OECT-Mikroarray in Kombination mit einer Pt-Gate-Elektrode verwendet. Diese Plattform zeigte eine gute Empfindlichkeit für DA bei gleichzeitig guter Selektivität gegenüber AA und UA. Die OECT-Mikroarrays wiesen eine zuverlässige Nachweisgrenze von nur 1 nM auf, während ein elektrochemischer Standardaufbau mit einer 3-Elektroden-Konfiguration und derselben Pt-Elektrode nur eine Nachweisgrenze von 1 µM erreichte. Eine Oberflächenmodifikation der Pt-Gate-Elektrode mit Chitosan verbesserte den selektiven Nachweis der OECTs gegen UA und AA erheblich. Darüber hinaus wurde die Auswirkung der PEDOT:PSS-Schichtdicke auf die Empfindlichkeit der DA-Detektion

charakterisiert. Die Ergebnisse zeigten, dass die Verringerung der Schichtdicke von 108 nm auf 45 nm zu einer erhöhten Empfindlichkeit der DA-Detektion führte. Die neuartige Plattform für die DA-Detektion zeigte das Potenzial für verschiedene Anwendungen, wie die Echtzeitüberwachung von Neurotransmittern, In-vivo-Anwendungen und neurologische Forschung.

In dieser Arbeit wurde ein bedeutender wissenschaftlicher Fortschritt durch die Herstellung stabiler und zuverlässiger PEDOT:PSS OECT-Mikroarrays im Wafer-Maßstab zur Erfassung der Konzentrationen von Ionen und DA erzielt. Multiplex-Sensorik mit hoher Empfindlichkeit und Selektivität für Na^+- und K^+-Ionen wurde erfolgreich mit 16-Kanal-PEDOT:PSS-OECT-Mikroarrays demonstriert, die mit ISMs integriert sind. Diese verbesserte Technik und Plattform hat das Potenzial, in Zukunft in verschiedenen Bereichen eingesetzt zu werden, darunter Umweltüberwachung, moderne Gesundheitsanwendungen, klinische Diagnostik und flexible und tragbare Elektronik.

Contents

Abstract I
Zusammenfassung III
Contents VII
1 Introduction 1
1.1 A general introduction to chemical sensors and biosensors 1
1.2 An introduction to conductive polymers 2
1.3 Exemplary applications in the chemical sensor and biosensor fields 3
1.4 Structure of the thesis 6
2 Fundamentals and theories 9
2.1 PEDOT:PSS 9
2.2 Organic electrochemical transistors 11
2.2.1 Working principle 11
2.2.2 Output and transfer characteristics 12
2.2.3 Applications 15
2.3 Solid-liquid interface and electrical double layer 19
2.4 Ion-selective membranes and ion detection 21
2.4.1 Chemical structure and the working mechanism of ion-selective membranes 21
2.4.2 Ion detection using PEDOT:PSS OECTs 23
2.5 Dopamine detection 25
2.5.1 Chemical structure of dopamine 25
2.5.2 Approaches for dopamine detection 26
3 Methods 31
3.1 Metal deposition 31
3.1.1 Metal evaporation 31
3.1.2 Metal sputtering 32
3.2 Lift-off process 34
3.3 Plasma enhanced chemical vapor deposition 35
3.4 Reactive ion etching 36
3.5 Van der Pauw method 37
3.6 Cyclic voltammetry 38

4 Experiments 41
4.1 Fabrication of OECTs 41
4.1.1 Chip design 41
4.1.2 Van der Pauw chip design 44
4.1.3 Preparation of PEDOT:PSS solutions 44
4.1.4 Fabrication flow for OECTs 46
4.1.5 Fabrication flow for Van der Pauw chip 48
4.2 Electrical characteristics of PEDOT:PSS OECTs 49
4.2.1 Preparation of buffer solutions 49
4.2.2 Measurement setup using a Keithley 4200 parameter analyzer 50
4.2.3 Measurement setup using the transfer function amplifier system 51
4.3 Microfluidic system 51
4.3.1 Design and fabrication of the microfluidic system 51
4.3.2 Measurement setup with the microfluidic system 53
4.4 Ion detection using ion-selective membrane integrated OECTs 54
4.4.1 Preparation of ion-selective membrane mixture solutions 54
4.4.2 Integration and optimization of ion-selective membranes on OECTs 55
4.5 Dopamine detection using OECTs 57
4.5.1 Preparation of dopamine, uric acid, ascorbic acid and chitosan solutions 57
4.5.2 Cyclic voltammetry characterization 59
4.6 Ion-selective textile sensors realized with PEDOT:PSS for ion detection 59
4.6.1 Materials for preparing ion-selective textile sensors 59
4.6.2 Fabrication process for ion-selective textile sensors 60
5 Results and discussion 61
5.1 Fabrication of OECTs 61
5.1.1 Optical lithography for fabrication of OECTs 61
5.1.2 Laser lithography for fabrication of OECTs 64
5.1.3 Wire bonding and chip encapsulation 66
5.2 Electrical characteristics of PEDOT:PSS OECTs 68
5.2.1 The electrical conductivity of PEDOT:PSS films 68
5.2.2 Electrical characteristics of OECTs using the transfer function amplifier system .. 69
5.2.3 Electrical characteristics of OECTs using the Keithley 4200 parameter analyzer . 72

5.2.4 Effect of contact materials on the electrical characteristics of OECTs 76
5.2.5 Effect of PEDOT:PSS film thicknesses on the electrical characteristics of OECT 80
5.3 Ion detection using ion-selective membrane integrated OECTs 83
5.3.1 Electrical characteristics of OECTs 83
5.3.2 Sensitivity of ISM-OECT microarrays for detection of Na^+ and K^+ ions 84
5.3.3 Selectivity of ISM-OECT microarrays for detection of Na^+ and K^+ ions 88
5.3.4 Reversibility of ISM-OECT microarrays for detection of Na^+ and K^+ ions 90
5.3.5 Multiplexed sensing of Na^+ and K^+ ions with OECT microarrays 91
5.4 Dopamine detection using the OECT microarrays 92
5.4.1 Cyclic voltammetry characterization 92
5.4.2 Transfer characteristics of the OECTs with PBS and dopamine solutions 94
5.4.3 Transfer characteristics of OECTs for DA detection with different gate electrodes 97
5.4.4 Effect of the PEDOT:PSS thickness on DA detection 98
5.4.5 Transfer characteristics of OECTs for detection of ascorbic acid and uric acid .. 100
5.4.6 Selectivity of OECT microarrays for detection of ascorbic acid and uric acid 101
5.4.7 Real-time measurement without a microfluidic system 103
5.4.8 Real-time measurement with a microfluidic system 104
5.4.9 Selectivity improvement by surface modification of the Pt gate electrode 105
5.5 Ion-selective textile sensors realized with PEDOT:PSS for ion detection 107
5.5.1 Microscopic characteristics of textile sensors integrated with ISMs 107
5.5.2 Electrical characteristics of the PEDOT:PSS based textile sensors 108
5.5.3 Electrochemical characteristics of the PEDOT:PSS based textile sensors 109
5.5.4 Stability and flexibility of the textile sensors 110
5.5.5 Ion detection using the textile sensors 111
6 Conclusion 115
7 Outlook 119
References 121
Acknowledgements 131
Table of Figures 133
Table of Tables 141
Appendix A: Abbreviations 143
Appendix B: Details of reagents and equipment 147

Appendix C: Supporting images for results 149
Appendix D: Publications and conferences 153
Curriculum Vitae 155

1 Introduction

This chapter introduces the basics and the evolution of chemical sensors and biosensors. It then presents the development of conductive polymers and several exemplary applications in the chemical sensor and biosensor fields. Finally, it demonstrates the main objectives, tasks and outline of this dissertation.

1.1 A general introduction to chemical sensors and biosensors

Chemical and biological sensors are devices that transform chemical or biological information into analytically useful signals [1-4]. The abbreviation for biological sensors is “biosensors”. The basic elements of chemical sensors or biosensors are presented in figure 1.1 [5, 6]. When operated, the chemical sensors and biosensors usually contain two basic components packaged together in the same unit: the receptor and the transducer [1, 3, 7]. In most of these sensors, the receptor interacts with the analyte molecules. As a result, certain physical or chemical properties are changed such that the transducer can gain an electrical signal [1, 7].

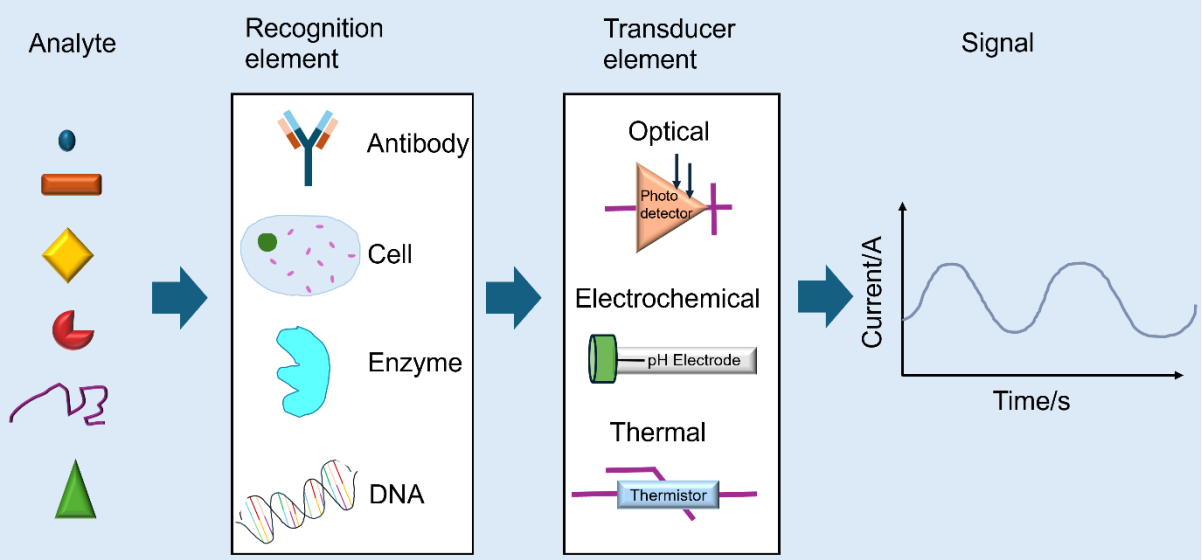

Figure 1.1: *The basic elements of a chemical sensor or a biosensor. Figure is adapted from reference [8].*

Over the past few decades, chemical sensors and biosensors have been constantly developed. In the early 20th century, the concept of pH was introduced by S. P. L. Sørensen [9]. By indicating the activity of the hydrogen (H^+) ions in a solution, the first glass electrode was developed and utilized as the chemical sensor to determine pH [1, 10]. In the middle of the 20th century, Leland C. Clark, who was considered as the “father of biosensors”, invented the first oxygen electrode which was used for measuring oxygen concentration in blood, water and other liquids [11, 12]. Based on the oxygen electrode, he created the first glucose sensor by using the glucose oxidase enzyme, laying the foundation for modern biosensors [13]. During this time, the development of ion-selective electrodes marked a significant advancement, and these sensors were able to measure the concentration of specific ions in solutions such as sodium and potassium [14, 15]. In the period from the 1970s to 1990s, the fiber optical sensor was developed to detect the concentration of glucose and other

metabolites [16], as well as to monitor the pH value for in vivo blood evaluation [17]. The first tissue-based biosensor was developed, where antennule structures from blue crabs were mounted in a chamber with a platinum electrode to detect amino acids with sensitive and selective responses [18]. The first commercial enzyme electrode and glucose analyzer were achieved by Yellow Springs Instruments [2]. Since then, numerous research has been conducted on the evolution of chemical sensors and biosensors, driven by the advances in material science [19-22], miniaturization [23, 24], flexible and wearable electronics [25, 26], and wireless communication [27, 28]. These developments have transformed chemical sensors and biosensors from simple detection devices into complex systems capable of providing real-time monitoring, highly sensitive and selective detection and enhanced precision data. Additionally, chemical sensors and biosensors have gained attention across various application fields, including environmental monitoring [29], clinical diagnostics [30], food quality control [31] and healthcare monitoring [32, 33]. Due to the continuous advancements in technology, materials and interdisciplinary research, the prospects for chemical sensors and biosensors are promising. The increasingly growing demand for the usage of chemical sensors and biosensors highlights the need for sensors with improved reliability, flexibility, reproducibility, biocompatibility, cost-effectiveness, and scalability.

1.2 An introduction to conductive polymers

Conductive polymers (CPs) have attracted numerous attentions and thus have been continuously improved in the past few decades [34]. Many CPs that were originally suitable mostly as laboratorial materials were developed over time to become commercially available as mature industrial products [35].

In 1977, Shirakawa, MacDiarmid, and Heeger have discovered the highly conductive polymer of polyacetylene (PA), which could be rendered to conduct electricity when doped with iodine [36]. This breakthrough work earned them the Nobel Prize in Chemistry in 2000, accelerating the development of conducting polymers at a rapid rate. However, PA was unable to be successfully processed in solution and was unstable in outdoor conditions due to oxidative degradation, resulting in the impossibility of commercialization [34, 37]. To address this problem, considerable efforts have been made to enhance the properties of new CPs such as stability, conductivity and solution-processability. Therefore, a variety of CPs including polypyrrole (PPy), polyaniline (PANi), polythiophene (PTh), and their derivatives have been explored and developed [38]. Furthermore, the structures of these CPs have been modified to improve the electrical properties, biocompatibility and solution-processability. Meanwhile, PPy, PANi, PTh, and their derivatives have been utilized in medical and food safety fields [38]. In 1988, poly(3,4-ethylenedioxythiophene) (PEDOT), one of the PTh derivatives, was first synthesized by scientists at Bayer AG research laboratories in Germany [39]. This remarkable breakthrough made PEDOT one of the most popular research projects in various academic fields. However, the most significant challenge remained that PEDOT was not processable in solution, which restricted its potential applications. Another breakthrough was the incorporation of a water-soluble poly(styrene sulfonate) (PSS) into PEDOT. Poly (3,4-

ethylenedioxythiophene):poly(styrenesulfonic acid) (PEDOT:PSS) contains both the conjugated PEDOT and the non-conjugated PSS, successfully addressing the problem of solution-processibility. Thereafter, it became commercially available in aqueous dispersion. Since then, there has been a notable increase in the research and application of PEDOT:PSS [39-42], due to its excellent properties including high electrical conductivity, superior optical transparency, satisfactory flexibility and stretchability, and good biocompatibility [43-45]. Since PEDOT:PSS can be readily obtained as an aqueous solution, it is compatible with a variety of manufacturing processes [46, 47]. As shown in figure 1.2, PEDOT:PSS has emerged as the most important and popular candidate in various application fields such as thermoelectric devices [48], organic electrochemical transistors (OECTs) [49, 50], chemical and bioelectrical sensors [40, 51], electronic skin and textiles [52, 53].

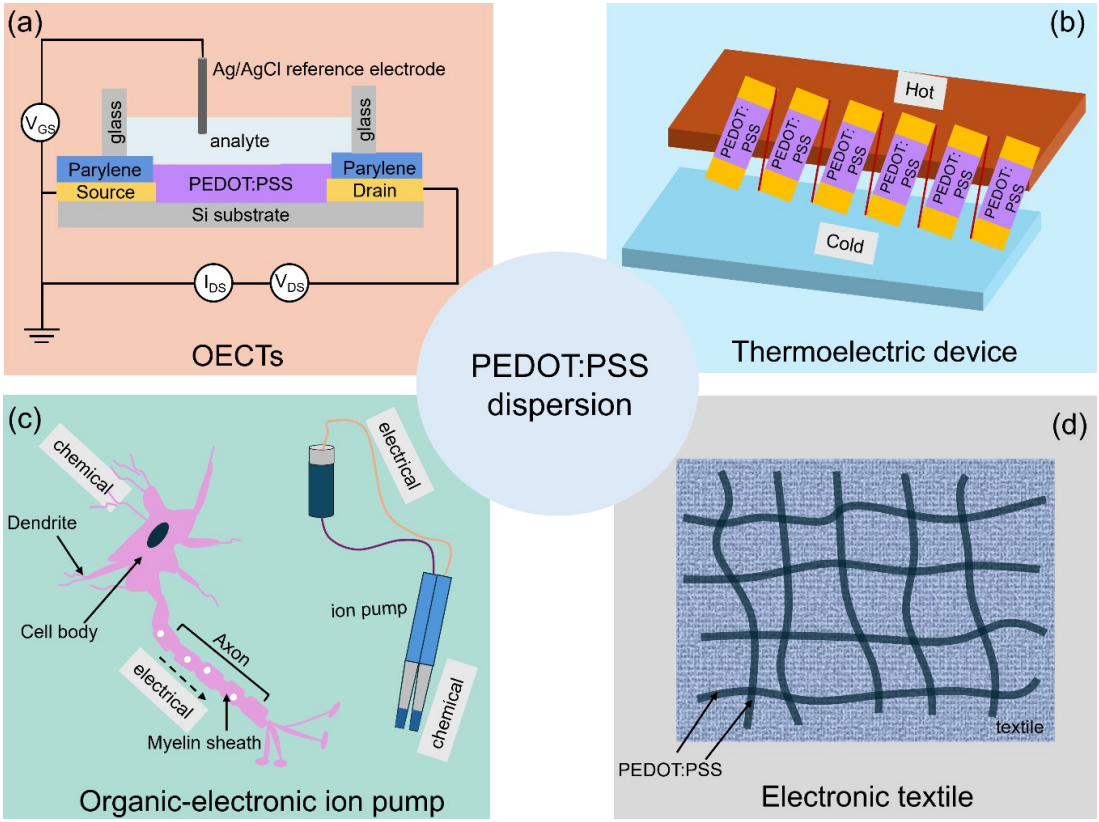

Figure 1.2: *Representative applications of PEDOT:PSS. Figure is adapted from reference [54]. It shows the schematics of OECTs (a), thermoelectric device (b), organic-electronic ion pump (c) and electronic textile (d).*

1.3 Exemplary applications in the chemical sensor and biosensor fields

In this section, several applications in the chemical sensor and biosensor fields will be introduced, including OECTs, ion concentration monitoring, DA detection and textile sensors. OECTs, a significant application of PEDOT:PSS, were developed by Wrighton and his colleagues in the mid-eighties [55]. PEDOT:PSS is typically integrated into OECTs with a three electrode configuration: source electrode, drain electrode and gate electrode. The PEDOT:PSS film is used as the channel material which contacts an electrolyte through an immersed electrode. Metal electrodes as source and drain establish the contacts to the

PEDOT:PSS film and define the channel. After the gate voltage is applied between the gate and source electrodes, the doping/de-doping state of PEDOT:PSS film can be controlled by introducing cations, positively charged ions, from the surrounding electrolyte solution into the polymeric film. This change shows a noticeable influence on the electrical conductivity of PEDOT:PSS, resulting in the alteration of the drain current on OECTs [55, 56]. Owing to their biocompatibility, mechanical flexibility, thin architecture, and high ionic conductivity [57], PEDOT:PSS OECTs are applied in a wide variety of fields, including neural interfaces [45, 58], biological and chemical sensing [59, 60], printed circuits [61] and neuromorphic devices [62, 63], flexible and wearable electronics [43, 49, 64].

Cations are highly abundant in various environments such as living organisms, various biofluids, water and gases [32, 49, 65]. Using human sweat as an example, the detailed physiological data and key biomarkers can provide valuable insights into health [66-69]. Sodium ions (Na^+) are an important biomarker and their concentration serves as a helpful tool to identify and assess electrolyte imbalances [70, 71]. Serious health problems, such as hyponatremia and dehydration, can result from excessive loss of Na^+ ions (e.g. during sports activities) [72]. Potassium ions (K^+) are another essential biomarker for maintaining healthy conditions, including body fluid balance, acid-base balance and the regulation of body processes [32]. A low K^+ ion level can cause serious conditions such as hypokalemia, which increases the risk of high blood pressure and stroke [73]. Therefore, there is a significant need to conduct an accurate measurement for the concentration of Na^+ and K^+ ion in sweat. Additionally, ion detection in sweat is a popular choice for biosensing applications due to its ease of access and non-invasive sample collection [74-77]. It requires sensors which have high selectivity, low detection limit and biocompatibility for continuous health monitoring. PEDOT:PSS OECTs are easy to fabricate, possess high signal amplification, outstanding flexibility and biocompatibility [49, 78]. Furthermore, as they are sensitive to the variations in ionic strength of the analyte because of their ion conductive properties, they are highly suitable to detect a wide range of cations in electrolyte solutions [79]. However, a significant challenge is to introduce a selectivity towards specific ions in PEDOT:PSS OECTs [80]. To address this issue, one effective method is the incorporation of ion-selective membranes (ISMs) in the OECTs, which allows the selection and monitoring of a specific ion type [81-83]. The concentration of a specific ion can be precisely measured and quantitatively assessed by using these tailored OECT configurations [84]. The first ion selective organic electrochemical transistor (IS-OECT) was reported in 2014 and since then, considerable effort has been made to achieve significant progress in this impressive field [80, 83].

By using a series of electrical impulses, neurons in the mammalian brain can convey information from the brain to the entire body. Signals are transmitted between nerve cells both electrically and chemically. After passing the cell membrane, electrical signals are converted into chemical signals that carry small molecules named neurotransmitters (NTs) [85]. Therefore, NTs serve as intrinsic chemical messengers released by neurons to convey signals to the target neuron synapse. Figure 1.3 shows a synaptic transmission process, where NTs

are stored within synaptic vesicles. Owing to the function of relaying, modulating, and enhancing signals, NTs are employed for communications with organs, muscle cells and other neurons [85]. According to their mode of action, NTs can be divided into two distinct classes. One is the excitatory class, which works to activate receptors on the postsynaptic membrane. The other is the inhibitory class, which works in a reverse mechanism. There are several common types of NTs, including gamma-aminobutyric acid (GABA), acetylcholine and dopamine (DA) [85].

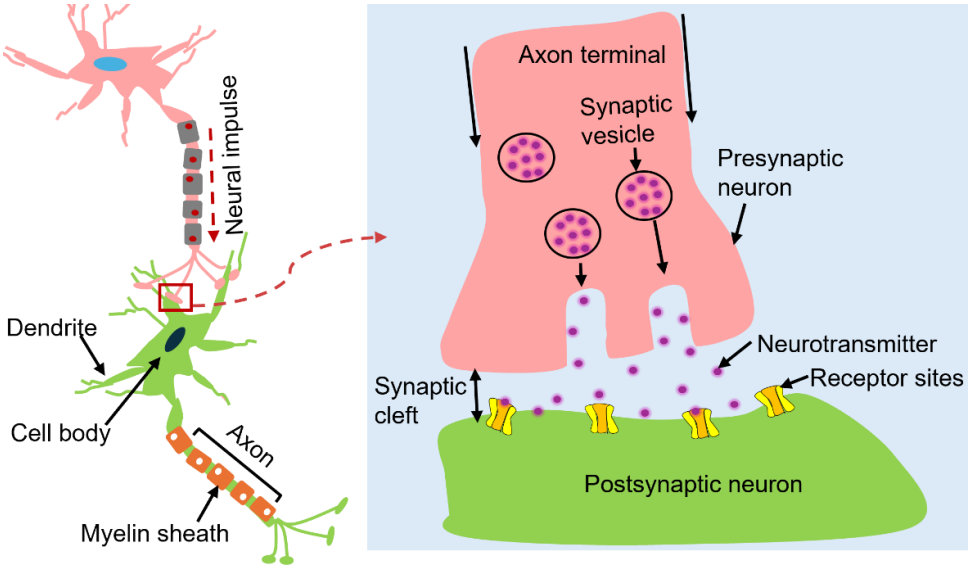

Figure 1.3: *A synaptic transmission process. Figure is adapted from reference [85].*

DA is an important NT which exists in the renal system, cardiovascular system, central nervous system (CNS) and other areas [86]. DA is connected to many various neurological functions, including cognition, motor control and learning. Apart from the processes in the CNS, DA affects a wide range of peripheral activities such as hormone release, sodium balance and blood pressure [87]. In the brain substantial nigra region, DA is produced by dopaminergic neurons and then transmitted throughout the whole body. In a healthy person, the concentration of DA is 0-0.25 nM in blood and 0.3-3 μM in urine [88]. Extremely abnormal concentrations of DA in the body can cause various physiological disorders. For example, high DA concentrations can result in cardiotoxicity which can cause hypertension, rapid heart rates and heart failure [89]. In contrast, low DA levels in the CNS are related to several neurological diseases, such as Parkinson's disease, Alzheimer's disease and depression [90]. Therefore, it is necessary to detect DA concentrations in vivo and in vitro, which plays a crucial role in clinical diagnosis, disease prevention and treatment efficacy monitoring [85]. However, the detection of DA is challenging due to its extremely low concentration, which in turn increases the requirements for selecting appropriate sensors. PEDOT:PSS OECTs have shown a promising ability for DA detection because of their high transconductance, low operating voltage and biocompatibility [91].

Since many analytes are fluids, such as sweat, blood and urine, it is essential to perform the analysis directly in the fluidic analytes, while keeping the required sample volume to a strict

minimum. A rapid analyte delivery can achieve real-time measurement with a controlled flow rate. Thus, a microfluidic system plays an important role here and can be adapted into the experiments. A microfluidic system is a technology that enables the manipulation of small fluid volumes, typically within the range of nanoliter to microliters, using small channels with dimensions of ten to hundreds of micrometers [92]. The fluid flow can be automated, enabling faster and more reproducible results. Microfluidic systems exhibit several distinct advantages [92]: first, a microfluidic system requires a very small amount of samples which reduces waste. Second, a microfluidic system allows for highly accurate and reproducible experiments due to the precise control of fluid flow. Subsequently, the small-scale microfluidic system can process samples quickly, providing faster results than traditional methods. Additionally, numerous microfluidic devices are portable, enabling in-situ monitoring and point-of-care testing. Therefore, microfluidic systems have been used in different applications, including medical diagnostics [93, 94], environmental monitoring [95, 96], and cell biology [97, 98].

Textile sensors play a significant role in various healthcare applications because they exhibit excellent properties such as comfortability, flexibility and breathability [99, 100]. In the near future, innovations based on textile sensors are expected to be commercially available in the medical and sports industries [100, 101]. Additionally, textile sensors can be utilized as a highly effective tool for real-time and non-invasive monitoring of numerous biological parameters, such as glucose levels [102-104], ion concentrations [105, 106] and pH changes [105, 107]. PEDOT:PSS can also be integrated into textile sensors, which is typically cost-effective and easily accessible [105, 108, 109]. Such integration extends its utility to diverse applications, including humidity monitoring [108] and gas sensing [109].

1.4 Structure of the thesis

Despite the countless applications of PEDOT:PSS OECTs in both academia and industry, research to improve the functionality and performance of such sensors is ongoing. The first main objective of this thesis focuses on enhancing the stability, reliability, and electrochemical performance of OECTs for biochemical applications. The second main objective is the development of sensors to detect ions and NTs with high sensitivity and selectivity, which can be used for sweat and environment monitoring. To achieve these objectives, micro-fabrication methods are introduced, which are used to realize PEDOT:PSS OECT microarrays at wafer-scale. A few crucial parameters of OECTs are also investigated, such as contact materials, the materials of the gate electrode, the electrical properties of PEDOT:PSS thin films and the device structures. The integration of an ISM onto the OECTs is needed to prevent undesired ions from entering the PEDOT:PSS film, enabling a selective detection of the desired ions (Na^+ and K^+), while the ISM is optimized to evaluate the sensitivity and selectivity of the sensors for ion detection. Additionally, PEDOT:PSS is integrated into the cotton yarn as the textile sensors for the detection of specific ions. A simple and reproducible fabrication process for manufacturing textile sensors based on PEDOT:PSS is demonstrated, and the stability and flexibility of these sensors is investigated by electrical measurements. Furthermore, a novel detection platform is developed to detect DA, achieving accurate and sensitive detection at

low concentrations while realizing a highly selective detection against interfering substances such as AA and UA. The functionality of the sensors is demonstrated by using a microfluidic system for real-time monitoring of ions and DA concentrations in the solution.

Chapter 2 explains the fundamentals and theories applied in this thesis. Section 2.1 introduces the conductive polymer PEDOT:PSS, including its chemical structure, electrical conductivity and enhancement of electrical properties. Following this, the OECTs are presented in section 2.2, where the working principle, output and transfer characteristics and their applications are discussed. Section 2.3 illustrates the solid-liquid interface and explains the different models of electrical double layer. In section 2.4, the theory of ISM and the working principle of ion detection using PEDOT:PSS OECTs are explained. The electrical circuit of PEDOT:PSS is also described. Section 2.5 presents the fundamental theory of DA and its detection using OECTs. The chemical structure of DA and its interferents in the biological samples are first introduced. Then, the state-of-art research in DA detection using PEDOT:PSS OECTs is summarized, including sensitivity, limit of detection and selectivity. Subsequently, the working principle and equations for DA detection using PEDOT:PSS OECTs are explained.

Chapter 3 covers all the methods that are used throughout this thesis. In section 3.1, the utilized metallization methods for evaporation and sputtering are discussed with relevant equipment presented in detail. Section 3.2 shows the lift-off process during the chip fabrication and its importance for successful fabrication of OECTs. Following this, section 3.3 introduces plasma enhanced chemical vapor deposition (PECVD). Section 3.4 shows the reactive ion etching (RIE) process, which is used for etching the silicon oxide passivation layer. Section 3.5 discusses the Van der Pauw method for measuring the electrical conductivity of PEDOT:PSS film, while section 3.6 focuses on the fundamental theory of cyclic voltammetry.

Chapter 4 presents the experimental procedures performed in this thesis. Details of the micro fabrication process for OECTs are discussed in section 4.1, including chip design, the preparation of different PEDOT:PSS solutions and the chip fabrication protocol. Section 4.2 introduces the buffer solution preparation and the measurement setup which are used for the electrical characterization of PEDOT:PSS OECTs. Section 4.3 shows the design and fabrication of the microfluidic system in the electrical measurement and application of PEDOT:PSS OECTs. Subsequently, section 4.4 displays the preparation of Na^+ and K^+ ISM solutions and the integration methods of ISM onto the OECTs. Section 4.5 describes the preparation process for DA, UA, AA and chitosan solutions, while presenting the cyclic voltammetry characterization for DA detection. In section 4.6, the detailed processes for the manufacturing of PEDOT:PSS based textile sensors are discussed.

Chapter 5 displays the results of the experiments within this thesis. Section 5.1 discusses the results of lithography fabrication, wire bonding and encapsulation for the OECT microarrays. Section 5.2 presents the electrical conductivity of PEDOT:PSS thin films and the electrical characteristics of OECTs. The effect of different contact materials (e.g., Au, Pt and IrO_x) and

various thicknesses of PEDOT:PSS films on the transistor performance are also investigated. In section 5.3, the highly sensitive and selective detection for different ions using PEDOT:PSS OECTs covered with ISMs is shown. Furthermore, the multiplexed sensing, real-time measurement and reversible detection of ions using the ISMs based PEDOT:PSS OECTs are studied. Section 5.4 focuses on DA detection using PEDOT:PSS OECTs, including sensitivity, selectivity and real-time measurement. The surface of the Pt gate electrode is modified to improve the selective detection of DA over AA and UA. Section 5.5 discusses the realization of ion selective textile sensors, where PEDOT:PSS is integrated for selective ion detection.

Chapter 6 summarizes the results and findings achieved in this thesis, such as an optimized microfabrication technique for manufacturing the OECTs, and specialized applications of these OECTs for ion and DA detection.

Finally, chapter 7 provides an outlook for further improvements and applications of the OECTs, such as by evaluating their performance in complex environments, monitoring Ca^{2+} and NH^{4+} ions and utilizing the OECTs in other fields.

2 Fundamentals and theories

In this chapter, the theorical background applied in this thesis is presented, including the working principle of PEDOT:PSS OECTs, the models of the electrical double layer and the detection mechanism of ions and DA. These fundamentals provide the significant basics for the following experiments and results.

2.1 PEDOT:PSS

Recently, PEDOT:PSS has attracted significant research attention [39-41], due to its outstanding properties, including high electrical conductivity, flexibility, transparency and biocompatibility [43-45]. PEDOT:PSS is a hole-conducting organic semiconductor, which provides both ionic and electronic conductivity [42]. It consists of positively charged conjugated PEDOT and negatively charged saturated PSS, as shown by its chemical structure in figure 2.1 (a). Mobile holes in the PEDOT chains are effectively compensated by the presence of sulfonate anions from the PSS chains. PEDOT has a low solubility in most common solvents while PSS is a polymer surfactant that increases the dispersion and stabilization of PEDOT in water and other solvents [56, 110]. The microstructure of PEDOT:PSS is commonly displayed as shown in figure 2.1 (b) [57]. PEDOT chains are polymerized onto the PSS template, presented in part a, forming the gel particles (part b) with a pancake-like morphology after the deposition. The resulting PEDOT:PSS film in parts c and d in figure 2.1 (b) exhibits signs of π-stacking. It is composed of the PEDOT:PSS phase in the color blue, while the PSS phase is exhibited in the color grey. A thin and reliable film can be fabricated by a spin-coating technique using commercially available solutions, where the resulting film consists of conductive and hydrophobic PEDOT-rich cores and hydrophilic and insulating PSS-rich shells [111].

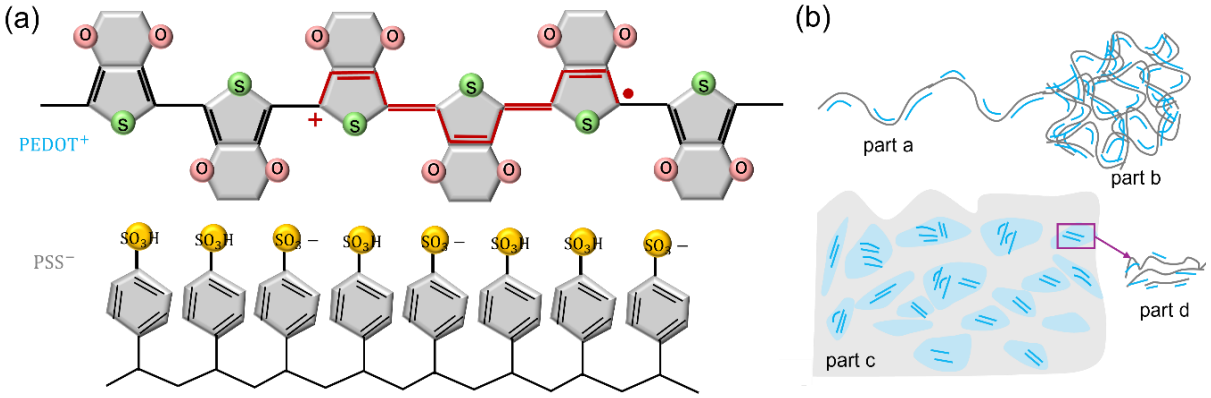

Figure 2.1: *(a) Chemical structure of PEDOT:PSS, (b) The described microstructure of the conducting polymer system. Part a shows the synthesis onto the PSS template, part b displays colloidal gel particles formed in dispersion, part c is the resulting film containing PEDOT:PSS-rich (blue) and PSS-rich (grey) phases, where crystallites (part d) support enhanced electronic transport. Figure is adapted from reference [57].*

PEDOT contains two distinct chemical structures: benzoid and quinoid structures [112]. Figure 2.2 (a) shows the benzoid structure of PEDOT, where two conjugated π-electrons are clearly presented on the C_α=C_β bond. The benzoid structure consists of coil conformation, where the conjugated π-electrons exhibit limited delocalization over the entire PEDOT chain, resulting in

a low charge-carrier mobility in PEDOT:PSS film. Conversely, as displayed in figure 2.2 (b), the quinoid structure lacks conjugated π-electrons on the C_α-C_β bond. The quinoid structure contains linear or expanded-coil conformations in which the adjacent thiophene rings within the PEDOT chains align parallel to one another and the conjugated π-electrons are delocalized through the whole chain. Thus, the charge-carrier mobility within the film will be enhanced [113].

In the case of pristine PEDOT:PSS, both benzoid and quinoid structures exist within the matrix. Through the application of tailored methods such as the incorporation of the organic compounds, it becomes feasible to initiate a structural transformation of PEDOT chains from their coiled conformation to a linear or expanded-coil conformation [114]. This transformation, involving a change in the bonding configuration from C_α-$C_{\alpha'}$ (C_β-C_β) to C_α=$C_{\alpha'}$ (C_β=C_β), enhances the charge-carrier mobility within PEDOT:PSS chains and the interchain interactions along the PEDOT chains. The quinoid structure exhibits enhanced electrical conductivity compared to the benzoid structure due to the presence of delocalized electrons within its molecular framework. Therefore, by tuning the chemical structures of PEDOT:PSS, its electronic characteristics can be flexibly adjusted [114].

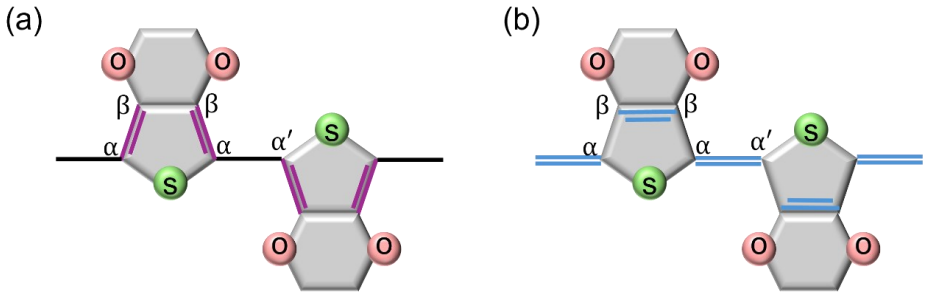

Figure 2.2: *Two distinct PEDOT structures: (a) Benzoid structure and (b) Quinoid structure. Figure is adapted from reference [114].*

The electrical conductivity of pristine PEDOT:PSS films is as low as 1 S/cm, limiting its practical applications [115]. Therefore, it is crucial to improve the electrical conductivity of the films. There are numerous approaches to this, such as light treatment [116, 117], thermal annealing [118] and the incorporation of various chemical materials [119]. Figure 2.3 illustrates several approaches that have been reported to significantly improve the conductivity values of PEDOT:PSS over the past few decades [119]. Mixing PEDOT:PSS with various chemical materials, including organic solvents (e.g. dimethyl sulfoxide (DMSO) [120] and ethylene glycol (EG) [121]), ionic liquids [122], salt solution [123, 124] and sulfuric acid (H_2SO_4) [125], improved the electrical conductivity of PEDOT:PSS films. Among these methods, a common technique is the organic solvent treatment. One strategy involves the direct addition of organic solvents (e.g. DMSO and EG) into the PEDOT:PSS aqueous solution. Both DMSO and EG have shown remarkable enhancements in the electrical conductivity of PEDOT:PSS films. For instance, the conductivity range of pristine PEDOT:PSS films (Clevios™ PH 1000) is typically between 0.2 and 1 S/cm, and can be increased to 600 S/cm after the addition of DMSO [48]. Likewise, the addition of EG can improve the conductivity of pristine PEDOT:PSS (Clevios™

PH 500) from 0.4 S/cm to 443 S/cm [126]. The post-treatment approach is another method of organic solvent treatment to improve the electrical conductivity of PEDOT:PSS films. As an example, treating the PEDOT:PSS films with EG through line patterning can significantly increase the conductivity of the films (Baytron P) up to 900 times [127]. Other solvents, such as hexafluoroacetone (HFA) and methanol, can be utilized during post-treatment. Employing the HFA post-treatment four times can increase the conductivity of PEDOT:PSS (Clevios™ PH 1000) from 0.3 to 1325 S/cm [128]. Similarly, the electrical conductivity of the films (Clevios™ PH 1000) can be enhanced from 0.3 to 1362 S/cm through post-treatment with methanol [129]. In addition to the organic solvent treatment, acid treatment can also achieve extremely high conductivities. For example, post-treatment of the PEDOT:PSS film with H_2SO_4 can lead to electrical conductivities as high as 4380 S/cm [125]. The enhancement in the electrical conductivity of PEDOT:PSS film can be attributed to two primary factors: the phase separation of the excess PSS from the PEDOT:PSS composite film [130, 131] and the conformational changes in the PEDOT structures [132].

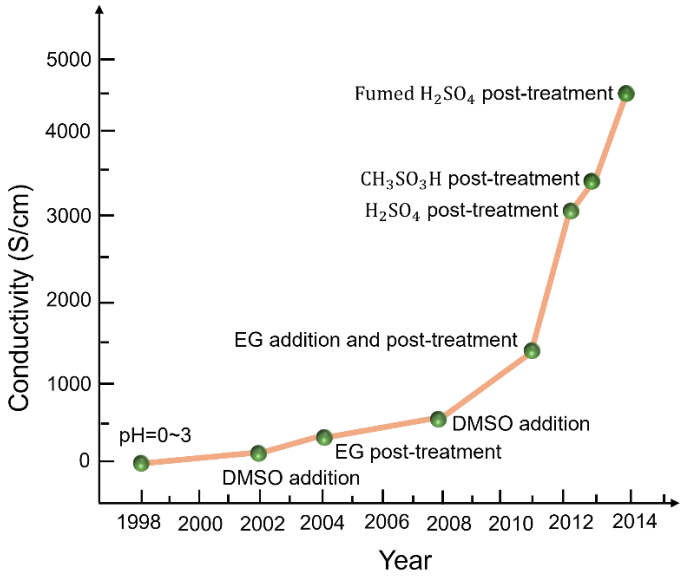

Figure 2.3: *Timeline of conductivity values for PEDOT:PSS. Figure is adapted from reference [119].*

2.2 Organic electrochemical transistors

2.2.1 Working principle

OECTs are promising devices for various biosensing applications, owing to their remarkable signal amplification, flexible organic materials and straightforward architecture [41, 55, 58]. An OECT typically consists of three terminals: source, drain and gate, as shown in figure 2.4 (a). The metallic source and drain electrodes form a contact to the conductive polymer and define the channel. The gate electrode is immersed into the electrolyte and establishes the electrical contact to the electrolyte solution [55].

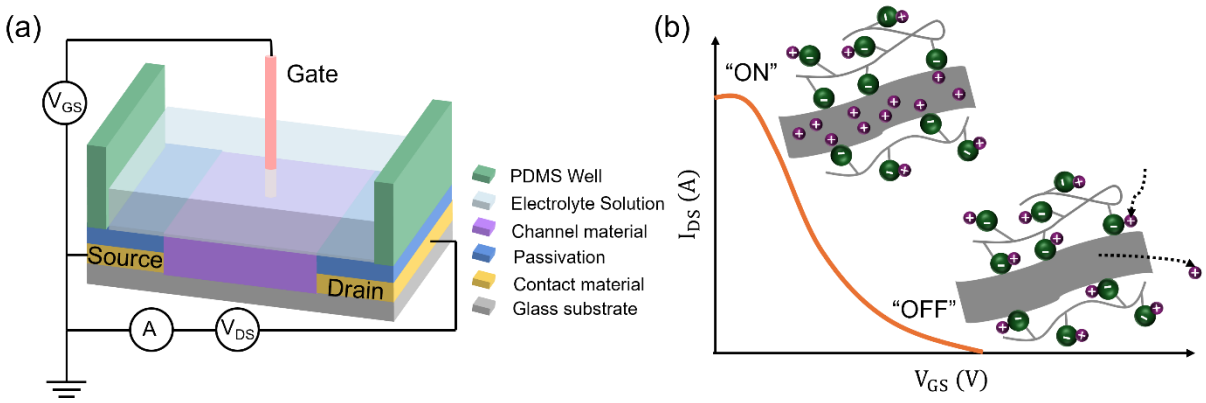

Figure 2.4: *(a) The schematic of an OECT, (b) Working principle of PEDOT:PSS OECTs. Figure is adapted from reference [55].*

In the OECTs, the source electrode is usually grounded, which serves as a reference potential. The source and drain electrodes are connected through the conductive polymer, which also acts as the channel material for charge transport. The gate electrode is in contact with the conductive polymer through the electrolyte solution. When drain voltage (V_{DS}) is applied between the source and drain electrodes, the mobile charge carriers flow through the channel and lead to the generation of the drain current (I_{DS}). After applying the various gate voltages (V_{GS}) between the source and gate electrodes, the magnitude of I_{DS} will be regulated due to the modulation of the electrical conductivity of the conductive polymer [55].

Over recent years, PEDOT:PSS has been commonly integrated into OECTs for various applications [39-41]. In PEDOT:PSS OECTs, the holes in the PEDOT chains carry the charge in the channel of the transistor. The negatively charged sulfonate groups in PSS chains provide charge compensation for the holes. PEDOT:PSS OECTs typically operate in depletion mode because PEDOT:PSS itself is conductive. Figure 2.4 (b) displays the working principle of PEDOT:PSS OECTs [55]. Without V_{GS} applied, the PEDOT:PSS channel has a current flow with the applied V_{DS} and the OECT is in the "ON" state. When a positive V_{GS} is applied, negatively charged anions in the electrolyte solution are attracted to the gate electrode and positively charged cations are pushed towards the channel. These cations will enter the PEDOT:PSS film and compensate the anionic sulfonate groups on the PSS chains. Therefore, the negative charge compensation for the positively charged carriers in the PEDOT will reduce, leading to a decrease in the number of the holes in the OECT channel and subsequently the reduction of I_{DS}. When a sufficiently high positive gate voltage is applied, all anionic sulfonate groups on the PSS chains are compensated by cations from the electrolyte, and the transistor remains in its "OFF" state.

2.2.2 Output and transfer characteristics

The recorded output and transfer characteristics of the OECTs evaluate their steady-state performance. Figure 2.5 (a) shows the output characteristics, presenting the relationship between I_{DS} and V_{DS}. The operation of the transistor exhibits two different regimes, which are the linear and saturation regimes. At each given V_{GS}, I_{DS} first increases linearly as the V_{DS}

value increases. After a certain value of V_{DS}, I_{DS} becomes constant, indicating that I_{DS} has reached the saturation regime. The pinch-off voltage (V_P) indicates the transition of the V_{DS} value from the linear to saturation regime [133, 134].

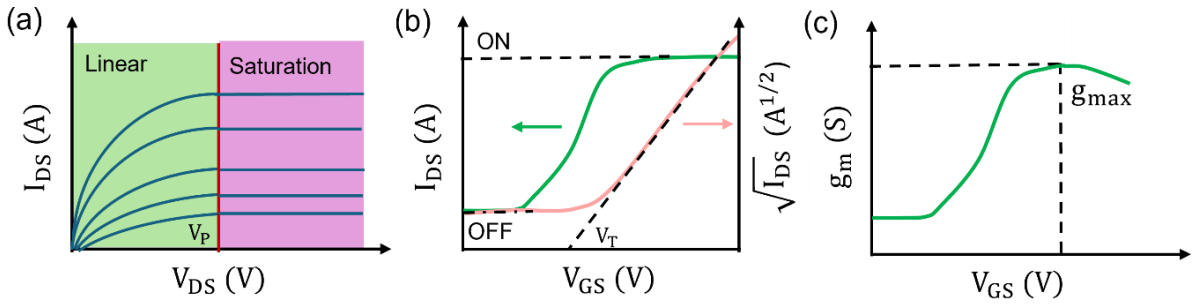

Figure 2.5: *(a) Output characteristics, (b) Transfer characteristics (green curve) and (c) Transconductance of an OECT. Figure is adapted from reference [133].*

The green curve in figure 2.5 (b) displays the transfer characteristics of the OECTs [133]. Transfer characteristics demonstrate the relationship between I_{DS} and V_{GS}. Certain key parameters of the transistors can be obtained from the transfer curve including threshold voltage (V_T), ON/OFF ratio and transconductance (g_m). There are a few approaches to determine and extract the value of V_T such as is displayed in figure 2.5 (b). The function between the square root of I_{DS} and V_{GS} is plotted and then the linear part of the slope with the maximum magnitude is plotted over the entire x-axis. Intersection with the x-axis determines V_T. Another widely used method for extracting V_T is the linear extrapolation method in the linear region of the transfer curve. At a certain constant value of V_{DS}, the linear extrapolation is performed where the transfer curve reaches its maximum slope point. V_T is then extracted at the point where the linear extrapolation intercepts the V_{GS} axis [135]. As shown in figure 2.5 (b), the ON/OFF ratio of the OECTs is determined as the ratio of the maximum I_D when the OECTs are in the "ON" state and the I_{DS} when the OECTs are turned off. A large and stable ON/OFF ratio is preferable for transistors as it is essential for the improvement of the signal-to-noise ratio (SNR) of the device in order to achieve the lower limit of detection (LoD) [133]. g_m is defined by the first derivative of the transfer characteristics at a constant V_{DS}. Figure 2.5 (c) shows the relationship between g_m and V_{GS}, in which the maximum value of transconductance (g_{max}) is one of the main performance metrics for the OECT. g_m values are typically impacted by the channel dimensions (width, length, and film thickness), the properties of the channel material, V_T and V_{GS}.

The operation of PEDOT:PSS OECTs can also be described using an "electrochemical doping" mechanism. By applying the positive V_{GS}, the cations will be injected into the PEDOT:PSS channel from the electrolyte solution, leading to the de-doping of PEDOT:PSS. The de-doping process of PEDOT:PSS can be described by the following equation (2.1) [136]:

$$n\,(PEDOT^+:PSS^-) + M^{n+} + ne^- \leftrightarrow n\,PEDOT + M^{n+}:PSS^- \qquad (2.1)$$

where M^{n+} represents the cations from the electrolyte, n is the number of charges of the cation. e^- refers to the electron from the source electrode. This mechanism leads to a reduction in available charge carriers in PEDOT, resulting in a decrease in conductivity of the PEDOT:PSS

and a change in the electrical characteristics of the transistors. Bernards et al. described the OECTs using the equation (2.2) below [137]:

$$I_{CH} = \begin{cases} \mu C^* \frac{Wd}{L}\left[1 - \frac{V_G - \frac{1}{2}V_D}{V_T}\right]V_D, & \text{for } V_D > V_G - V_T \\ -\mu C^* \frac{Wd}{L}\frac{|V_G - V_T|^2}{2V_T}, & \text{for } V_D < V_G - V_T \end{cases} \quad (2.2)$$

where I_{CH} is the channel current, μ is the hole mobility, C* is the volumetric capacitance, V_G is the gate voltage, V_D is the drain voltage, V_T is the threshold voltage and W, d, L are the width, thickness and length of the channel film, respectively.

g_m describes the amplification properties of the device and quantifies how effectively the OECTs can convert the voltage changes at the gate electrode into the changes in the drain current [56]. The steeper transfer curves of the OECTs exhibit a higher transconductance, indicating a stronger conversion of the gate voltage signal to the drain current. As a result, the amplification capabilities at the gate electrode will be enhanced. By taking the first derivative of equation (2.2) with respect to the gate voltage, the g_m of the transistor can be obtained as shown in equation (2.3) [56]:

$$g_m = \begin{cases} -\mu C^* \frac{Wd}{L} V_D, & \text{for } V_D > V_G - V_T \\ \mu C^* \frac{Wd}{L}[V_G - V_T], & \text{for } V_D < V_G - V_T \end{cases} \quad (2.3)$$

Figure 2.6 (a) presents the relationship between g_m and the channel geometry (Wd/L) for microscale OECTs when various channel materials are utilized [56]. The fitted dotted lines depict that $g_m = \alpha Wd/L$, where α is the proportionality value and is different for each channel material. Each line exhibits a linear function to the channel geometry, indicating that g_m is proportional to Wd/L [138]. The performance of the OECTs can be designed and tuned using different channel geometries. The relationship between g_m and Wd/L of PEDOT:PSS OECTs is displayed by the right-facing, green triangles in figure 2.6 (a). Using impedance spectroscopy, the channel capacitance, C_{CH}, for the devices with different geometries was investigated [58, 139-141]. Figure 2.6 (b) shows that C_{CH} is proportional to WdL over more than six orders of magnitude of variation in the channel volume. The volumetric capacitance, C*, can be obtained by the slope of the linear curve [56].

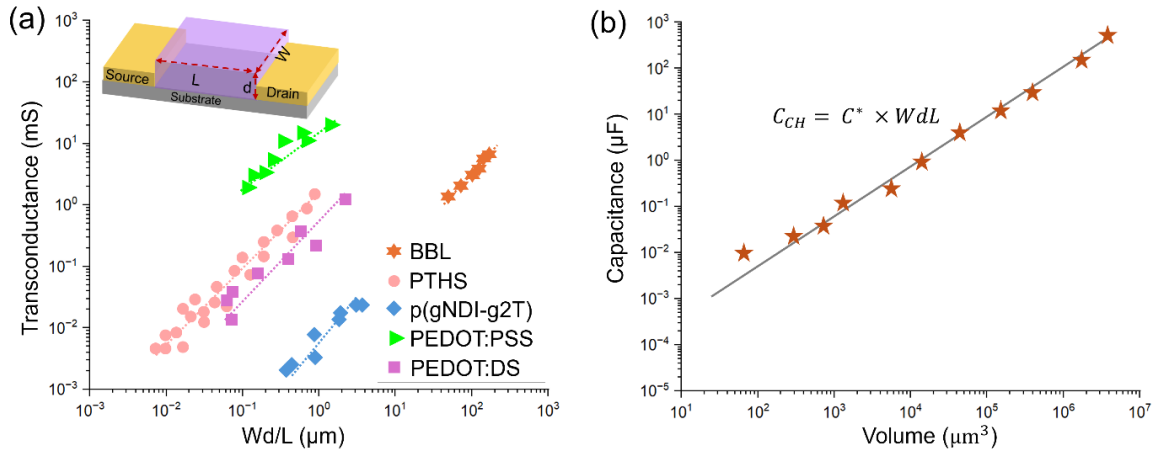

Figure 2.6: *(a) The relationship between the transconductance (gm) and the channel geometry (Wd/L) for microscale OECTs with various materials, (b) The relationship between channel capacitance (C_{CH}) and channel geometry (WdL) of OECTs. Figure is adapted from reference [56].*

2.2.3 Applications

OECTs exhibit numerous advantages including low operating voltage, excellent biocompatibility, and stable operation in aqueous environments. These properties make them well-suited for in-situ detection applications. In recent years, the utilization and applications of OECTs have increased, including in chemical and biological sensing, neural interfaces, flexible and wearable electronics.

In chemical sensing, OECTs offer remarkable sensitivity and selectivity to a range of chemical analytes in various environments. One of these analytes is ion and the OECTs can be used to transduce ion concentrations into electrical signals with high sensitivity, selectivity, and real-time response. Lin et al. conducted a comprehensive investigation into the ion-sensitive properties of OECTs utilizing a simple device configuration (Figure 2.7 (a)). Au was used as the drain and source electrodes, while the gate electrodes consisted of Cr/Au, Ag/AgCl and Pt. In their study, the different gate electrodes significantly impacted the performance of the OECT devices, offering a valuable understanding of the physical and chemical mechanisms of the OECT operation. Additionally, the performance of ion detection using PEDOT:PSS OECTs was systematically examined in diverse aqueous solutions containing various cations, such as H^+, K^+, Na^+, Ca^{2+} and Al^{3+} [78]. Sessolo et al. introduced an ISM between the conductive polymer and the reference gel electrolyte, indicating an enhanced g_m of the OECTs (Figure 2.7 (b)). Their work highlighted the potential of OECTs as solid-state ion sensors and demonstrated the high sensitivity of approximately 50 μA/decade for K^+ ion detection in a concentration range from 0.1 mM to 0.1 M. Meanwhile, their findings revealed a significant selectivity compared to similar cations like Na^+ ion [83]. Ghittorelli et al. reported for the first time that OECTs can overcome the sensitivity limitations of conventional transistor-based approaches. Their work displayed sensitivity with the values of 414 mV/decade for K^+ ion detection and 516 mV/decade for Na^+ ion detection. These remarkable results represented

improvement compared to previously reported electrochemical ion sensors, demonstrating the potential of OECT technology in advancing ion detection capabilities [81].

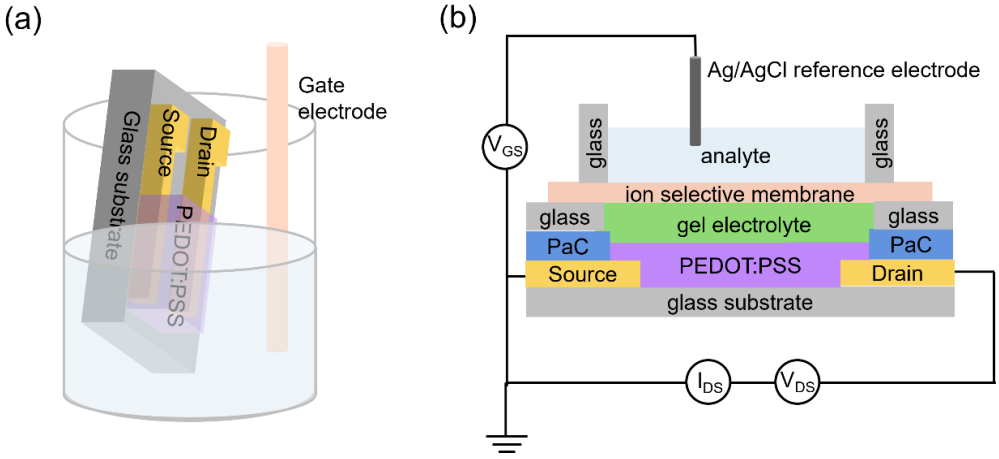

Figure 2.7: *(a) Schematic configuration of an PEDOT:PSS based OECT. Figure is adapted from reference [78], (b) Schematic of the OECT integrated with an ISM. Figure is adapted from reference [83].*

Accurate and selective detection of ions by OECTs within physiological fluids, such as blood, sweat and saliva, shows their importance in healthcare applications. Flexible and wearable sensors present a promising solution for the development of a new generation of devices for real-time and in-suit physiological monitoring. These sensors have the potential to be integrated into daily life due to their non-invasive properties. To monitor the concentration of NaCl in water, Tarabella et al. integrated PEDOT:PSS into natural cotton fiber through a soaking process. This conductive cotton fiber served as the transistor channel and was directly connected with a liquid electrolyte using the Ag wire gate electrode. Their results indicated that the cotton-based OECTs were effective in sensing the concentration of NaCl [142]. Demuru et al. developed a sensing platform integrated with the microfluidics and inkjet-printed ion-selective OECT arrays for flexible and wearable detection of K^+, Na^+ and H^+ ions (Figure 2.8 (a)). This platform was successfully fabricated by coating the PEDOT:PSS channel of the OECTs with K^+, Na^+ and H^+ ISMs. The electrical characteristics of the devices indicated that the effect of these membranes on the electrical and time responses of the OECTs can be disregarded, while these sensors enabled good ion selectivity as well as excellent sensing capabilities for K^+, Na^+ and pH detection [143].

Keene et al. designed the flexible and wearable PEDOT:PSS OECTs for the multiplexed detection of ammonium (NH_4^+) and calcium (Ca^{2+}) concentrations in sweat during physical exercise. The OECTs contained two planar gates and two PEDOT:PSS films were integrated with the ISMs. Flexible and stretchable styrene-ethylene-butene-styrene (SEBS) material was chosen as the substrate, while a laser-patterned microcapillary layer was utilized to acquire the sweat sample (Figure 2.8 (b)). The output and transfer curves proved that the ISM had minimal impact on the electrical characteristics of the devices, while the calibration curves showed that the OECTs exhibited highly selective detection to NH_4^+ and Ca^{2+} ions. Finally, the on-body measurements using the patch-type OECTs were conducted. Furthermore, the

OECTs enabled the detection of NH_4^+ and Ca^{2+} ion concentration within the range from 0.01 to 100 mM, which effectively covered the physiological levels of both ions in sweat [49].

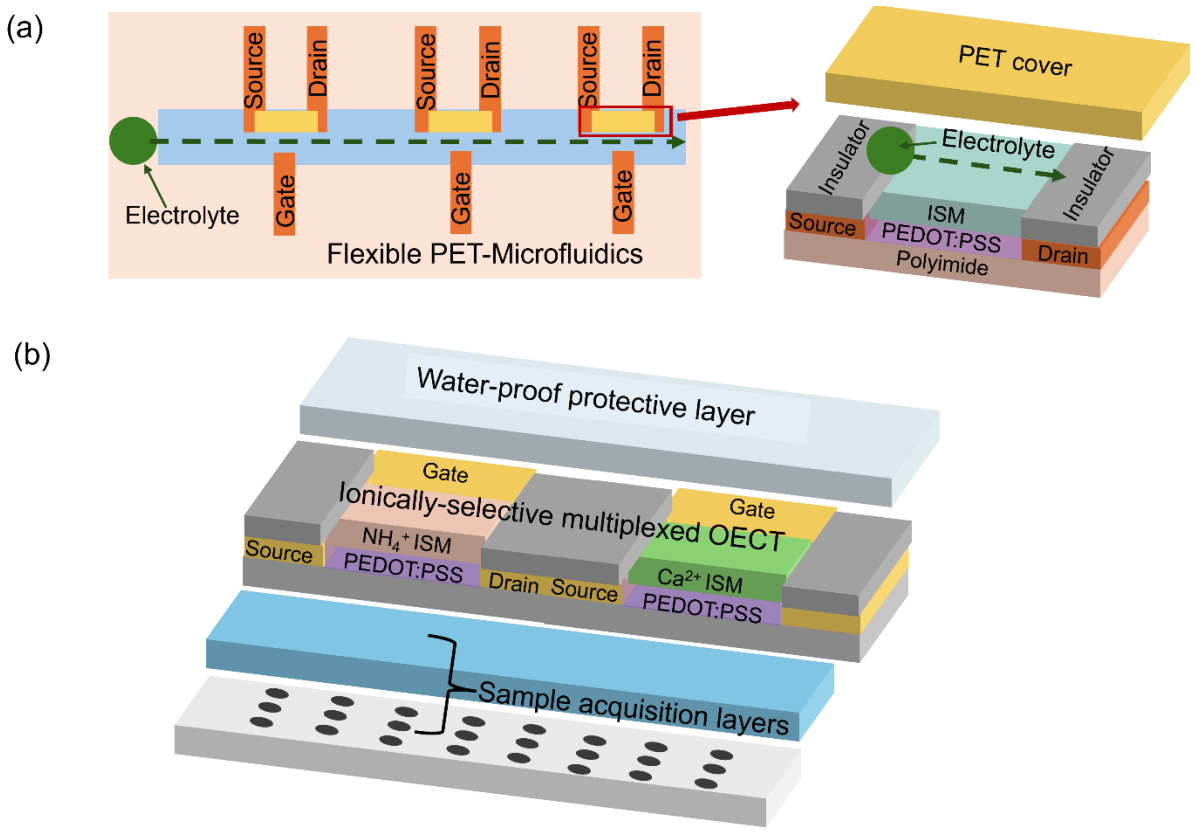

Figure 2.8: *(a) The schematic of the flexible OECTs integrated into the microfluidic system. Figure is adapted from reference [143], (b) Schematic presentation of the wearable OECTs based on ISMs for multiplexed detection of ammonium and calcium ions. Figure is adapted from reference [49].*

OECTs can be applied in biological sensing to monitor the concentrations of various analytes such as glucose, lactate, and neurotransmitters. Macaya et al. investigated the glucose detection using PEDOT:PSS OECTs with a Pt gate electrode. These devices operated based on the enzymatic reaction between glucose and glucose oxidase (GO_x), leading to the production of hydrogen peroxide (H_2O_2) and the generation of an additional gate current. This resulted in a decrease in the electrical conductivity of the PEDOT:PSS and subsequently the drain current of the devices. Moreover, the reduced drain current was proportional to the glucose concentrations in the electrolyte solution. Their work demonstrated the capability of these OECTs to effectively detect glucose concentrations within the micromolar range, aligning well with the typical glucose concentrations in human saliva [144]. Tarabella et al. systematically studied the influence of the gate electrode materials on the performance of PEDOT:PSS OECTs. In comparison to using a Pt gate electrode, OECTs demonstrated enhanced current modulation for NaCl concentration detection when Ag was utilized as the gate electrode [145]. Tang et al. fabricated the PEDOT:PSS OECTs with Au as the source and drain electrodes and a modified Pt gate electrode to detect glucose concentrations. As shown in (Figure 2.9 (a)), the surface of the Pt gate electrode was modified by multi-wall carbon

nanotubes (MWCNT) or Pt nanoparticles (NPs). The morphologies of these two nanomaterials were characterized using the TEM technique, indicating that the diameter of the MWCNT was 10-40 nm and furthermore that the Pt NPs with the average size of 100 nm were uniformly distributed. A real-time measurement was performed for glucose detection using the devices with modified Pt gate electrode, demonstrating a significant enhancement in the sensitivity with a detection limit as low as 5 nM. Moreover, the devices exhibited stable performance in consecutive measurements for 8 days, highlighting their possibility in real applications [60]. Pappa et al. designed a novel sensors platform consisting of three different PEDOT:PSS OECTs with the planar gate configuration. Functionalized PEDOT:PSS was utilized as the gate electrode to detect the concentration of glucose, lactate and cholesterol. This platform was combined with the PDMS microfluidics, enabling the simultaneous detection for various biomarkers in complex media with avoiding electrical disturbance between each OECT (Figure 2.9 (b)). Finally, this biosensing platform was utilized to quantitatively monitor the concentrations of these analytes in human saliva samples in real-time with high sensitivity and selectivity, covering the physiological levels in saliva [146].

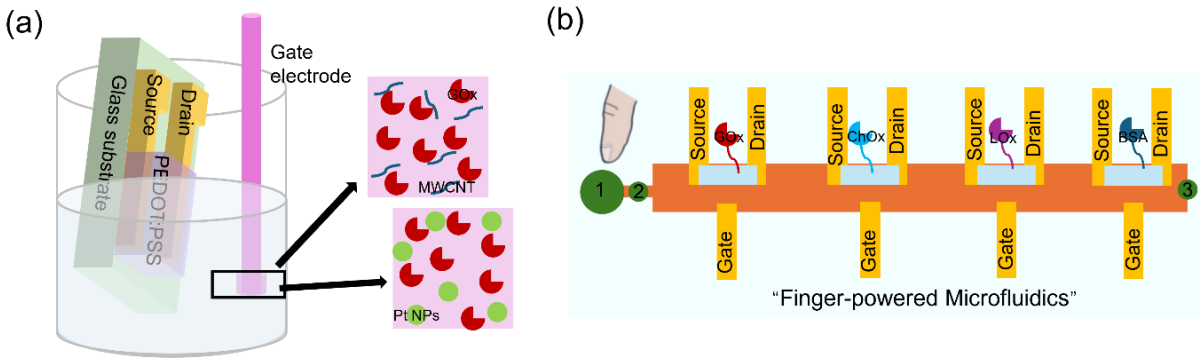

Figure 2.9: *(a) The schematic presentation of PEDOT:PSS OECTs for glucose detection. Figure is adapted from reference [60], (b) Schematic of the biosensing multiplatform using "finger-powered" PDMS microfluidics. Figure is adapted from reference [146].*

DA is one of the important NTs in the functions of the cardiovascular, central nervous, and renal systems. An abnormal level of DA can result in serious diseases, thus making DA detection crucial. Gualandi et al. fabricated the OECTs using PEDOT:PSS as the source, drain and gate electrodes for DA detection with high selectivity over AA and UA molecules. For comparison, traditional techniques of CV and differential pulse voltammetry (DPV) involving varied gate voltages and scan rates were also employed for DA detection. The electrical analysis showed that all the OECTs exhibited an advanced sensitivity and limit of detection, highlighting their potential as promising alternatives for DA detection [147]. Ji et al. fabricated OECTs using a metal-free gate electrode integrated with the Nafion and reduced graphene oxide-wrapped carbonized silk fabric (Nafion/rGO/CSF). The morphology of the samples was characterized using SEM and the cross-section was observed by TEM, indicating that the distribution of Nafion was uniform and had minimal impact on the structure of Nafion/rGO/CSF. The transfer characteristics of OECTs were evaluated using a PBS solution, with an obvious shift in the transfer curve to lower current values after a 0.1 M DA solution was added. Following this, a real-time measurement was performed using these functional devices,

demonstrating their sensing capabilities for DA detection with high sensitivity and selectivity within the concentration range of 1 nM to 30 µM.

Eventually, the stability of these OECTs was tested under bend states for 1000 times and a negligible change of the transfer curves was observed, highlighting their use as flexible sensors. The reliability of the devices was further investigated using artificial urine, facilitating the DA detection in practical application [148].

Besides the aforementioned applications, researchers have expanded the applications of OECTs into other fields. Hempel et al. introduced a novel PEDOT:PSS OECT platform for cell-substrate adhesion assays, enabling the precise sensing of cell impedance at the single-cell level. These OECT devices showed outstanding stability and rapid response characteristics, making them suitable for investigating cellular interactions [40]. Moreover, Hempel et al. extended the capabilities of OECT devices to monitor the electrophysiological activity of cardiac cell lines, particularly HL-1 cells. The OECTs exhibited a satisfactory SNR and the capability to detect rapid extracellular signal components, allowing for the observation of cardiac cell behavior and function [51]. Khodagholy et al. reported the utility of OECTs for in vivo recordings of electrophysiological activities on the brain surface. They fabricated highly conformable arrays of OECTs and used them to perform electrocorticography on the cortex of rats. The detection involved choosing various voltage signals through the gate electrodes of the OECTs. These signals induced changes in the g_m of the devices, subsequently influencing the drain current. Due to the high g_m, the OECTs were able to detect the low signals with remarkable high SNR [62]. In conclusion, the multiple examples of successful application of OECTs provided in this section highlight their adaptability and capacity to be used in countless fields of research.

2.3 Solid-liquid interface and electrical double layer

The solid-liquid interface is the boundary or region where a solid substance contacts a liquid substance. This interface is particularly interesting in various scientific and engineering fields, including physics, chemistry, and materials science. Due to the high dielectric constant, water is a decent solvent and therefore the most important liquid for ions. The majority of surfaces in water are charged. Surface charging can also be generated by the absorption or dissociation of ions from a surface. For example, in water, oxides often exhibit a negative charge resulting from the dissociation of a proton from the surface hydroxyl group [149]. Charging the surface can also be accomplished by subjecting it to an external electrical potential between the surface and a corresponding counter electrode. This will induce the accumulation or depletion of charge on the surface depending on the polarity of the applied potential. Surface charges create an electric field that attracts counter ions. At the solid-liquid interface, the layer of surface charges and counter ions is named the ‘electric double layer’ (EDL) [149].

In 1853, Helmholtz defined the term ‘electric double layer’ when he observed the formation of two layers of opposite polarity at the interface between a metal electrode and an electrolyte. This phenomenon was modeled as a parallel-plate capacitor, where the counter ions directly bind to the surface and neutralize the surface charge [149]. While this model offers a basic overview of the charged electrode/electrolyte interface, it neglects a few crucial factors, including the thermal motion of ions on the measured capacity, the impact of electrode potential and electrolyte concentrations. Gouy and Chapman expanded the Helmholtz model by incorporating a diffusion layer close to the charged electrode surface. The diffuse double layer comprises counter ions and the co-ions, distributed according to the Poisson-Boltzmann differential equation. Nevertheless, in Gouy-Chapman model, all ions are in thermodynamic equilibrium and statistical correlations are ignored. This model is effective for low concentrations of electrolyte, while it is unsuitable for the electrolyte with a high concentration of ions [149]. Furthermore, Stern improved the Gouy-Chapman model by introducing a layer of ions that was directly and strongly adsorbed onto the charged electrode surface. This model is named Stern model or Gouy-Chapman-Stern model. Stern model acknowledges the presence of the diffuse layer and the layer of absorbed ions within the electric double layer near the electrode interface, providing a more comprehensive understanding of electrochemical phenomena.

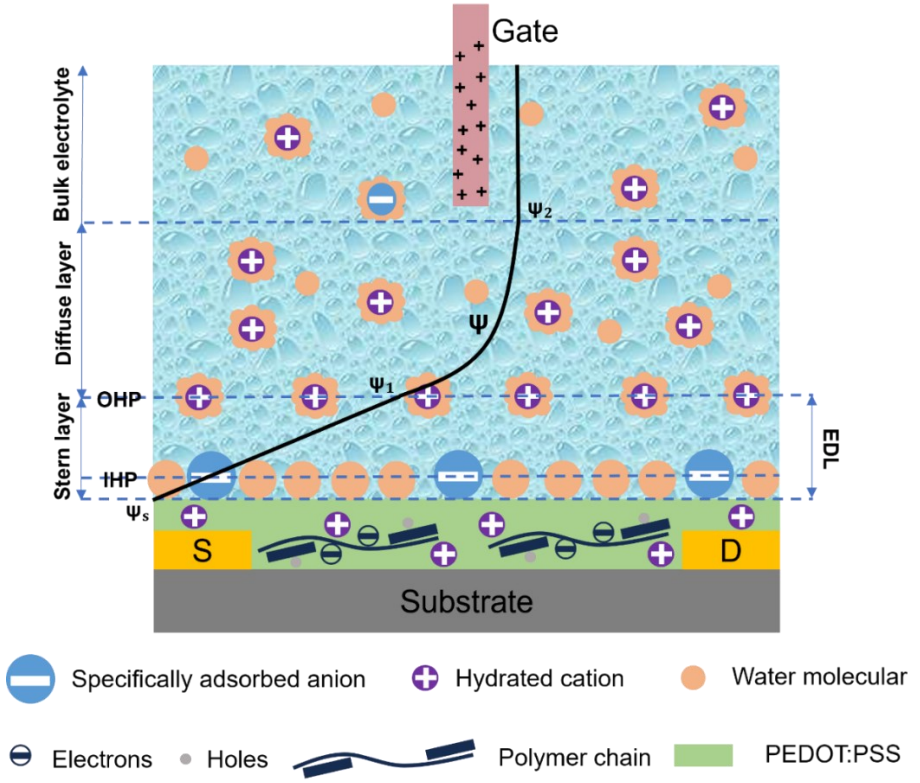

Figure 2.10: *Schematic of electrical double layer at the interface between PEDOT:PSS channel and electrolyte using the Gouy-Chapman-Stern model when a positive gate voltage is applied. Figure is adapted from reference [149-151].*

In PEDOT:PSS OECTs, two distinct interfaces exist: one is between the gate electrode and electrolyte, and the other is between the electrolyte and PEDOT:PSS. When the gate electrode is submerged into the electrolyte solution alongside an applied gate voltage, the opposite

charges in the electrolyte gather at the electrolyte/electrode interface. Thus, an EDL is formed at the electrolyte/electrode interface and another EDL is generated at the electrolyte/PEDOT:PSS interface.

Figure 2.10 presents the schematic of EDL at the PEDOT:PSS channel/electrolyte interface using the Gouy-Chapman-Stern model when the positive gate voltage is applied on the gate electrode [149-151]. The cations in the electrolyte solution are pushed towards the PEDOT:PSS channel and combine with the negatively charged PSS chain. Specifically absorbed anions strongly bind to the surface of the PEDOT:PSS channel at a short distance and this distance characterizes the inner Helmholtz plane (IHP). The next layer of non-specifically absorbed counter ions with their hydration shell determines the outer Helmholtz plane (OHP). The Stern layer is the layer of ions which is directly absorbed by the surface. The final layer is the diffuse layer which is formed from the OHP to the bulk electrolyte. In figure 2.10, the black curve illustrates the variation in potential across distinct layers. Within the Helmholtz layer, the potential decreases following a linear trend, while it drops exponentially within the diffuse layer. In the bulk electrolyte, the potential remains consistent.

2.4 Ion-selective membranes and ion detection

2.4.1 Chemical structure and the working mechanism of ion-selective membranes

ISMs are designed to be selectively permeable to certain ions, allowing only specific ions to pass through while blocking others. This unique property makes them suitable for diverse applications such as pH sensors, ion-selective electrodes and various electrochemical devices. The ISMs in this thesis are polymeric membranes, which are composed of polyvinyl chloride (PVC), ionophores and other ion-selective materials. As it is inexpensive and readily accessible, PVC is commonly used as a matrix material to create ISMs. PVC matrix offers structural integrity and mechanical stability for the ISMs. It serves as a physical barrier that separates the two sides of the membrane [152]. Additionally, PVC is incredibly adaptable and easily modified to achieve various properties of ISMs, including increased ion selectivity or improved stability [153].

However, PVC is also a rigid and brittle material that can crack at low temperatures. To overcome this issue, plasticizers are usually added to PVC to increase its flexibility and enhance the mechanical properties of the membranes [153]. Since the addition of plasticizers can also affect the transport of ions across the film, the choice of plasticizer should depend on the specific application and the desired properties of the ISMs [154]. In this thesis, Dioctyl sebacate (DOS) has been chosen as the plasticizer.

Tetrahydrofuran (THF) is widely used in various industrial applications, including as a solvent for polymerization reactions, a reaction medium in organic synthesis and a component in coating formulations [155, 156]. THF has a dielectric coefficient of 7.6, which makes it a versatile solvent that can dissolve the PVC and other components into the ISM solutions

during the membrane preparation. Additionally, THF can enhance the solubility of the components and homogeneously distribute them within the PVC matrix material.

An ionophore is the key component that is responsible for the selective transport of specific ions across the ISMs. Figure 2.11 displays the chemical structure of the representative ionophores including K^+, NH_4^+, Na^+ and Ca^{2+} ionophores [80]. The ionophores are commonly crown ethers, which can trap or coordinate desired ions in their cavities based on size, and phosphoric acid ethers, which can selectively bind cations through their free phosphate groups [157]. By forming complexes with target ions and effectively enhancing their permeability to pass through the membrane, ionophores act as the carriers for their transportation within ISMs. Normally, the ionophore is incorporated into the PVC matrix of the membrane, either independently or as a component of the ion exchange material. Ionophores can be selective for various types of ions, including positively and negatively charged ions [158].

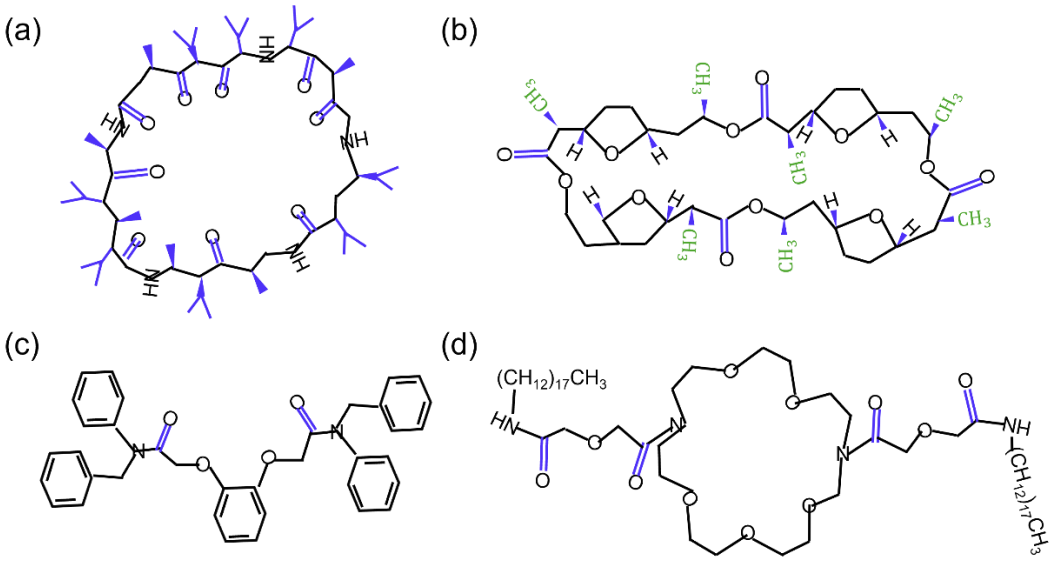

Figure 2.11: *Chemical structures of K^+ (a), NH_4^+ (b), Na^+ (c) and Ca^{2+} (d) ionophores. Figure is adapted from reference [80].*

Ion exchangers are solid materials which can selectively exchange the ions in a reversible manner. This process is based on the structure of the ion exchanger and the properties of the ions in the electrolyte solution. Ion exchangers provide selectivity to the membranes, allowing ISMs to transport specific ions while excluding others, making them an important tool for a variety of applications in fields such as sensing, biochemistry, and environmental science [158]. Figure 2.12 displays the structural composition and working mechanism of a PVC-based K^+ ISM. By forming complexes with K^+ ions, the ion-exchange material allows the transport of target ions while excluding Na^+ and Cl^- ions. When an ISM is integrated into an ion-selective electrode (ISE) system, an electrical potential difference arises between the ISM and the reference electrode, corresponding to the concentration of target ions in the solution [80, 159]. This observed electrode potential, commonly known as the electromotive force (EMF), can be determined using the Nernst equation (2.4):

$$E = E^0 + \frac{RT}{nF} \ln a_i = E^0 + \frac{2.303RT}{nF} \log a_i \quad (2.4)$$

where E^0 is the formal potential, R is the molar gas constant, T is the temperature, F is the Faraday constant and a_i is the concentration of ions with charge n.

As shown in equation (2.4), the potential E exhibits a linear relationship with the logarithmic scale of ion concentration, and the slope of this Nernstian response is $\frac{RT}{nF}$. For monovalent ions, the Nernstian detection slope is 59.2 mV/decade at room temperature, which is calculated using the equation (2.4) [80].

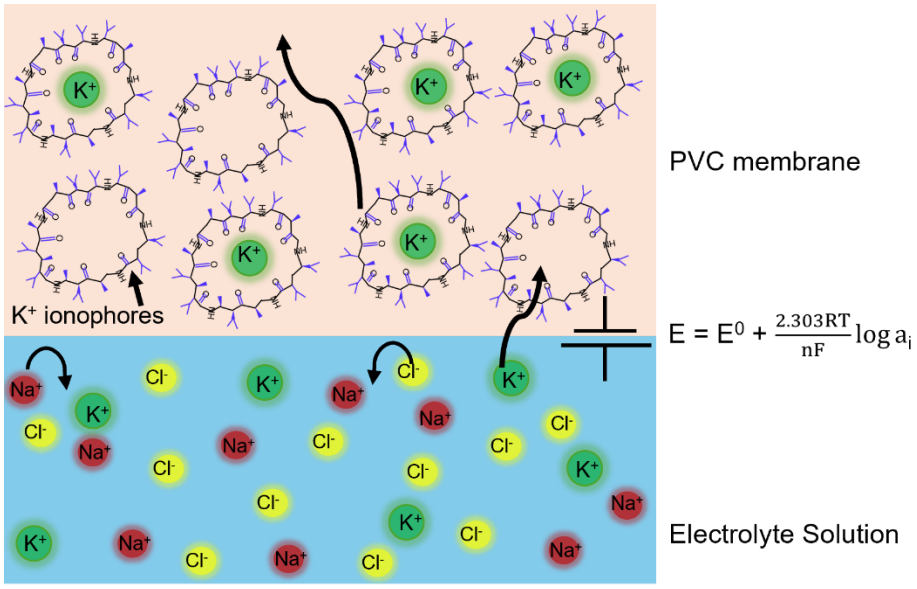

Figure 2.12: *Structural composition and working mechanism of a K^+ ion-selective membrane. Figure is adapted from references [80, 159, 160].*

2.4.2 Ion detection using PEDOT:PSS OECTs

Owing to its ion conductive properties, PEDOT:PSS OECTs exhibit remarkable sensitivity to the variations in the ionic strength of the analyte solution. Therefore, PEDOT:PSS OECTs can be used for ion detection in the solution. After applying a positive voltage at the gate electrode, cations from the electrolyte solution are pushed towards the PEDOT:PSS channel. These cations then bind to the negatively charged sulfonate groups in PSS chains, resulting in the reduction of negative change compensation for the positive charge carriers in the PEDOT chains. The number of holes in PEDOT:PSS channel decreases, leading to the de-doping of the PEDOT:PSS channel and the reduction of the electrical conductivity of the PEDOT:PSS film. Accordingly, the I_{DS} of OECTs decreases, indicating the modulation of the gate voltage on the channel current.

In PEDOT:PSS OECTs, the amplification mechanism depends on the significant difference in electrical conductivity between two forms of PEDOT, enabling minor variations of V_{GS} to result in significant changes in I_{DS} [55]. This phenomenon can be described by the transfer

characteristics of PEDOT:PSS OECTs (I_{DS}~V_{GS}). Furthermore, the transient behavior of the OECTs can be explained by the Bernards model [137]. As shown in figure 2.13 (a), this model divides the OECT into two distinct circuits: an electronic circuit and an ionic circuit [74]. Within the electronic circuit, the movement of the holes or electrons across the organic channel material occurs between the source and drain electrodes. This process can be described by Ohm's law. When gate voltages are applied, the doping state of the organic channel material is altered throughout its entire volume, leading to the modification of the resistance of the electronic circuit. The ionic circuit consists of several components including the gate/electrolyte capacitor, channel/electrolyte capacitor and a resistor. This resistor is used to describe the flow of ions within the electrolyte depending on the ionic strength of the electrolyte [74, 137].

As illustrated in section 2.3, two different EDLs are formed in the OECTs, creating the capacitance on each interface. The two capacitances represent the capacitance at the gate/electrolyte (C_g) and channel/electrolyte (C_{ch}) interfaces, respectively. In most applications, C_g is significantly bigger than C_{ch}, causing most of the applied gate voltage drops at the channel/electrolyte interface. This results in an efficient gating of the channel, illustrated by the dashed line in figure 2.13 (b). Conversely, when C_{ch} is greatly larger than C_g, most of the applied gate voltage drops at the gate/electrolyte interface, leading to poor gating, as shown by the solid line in figure 2.13 (b) [55].

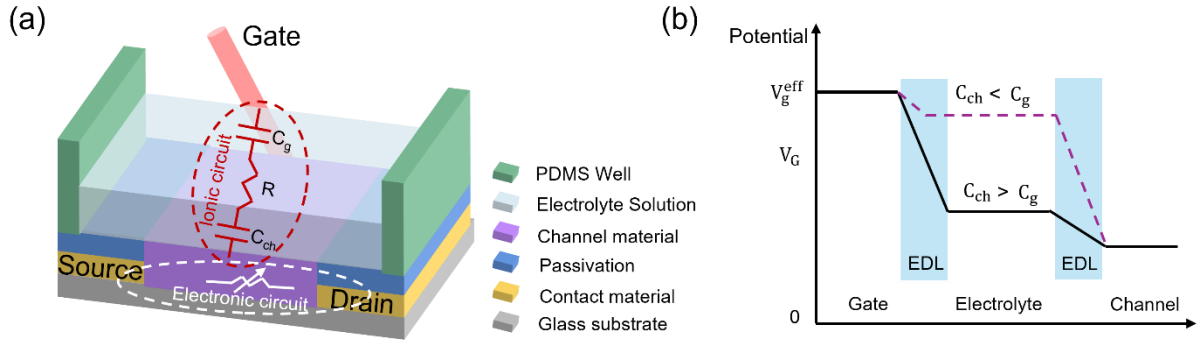

Figure 2.13: *(a) Model of OECTs consisting of an electronic circuit and ionic circuit. Figure is adapted from reference [74], (b) The distribution of potential in the ionic circuit with capacitances at the gate/electrolyte (C_g) and channel/electrolyte (C_{ch}) interfaces, respectively. Figure is adapted from reference [55].*

Apart from biosensing applications, ion detection using PEDOT:PSS OECTs have shown other promising applications such as in environmental monitoring and clinical diagnostics. Xiong et. al fabricated PEDOT:PSS OECTs with a planar gate configuration using Au as source and drain electrodes. The transfer characteristics of the devices were continuously evaluated in buffer solutions over five days and the results demonstrated a stable performance of the OECTs. These devices were then employed for real-time monitoring of Copper (Cu^{2+}) ions with a limit of detection as low as 100 nM. Moreover, the interfering measurements demonstrated a promising selectivity of the OECTs against other metal ions. Eventually, the fabricated OECTs detected Cu^{2+} ions in a tap water sample, demonstrating the reliability and

applicability of the devices [161]. In clinical diagnostics, PEDOT:PSS OECTs can be used to detect ions in bodily fluids for diagnostic purposes. For instance, they can detect specific ions that are relevant to some diseases or health conditions, providing valuable diagnostic information. Meng et. al introduced the detection of Na^+ ion concentrations in aqueous solutions and blood serum using PEDOT:PSS OECTs. The Na^+ ISM was incorporated directly on the channel material of the OECTs to realize the ion detection. The transfer characteristics showed the reliable functionality of the devices, and the transient response using three cyclical pulses demonstrated stable electrochemical properties of the OECTs. After conducting the real-time measurement for Na^+ concentrations using three devices, the results demonstrated a sensitivity value as high as 126 µA/decade. The OECTs exhibited good selectivity for Na^+ detection over K^+ and Ca^{2+}. Moreover, Na^+ ion concentrations in the blood serum were measured, and the results presented a linear response in the logarithmic scale for Na^+ ion concentrations ranging from 100 mM to 160 mM. This concentration range corresponded to the physiological range of Na^+ ion in blood serum, which showed their potential for point-of-care applications [162].

2.5 Dopamine detection

2.5.1 Chemical structure of dopamine

DA plays a role as a “reward center” and is involved in many bodily functions such as movement, memory and attention. DA has an isoelectric point (pK_a) of 8.87 and is positively charged when in a solvent with a pH of 7.0. However, under alkaline conditions, DA can be easily oxidized, leading to the formation of polydopamine through self-oxidation and polymerization, and causing a noticeable color change to brown. The early stages of DA oxidation can be explored using biomimetic oxidants such as peroxidase/H_2O_2 and peroxidase mimics [86]. DA has several analogues and interferents such as tyramine, tryptamine, UA and AA, as shown in figure 2.14 [86]. These analogues are components that mimic the structure or function of DA and some of them can interact with DA receptors. AA and UA are two interferents that may impact the detection, measurement, and function of DA in biological systems due to their similar electrochemical behavior to DA. Therefore, the detection of DA concentrations with high sensitivity and selectivity is challenging because of the presence of these analogues and interferents.

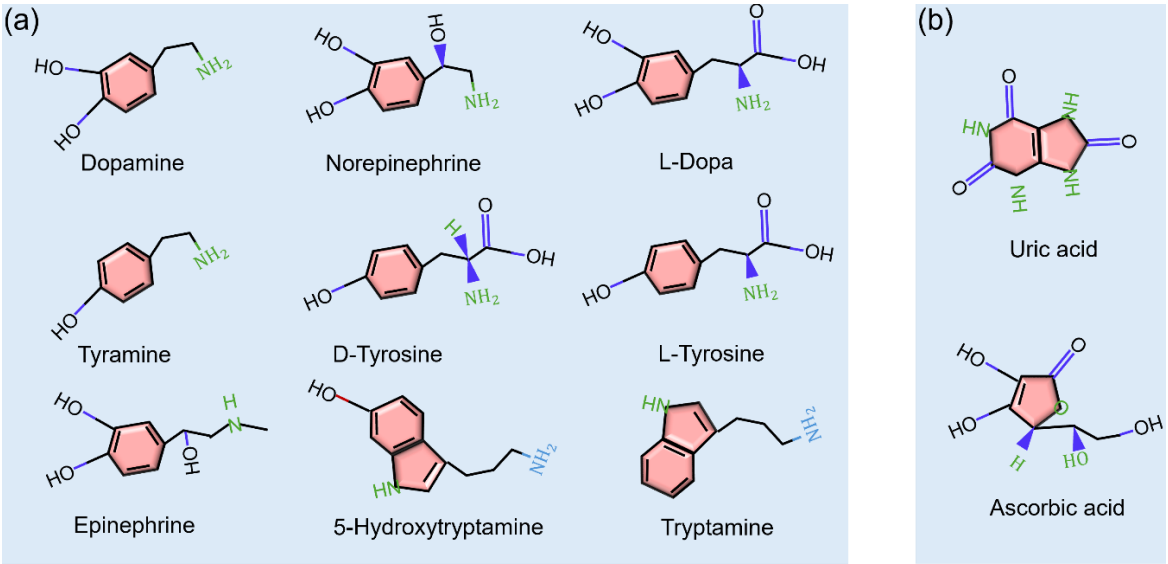

Figure 2.14: *(a) The chemical structure of DA and its several analogues, (b) two interferents of DA. Figure is adapted from reference [86].*

2.5.2 Approaches for dopamine detection

Numerous approaches, such as high-performance liquid chromatography (HPLC) [163], capillary electrophoresis [164], mass spectroscopy [165], ultraviolet–visible spectrophotometry [166], fluorescence spectrometry [167], chemiluminescence (CL) microdialysis techniques [168], enzymatic methods [169], electrochemical (EC) methods [170-172] and others, have been developed for monitoring DA concentrations. Several conventional techniques like HPLC and mass spectroscopy offer remarkably low detection limits for DA concentrations. However, a few drawbacks in these methods for portable and effective analytical monitoring include the requirement for expensive specialized instruments, long response time and complicated operational procedures. Various electrochemical methods have emerged as promising alternatives, such as amperometry [173], cyclic voltammetry (CV) [147, 174] and differential pulse voltammetry (DPV) [175]. Quantification of DA concentrations is achieved by measuring the currents generated by the electrons released during their oxidation. Although these methods have several advantages, including rapid response, simplicity and portability, they still face challenges in the selective detection of DA levels in the presence of AA and UA which can undergo oxidation at close potentials [176].

In recent years, several research groups have employed PEDOT:PSS OECTs for the investigation of DA detection. Tang et al. demonstrated the DA biosensors based on PEDOT:PSS OECTs using various gate electrodes (graphite, Au and Pt electrodes) for DA detection with high sensitivity. Among these gate electrodes, the Pt gate electrode exhibited the lowest limit of detection (LoD) for DA of approximately 5 nM. This LoD was two orders of magnitude greater than that of traditional electrochemical measurements. However, the pure Pt gate electrode displayed remarkable electro-catalytic activity towards numerous analytes including common interferents such as AA and UA. This reduced the selectivity of the OECTs to DA detection, resulting in limitations to their practical applications [91]. Liao et al. reported

that the modification of the surface of the Pt gate electrode significantly enhanced the selectivity of DA detection using the OECTs. In their work, the OECTs with Nafion (1.0%)–graphene/Pt gate displayed sensitivity to DA concentrations ranging from 5 nM to 1 μM when interferents of AA and UA are present [177]. After that, PEDOT:PSS OECTs with different gate electrodes were utilized to monitor the DA concentrations. Table 2.1 presents the state-of-art research in PEDOT:PSS-based OECTs for DA detection. In this table, CNE stands for carbon nano electrode and MIP refers to molecularly imprinted polymer. rGO means reduced graphene oxide, CSF is carbonized silk fabric and FSP is fast-scanning potential. Although many researchers have invested significant efforts into detecting DA concentrations, numerous challenges persist regarding selective, sensitive and compatible DA detection within complex biological samples.

Table 2.1: *The state-of-art research in PEDOT:PSS-based OECTs for dopamine detection.*

Gate	Limit of detection	Sensitivity (linear range)	Selectivity	Reference
Pt	5 nM	174 mV/decade (50 nM - 3 μM)	-	[91]
Nafion (1.0%)–graphene/Pt	5 nM	281 mV/decade (5 nM - 1 μM)	5 nM to 1 μM	[177]
PEDOT:PSS	6 μM	9.1 S M^{-1} (5–100 μM)	0.15 mM	[147]
Nafion/rGO/CSF	1 nM	60 mV/decade (30 nM – 10 μM)	1 nM – 30 μM	[148]
Pt	30 nM	(30− 100 μM)	-	[178]
CNE needle-type	1pM	(1 - 160 pM) (2 - 700 nM)	-	[179]
Aptamer-modified Au	0.5 fM	(5 fM–1 nM)	10 μM	[180]
o-MIP/Pt	34 nM	-	∼0.4 and ∼10 μM	[181]
FSP	5 nM	0.899 S M^{-1} (1− 6 μM)	50 μM	[182]

Figure 2.15 (a) shows the schematic of the working principle of DA detection using PEDOT:PSS OECTs. The OECTs are fabricated onto the glass substrate, while the source and drain electrodes are Au material. The source and drain electrodes are covered by a passivation layer and connected using the PEDOT:PSS channel. Pt is utilized as the gate electrode, while the PDMS well is used to encapsulate the transistors and store the electrolyte solutions. In this schematic, the source electrode is grounded. A voltage is applied between the source and gate electrodes, while another voltage is applied between the source and drain electrodes. The added DA in the electrolyte solutions is then electro-oxidized to o-dopamine quinone at the surface of the Pt gate electrode. A Faradic current is generated by this electro-oxidation of DA, leading to the reduction of potential drop at the gate/electrolyte interface. Afterwards, the effective gate voltage delivered to the OECTs is increased, and then the drain current between the source and the drain electrodes decreases accordingly.

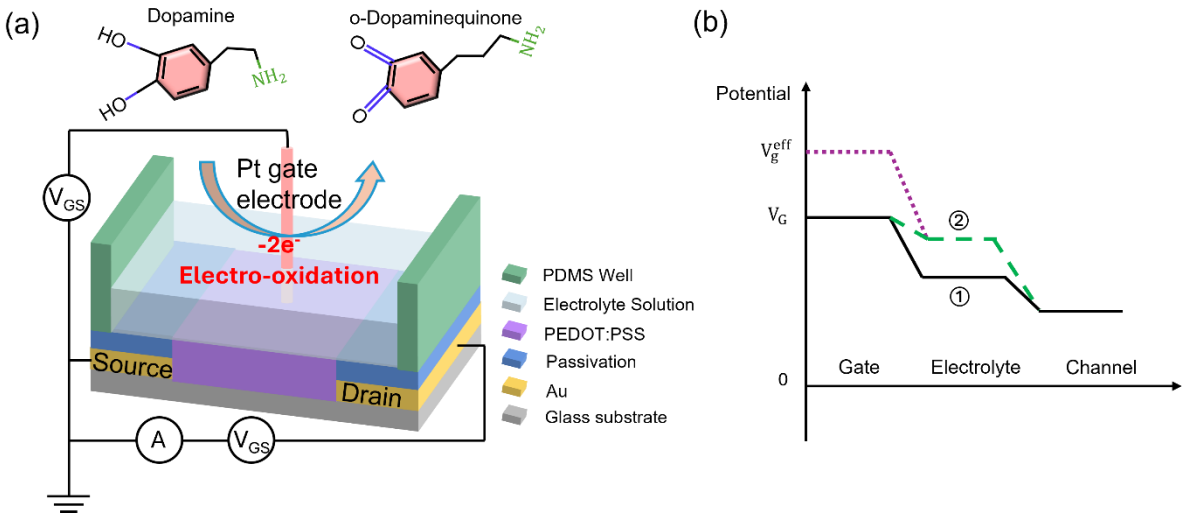

Figure 2.15: *(a) Working principle of dopamine detection using PEDOT:PSS OECTs, (b) Potential changes of the OECT in the absence of dopamine (solid line), the presence of dopamine (dashed line) and the effective gate voltage (dotted line). Figure is adapted from reference [183].*

Figure 2.15 (b) displays the potential variation between the gate electrode and PEDOT:PSS channel when DA undergoes the electro-oxidation process. The solid line presents the potential changes of OECTs when the DA is absent in the electrolyte solution, while the dashed line shows the variations in the potential with the presence of DA. Additionally, the dotted line represents the change of effective gate voltage between the gate electrode and the channel. The electrolyte potential (1) in the solid line is determined by the relative capacitances at the gate and channel interfaces, while the electrolyte potential (2) in the dashed line is increased according to the Nernst equation. The effective gate voltage (dotted line) is the gate voltage that is required to produce the same electrolyte potential (2) when the Faradaic effects are absent. When the DA is electro-oxidated, the generated faradaic current leads to the decrease of the potential drop at the gate/electrolyte interface. As a result, the electrolyte potential (2) and the effective gate voltage will rise, and the changes in the drain current will occur. Thus, the relationship between the drain current and DA concentrations are established. The effective gate voltage is given by the following equation (2.5) [91, 177]:

$$V_g^{eff} = V_G + 2.30(1+\gamma)\frac{kT}{2q}\log[C_{DA}] + A \tag{2.5}$$

where $\gamma = C_c/C_G$ is the ratio between the capacitances of the channel/electrolyte interface (C_c) and the gate/electrolyte interface (C_G); k is the Boltzmann constant; T is the Kelvin temperature; $[C_{DA}]$ is the molar concentration of DA; A is a constant.

Therefore, the concentration of DA impacts the effective gate voltage, resulting in the change in the drain current of the OECTs. The drain current of PEDOT:PSS OECTs is given by the equation (2.6) below [177]:

$$I_{ds} = \frac{q\mu p_0 dW}{LV_p}\left(V_p - V_g^{eff} + \frac{V_{ds}}{2}\right), \left(|V_{ds}| \ll |V_p - V_g^{eff}|\right)$$

$$V_p = \frac{qp_0 t}{c_i},$$
$$V_g^{eff} = V_G + V_{offset}. \quad (2.6)$$

where q is electron charge; μ is the hole mobility; p_0 is the initial hole density; d is the thickness of the active layer; W and L are the width and length of the OECT device, respectively; V_p and V_g^{eff} are the pinch-off voltage and the effective gate voltage on the electrolyte/active layer interface, respectively; c_i is the effective gate capacitance per unit area; V_{offset} is the offset voltage on the surface of the gate or the channel.

The modulation of the channel current by DA is primarily caused by the change of effective gate voltage given by equation (2.5). As the DA concentrations increase, V_g^{eff} will also increase, which leads to the reduction of drain current according to equation (2.6).

DA detection has various applications across different fields including neuroscience research, drug development and behavioral studies. Since DA plays a critical role in some neurological disorders, accurate detection of DA concentrations in the brain can help researchers study DA dynamics to understand their influence on health conditions such as Parkinson's disease, addiction, and mood disorders. Furthermore, detection of DA levels is beneficial for developing and testing potential drug candidates that target the DA system. Additionally, as DA levels are strongly connected to the reward-motivated behavior in animals and humans, DA detection during behavioral experiments allows researchers to develop a comprehensive understanding of neural mechanisms which control the motivation, reward process and decision-making process.

3 Methods

In this chapter, the methods, such as metallization, lift-off, PECVD and RIE processes, and relevant equipment utilized to fabricate the OECT microarrays on the wafer scale are described. Following this, the Van der Pauw method for determining the electrical conductivity of PEDOT:PSS film is explained and the basics of cyclic voltammetry are presented.

3.1 Metal deposition

3.1.1 Metal evaporation

In this thesis, the evaporation system Leybold A700QE is used to evaporate Au layers onto the glass substrate. Figure 3.1 shows the images of the exterior (a) and interior (b) of this system, which is operated only in the clean room. The system contains a 10 kW high-voltage power unit and two different guns, with one gun connected to a large crucible that can generate thick layers reaching over 1000 nm. The second gun holds six liners for different evaporation materials, making it possible to evaporate titanium (Ti) and Au layers in a single run without breaking the vacuum. This vacuum is created using a cryopump and its zero point is about 4×10^{-8} mbar. During the evaporation process, the pressures for evaporating the Ti layer are approximately 8×10^{-8} mbar, while the pressures for Au are roughly 5×10^{-7} mbar. Due to its excellent adhesion properties and ability to form strong bonds with both the glass substrate and Au layer, the Ti layer serves as an adhesive in the evaporation process, playing a significant role in the deposition of Au onto the glass substrate. Table 3.1 shows the main parameters for depositing 5 nm of Ti and 50 nm of Au on the glass wafer. The coating process in the system runs automatically once the recipe has been programmed. For the lift-off processes, a special wafer holder which can load and deposit a maximum of twelve wafers simultaneously is utilized, improving the efficiency of the deposition significantly. Additionally, the wafer holder can be rotated to ensure the uniformity of the deposition.

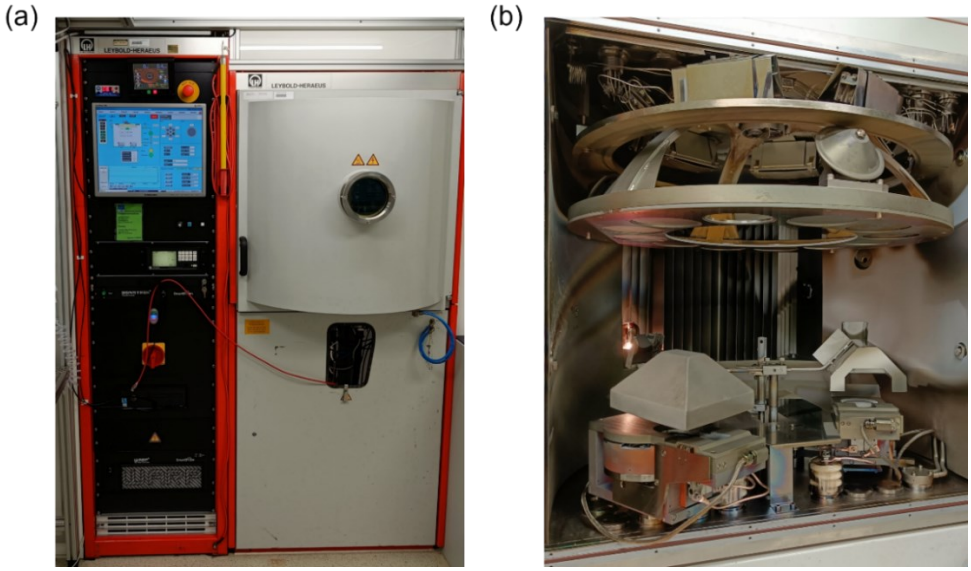

Figure 3.1: *Image of exterior (a) and interior (b) of the evaporation system of Leybold A700QE. This machine is located in Room 007, ZMNT, RWTH university, and the photos were provided by Jochen Heiss.*

Table 3.1: *Main parameters for evaporating 5 nm of Ti and 50 nm of Au.*

Basic pressure (mbar)	Target	Process pressure (mbar)	Power (%)	Time (min)
3.30E-08	Ti	3.30E-07	4.4	1.29
5.00E-08	Au	2.20E-07	19.8	4.09

Figure 3.2 displays the schematics of an electron-beam evaporation system which includes several main evaporation sources such as crucibles, evaporation materials and filaments [184]. Crucibles are made from high temperature resistant materials and are commonly used in electro-beam evaporation techniques to hold the evaporation materials, which can be used to form thin films during the evaporation process. Filaments are typically composed of materials such as tungsten or tantalum and heated by applying a very high voltage. The filament emits a high-power electron beam which is deflected onto the crucibles using a magnetic field, creating very high temperatures that heat the evaporation materials until they start to evaporate. As the high temperatures are limited to a small area, only this small area is evaporated while the surrounding area is cooled. The evaporated material goes directly to the surface of the substrate, then starts to condense and form a thin film. Since the evaporation process takes place in a vacuum chamber, this prevents contamination of the substrate surface with any unwanted particles, guaranteeing that only the evaporation material lands on the substrate to generate the thin films [184]. To achieve different thin film properties and characteristics, the whole process can be performed in a range of conditions such as by varying temperatures, gas environments and pressures.

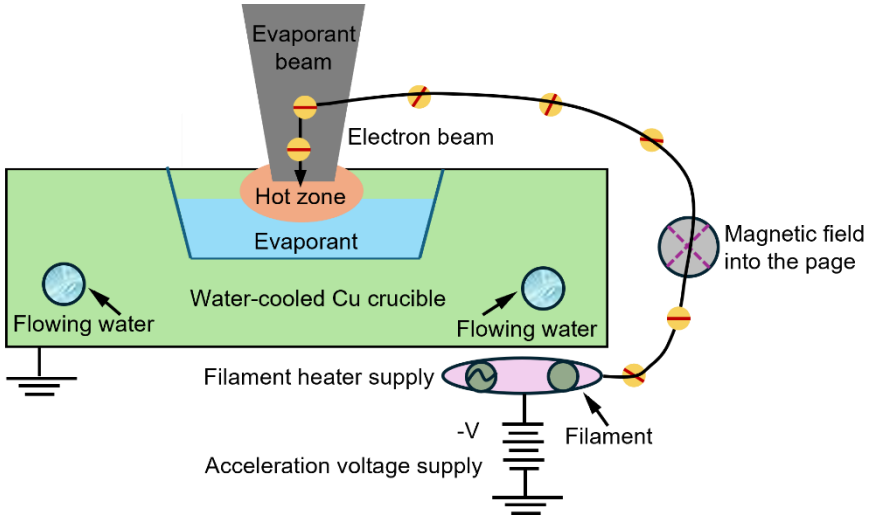

Figure 3.2: *Schematic of an electron-beam evaporation system. Figure is adapted from reference [184].*

3.1.2 Metal sputtering

Sputtering deposition is one form of physical vapor deposition that is commonly used to deposit thin films on substrates. The process occurs in a vacuum chamber, where air and other gases are evacuated to create a controlled environment. A target material is placed in the chamber and is deposited onto the substrate which is typically placed opposite the target material. An inert gas, usually argon, is introduced into the chamber and ionized by an applied

high voltage. This ionization creates a plasma which contains positively charged ions that are accelerated towards the negatively charged target material. When these ions collide with the target, they dislodge atoms or molecules from the target surface, which then travel through the vacuum and eventually land on the substrate, forming a thin film. The process can be controlled to achieve the desired film thickness and uniformity. Depending on the properties of the targets, there are various types of power sources. Electrically conductive target materials often use a direct current (DC) power source, while a radio frequency (RF) power source is commonly used for conductive and non-conductive target materials [185].

The sputtering equipment used in this thesis is the Nordiko NS2550 system, shown in figure 3.3. Several targets are installed in the chamber, including Ti, platinum (Pt) and iridium (Ir). A DC power source was used for sputtering Pt, TiN, ITO and IrO_x materials on the glass wafer, with their main parameters listed in Table 3.2. The system sputters from above onto a rotating table where the substrates are placed. Additionally, this table can be rotated at various speeds, while the distance between the table and the targets is adjusted. Up to six 100 mm wafers can be held on the substrate table, thus enhancing the sputtering efficiency. To sputter the wafers homogeneously, the size of the targets is kept at 150 mm. The basic pressure of the vacuum chamber is approximately 1×10^{-6} mbar, while the pressure for the sputtering process is usually 1.5×10^{-2} mbar. This process will run automatically after the recipe is set up and programmed.

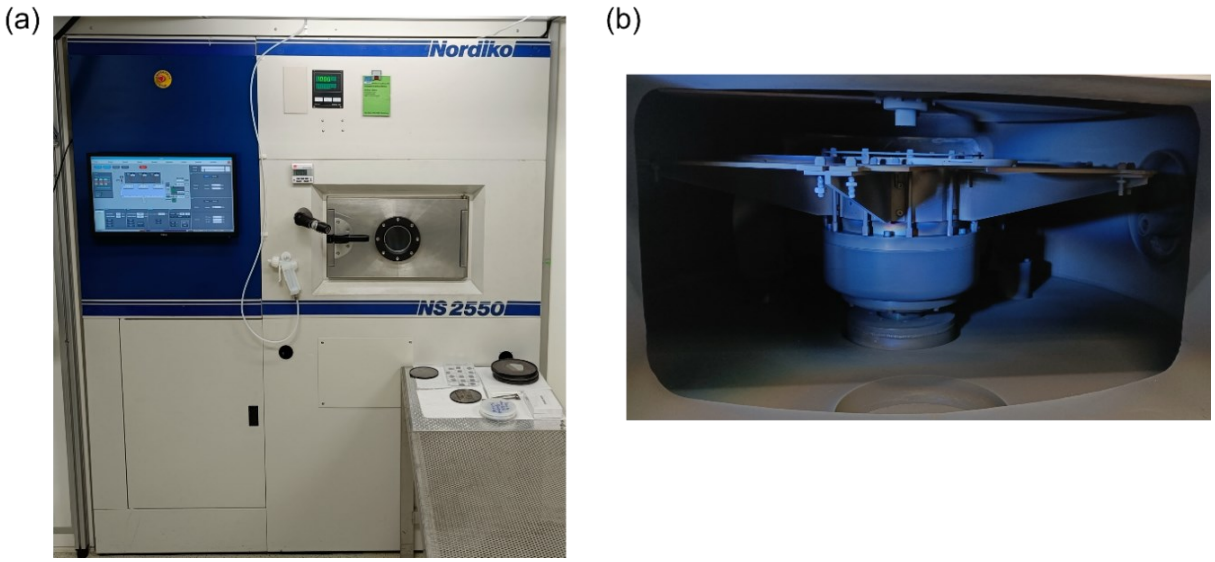

Figure 3.3: *Image of exterior (a) and interior (b) of the Nordiko NS2550 sputtering system. This machine is in Room 007, ZMNT, RWTH university, and the photos were provided by Jochen Heiss.*

Table 3.2: *Main parameters for sputtering Pt, TiN, IrO_x and ITO.*

Materials	Basic pressure (mbar)	Target	Ar (sccm)	P (W)	Target Bias (V)	Pressure plasma baratron (mbar)	Thickness (nm)
Pt	2.85E-06	Ti	55	250	239	2.01E-02	5
		Pt	75	100	378	1.84E-02	100
IrO_x	1.67E-06	Ir	100	100	500	8.25E-03	150
TiN	3.67E-06	Ti	55	250	268	3.56E-02	5
		Ti	50	1000	462	6.13E-03	150
ITO	2.96E-06	ITO	55	1500	354	4.10E-03	150

3.2 Lift-off process

The lift-off process is a microfabrication process for creating a patterned material on the surface of substrates, as presented by the schematic in figure 3.4 [186]. First, a photoresist which has a specific lift-off profile is patterned on top of the substrate (Figure 3.4 (a)). The materials are then deposited onto the substrate either by the evaporation or sputtering technique (Figure 3.4 (b)). Following that, the photoresist is dissolved in an organic solvent such as acetone and removed from the substrate (Figure 3.4 (c)). This will also result in the removal of the materials that are deposited on top of the photoresist. Finally, only the materials deposited directly onto the substrate remains, as can be seen in figure 3.4 (d).

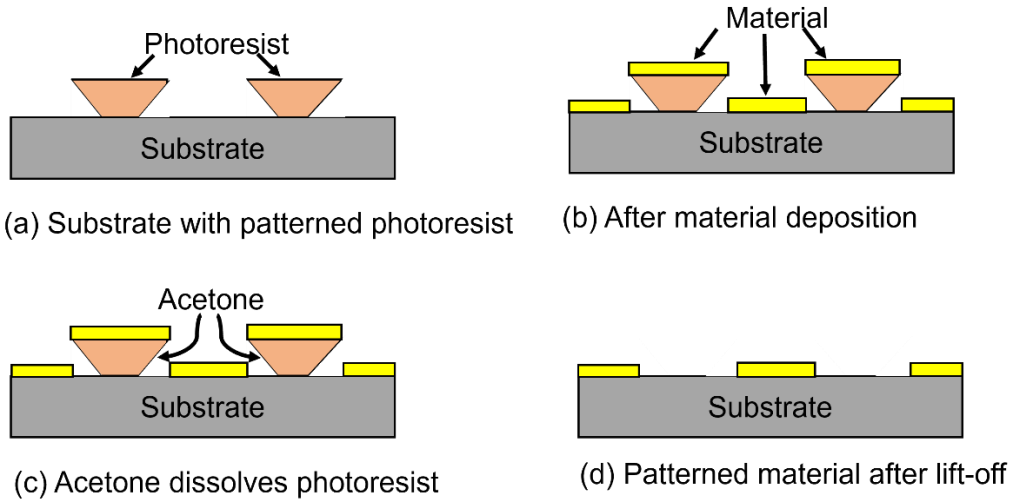

Figure 3.4: *Schematic of lift-off process. Figure is adapted from reference [186].*

The lift-off process has been employed to obtain the patterned material of Au, Pt, TiN, ITO and IrO_x. The process began with the immersion of the wafers into the acetone for approximately 5 minutes, followed by the ultrasonication of the wafers for roughly 20 seconds. Afterward, the wafers were rinsed using isopropanol and dried with nitrogen. The lift-off process is not always successful due to the following reasons: first, the materials sitting on the photoresist and the materials directly on the substrate may be connected, providing limited access for the acetone

to dissolve the photoresist. Secondly, if an undercut is not present in the lower part of the photoresist, this results in the deposition of the material on the sidewalls of the photoresist, which cannot be dissolved by acetone. Therefore, it is essential to observe the structures under a microscope at the end of each step during the lift-off process. To obtain optimal lift-off results, the ultrasonication procedure may need to be repeated multiple times, with a duration of 3 seconds for each repetition.

3.3 Plasma enhanced chemical vapor deposition

Plasma enhanced chemical vapor deposition (PECVD) was utilized to deposit silicon oxide as a passivation layer on the wafer substrate. An image of the equipment is shown in figure 3.5. The deposition process started with the heating of the platform to 300°C. Next, the wafers were loaded onto the platform and the chamber was evacuated until 1000 Pa. Afterward, a mixture of precursor gases (2% SiH_4 and 100% N_2O) was introduced into the vacuum chamber containing the substrates. Plasma was then created in the gas mixture by using RF and used to activate the precursor gases into reactive species. Following this, these species reacted with one another and were deposited onto the substrates to form a thin film layer of silicon oxide. The PECVD technique exhibits several advantages including low deposition temperatures, high deposition efficiency and controllable parameters, such as air pressure, temperature and plasma power. By adjusting these parameters, the properties of the silicon oxide film can be optimized, for example, depending on the desired film thickness, the deposition time can be modified. Furthermore, unlike the conventional CVD process, plasma used during the PECVD process increases the energy of the reactant when it hits the surface. Table 3.3 displays the main parameters for depositing a 300 nm silicon oxide layer on a glass wafer.

Figure 3.5: *Image of PECVD equipment.*

Table 3.3: *Main parameters of PECVD process for depositing a 300 nm silicon oxide layer.*

Chamber pressure	HF power	Temperature of platform	2% SiH_4	100% N_2O	N_2
1000 Pa	20 W	300 °C	425 sccm	710 sccm	1000 sccm

3.4 Reactive ion etching

Reactive ion etching (RIE) is a dry etching technique that removes materials deposited on substrates with high resolution. Figure 3.6 displays the RIE machine that was used to etch the silicon oxide passivation layer on the wafer. The etching process began by first loading the wafers on the wafer chuck in the external vacuum chamber. Next, this external chamber was evacuated until a certain vacuum value was reached. The wafers were then transferred into the internal vacuum chamber and placed on the platform. Reactive gas (SF6) was introduced into this internal chamber, and plasma was created by using an electric field with electrodes. High-energy ions in the plasma were accelerated by the electric field toward the substrates, leading to both physical sputtering and chemical reactions on the surface.

Figure 3.6: *Image of RIE machine.*

Figure 3.7 shows the schematic of the RIE process for etching the silicon oxide layer. Firstly, by using a lithography process, the AZ5214E photoresist was patterned onto the wafer substrate, upon which material such as Au was deposited prior (Figure 3.7 (a)). As shown in figure 3.7 (b), the materials on the substrate were selectively removed to obtain the desired patterns after the etching process. During this process, the photoresist served as a shield to protect the areas that needed to remain. Table 3.4 shows the parameters of the RIE process for etching a 300 nm silicon oxide layer. Approximately 300 seconds was needed for the silicon oxide layer on the contact pads to be completely etched away. After the etching process, the remaining photoresist on the wafer was removed by an oxygen plasma flash with 50 W of power, 300 m Torr of pressure and 100 sccm of O_2 flux for 3 minutes. Figure 3.7 (c) presents the schematic of the Au material on the wafer after the remaining photoresist was removed.

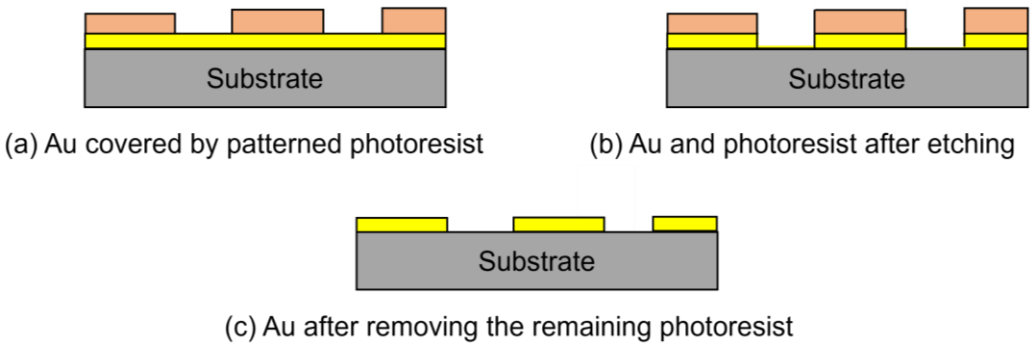

(a) Au covered by patterned photoresist (b) Au and photoresist after etching

(c) Au after removing the remaining photoresist

Figure 3.7: *Schematics of reactive ion etching process. Figure is adapted from references [184, 187].*

Table 3.4: *Parameters of the RIE process for etching a 300 nm silicon oxide layer*

Pressure	SF6	HF power	Temperature of the holder	ICP power	O_2
1 Pa	20 sccm	75 W	30 °C	150 W	2 sccm

However, problems with the function of this machine caused some failed etching results. It is crucial, therefore, to pay attention to several key parameters such as pressure, HF power and voltage bias. To obtain optimal etching results, a pre-run process on a dummy wafer is always recommended to verify the parameters. Additionally, the wafers should stay on the wafer chuck during the whole etching process. If necessary, several small pieces of high temperature resistant tape can be used to stick the edges of the wafer to the wafer chuck, ensuring the stabilization of the wafer on the holder.

3.5 Van der Pauw method

The Van der Pauw (VDP) method is a commonly used technique for the measurement of the resistivity and the Hall coefficient of a sample. It was created by Leo J. van der Pauw in 1958 [188] and can accurately measure the resistive properties of a sample with any shape. To conduct a precise VDP measurement using this technique, five conditions must be satisfied:

1) The sample that will be measured should have a flat form with uniform thickness
2) The sample should have a closed area without holes
3) The sample must be homogeneous
4) All four contacts must be located at the edges of the sample
5) The area of any individual contact must be at least an order of magnitude smaller than the area of the whole sample

Figure 3.8 (a) shows the schematic of the VDP configuration with four contacts on a square sample. A semiconductor characterization system with four probes can be used for measurement. Current is applied through the two contacts on the sample, then the voltage at the two opposing contacts is measured.

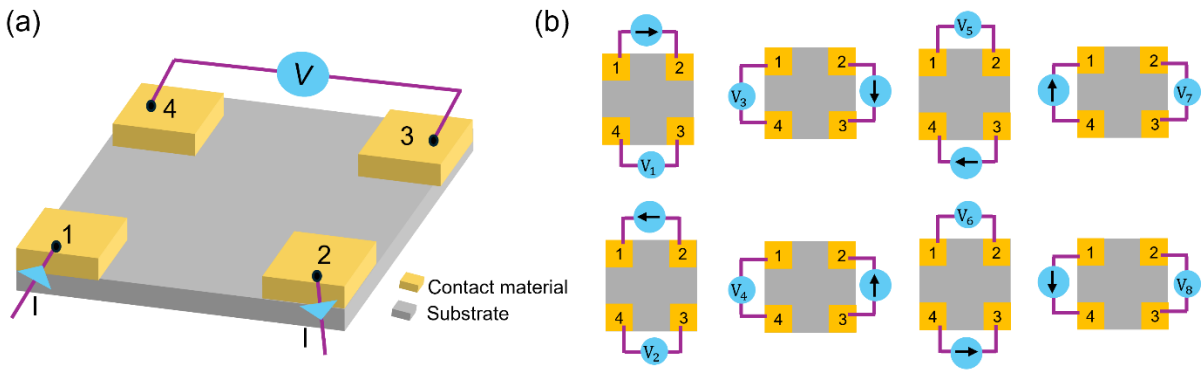

Figure 3.8: *(a) Van der Pauw configuration on a square sample, (b) Van der Pauw sheet resistance value measurement configuration. Figure is adapted from reference [189].*

To obtain an accurate sheet resistance value, the VDP measurement is repeated eight times around the periphery of the sample, which is shown in figure 3.8 (b). The sheet resistance can be calculated by using the series of eight voltage measurements (V1-V8) and the applied current (I) [189]. The sheet resistance R_{sh} can be calculated with the following equations:

$$R_{sh1} = \frac{\pi}{\ln 2} \frac{(V_1 - V_2 + V_3 - V_4)}{4I} F \tag{3.1}$$

$$R_{sh2} = \frac{\pi}{\ln 2} \frac{(V_5 - V_6 + V_7 - V_8)}{4I} F \tag{3.2}$$

$$R_{ave} = \frac{R_{sh1} + R_{sh2}}{2} \tag{3.3}$$

where F is the geometrical factors based on the shape of the sample and F is 1 for the squares; V1-V8 represents the voltages measured by the probes; I is the applied current through the samples; R_{sh1} is the sheet resistance which is calculated using the equation 3.1; R_{sh2} is the sheet resistance measured with an opposing current in comparison to R_{sh1} and calculated by the equation 3.2; R_{ave} is the average sheet resistance which is calculated by R_{sh1} and R_{sh2} with the equation 3.3.

Furthermore, the electrical resistivity (ρ) of the sample can be calculated using the equation 3.4, while t is the thickness of the sample.

$$\rho = R_{ave} \times t \tag{3.4}$$

3.6 Cyclic voltammetry

Cyclic voltammetry (CV) is a method which can evaluate the electrochemical behavior of a system. In recent years, CV has been widely used to obtain qualitative information of electrochemical reactions including coupled chemical reactions, electron-transfer reactions and reduction/oxidation potentials of species [190, 191]. Therefore, CV has been applied in various fields such as analytical chemistry, electrochemistry and materials science. A standard CV setup is conducted in the electrochemical cell with three different electrodes: reference electrode (RE), working electrode (WE) and counter electrode (CE). These three electrodes are all immersed in the cell with the electrolyte. The electrochemical reaction takes place on

the WE, while the RE is used to maintain a constant potential. The utilization of the CE completes the electrical circuit during CV [192]. The potential applied between the WE and RE is usually linearly swept at a constant scan rate between two distinct potential limits. Typically, the potential cycles from a starting potential with a more negative value to an ending potential with a more positive value, then the cycle is reversed. When the potential is swept, the current between the WE and CE will be recorded during CV. The resulting current-potential curve is called a voltammogram, which is plotted with current on the y-axis and potential on the x-axis. Various features of the voltammogram can be extracted, such as peak positions, peak shapes and peak currents. These features are used to determine valuable information, including the electrochemical reaction kinetics, the number of transfer electrons and the concentration of analyte. The Nernst equation (3.5) can be used to predict the relationship between the potential and the concentration of the species in solution near the electrode as the potential is linearly swept over time [192]:

$$E = E^0 - \frac{RT}{nF} ln \frac{(Ox)}{(Red)} \tag{3.5}$$

where E is the potential of an electrochemical cell, E^0 is the standard potential of a species, R is the universal gas constant, T is the temperature in Kelvin, n is the moles of electrons, F is Faraday constant, (Red) is the concentration of the reduced species and (O_x) is the concentration of the oxidized species.

Figure 3.9 (a) shows the potential waveform applied between the WE and RE during a typical CV. The potential is linearly swept between two voltage limits at a certain speed of the scan rate. The potential increases from its initial value and reaches a maximum, as shown by the green line in figure 3.9 (a). Subsequently, the potential is reversed within the same voltage range, as indicated by the orange line. As shown in figure 3.9 (b), the resulting current is measured and recorded as the voltammogram during the potential sweep [193].

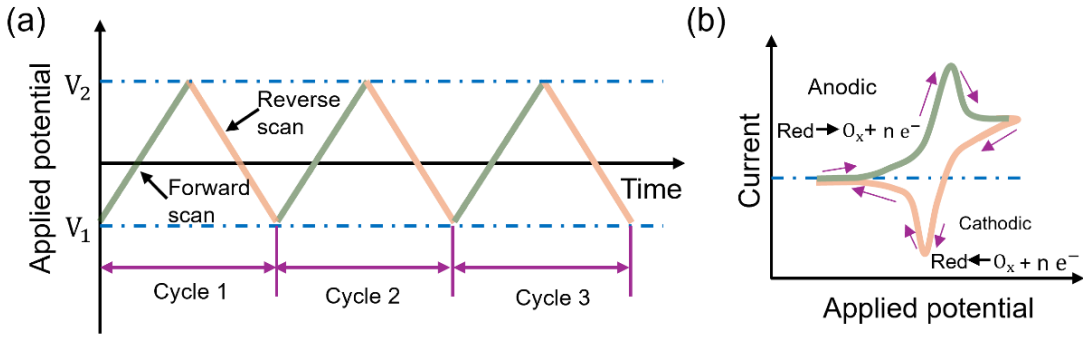

Figure 3.9: *(a) The potential versus time waveform showing the forward and reversed linear potential sweep, (b) Cyclic voltammogram of the measured current-potential curve. Figure is adapted from reference [193].*

As the potential is increased from lower to higher voltage during the positive (anodic) sweeping, the reducing agent undergoes an oxidation process. During this process, an oxide will be formed as electrons are lost, leading to an increase of the current up to its peak oxidation level.

Following this, the consumption of the reduction products causes a subsequent decline in current. When the maximum potential value is reached, the direction of the potential sweep is reversed, and the scan proceeds negatively (cathodically) from higher to lower voltage. During this reversed scanning, the oxide is reduced back to the reducing agent, acquiring electrons in the process. This reduction process results in a reduction peak [193].

4 Experiments

In this chapter, the experimental procedures performed in this thesis are presented. First, details of the fabrication process for OECT microarrays are discussed, including chip design, the preparation of PEDOT:PSS solutions and the chip fabrication flow. Subsequently, the preparation of the buffer solution, the measurement setup and the fabrication of the microfluidic system are demonstrated for the electrical characterization and application of the PEDOT:PSS OECTs. Then, the preparation of different membrane solutions and the integration of ISMs on OECTs for ion detection are described in detail. The preparation procedures for DA, UA, AA and chitosan solutions are explained, while the various measurement setups of cyclic voltammetry characterization for DA detection are displayed. Finally, detailed processes for fabricating the PEDOT:PSS based textile sensors are discussed.

4.1 Fabrication of OECTs

4.1.1 Chip design

Interdigitated electrodes (IDEs) are a type of electrode where multiple fingers or comb-like structures alternate with each other. These electrodes display promising advantages such as increased surface area, ease of fabrication and enhanced sensitivity. IDEs are commonly used in various technological and analytical applications, especially in the fields of chemical sensors and biosensors. In this thesis, IDEs are utilized to design the chips with OECT structures on a 4-inch mask. There are two different ways of placing OECT structures on each chip, which are 8 x 2 positioning and 4 x 4 positioning [194]. For instance, figure 4.1 displays the detailed layout of a chip with 4 x 4 positioning. A single source contact line is located horizontally in the center of the chip with one square contact pad placed at each end. The chip also contains 16 drain contact lines, with 8 lines placed both above and below the source contact line. Each drain contact line has a square contact pad at the end. Additionally, a square marker is located in each corner of the chip to assist with the alignment of each mask layout during the fabrication process. To ensure sufficient electrical contact for the OECTs, the size of all the contact pads is designed to be large enough to bond with up to six wire contacts. As shown in figure 4.1, 16 IDE structures with 10 fingers are positioned in the center of the chip. There are two different square openings on IDE structures, while the inner square is the opening for IDEs and the outer square provides the opening for channel materials.

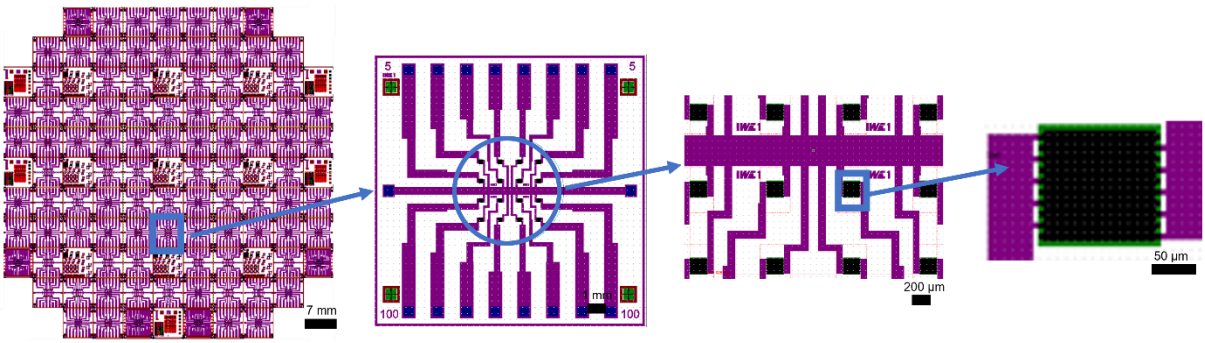

Figure 4.1: *Chip design of IDE structures with 10 fingers.*

The entire wafer layout has chips with 10 different IDE configurations containing varied geometries and sensing areas, as presented in Table 4.1. Finger width refers to the width of each electrode. Gate length is the distance between two adjacent electrodes, while gate width is the size of the opening of the inner square in the horizontal plane. The different geometry results in varied *W/L* ratios, which can be calculated by the formula: *W/L* ratio = (number of fingers - 1) x gate width/gate length.

Figure S1 in Appendix C shows the layout of the whole wafer with all masks for fabricating the chips with OECT structures in the clean room. First, mask 1, which is shown in the color purple, is designed to pattern the contact lines for the chips, including both the source and drain contact lines. Additionally, 16 IDE structures are designed in the center of each chip and one alignment marker is placed at each of the 4 corners of the chip. Once the design of mask 1 is completed, mask 2, displayed in red, is designed to create small square openings at the end of each source and drain contact line, as well as the inner square opening on the IDEs. The green wafer layout represents mask 3 which is designed to pattern the opening of the channel materials on IDEs. The opening squares on IDEs in mask 3 are slightly bigger than those in mask 2, ensuring that the transistors are properly defined. Each chip contains 16 individual addressable transistor channels in a common source configuration. To miniaturize the chips, the size of each chip is designed to be 7 mm x 7 mm. The entire wafer layout has 129 chips, which significantly improves cost effectiveness.

Table 4.1: *Different chip geometries on the wafer.*

ID	Number of fingers	Finger width	Gate length	Gate width	W/L ratio
1	8	5 µm	6 µm	100 µm	116.67
2	2	5 µm	6 µm	100 µm	16.67
3	10	5 µm	5 µm	100 µm	180
4	2	5 µm	6 µm	50 µm	8.33
5	4	5 µm	20 µm	100 µm	15
6	2	5 µm	20 µm	100 µm	5
7	2	5 µm	10 µm	100 µm	10
8	2	5 µm	6 µm	50 µm	8.33
9	2	5 µm	5 µm	20 µm	4
10	4	5 µm	6 µm	50 µm	25

Figure 4.2 (a) shows one test chip which contains various test structures. Seven distinct four-point-measurement structures are positioned in the bottom left area. The contact lines and their respective positions on each structure are designed in a uniform manner. These structures exhibit consistent spacing between each contact line and varying contact opening widths, while the contact pads of each structure provide sufficient space for the electrical contacts. Figure 4.2 (b) gives an example of the structure for four-point measurements. Above

these seven test structures, there are another eight test structures with varied spacing between each contact line for four-point-measurements. In these eight structures, the contact pads of each structure also provide sufficient space for the electrical contacts and the widths of each contact opening are kept consistent. The other structures on the test chip are Van der Pauw structures with different geometries and contact openings.

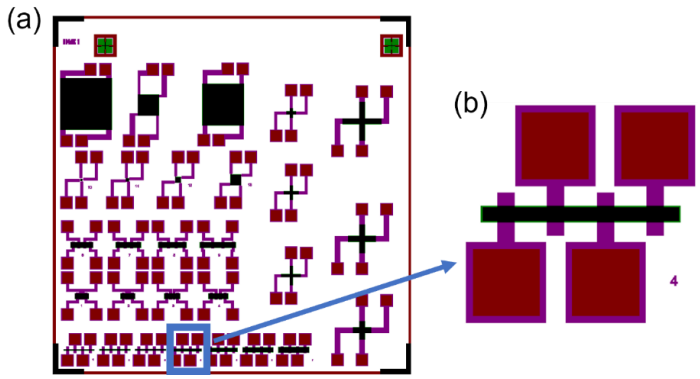

Figure 4.2: *(a) Test structures on the test chip, (b) A four-point measurement structure.*

Other masks are designed for fabricating OECTs where the contact lines and IDEs use different materials. As shown in figure 4.3 (a), the common source contact line is indicated in red in the horizontal center, while the individual drain contact lines (red) are vertically designed on the chip. In the center of the chip, the open areas between the source and drain lines are where IDE structures (light blue) are placed. IDE structures contain several different chip geometries, and the edges of the IDE structures slightly overlap with the contact lines to provide optimal electrical contacts. Following this, the channel opening (dark green) on the IDEs is designed on the chip. Finally, the PEDOT:PSS opening area is patterned on each transistor, as shown in light green in figure 4.3 (b). The opening square for patterning the PEDOT:PSS thin film is slightly larger than the channel opening square on the IDEs, ensuring complete coverage of the film on the transistors.

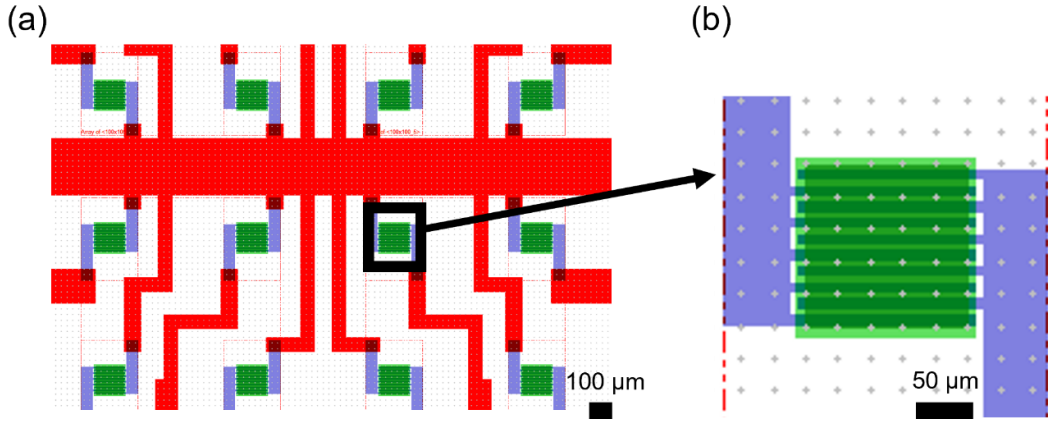

Figure 4.3: *(a) IDE structures (light blue) are placed between the source and drain contact line, (b) PEDOT:PSS area is designed on the IDE structures to be slightly bigger than the channel opening area.*

4.1.2 Van der Pauw chip design

The chips with Van der Pauw structures are designed to determine the sheet resistance of the PEDOT:PSS film. As shown in figure 4.4, the chips are designed on a 4-inch wafer and the whole wafer layout includes three different masks. Figure 4.4 (a) presents the layout of mask 1, which is designed to pattern the contact path for each chip that contains a contact pad at each corner and four contact lines pointing towards the center of the chip. Each chip is 1.5 cm x 1.5 cm in size. Mask 2 is created to facilitate the opening on contact pads and the opening area in the center of each chip. This mask contains three different square sizes in the center which are 2 µm x 2 µm, 3 µm x 3 µm and 5 µm x 5 µm. Lastly, the third mask is designed to pattern the opening area for the PEDOT:PSS film. The openings are slightly larger than the openings at the chip centers on the second mask, thus guaranteeing full coverage of the PEDOT:PSS film.

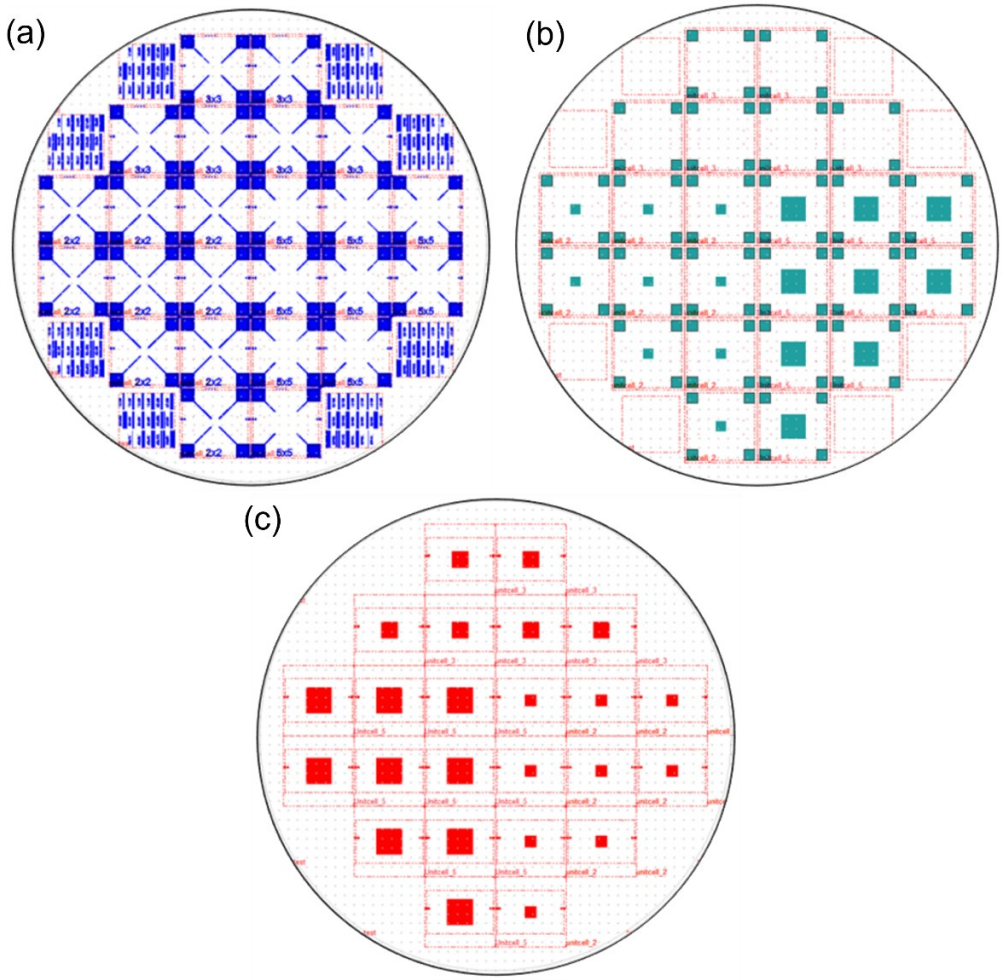

Figure 4.4: *Wafer layout for Van der Pauw structures (a) mask 1 for patterning the contact path, (b) mask 2 for opening the contact pads, (c) mask 3 for opening the PEDOT:PSS area.*

4.1.3 Preparation of PEDOT:PSS solutions

The effect of PEDOT:PSS films with varying thicknesses on the transistor performance and applications was investigated. Four different PEDOT:PSS mixture solutions (named as A, B, C and D) were prepared to obtain the different films. PEDOT:PSS solution (Clevios PH 1000)

was purchased from Heraeus, Germany. Ethylene glycol (EG) and 3-glycidyloxypropyl-triethoxysilan (GOPS) were purchased from Sigma-Aldrich, Taufkirchen, Germany.

First, the PEDOT:PSS solution was filtered using a 200 nm syringe filter (Luer Solo, B. Braun Melsungen AG, Germany) to remove the bigger particles. In order to obtain the PEDOT:PSS mixed solution A, the filtered PEDOT:PSS solution was then mixed with EG and GOPS in a ratio of 500:25:4 (v/v) respectively [62, 84]. The addition of EG and GOPS has been shown to improve the electrical conductivity and stability of PEDOT:PSS thin films in aqueous solutions [49]. The detailed preparation process for PEDOT:PSS mixture A is shown as follows:

(1) The first syringe was used to take 6-7 mL of the PEDOT:PSS solution, then the solution was filtered through the 200 nm syringe filter to obtain 5 mL of filtered PEDOT:PSS solution. After that, the filtered PEDOT:PSS solution was stored in a centrifuge tube at room temperature.
(2) The second syringe was used to withdraw 1 mL of the EG solution. Subsequently, 250 µL of this EG solution was pipetted and transferred to the same centrifuge tube containing 5 mL of filtered PEDOT:PSS solution.
(3) The third syringe was utilized to withdraw 1mL of the GOPS solution. Then, 43 µL of the GOPS solution was transferred using a micropipette to the centrifuge tube containing 5 mL of filtered PEDOT:PSS solution and 250 µL of EG solution.
(4) The obtained PEDOT:PSS/EG/GOPS mixture solution A was ultrasonicated. This centrifuge tube was placed in a beaker that was half-filled with water, then the beaker was placed in the ultrasonication machine. This bath ultrasonication took place at 50% sonication power for 1 hour at room temperature.
(5) After the ultrasonication was completed, the centrifuge tube containing the prepared PEDOT:PSS mixture solution A was stored at room temperature with the date and name clearly marked.

Figure 4.5 displays the detailed preparation procedure for these four PEDOT:PSS mixture solutions. After obtaining solution A, solution B was obtained by diluting solution A with DI water in a ratio of 1:2 (v/v) and ultrasonicating it for 1 hour. Subsequently, the dilution of solution B with DI water in a ratio of 1:2 (v/v) and ultrasonication for 1 hour were performed to obtain solution C. Finally, solution C was diluted with DI water in a ratio of 1:2 (v/v) and ultrasonicated for 1 hour to obtain solution D. Once the preparation procedure for the four solutions was completed, all were stored at room temperature. These four PEDOT:PSS mixture solutions were employed to prepare PEDOT:PSS films with varying thicknesses, to fabricate OECTs with distinct PEDOT:PSS films, and to investigate the influence of different PEDOT:PSS films on the electrical characterization of OECTs. Additionally, the impact of these varying films on the chemical applications of OECTs was investigated.

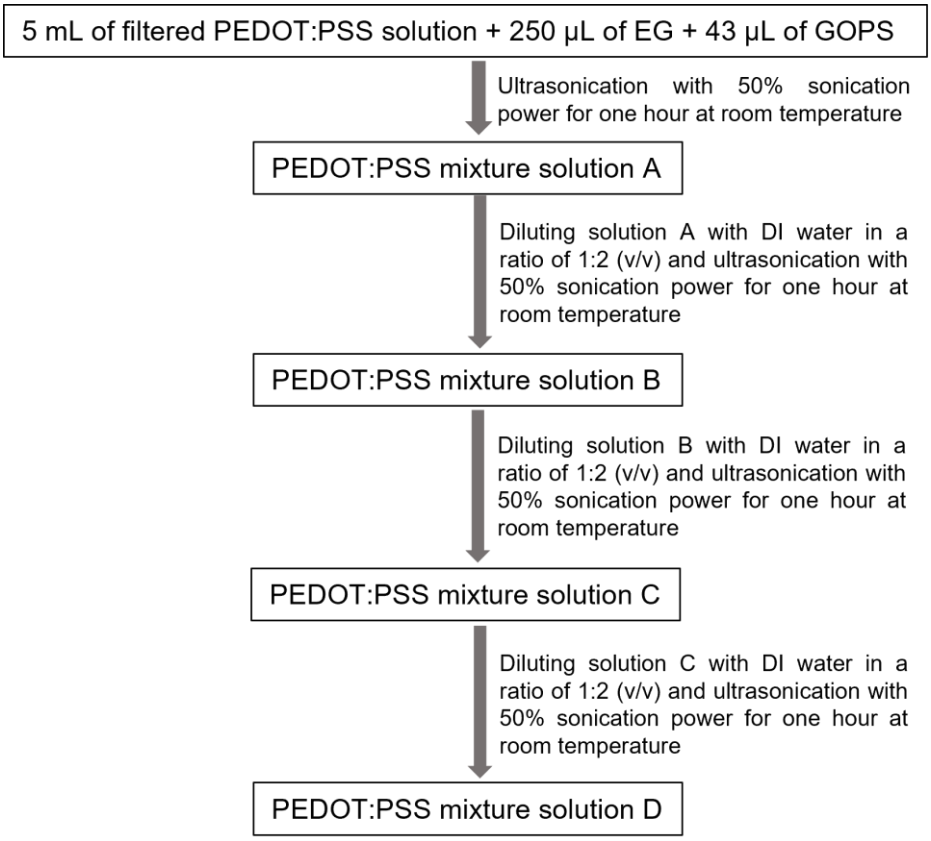

Figure 4.5: *Preparation procedure for four different PEDOT:PSS mixture solutions.*

4.1.4 Fabrication flow for OECTs

PEDOT:PSS-based OECTs were fabricated on 4-inch glass wafers using standard microfabrication techniques. Figure 4.6 shows the detailed fabrication process for OECT microarrays with Au contact material on the glass wafer. Firstly, the glass wafer was cleaned by submerging it in acetone and isopropanol for 5 minutes each. Next, hexamethyldisilane (HMDS) was applied on the wafer surface to provide appropriate adhesion for the photoresist. Then, AZ5214 photoresist (Microchemicals GmbH, Germany) was spin-coated on the wafer with the speed of 1300 rpm using a spin coater (Sawatec AG, Switzerland). Following this, the wafer was exposed under UV light for 2.5 seconds with the power of 12 mW/cm^2 and then developed in AZ726 MIF developer (Microchemicals GmbH, Germany) for 60 seconds. IDE microarrays and their contact lines were fabricated using e-beam evaporation of 5 nm Ti and 100 nm Au. A lift-off process was carried out by immersing the wafer into acetone for 5 minutes and then transferring it into the ultrasound machine for approximately 20 seconds. After establishing the contact lines and IDEs, the whole wafer was passivated using a 300 nm silicon oxide layer, which was deposited through a PECVD process at a temperature of 300°C. Subsequently, the second lithography process was carried out to pattern the opening of the contact pads and channel area, and these openings were then etched through a RIE process. The wafer was half-diced from the backside to ensure easy separation of the transistors by hand at the final stage of the process. The cutting area is 7000 µm x 7000 µm and the depth is 500 µm. The spindle speed of the dicing tool was set to 40000 rpm, and the cutting speed to 2 rpm. The third lithography process was then carried out to structure the PEDOT:PSS

channel area. Before depositing the PEDOT:PSS on the transistors, an oxygen plasma flash with 50 W of power, 300 m Torr of pressure and 100 sccm of O_2 flux was conducted on the wafer for 1 minute to activate the sample surface and improve the adhesion of the PEDOT:PSS. The PEDOT:PSS mixture solution was then spin-coated onto the wafer at a speed of 4000 rpm for 40 seconds and subsequently baked at 110°C for 1 minute on the hotplate. The lift-off process for the PEDOT:PSS was carried out by putting the wafer in acetone for 5 minutes, followed by 5 seconds of ultrasonication. The wafer was then cleaned in isopropanol and dried with nitrogen gas. After the lift-off process, the PEDOT:PSS was annealed on a hotplate at 140°C for 1 hour. Due to the half dicing process, the chips could be separated by manually breaking the glass substrate. Finally, the OECTs were wire-bonded and encapsulated for electrical characterization and applications. Using an identical fabrication process, OECT microarrays with other contact materials (Pt, IrO_x, TiN and ITO) were manufactured.

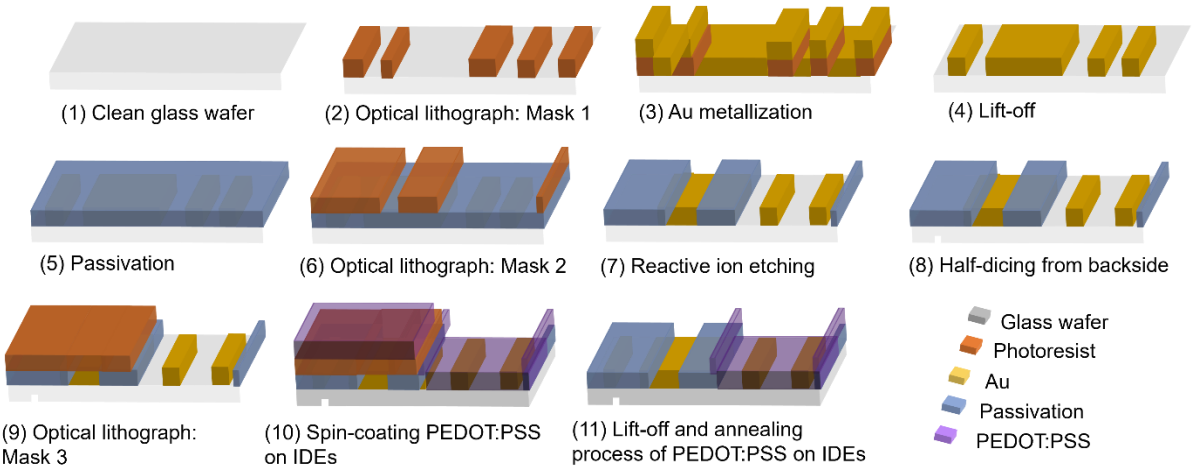

Figure 4.6: *Fabrication process for OECT microarrays with gold (Au) contact material using the mask layout shown in figure S1 in Appendix C.*

Figure 4.7 displays the microfabrication process for the PEDOT:PSS OECTs using Au as contact lines and IrO_x as IDEs on the wafer scale. The blank wafer was first cleaned in the acetone and isopropanol for 5 minutes each. Then, the application of HMDS on the wafer surface ensured the proper adhesion for the photoresist. Afterwards, AZ5214 photoresist was spin-coated on the wafer at a speed of 1300 rpm. Following this, the exposure process was performed on the wafer for 2.5 seconds with the power of 12 mW/cm^2, and the wafer was developed in AZ726 MIF developer for 60 seconds. The contact lines were fabricated using e-beam evaporation of 5 nm Ti and 100 nm Au, which were structured by the lift-off process. The wafer was then cleaned again by submerging it in acetone and isopropanol for 5 minutes each. HMDS was also applied again on the wafer surface before spin-coating the AZ5214 photoresist. Next, the first laser writing process with a light source of 405 nm and the power of 502 mJ/cm^2 was employed to pattern the IDE structures, and the wafer was developed in AZ726 MIF developer for 60 seconds. Subsequently, 30 nm Ti and 200 nm IrO_x were sputtered on the wafer, and a lift-off process was conducted to fabricate IrO_x IDE structures.

After the fabrication of the contact lines and IDEs was completed, a 300 nm silicon oxide layer was deposited using the PECVD process to passivate the entire wafer. The second laser lithography process was carried out to pattern the openings of the contact pads on each contact line and the openings on the IDEs. Following this, the wafer was etched using the RIE process to obtain these openings, and was half-diced from the back side.

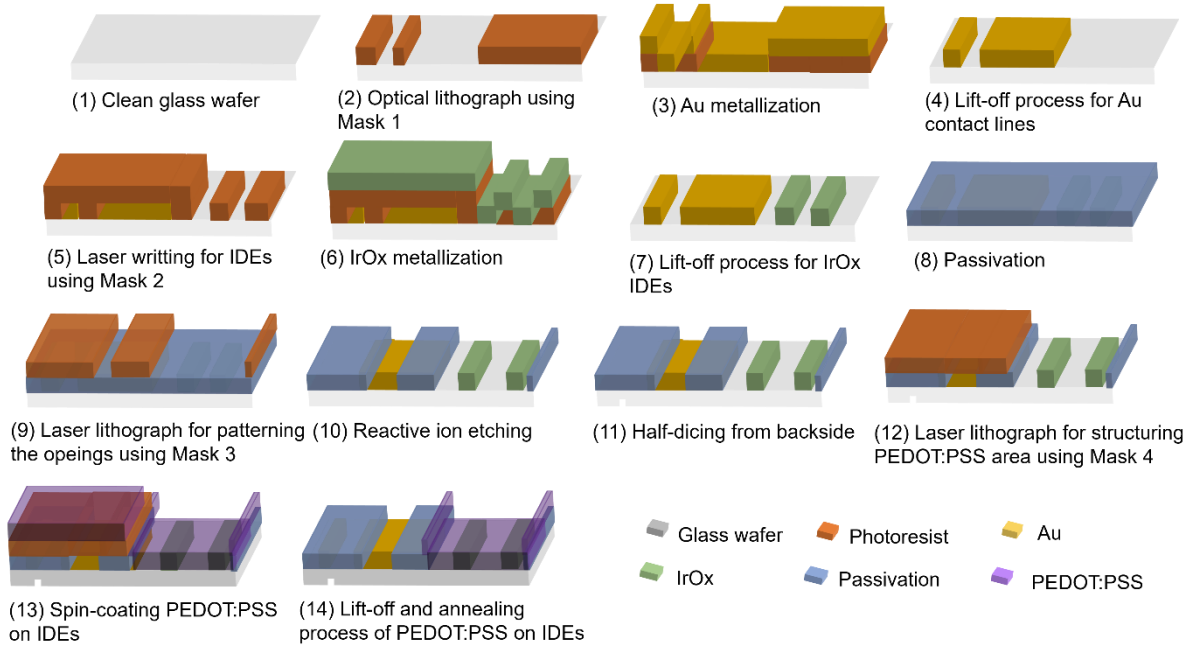

Figure 4.7: *Fabrication process for OECTs with Au as contact lines and IrO_x as IDEs.*

Afterwards, the last laser lithography process was carried out to structure the PEDOT:PSS area. Prior to spin-coating the PEDOT:PSS solution, the wafer was cleaned and activated with oxygen plasma (300 W, 300 sccm) for 1 minute. The PEDOT:PSS/EG/GOPS mixture solution was spin-coated onto IDE arrays at a speed of 4000 rpm, and the wafer was then baked on a hot plate at 110°C for 1 minute. Subsequently, the lift-off process was carried out using acetone to remove the photoresist and the wafer was annealed at 140°C for 1 hour. As the wafer had been half-diced from the back side, the transistors were easily separated by breaking the glass substrate by hand. Finally, the fabricated chips were wire-bonded and encapsulated for electrical characterization.

4.1.5 Fabrication flow for Van der Pauw chip

The chips with Van der Pauw (VDP) structure were fabricated using the standard optical lithography fabrication techniques on the wafer. Mask 1 displayed in figure 4.4 was utilized for the fabrication process in this thesis. The fabrication process started with cleaning the glass wafer in acetone and isopropanol for 5 minutes each. Subsequently, HMDS was applied on the wafer surface to provide proper adhesion for the photoresist, and the AZ5214 photoresist was then spin-coated on the wafer at a speed of 1300 rpm. Following this, the wafer was exposed for 2.5 seconds at the power of 12 mW/cm^2, and then developed in AZ726 MIF developer for 60 seconds. Afterwards, 5 nm Ti and 100 nm Au were evaporated on the wafer and a lift-off process was performed to obtain the contact lines and pads of the VDP structure. The wafer was diced to have a single chip with the size of 1.5 cm x 1.5 cm. The PEDOT:PSS

mixture solution was spin-coated at 4000 rpm on each VDP chip, then the chip was baked at 140°C for 1 hour. These fabricated VDP chips were characterized to determine the sheet resistance of the PEDOT:PSS film using the VDP method.

Masks 2 and 3 in figure 4.4 can be used to fabricate VDP chips with varying PEDOT:PSS areas (2 µm x 2 µm, 3 µm x 3 µm, 5 µm x 5 µm). After obtaining VDP structures with contact lines and pads, the whole wafer is passivated by the silicon oxide layer using the PECVD process. With mask 2, the second optical lithography is carried out to pattern the openings of contact pads and the openings in the chip center. Following this, the silicon oxide is etched away by the RIE process, and the wafer is half-diced from the back side. With mask 3, the third optical lithography is performed to structure the PEDOT:PSS area in the center of the chip. Subsequently, spin-coating the PEDOT:PSS mixture solution, and the lift-off and annealing processes are carried out to obtain the PEDOT:PSS film on the VDP chips. The individual chip can be easily separated by manually breaking the glass substrate.

4.2 Electrical characteristics of PEDOT:PSS OECTs

4.2.1 Preparation of buffer solutions

Sodium phosphate dibasic (Na_2HPO_4), sodium phosphate monobasic (NaH_2PO_4), potassium phosphate dibasic (K_2HPO_4) and potassium phosphate monobasic (KH_2PO_4) were all purchased from Sigma-Aldrich Chemie GmbH, Taufkirchen, Germany, and were used to prepare sodium and potassium buffer solutions. Figure 4.8 shows an image of the commercial equipment HANNA (Hanna Instruments Deutschland GmbH, Vöhringen, Germany) which was utilized to measure the pH and conductivity of these buffer solutions. HANNA equipment has three different electrodes: a temperature electrode, pH electrode and conductivity electrode. A certain amount of chemicals Na_2HPO_4 and NaH_2PO_4 were dissolved in DI water separately. The sodium buffer solutions were obtained by mixing Na_2HPO_4 and NaH_2PO_4 solutions. The pH value of the sodium buffer solutions was adjusted to a pH of 7 using the pH electrode, while the conductivity of these buffer solutions was controlled by the use of the conductivity electrode. Likewise, a certain amount of the chemicals K_2HPO_4 and KH_2PO_4 was dissolved in DI water separately. The potassium buffer solutions were then prepared by thoroughly mixing the K_2HPO_4 and KH_2PO_4 solutions. The pH value of 7 and the conductivity of these potassium buffer solutions were controlled and measured by using the pH and conductivity electrodes. Several different concentrations of sodium and potassium buffer solutions (1 mM, 5 mM, 10 mM, 50 mM and 100 mM) were prepared and used for the electrical characterization of the OECTs, and chemical and biosensing applications. The buffer solutions with lower concentrations were subsequently obtained by diluting 100 mM buffer solution with DI water.

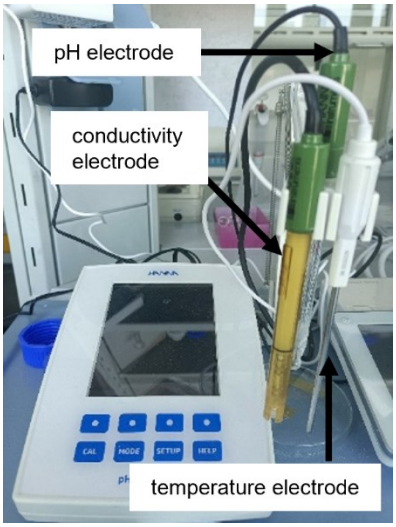

Figure 4.8: *HANNA instrument with pH, conductivity, and temperature electrodes.*

4.2.2 Measurement setup using a Keithley 4200 parameter analyzer

Figure 4.9 presents an image of the Keithley 4200A-SCS commercial semiconductor characterization system (Keithley Instruments, USA) in a laboratory at IWE1 Institute. It mainly consists of a probe station, measurement modules and a computer with Microsoft Windows operating system. The Keithley 4200A-SCS parameter analyzer is a fully integrated characterization system providing advanced capabilities. It can perform various electrical characteristics for semiconductor devices including transistors, diodes and other electronic components. This instrument can simultaneously characterize several semiconductor devices due to its multiple measurement channels. It facilitates the precise and repeatable positioning of probes on the semiconductor devices using its probe station. The Keithley 4200A-SCS parameter analyzer can be controlled by using specialized software, allowing users to easily set up the parameters of the experiments, perform measurements and analyze the data. In this thesis, this setup was used to measure the electrical characteristics of PEDOT:PSS OECTs, including I-V characteristics, real-time recording, output and transfer characteristics. This instrument was also employed for chemical and biosensing applications such as monitoring the concentrations of ions and DA.

Figure 4.9: *A commercial Keithley 4200A-SCS semiconductor characterization system.*

4.2.3 Measurement setup using the transfer function amplifier system

A customized transistor transfer function (TTF) amplifier system was employed to characterize the OECTs and perform their applications, and it has been described in detail in previous works [40, 195, 196]. Figure 4.10 (a) shows an image of this TTF amplifier system and (b) the schematic of the working principle of the read-out system. The TTF amplifier system facilitates simultaneous measurement for the 16 channel PEDOT:PSS OECT microarrays. Additionally, custom-made software for controlling and analyzing the data was developed using Delphi 5.0, a programming tool for creating Windows applications. The system can control and maintain precise temperature levels, which is critical for certain applications, especially those that are sensitive to temperature fluctuations. This TTF amplifier system is available for amplifier stages with different amplification factors of 1×, 10×, 30× and 100×, allowing the system to adapt to various signal strengths and improve the accuracy of measurements. The system is designed to be portable, facilitating ease of transportation. It connects to a PC via a USB interface, which enables convenient adaptation to various settings and locations. An electrochemical Ag/AgCl reference electrode (DRIREF-2SH, WPI Europe, Germany) which can provide a stable and constant potential for an analyte solution was used as a gate electrode. For the electrical measurements, different buffer solutions were applied to the OECTs, and the required V_{DS} and V_{GS} were set. Furthermore, the real-time recording of the 16 channel OECTs was performed using the TTF system at fixed V_{DS} and V_{GS}.

(a) (b)

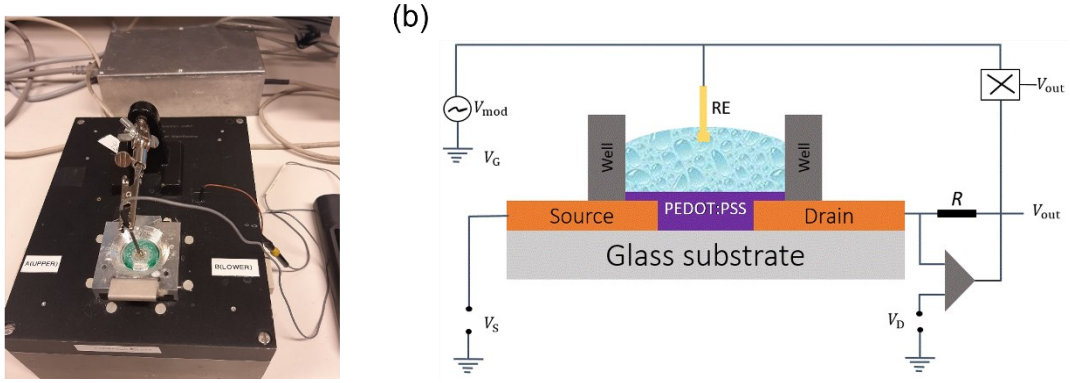

Figure 4.10: *(a) An image of the transistor transfer function (TTF) amplifier system, (b) The schematic of working principle of the real-out system.*

4.3 Microfluidic system

4.3.1 Design and fabrication of the microfluidic system

Figure 4.11 (a) shows the microfluidic flow cell made of polymethyl methacrylate (PMMA). This flow cell was manufactured by the Gemeinschaftswerkstatt Walter-Schottky-Haus (GWSH) and detailed information about the design can be found in this work [197]. This flow cell contains several modular parts such as base, clip, electrode hole, inlet and outlet. The base and the clip were fabricated to be compatible with an IC51-0684-390 Yamaichi socket (Yamaichi Electronics Deutschland GmbH, Frankfurt, Germany) and TTF amplifier system. The gate electrode can be immersed in the liquid in the electrode hole. As displayed in figure 4.11 (b), in the central area of the flow cell is a transparent window, which allows the user to check the position of the chips with bare eyes or the magnifying lens of a microscope.

Moreover, a clear central cross in the middle of the window is designed to assist with alignment. The liquid first enters the microfluidic system from the inlet via a connecting tube on one side of the setup (left or right side). It flows into the chip and then through the designed channels, and finally accumulates in another connecting tube after passing through the outlet on the other side (right or left side).

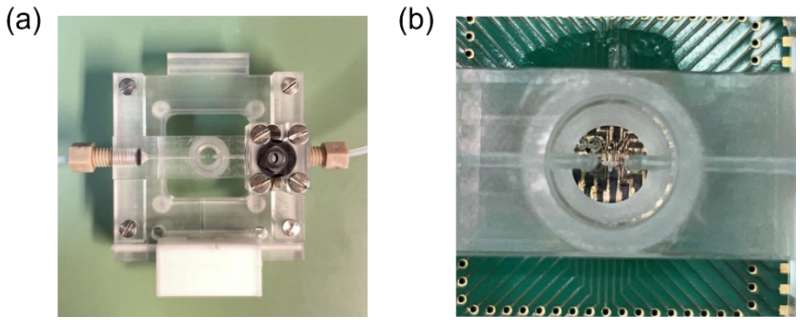

Figure 4.11: *(a) A fabricated flow cell made of PMMA, (b) The center area of the flow cell.*

Figure 4.12 (a) shows the top view of the schematic of the microfluidic poly(dimethylsiloxane) (PDMS) channel mold which was designed using the software Fusion 360 [197]. The height of all microfluidic chambers is 0.5 mm. From left to right on the mold, the widths of the chambers are 1.4 mm, 1.2 mm, 1.0 mm, and 0.9 mm, respectively. Figure 4.12 (b) and (c) present images of the cover plate and the mold form respectively, which were fabricated using aluminum. To ensure that these two components fit together perfectly, two large holes on the edge of each mold kit were designed for connecting rods. To make holes for the PDMS channels, several smaller pins were also fabricated on the mold form (figure 4.12 (c)).

In preparation for the formation of the PDMS channels, the cover plate and the mold form were first cleaned with isopropanol. Then, silicon elastomer adhesive was thoroughly mixed with a curing agent in a weight ratio of 10:1. The mixture was degassed in the desiccator for approximately 30 minutes until there were no air bubbles. After that, the cleaned mold form (figure 4.12 (c)) was filled with the adhesive mixture and degassed again for around 90 minutes to remove the air bubbles. The mold form was closed with the cover plate (figure 4.12 (b)) and then baked in the oven at 130°C for 1 hour. Finally, the two parts of the mold kit were separated by hand and each PDMS channel was carefully peeled from the mold form using tweezers. An image of two PDMS channels is shown in figure 4.12 (d).

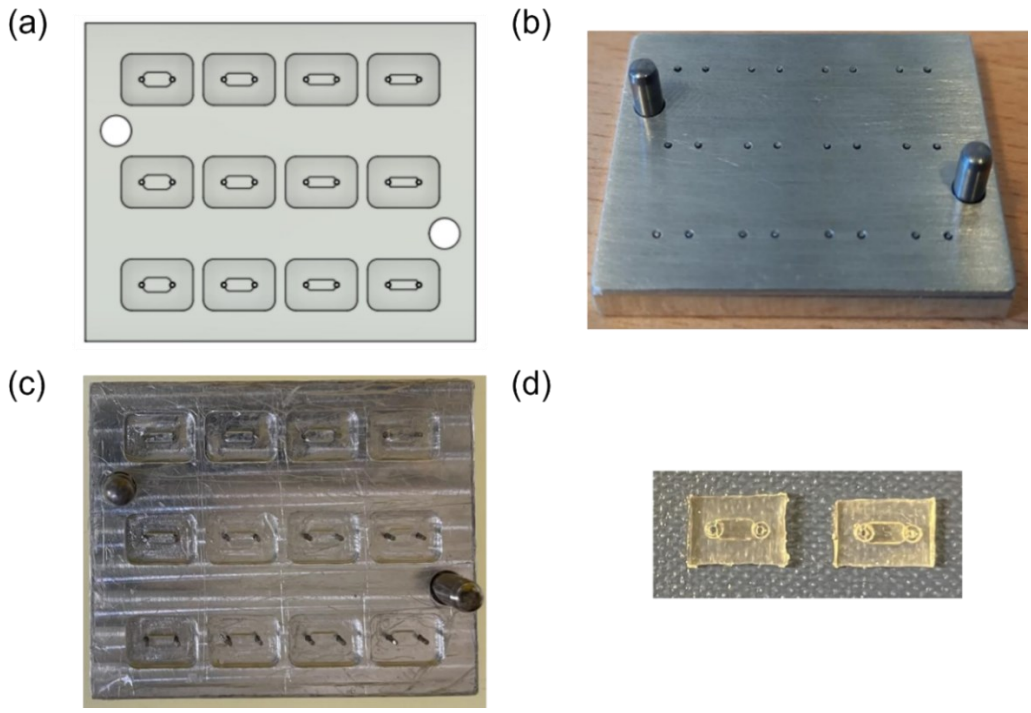

Figure 4.12: *(a) Schematic of the microfluidic channel mold (top view), (b) The cover plate of the fabricated microfluidic channel mold, (c) Fabricated mold form for PDMS channels, (d) Two fabricated PDMS channels.*

4.3.2 Measurement setup with the microfluidic system

Figure 4.13 illustrates the schematic of the electrical characteristics and the detection of ions (Na^+ and K^+) in the buffer solutions using PEDOT:PSS OECTs integrated with the fabricated microfluidic system. An Infuse/Withdraw AL-1000 syringe pump was ordered from Landgraf Laborsysteme HLL GmbH (Langenhagen, Germany) and utilized to withdraw the liquid in the flow system. Sterile syringes were purchased from B. Braun Melsungen AG (Melsungen, Germany) to facilitate a flow rate of hundreds of microliters per minute. An electrochemical Ag/AgCl reference electrode was used as a gate electrode. The customized TTF amplifier system was utilized for the electrical characterization and ion detection within the PEDOT:PSS OECTs. As shown in figure 4.13, the buffer solutions were pumped through the microfluidic system via a 50 mL syringe pump. First, these buffer solutions interacted with OECTs covered with different ISMs (Na^+ and K^+ ISMs) within the microfluidic system. Then, they were collected by the same syringe pump. This microfluidic system facilitated the buffer solutions to flow through the entire system with a flow rate of 150 µL/min. To establish the transfer characteristics, V_{GS} was systematically swept from -0.8 V to 0 V with 30 steps. V_{DS} from -0.1 V to -0.4 V with a step of -0.1 V was applied. This microfluidic system was also integrated in the OECTs for real-time and multiplexed sensing of ion detection. The different buffer solutions were pumped through the microfluidic system consecutively to ensure a continuous solution supply. For the real-time and multiplexed sensing of ion concentrations, V_{DS} of -0.4 V and V_{GS} at the maximum g_m were selected as the working points. The value of the drain current was obtained with a sampling time of 1 second. Additionally, this microfluidic system integrated with OECTs was utilized for the real-time monitoring of DA concentrations.

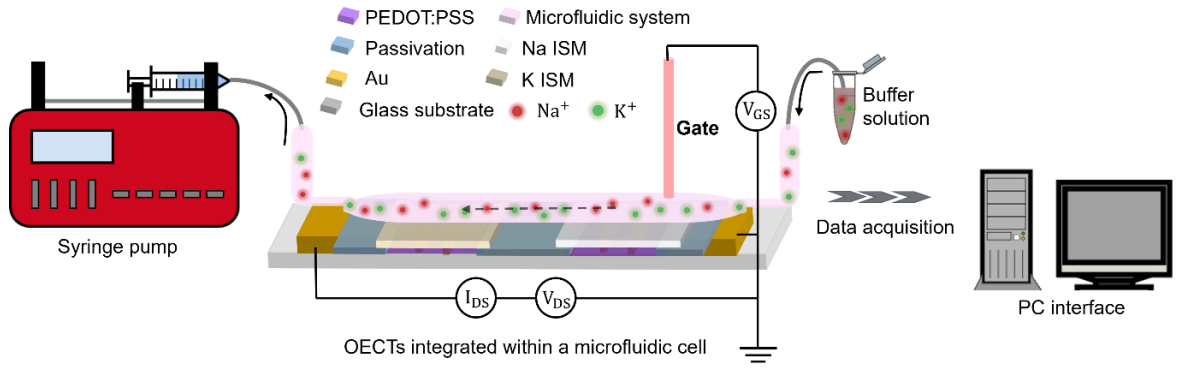

Figure 4.13: *Schematic representation of electrical characteristics of OECTs integrating with the microfluidic system.*

4.4 Ion detection using ion-selective membrane integrated OECTs

4.4.1 Preparation of ion-selective membrane mixture solutions

The Na^+ ISM mixture solution with composition 0 was composed of Na ionophore X, Na-TFPB, PVC and DOS at the ratio of 1:0.55:33:65.45 (w/w, 100 mg) [143, 198]. 100 mg of the mixture was dissolved in 660 µL of THF by shaking it for 10 minutes until the solution was homogenous. Similarly, the K^+ ISM mixture solution with composition 0 consisted of Kalium-ionophore Ⅲ, KTB, PVC and DOS at the ratio of 2:0.5:32.7:64.7 (w/w), and 100 mg of the mixture was dissolved in 660 µL of THF by thoroughly mixing for 10 minutes to obtain a homogenous membrane solution [143, 198]. Both ISM solutions were sealed and stored at 4°C without light exposure.

Figure 4.14 shows the image of the Na^+ ISM mixture solution (a) and K^+ ISM mixture solution (b). After being thoroughly mixed, the Na^+ ISM solution exhibits a transparent appearance, while the K^+ ISM solution displays a yellow color.

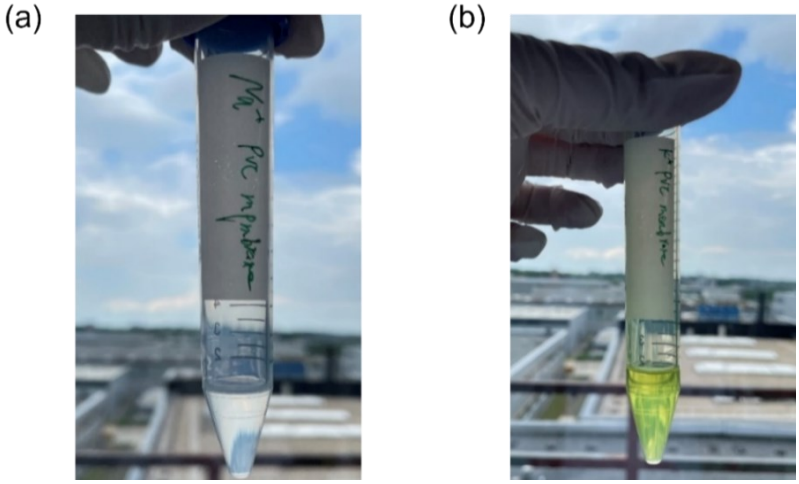

Figure 4.14: *(a) Na^+ ion-selective membrane (ISM) mixture solution, (b) K^+ ion-selective membrane (ISM) mixture solution.*

An identical experimental procedure was applied for the preparation of the other modified Na^+ ISM solutions: composition 1 of Na^+ ISM solution contains 1.82 mg of Na ionophore X, 1 mg

of Na-TFPB, 30 mg of PVC, 59.5 mg of DOS and 1200 µL of THF. Composition 2 of Na^+ ISM solution contains 1.82 mg of Na^+ ionophore X, 1 mg of Na-TFPB, 19.8 mg of PVC, 39.27 mg of DOS and 1200 µL of THF. All the compositions of the Na^+ ISM solutions are shown in Table 4.2.

Table 4.2: *Three different compositions of Na^+ ion-selective membrane (ISM) solutions.*

Na^+ ISM solutions	Sodium-ionophore X (mg)	Na-TFPB (mg)	PVC (mg)	DOS (mg)	THF (µL)
Composition 0	1.82	1	60	119	1200
Composition 1	1.82	1	30	59.5	1200
Composition 2	1.82	1	19.8	39.27	1200

The same process was utilized to prepare the K^+ ISM mixture solutions with other compositions: composition 1 of K^+ ISM contains 4 mg of Kalium-ionophore Ⅲ, 1 mg of KTB, 32.5 mg of PVC, 64.5 mg of DOS and 1200 µL of THF. Composition 2 of K^+ ISM contains 4 mg of Kalium-ionophore Ⅲ, 1 mg of KTB, 21.6 mg of PVC, 42.7 mg of DOS and 1200 µL of THF. All the compositions of the K^+ ISM solutions are shown in Table 4.3.

Table 4.3: *Three different compositions of K^+ ion-selective membrane (ISM) solutions.*

K^+ ISM solutions	Kalium ionophore Ⅲ (mg)	KTB (mg)	PVC (mg)	DOS (mg)	THF (µL)
Composition 0	4	1	65	129	1200
Composition 1	4	1	32.5	64.5	1200
Composition 2	4	1	21.6	42.7	1200

4.4.2 Integration and optimization of ion-selective membranes on OECTs

Figure 4.15 (a) shows the process of integrating the ISMs onto the PEDOT:PSS OECTs. First, all the aforementioned chemicals in section 4.4.1 were dissolved and thoroughly mixed into a THF solvent. Then, 40 µL of the ISM solution was pipetted onto the center of the OECTs and immediately spin-coated at the speeds of 3000 rpm, 4000 rpm and 5000 rpm. After this, the ISM mixture solution was left to evaporate overnight at room temperature.

For the optimization of the ISMs, first the spin-coating technique was carried out to modify the thicknesses of the membranes. After the integration of the membrane mixture solution with composition 0 onto the chips, a stylus profilometer (DektakXT, Bruker, Germany) was utilized to determine the membrane thicknesses by measuring the step height on multiple points distributed on the sample. Different rotational speeds yielded various thicknesses of ISMs. The results presented that the membrane thickness reduced from 1600 ± 87 nm (n=6) to 1300 ± 90 nm (n=5) with an increase of the spin-coating speed from 3000 rpm to 5000 rpm.

The ratio of PVC and DOS in the membrane mixture solution is crucial to obtain membranes with varied thicknesses [153]. Therefore, the optimization of the ISM can be evaluated by modifying the compositions of the ISM mixture solution. As described in section 4.4.1, three

different compositions of the Na^+ and K^+ ISM solutions were prepared for this purpose. With the spin-coating speed at 5000 rpm, the membrane thickness with composition 1 was measured to be 600 ± 88 nm (n=8), while the membrane solution of composition 2 yielded a thickness of only 80 ± 13 nm (n=5).

The impact of these membranes on the electrical characteristics of PEDOT:PSS OECTs during the fabrication process was investigated. Two-probe resistance measurement using the Keithley 4200 parameter analyzer was performed between source and drain electrodes after the deposition of PEDOT:PSS (step 1), spin-coating of ISM (step 2) and chip encapsulation (step 3). The voltage was systematically swept from -0.1 V to 0.1 V between the source and drain electrodes of the OECTs. By calculating the slope of the linear IV curve using the formula R = V/I, the resistance was determined. Here, V refers to the applied voltage and I represents the measured current value. In figure 4.15 (b), the resistance value between source and drain electrodes exhibits a slight increase after the integration of the ISM and chip encapsulation, compared to the resistance value acquired after the deposition of the PEDOT:PSS on OECTs. Nevertheless, such minuscule changes in the electrical resistance can be disregarded. Therefore, the successful integration of ISM on the chips during the fabrication process allowed for the actualization of ion-selective OECTs.

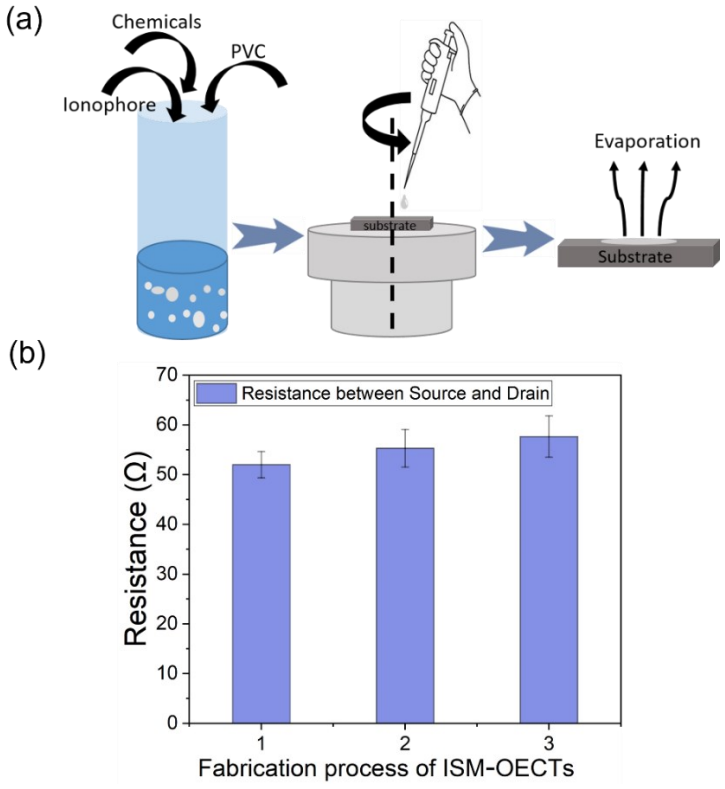

Figure 4.15: *(a) Schematic representation of integrating the ion-selective membranes (ISMs) onto OECTs, (b) Resistance between source and drain electrodes during the fabrication process of ISM-based PEDOT:PSS OECTs. Step 1 means after depositing the PEDOT:PSS on OECTs, step 2 refers to after integrating ISMs on PEDOT:PSS OECTs, step 3 means after chip encapsulation process (n=3).*

4.5 Dopamine detection using OECTs

4.5.1 Preparation of dopamine, uric acid, ascorbic acid and chitosan solutions

Dopamine hydrochloride, UA, AA, chitosan and phosphate buffered saline (PBS) solution (pH=7.4) were all purchased from Sigma-Aldrich, Taufkirchen, Germany. Acetic acid (100%) was purchased from Merk KGaA Company. Dopamine hydrochloride was stored at 4°C when not in use. The other chemicals were stored at room temperature.

DA solutions ranging in concentrations (10 mM, 3 mM, 1 mM, 300 µM, 250 µM, 100 µM, 30 µM, 10 µM, 3 µM, 1 µM, 100 nM, 10 nM and 1 nM) were prepared. First, a DA solution with 10 mM was obtained by dissolving 18.964 mg of DA powder into 10 mL of PBS solution. Then, DA solutions with lower concentrations were prepared by gradually diluting the 10 mM DA solution with PBS solution. The detailed preparation steps are shown as follows:

(1) 18.964 mg of DA powder was dissolved in 10 mL of PBS solution to obtain the 10 mM DA solution;
(2) 300 µL of 10 mM DA solution was mixed with 700 µL of PBS solution to obtain 1 mL of the 3 mM DA solution;
(3) 100 µL of 10 mM DA solution was mixed with 900 µL of PBS solution to obtain 1 mL of the 1 mM DA solution;
(4) 30 µL of 10 mM DA solution was mixed with 1 mL of PBS solution to obtain 1 mL of the 300 µM DA solution;
(5) 10 µL of 10 mM DA solution was mixed with 1 mL of PBS solution to obtain 1 mL of the 100 µM DA solution;
(6) 30 µL of 1 mM DA solution was mixed with 1 mL of PBS solution to obtain 1 mL of the 30 µM DA solution;
(7) 10 µL of 1 mM DA solution was mixed with 1 mL PBS solution to obtain 1 mL of the 10 µM DA solution;
(8) 30 µL of 100 µM DA solution was mixed with 1 mL PBS solution to obtain 1 mL of the 3 µM DA solution;
(9) 10 µL of 100 µM DA solution was mixed with 1 mL PBS solution to obtain 1 mL of the 1 µM DA solution;
(10) 10 µL of 10 µM DA solution was mixed with 1 mL PBS solution to obtain 1 mL of the 100 nM DA solution;
(11) 10 µL of 1 µM DA solution was mixed with 1 mL PBS solution to obtain 1 mL of the 10 nM DA solution;
(12) 10 µL of 100 nM DA solution was mixed with 1 mL PBS solution to obtain 1 mL of the 1 nM DA solution.

Figure 4.16 displays the prepared DA solutions with concentrations ranging from 1 nM and 3 mM. The first two DA solutions from the left are with mM concentrations and the other DA solutions are with nM or µM concentrations. DA solutions oxidize rapidly at room temperature

and will become darker in color. Therefore, they should be used immediately after preparation and always stored in the fridge at 4°C when not in use.

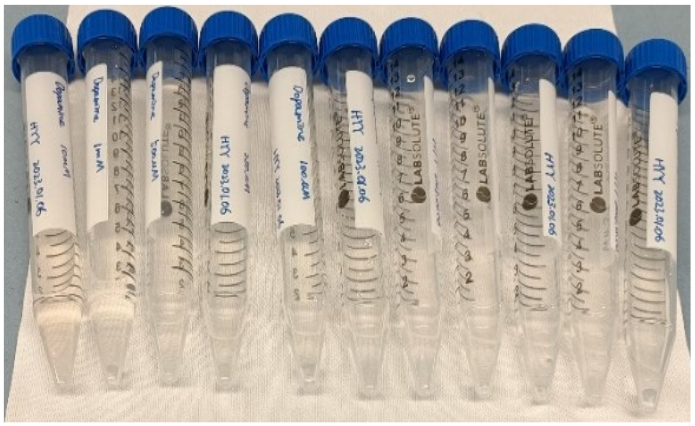

Figure 4.16: *Fresh dopamine solutions with concentrations ranging from 1 nM to 3 mM.*

Following the same experiment procedure, AA solutions were prepared with concentrations ranging from 1 nM to 3 mM, as well as UA solutions with concentrations ranging from 1 nM to 1 mM were prepared. All the prepared solutions were stored at 4°C in the fridge for long-term use.

The chitosan solution (1.0%) was prepared by dissolving 1.0 g of chitosan powder in 100 mL of acetic acid solution (1.0 wt.%). The mixed solution was continuously stirred for 24 hours at room temperature to ensure complete dissolution. It was then refrigerated at 4°C for storage. The detailed preparation steps are shown as follows:

(1) 1.0 g of acetic acid (100%) was added to 100 mL DI water to get 100 mL of acetic acid solution (1.0 wt.%);
(2) 1.0 g of chitosan powder was dissolved in 100 mL of acetic acid solution (1.0 wt.%) and stirred using the magnetic stirrer at room temperature for 24 hours until complete dissolution. As shown in figure 4.17, the obtained 1.0% chitosan solution exhibits a light yellow color;
(3) The prepared chitosan solution (1.0%) was stored at 4°C in the refrigerator when not in use [199].

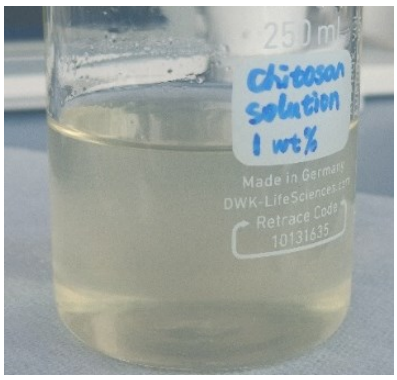

Figure 4.17: *Image of 1.0% chitosan solution.*

4.5.2 Cyclic voltammetry characterization

Figure 4.18 (a) and (c) show the schematic and the image of the first setup for CV characterization. The WE and CE were Pt wires, while the RE was an Ag/AgCl reference electrode. These three electrodes were all immersed in the electrolytic cell with electrolyte solutions. Figure 4.18 (b) and (d) present the schematic and the image of the second measurement setup for CV characterization. In this setup, the source and drain electrodes were connected and served as the WE. A Pt wire was used as the CE and an Ag/AgCl reference electrode was used as the RE. These three electrodes were all immersed in PEDOT:PSS OECTs with electrolyte solutions. A voltage was swept linearly from -0.2 V to 0.8 V with the scan rate of 0.05 V/s between the WE and RE. Then, the voltage sweep reversed from 0.8 V to -0.2 V once the voltage reached the pre-set limit (0.8 V). This process was repeated multiple times, and the current changes between WE and CE were recorded.

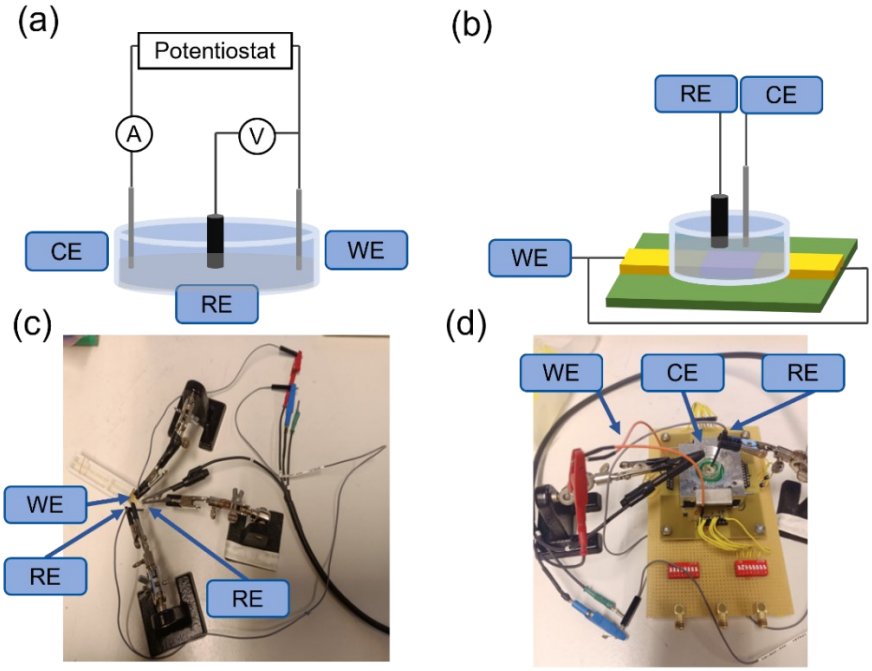

Figure 4.18: *Schematic (a) and image (c) of the first setup for CV characterization, schematic (b) and image (d) of the second setup for CV characterization.*

4.6 Ion-selective textile sensors realized with PEDOT:PSS for ion detection

4.6.1 Materials for preparing ion-selective textile sensors

In this thesis, the cotton yarn (17.HIN.13 831, Søstrene Grene, Germany) utilized for preparing the textile sensors was purchased from the commercial market. The metal wires (TW-MP-10, Twin Industries, Germany) had a length of 10 cm. Additionally, curing adhesive silver glue (No. T1312109, Kemo Electronic GmbH, Germany) was used to effectively bond different parts of the textile sensors at low temperatures. The silicone adhesive (No. 96-083, Dow Silica, United States) containing a base component A and a curing agent B was used. The silicone adhesive gained its adhesive properties when components A and B were mixed in a ratio of 10:1 (w/w) and subsequently exposed to heat.

PEDOT:PSS mixture solution A was prepared using the procedure described in section 4.1.3 and then used for the fabrication of the PEDOT:PSS based textile sensors. Additionally, these textile sensors were immersed in the Na^+ or K^+ ISM mixture solution with composition 0 to obtain the Na^+ or K^+ ion-selective textile sensors. The Na^+ and K^+ buffer solutions with the pH value of 7 and the concentrations of 1, 5, 10, and 50 mM were prepared and controlled using the identical procedure shown in section 4.2.1.

4.6.2 Fabrication process for ion-selective textile sensors

Figure 4.19 (a) presents the schematic of the fabrication process for the textile sensors. First, the cotton yarn was cleaned using DI water and trimmed to a length of 1.5 cm, while the diameter of the cotton yarn was maintained at 0.6 mm. Following this, different pieces of yarn were submerged in the PEDOT:PSS mixture solution (figure 4.19 (b)) for varying durations of time, ranging from 2 to 12 seconds. The PEDOT:PSS coated yarn was then baked in an oven at 80°C for 1 hour.

According to step 2 in figure 4.19 (a), the PEDOT:PSS coated yarn was connected to metal wires by using silver glue and then air-dried at room temperature. Next, a layer of silicone adhesive was applied to the connection points of the wire and cotton yarn to insulate these points from the surrounding air or solutions. Afterwards, the samples were carefully transferred to the oven and dried at 50°C for 24 hours, thus completing the fabrication of the PEDOT:PSS based textile sensors. In order to fabricate Na^+ or K^+ ion-selective textile sensors, the PEDOT:PSS coated yarn was further immersed in the Na^+ or K^+ ISM solutions for 10 seconds and subsequently air-dried for 10 minutes.

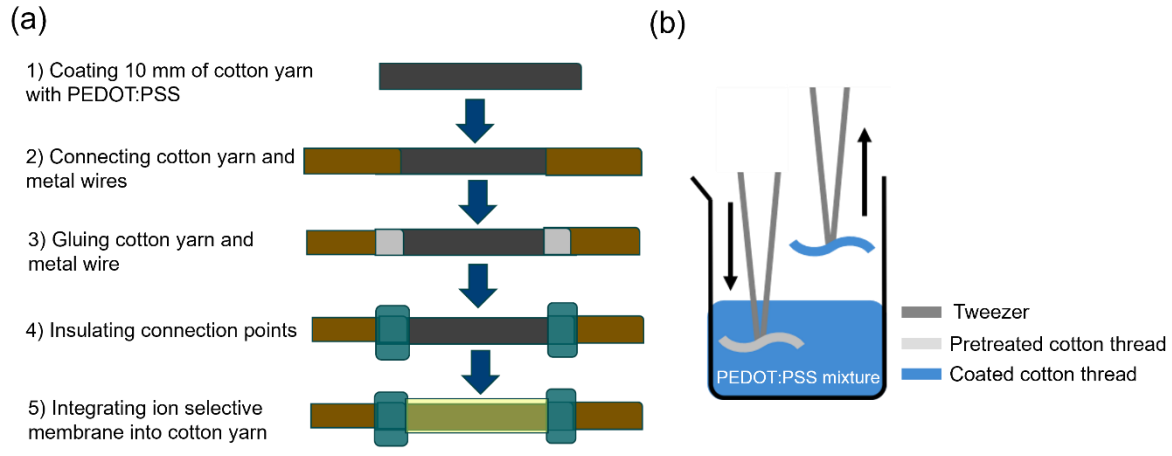

Figure 4.19: *(a) Schematic presentation of the fabrication process for textile sensors integrated with ion-selective membrane (ISM), (b) Schematic of coating the cotton yarn with the PEDOT:PSS mixture solution.*

5 Results and discussion

This chapter presents the results of the lithography fabrication, wire bonding and encapsulation for the OECT microarrays. The electrical conductivity of PEDOT:PSS thin films and the electrical characteristics of the OECTs are then demonstrated. Subsequently, the performance of the OECTs is evaluated by investigating the various electrode materials and PEDOT:PSS film thicknesses. Afterwards, the highly sensitive and selective detection of different ions using PEDOT:PSS OECTs integrated with ISMs is discussed. In the following section, the multiplexed, real-time and reversible detection in different electrolytes is displayed. Then, a novel platform for DA detection using an OECT microarray in combination with a Pt gate electrode is presented. The characteristics of the platform are showcased with a focus on the sensitivity, selectivity and limit of detection. The results of real-time measurements for DA detection are also discussed. Finally, the realization of ion selective textile sensors based on PEDOT:PSS is discussed.

5.1 Fabrication of OECTs

5.1.1 Optical lithography for fabrication of OECTs

The microfabrication process for the PEDOT:PSS OECTs is described in section 4.1.4 and the results will be presented in this section. Figure 5.1 (a) shows the microscope image of the glass wafer after completing the first optical lithography process (step 2 in figure 4.6). The light green areas exhibit homogenous properties, demonstrating that the photoresist AZ5214 was uniformly distributed on these areas during the spin-coating process and maintained its integrity after the development. Moreover, the clearly patterned dark green areas in figure 5.1 (a) indicate the successful development of the contact lines and IDE structures. The contact line placed in the middle of the chip shows the structure of the common source electrode, while the contact lines placed vertically connecting to the source electrode are drain electrodes. The IDE structures with 8 fingers were patterned between the source and drain contacts. Figure 5.1 (b) presents the test structure on the wafer that will be used for four-point measurements. The clearly patterned dark green areas are the test structure, and the other areas are covered by the photoresist. The four squares in the corners of the figure represent the four contact pads of the test structure. Additionally, the four different lines connected with each contact pad are the contact lines of the test structure.

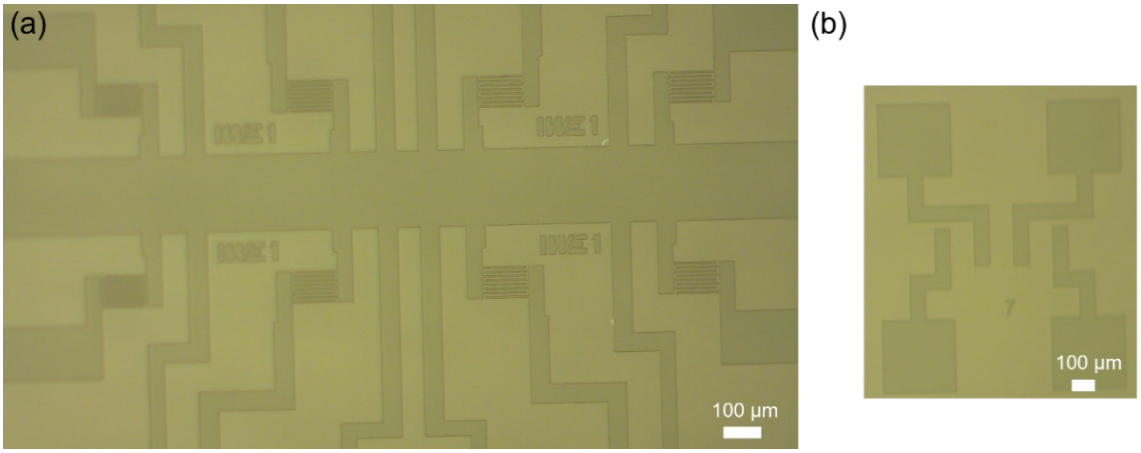

Figure 5.1: *Microscope image of glass wafer after the development process. (a) The patterned contact lines and IDE structures, (b) The patterned test structure for four-point measurements.*

After patterning the contact lines and IDE structures on the glass wafer, a metallization process for five different materials (Au, Pt, TiN, ITO and IrO_x) using either e-beam evaporation or magnetron sputtering was conducted. Following that, a lift-off process was carried out. Figure 5.2 shows the patterned contact lines and IDE structures with different contact materials. In figure 5.2 (a), the yellow color shows the evaporated Au contact lines and IDE structures homogenously distributed on the wafer. Similarly, figure 5.2 (b) displays the Pt contact lines and IDE structures after the lift-off process, while TiN contact lines and IDE structures are presented in figure 5.2 (c). In figure 5.2 (d), the bright blue color is uniformly distributed on the wafer, indicating the sputtered ITO contact lines and IDE structures. Lastly, figure 5.2 (e) shows the patterned IrO_x contact lines and IDE structures on the wafer when the lift-off process was completed. All the contact materials were deposited homogenously on the contact lines and IDE structures, highlighting the reliability of the metallization and lift-off processes for various materials.

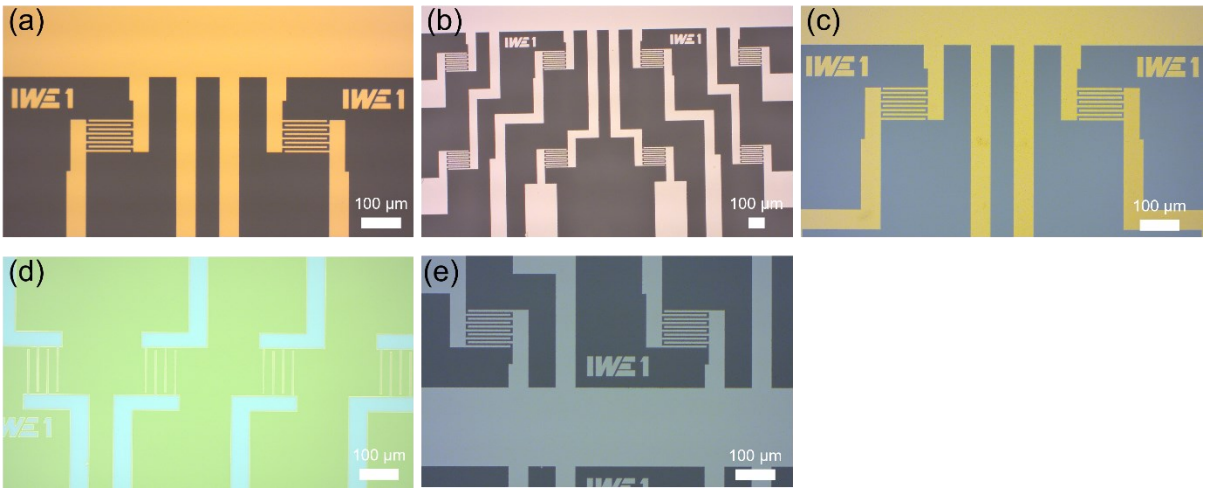

Figure 5.2: *(a) 50 nm of evaporated Au contact material, (b) 100 nm of sputtered Pt material, (c) 150 nm of sputtered TiN material, (d) 150 nm of sputtered ITO material, (e) 150 nm of sputtered IrO_x contact material.*

The passivation layer was employed by depositing 300 nm of silicon oxide on the entire wafer using the PECVD process. Afterwards, the second optical lithography was carried out to pattern the openings for the contact pads and the IDEs (step 6 in figure 4.6). HMDS was applied on the wafer surface and the AZ5214 photoresist was spin-coated on the wafer. The wafer was then exposed and developed using the same parameters as the first optical lithography. After the development process, the silicon oxide layer on the wafer was etched using the RIE process. Figure 5.3 (a) shows the microscope image of the wafer with an opening square on each IDE structure after the RIE process. The area inside the square that appears bright yellow indicates the color of Au. This result demonstrates that the silicon oxide layer was completely etched away, and the Au was exposed to air. The area outside of the square is a homogenous light yellow, showing that the silicon oxide passivation layer maintained its integrity.

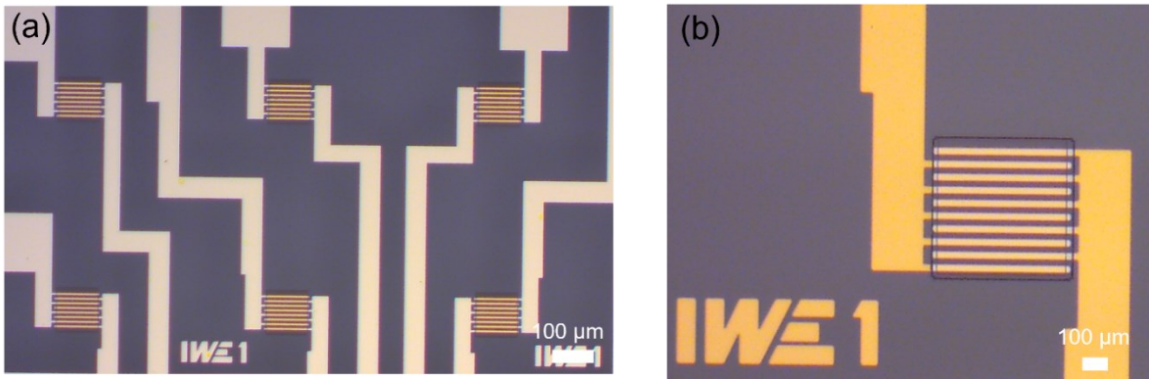

Figure 5.3: *(a) Microscope image of glass wafer after etching the silicon oxide layer using the reactive ion etching (RIE) process, (b) Microscope image of one IDE structure after patterning the PEDOT:PSS area.*

The wafer was half-diced from the backside to ensure easy separation of the transistors by hand at the final stage of the process. Following this, the last optical lithography was performed to pattern the PEDOT:PSS areas (step 9 in figure 4.6). The optical lithography process was identical to the previous lithography processes. Figure 5.3 (b) presents an image of an IDE structure after the third lithography process has been completed. The inner square displays the exposed Au, while the outer square shows the patterned PEDOT:PSS area. The opening area for the PEDOT:PSS is slightly bigger than that for the IDEs, ensuring that the PEDOT:PSS solution can completely cover the IDEs opening area during the deposition process. Figure 5.4 shows an OECT structure with 8 fingers after the deposition process of the PEDOT:PSS on the transistors was finished. The PEDOT:PSS film is homogenously distributed on the IDE structure, indicating the lift-off and annealing process of the PEDOT:PSS film on the transistor was successful. An identical microfabrication process was carried out to fabricate the OECTs with other contact materials (Pt, TiN, ITO and IrO_x). The microscope images of these transistors after depositing PEDOT:PSS are presented in figure S2 in Appendix C.

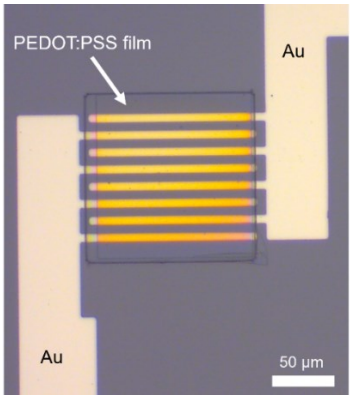

Figure 5.4: *Microscope image of an OECT structure with Au material after depositing PEDOT:PSS solution on the transistor.*

5.1.2 Laser lithography for fabrication of OECTs

The detailed fabrication flow is shown in figure 4.7 and the results will be discussed in this section. The contact lines were first fabricated using optical lithography (step 2 in figure 4.7). Figure 5.5 (a) presents the microscope image of the patterned contact lines after the development process. The darker lines indicating the contact lines of the transistors are symmetrically distributed on the wafer. The contact line lying horizontally in the center is the patterned common source contact line, while the contact lines vertically distributed around the source contact line are patterned drain contact lines. The lighter areas with uniform properties indicate the homogenous distribution of the AZ5214 photoresist.

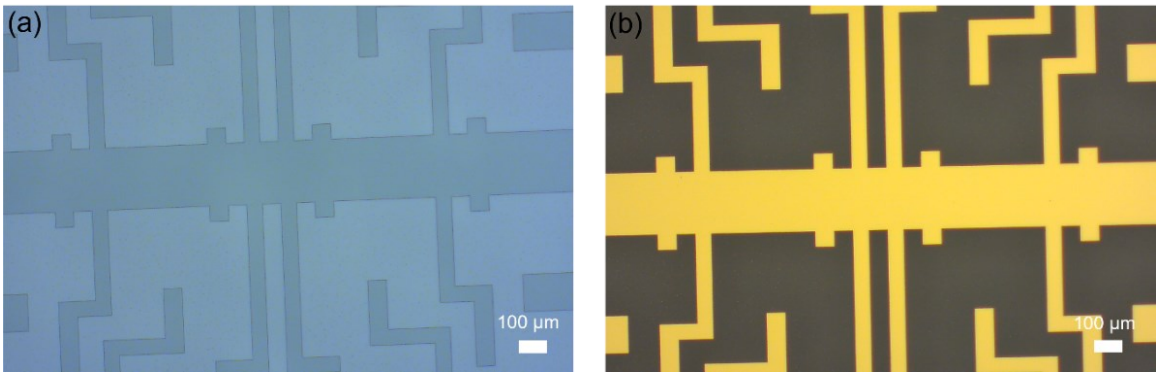

Figure 5.5: *(a) Microscope image of the patterned contact lines after optical lithography, and (b) after lift-off process for Au contact material.*

Metallization was carried out with Au using the standard evaporation procedure and the lift-off process was then performed. Figure 5.5 (b) displays the microscope image of the transistor with Au contact material after the lift-off process. The contact lines exhibit a yellow color and smooth distribution, showing that the Au contact material was successfully patterned on the wafer. The first laser lithography (step 5 in figure 4.7) was performed on the wafer to pattern the IDE structures and the microscope image of these structures is shown in figure 5.6 (a). The IDE structures were patterned between the source and drain contact lines, and a small section of each structure was overlapped with the Au contact lines to ensure a secure electrical connection. Afterwards, IrO_x was sputtered on the wafer and the lift-off process was conducted.

Figure 5.6 (b) shows a microscope image of the transistors after the lift-off process (step 7 in figure 4.7). The uniform grey-brown color indicates the homogenous deposition of IrO_x on the IDE structure.

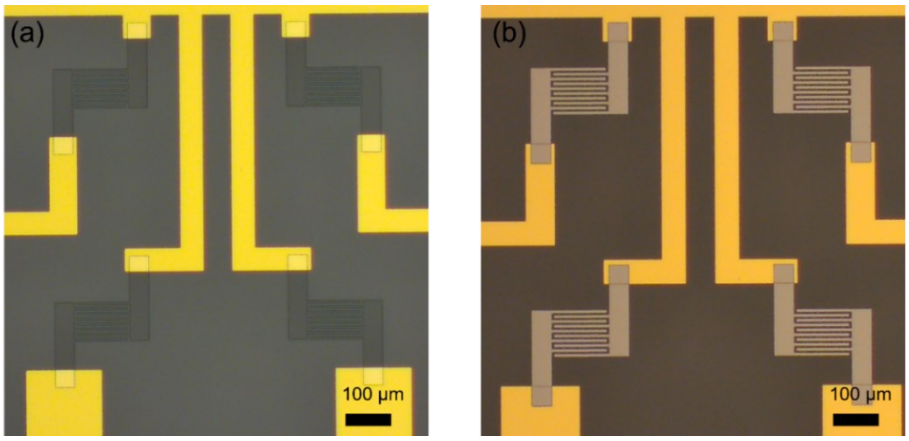

Figure 5.6: *(a) Microscope image of the IDE structure after the laser writing process, and (b) the IDE structures with IrO_x after sputtering and the lift-off process.*

The whole wafer was then passivated with silicon oxide using the PECVD process with the same parameters described in section 3.3. A second laser lithography process (step 9 in figure 4.7) was performed to pattern the openings of the IDEs and contact pads on the transistors. Then, the silicon oxide passivation layer was etched using the RIE process to obtain these openings on the IDEs and contact pads. Figure 5.7 (a) and (b) present the microscope images of the openings of the IDEs and contact pads after the RIE process. As shown in figure 5.7 (a), a square is observed on the IDE structure, indicating the silicon oxide layer has been completely etched away and the Au is exposed to air. Several squares displayed in figure 5.7 (b) represent the openings on contact pads. Thus, figure 5.7 demonstrates that the laser lithography process has been successfully employed in patterning the openings of the IDEs and contact pads. Furthermore, the RIE process utilized to etch away the silicon oxide layer has also been proved to be highly efficient.

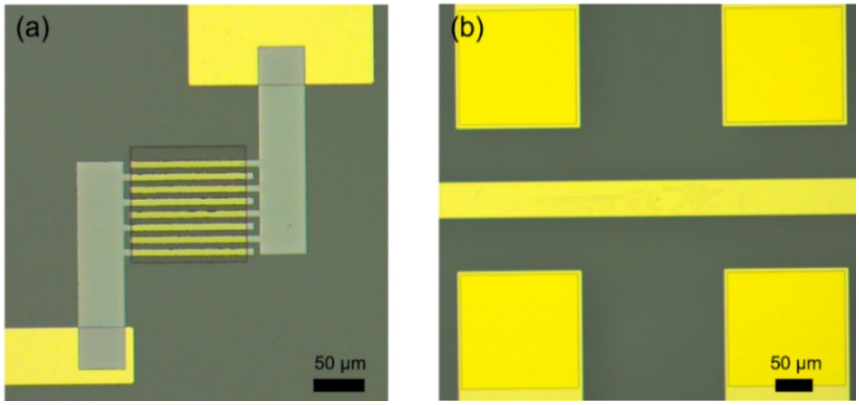

Figure 5.7: *(a) Microscope image of the opening on the IDE structure and (b) the openings of the contact pads after silicon oxide passivation layer was completely etched away.*

After the etching process, the wafer was half-diced from the backside. The third and final laser lithography (step 12 in figure 4.7) was then performed to pattern the PEDOT:PSS area on the

IDEs. In figure 5.8, the patterned PEDOT:PSS area is clearly shown by the outer square on the IDE. The inner square indicates the IDE opening area which is slightly smaller than the PEDOT:PSS area, ensuring the complete coverage and deposition of the PEDOT:PSS on the IDE. The lighter blue areas represent the IDE structure with IrO_x material and the yellow shows the Au contact material. These results display the successful microfabrication process for the transistors with Au as contact line and IrO_x as IDEs, aligning with the mask design in figure 4.3.

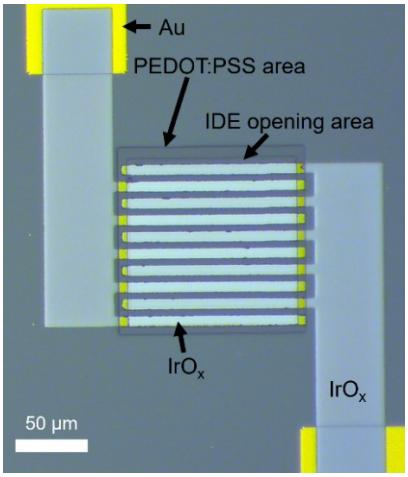

Figure 5.8: *Microscope image of the IDE after patterning the PEDOT:PSS area using laser lithography.*

5.1.3 Wire bonding and chip encapsulation

After depositing the PEDOT:PSS on the transistors, the half-diced wafer was easily separated by hand, and the individual chips were obtained and glued to the chip carriers. A glue mixture was applied to the four corners of the chip carrier, and the chip was carefully placed at the center of chip carrier with a slight push to ensure a secure connection. The chip carrier was then baked in an oven at 80°C for 1 hour, speeding up the curing process of the glue. Subsequently, the wire bonding process was performed on the chip and its carrier using a wire bonder machine (K&S4123 Wedge Boder, Kulicke & Soffa, Singapore). The K&S4127 wire bonder machine is a wedge-wedge bonder that utilizes ultrasonic energy and force to form bonds between the aluminum (Al) wires and the designated connection points. This bonding technique ensures reliable and stable electrical connections between the transistors and their carriers, playing a critical role in achieving the desired electrical performance and overall function of the fabricated devices.

Figure 5.9 (a) shows the bonding plan for connecting the chip and its carrier. The contact pads of the drain electrodes connect to the contact pads on the carrier, numbered 2, 4, 6, 8, 10, 12, 14 and 16. Additionally, the contact pads of the source electrodes on the chip bond to contact pads 8 and 10 on the chip carriers. Figure 5.9 (b) shows three bonded Al wires on the contact pads between the chip and its carrier. The Al wires at the bonding points on the contact pads appear flat, indicating sufficient melting and thus a secure bonding connection between the chip and carrier.

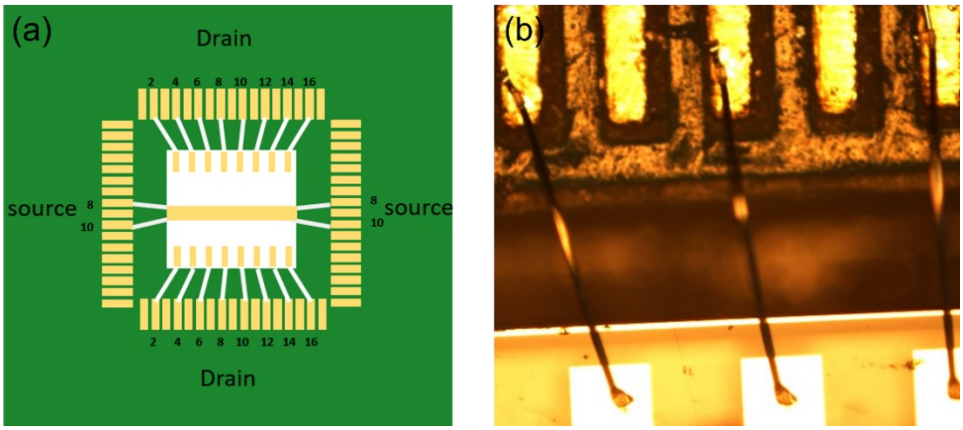

Figure 5.9: *(a) Wire bonding plan for connecting the chip and its carrier, (b) Boned aluminum (Al) wire on the contact pads of chip and carrier.*

After the wire bonding process, the transistors were encapsulated using PDMS. First, the encapsulation process started with the preparation of small silicone hoppers by thoroughly mixing silicone elastomer and the curing agent at a ratio of 10:1 (w/w). After that, the PDMS mixture was degassed in a desiccator for 30 minutes to remove the trapped air bubbles. The precleaned hopper mold was then completely filled with this mixture. Again, a degassing process was performed for roughly 90 minutes to remove all the air bubbles in the mixture in the mold. Once the degassing process was completed, the hopper mold was properly sealed using a cover and screws and then placed into an oven at a temperature of 150°C for 1 hour. This baking process allowed for faster and proper curing of the PDMS mixture in the hopper mold. Once the mold had cooled down to room temperature, the hoppers were released using a tweezer. Figure 5.10 (a) shows the prepared silicone hoppers that were used to encapsulate the transistors. The hoppers have a small hole in the center and appear transparent.

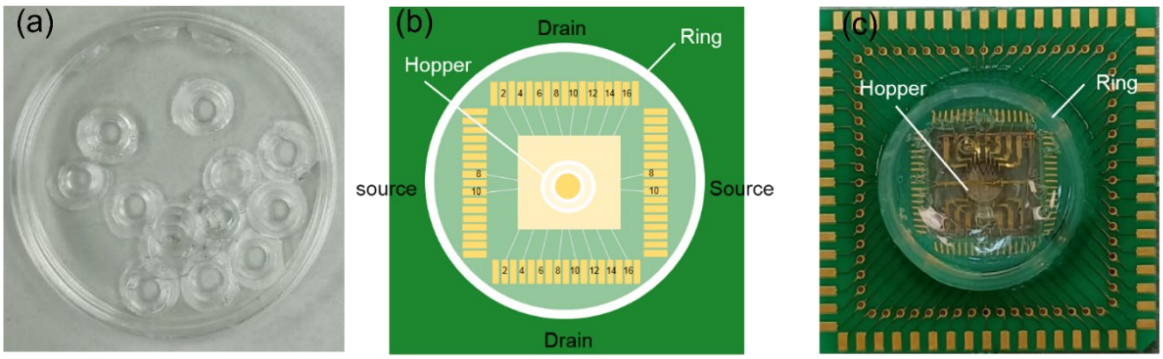

Figure 5.10: *(a) Prepared PDMS hoppers, (b) Schematic of an encapsulated chip, (c) Image of an encapsulated chip.*

Figure 5.10 (b) presents a schematic of the encapsulated chip. The first step of the encapsulation involved preparing the silicone adhesive solution (No. 96-083, Dow Silica, United States). A base component A and a curing agent B were mixed in a ratio of 10:1 (w/w), and the mixture was degassed in a desiccator for approximately 30 minutes to remove the air bubbles. Following this, a thin layer of this prepared adhesive solution was evenly applied on the bottom of the small hole in the PDMS hopper. Subsequently, the PDMS hopper was carefully transferred to the center of the chip, ensuring that no IDE channels were covered by

the adhesive solution. The bottom of a large plastic ring was coated with a thin layer of this adhesive solution and then gently placed on the chip carrier to surround all the contact pads. The carrier was baked in an oven at 120°C for 30 minutes, allowing the adhesive solution to cure. Afterwards, the gap between the hopper and the large plastic ring was filled with the adhesive solution and the chip was again placed in the oven at 130°C for 1 hour. Figure 5.10 (c) displays an image of an encapsulated chip. 16 channels can be observed in the central area of the chip and the surrounding area is completely covered by the cured silicon adhesive, ensuring the protection of the chip from the external environment. Once the encapsulation process is completed, the chips can be used to investigate the electrical characteristics of the OECTs and detect the concentrations of ions and DA.

5.2 Electrical characteristics of PEDOT:PSS OECTs

5.2.1 The electrical conductivity of PEDOT:PSS films

The Van der Pauw (VDP) measurement technique was used to characterize the sheet resistance R_{sh} of the PEDOT:PSS films in air, as shown in figure 5.11 (a). The VDP structures were created on the silicon substrate using the standard microfabrication techniques, while 100 nm Au was deposited on each corner of the chip with each contact line pointing towards the center. The deposition of the PEDOT:PSS film on the chip was obtained by first spin-coating the PEDOT:PSS solution at 4000 rpm for 40 seconds, followed by baking the chip on a hotplate at 140°C for 1 hour. The electrical characteristics were facilitated using the probe station of the Keithley 4200 parameter analyzer. A constant current of 100 µA was systematically applied to two adjacent pads, and the voltage between the other two pads was measured. This VDP measurement was automatically repeated eight times around the periphery of the chip. The resulting sheet resistance was determined using the equations (3.1), (3.2) and (3.3).

Additionally, the thickness of 60 ± 3 nm (n=3) of the PEDOT:PSS film was determined by measuring the step height with a stylus profilometer on multiple points distributed throughout the chip. The electrical conductivity of the PEDOT:PSS film was further calculated using the formula:

$$\sigma = 1/\boldsymbol{\rho} = 1/(R_{sh} \times t) \qquad (5.1)$$

where R_{sh} and t represent the obtained sheet resistance and film thickness, respectively. Figure 5.11 (b) presents the electrical conductivity of 106.5 ± 20.5 S/cm (n≥3) for the pristine PEDOT:PSS films and 1086.3 ± 183.4 S/cm (n≥3) for the PEDOT:PSS/EG/GOPS films. These results indicate that the addition of EG/GOPS leads to a tenfold enhancement in the electrical conductivity of the film, aligning with the theory in section 2.1.

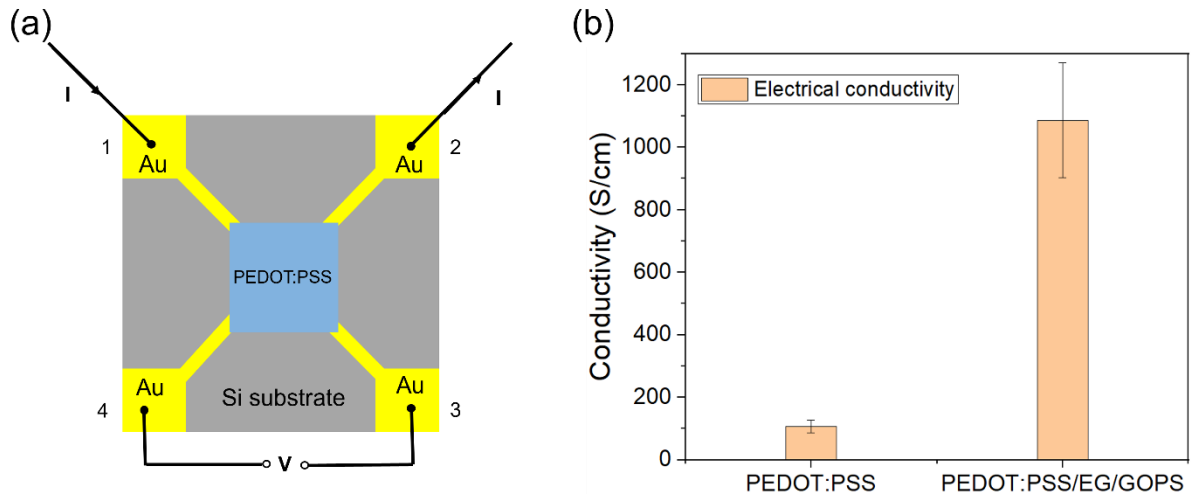

Figure 5.11: *(a) The schematic of electrical characterization using Van der Pauw (VDP) measurement technique, (b) The electrical conductivity of the pristine PEDOT:PSS films and the PEDOT:PSS/EG/GOPS films (n≥3).*

5.2.2 Electrical characteristics of OECTs using the transfer function amplifier system

Transfer characteristics of the fabricated PEDOT:PSS OECTs with Au contact material were investigated using the customized TTF amplifier system. V_{GS} sweeps ranging from -0.6 V to 0.3 V were systematically applied between the source and gate electrodes. Additionally, V_{DS} from -0.4 V to -0.1 V, with a step of -0.1 V were applied between the source and drain electrodes. An electrochemical Ag/AgCl reference electrode was used as a gate electrode. Figure 5.12 illustrates the transfer characteristics of an OECT when a 10 mM buffer solution was applied. The purple curve shows the transfer characteristics of the OECTs when applying the V_{DS} of -0.4 V, and it exhibits the largest negative current. The OECTs with -0.3 V of V_{DS} (yellow curve) have a decreased current, while for the OECTs with -0.2 V of V_{DS} (red curve), the current decreases further. The smallest current values were measured for the OECTs at -0.1 V of V_{DS} (blue curve). All 16 channels were functional, and each transfer curve exhibited a depletion-mode transistor performance. The cations in the buffer solution diffused into the PEDOT:PSS film, leading to its the de-doping process. This principle can reduce the available charge carriers in PEDOT, resulting in a decrease in the electrical conductivity of the PEDOT:PSS film and a change of the electrical characteristics of the transistors. As shown in figure 5.12, the majority of the channels present similar transfer characteristics, highlighting the reliability of this microfabrication process and uniformity of the film deposition for the creation of 16 functional channels.

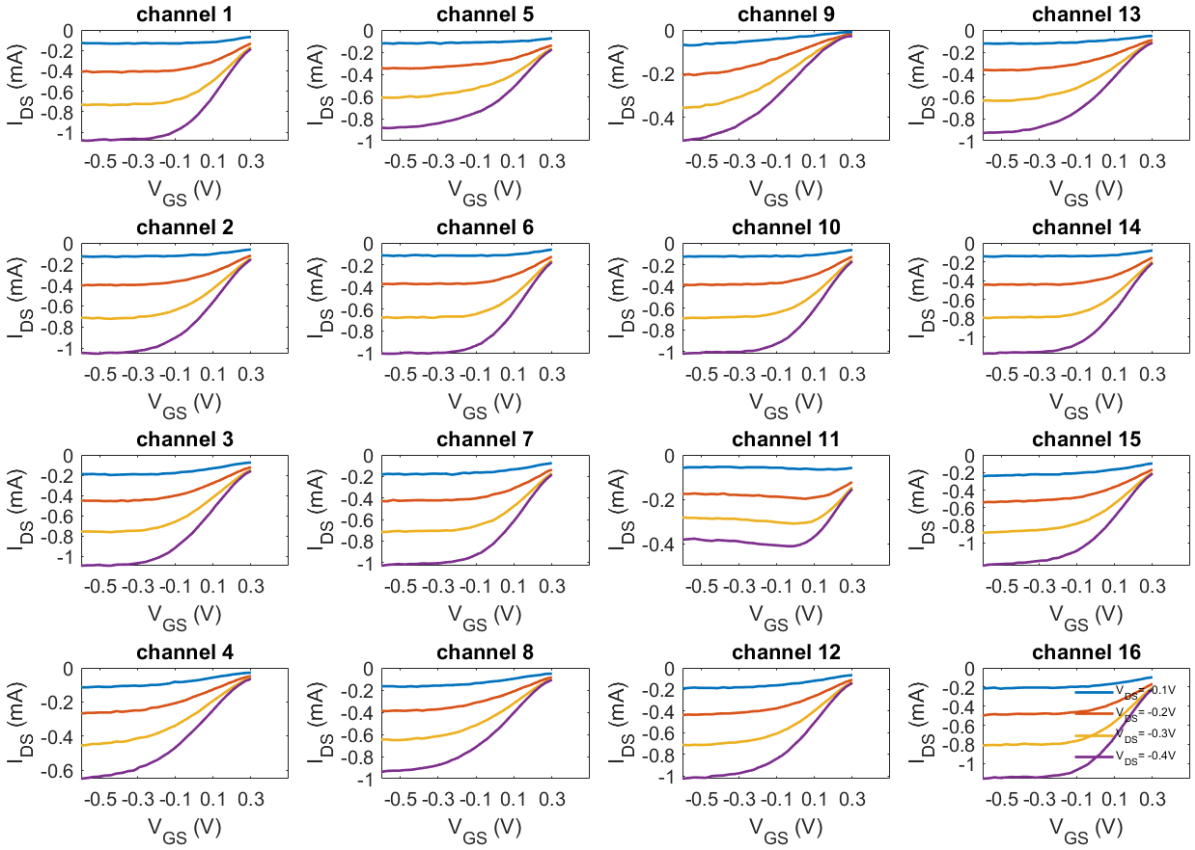

Figure 5.12: *Transfer characteristics of a transistor measured in 10 mM buffer solution with an Ag/AgCl reference electrode when V_{GS} swept from -0.6 V to 0.3 V and V_{DS} is -0.1 V (blue), -0.2 V (red), -0.3 V (yellow), -0.4 V (purple).*

The output characteristics of the fabricated PEDOT:PSS OECTs with Au contact material was studied using the customized TTF amplifier system. The V_{DS} was systematically swept between the source and drain electrodes, with a range of -0.8 V to -0.1 V. Moreover, the V_{GS} ranging from 0 V to 0.3 V with a step of 0.1 V were applied between the source and gate electrodes. An Ag/AgCl reference electrode was used as the gate electrode and immersed in the buffer solution during the measurement. Figure 5.13 displays the output characteristics of the OECTs when a 10 mM buffer solution was applied. The purple curve which has the largest negative current represents the output characteristics of the transistors when 0 V of V_{GS} was applied to the system. The yellow curve refers to the output curve when 0.1 V of V_{GS} was applied, while the red curve displays the output characteristics of the chip when 0.2 V of V_{GS} was applied. Lastly, the blue curve shows the output characteristics of the OECTs after 0.3 V of V_{GS} was applied. Due to the conductive property of the PEDOT:PSS film, the transistor stays in the “ON” state when V_{GS} was 0 V. Furthermore, the drain current reduced when the V_{GS} increased, indicating that the OECTs exhibit a depletion-mode performance. Moreover, the results indicated that an increase in V_{DS} led to the enhancement of the drain current. This can be attributed to the increased flow of mobile charge carriers through the channel with higher V_{DS}, resulting in the increased value of the drain current.

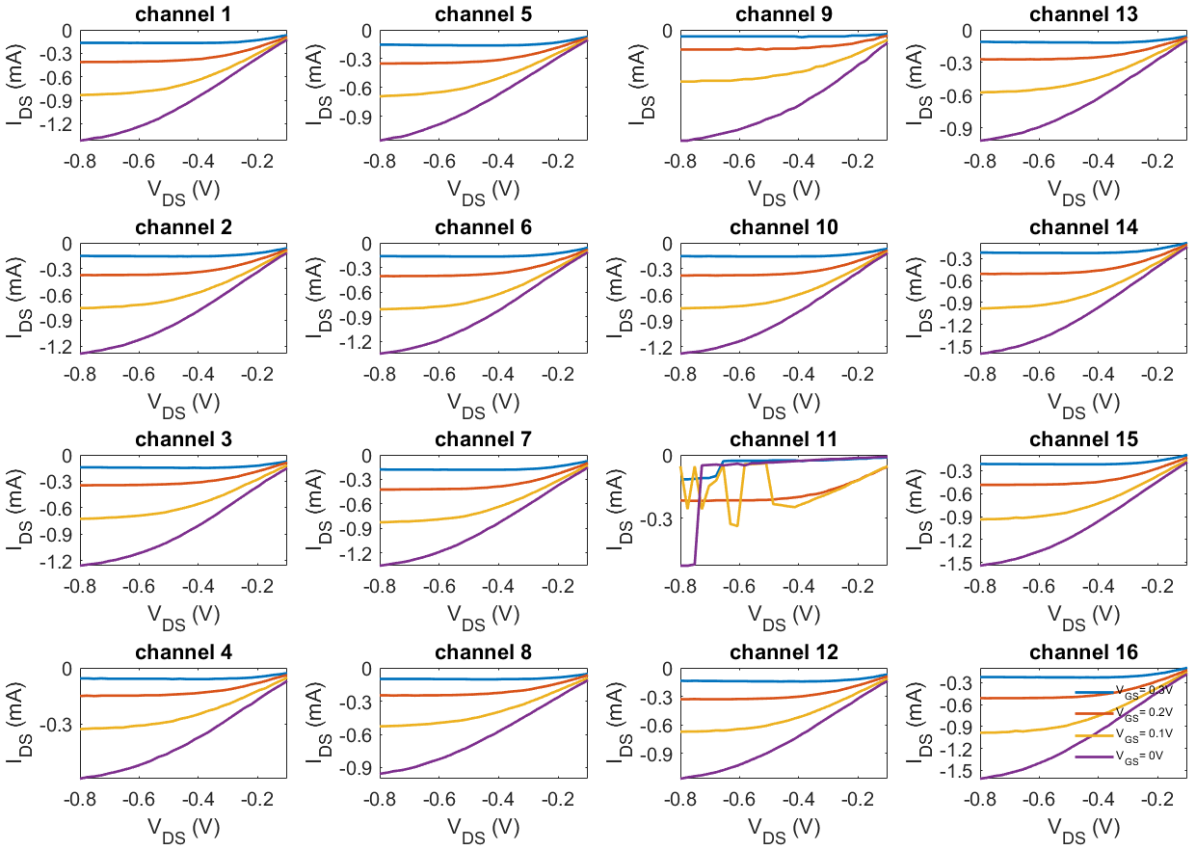

Figure 5.13: *Output characteristics of an OECT with an Ag/AgCl reference electrode immersed in 10 mM buffer solution when V_{DS} swept from -0.8 V to -0.1 V and V_{GS} is 0 V (purple), 0.1 V (yellow), 0.2 V (red), 0.3 V (blue).*

g_m of the OECTs was obtained by taking the first derivative of the transfer characteristics with respect to the V_{GS}. Figure 5.14 displays the g_m of the transistor measured in 10 mM of the buffer solution with an Ag/AgCl reference electrode when V_{GS} swept from -0.6 V to 0.2 V and V_{DS} was -0.1, -0.2, -0.3, -0.4 V. The corresponding transfer characteristics of the transistor are shown in figure 5.12. As shown in figure 5.14, most of the channels reach the maximum g_m value at approximately 2.8 mS when the V_{GS} is 0.14 V and V_{DS} is -0.4 V. The obtained electrical characteristics of the PEDOT:PSS OECTs measured with the TTF amplifier system provide evidence that this microfabrication technique is highly reliable. Furthermore, the fabricated transistors exhibit their uniformity needed for meaningful research such as ion and DA detection applications.

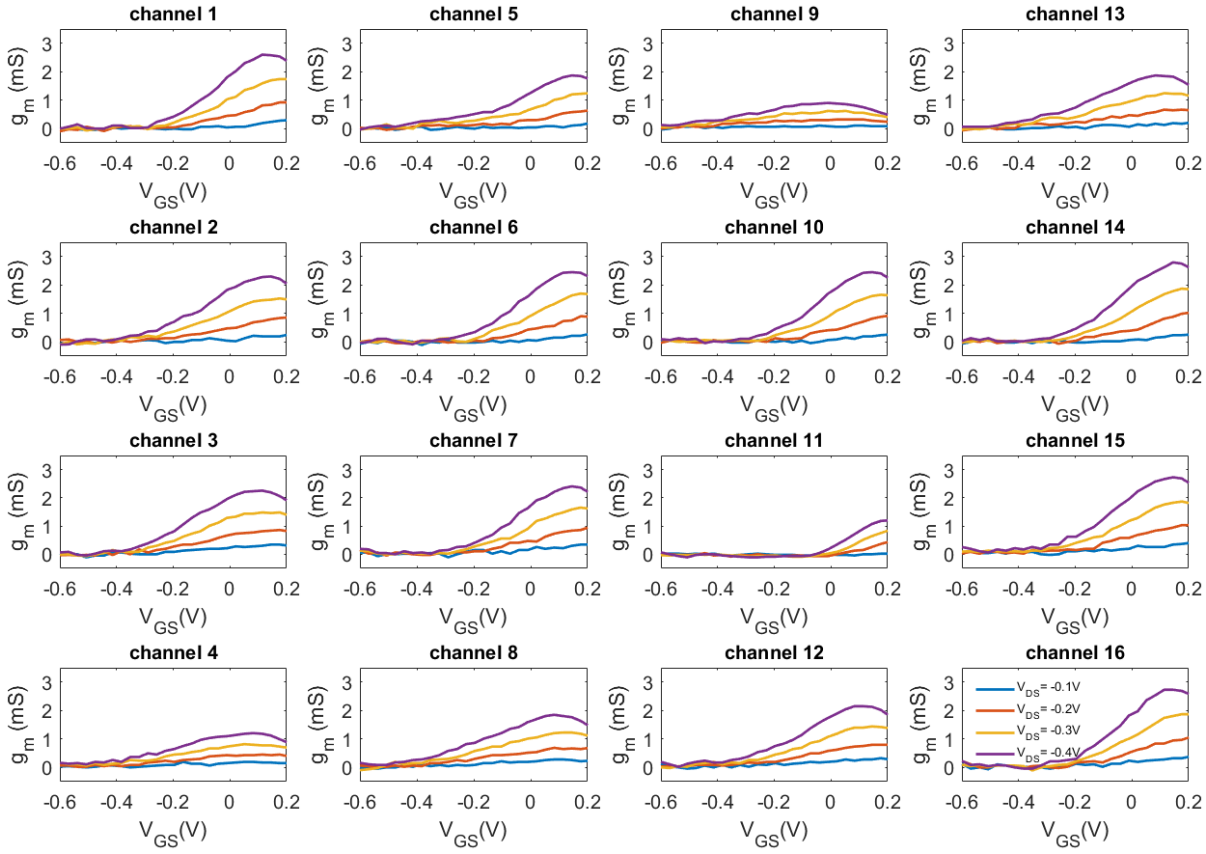

Figure 5.14: *Transconductance of a transistor measured in 10 mM buffer solution with an Ag/AgCl reference electrode when V_{GS} swept from -0.6 V to 0.2 V and V_{DS} was -0.1 V (blue), -0.2 V (red), -0.3 V (yellow), -0.4 V (purple).*

5.2.3 Electrical characteristics of OECTs using the Keithley 4200 parameter analyzer

TTF amplifier system provides the benefit of simultaneous measurement for 16 channels. However, this simultaneous application of a voltage through the common source contact line can more quickly deteriorate the performance of transistors. Furthermore, the Keithley 4200 parameter analyzer which provides more accurate and stable transistor characteristics facilitated the transfer characteristics of the PEDOT:PSS OECTs. Figure 5.15 (a) illustrates the transfer characteristics of fabricated PEDOT:PSS OECTs with Au contact material when a 1 mM buffer solution was applied. A systematic application of V_{GS} sweeps ranging from -0.6 V to 0.2 V was conducted between the source and gate electrodes. Meanwhile, V_{DS} was applied between the source and drain electrodes and the voltage ranged from -0.4 V to -0.1 V with a step of -0.1 V. An Ag/AgCl reference electrode was immersed in the buffer solution as a gate electrode. The black curve represents the transfer characteristics when V_{DS} of -0.4 V was applied, while the red curve shows the transfer curve when -0.3 V of V_{DS} was applied. Furthermore, the blue and green curves refer to the transfer characteristics with the application of V_{DS} at -0.2 V and -0.1 V, respectively. For each transfer curve, the statistical data of the working channels (n>3) on one chip was obtained. Results are displayed as mean values with small error bars, indicating the high reliability of this microfabrication process. Similarly, the transistor exhibits a depletion-mode performance and the drain current decreases when more

positive V_{GS} is applied. Owing to the de-doping process of PEDOT:PSS, the electrical conductivity of PEDOT:PSS decreases, leading to changes in the electrical characteristics of the transistors.

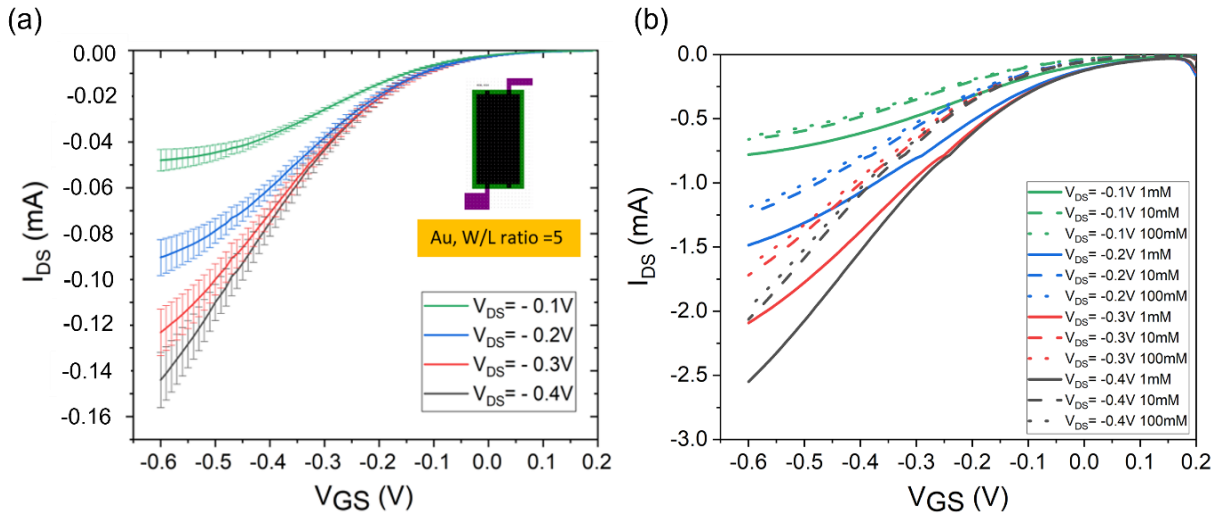

Figure 5.15: *(a) Transfer characteristics of the PEDOT:PSS OECTs with Au contact material after applying 1 mM of buffer solution (n>3), (b) Transfer characteristics of PEDOT:PSS OECTs with Au contact material when different buffer solutions were applied.*

Furthermore, the general impact of changes in the ionic strength of the electrolyte solution on the electrical characteristics of the fabricated OECTs was investigated. The transfer characteristics of the same device were recorded using the Keithley 4200 parameter analyzer and the buffer solutions with various concentrations ranging from 1 mM to 100 mM. In figure 5.15 (b), the solid lines represent the transfer curves when 1 mM of the buffer solution was used. The dashed and dotted lines refer to the transfer characteristics after applying the buffer solutions with concentrations of 10 mM and 100 mM respectively. After applying each gate voltage, the OECTs show the depletion-mode of performance and an increase in the concentrations of the buffer solution leads to the reduction of the drain current. Compared to the buffer solution with lower concentration, the solutions with higher concentrations allowed for more cations to be injected into the PEDOT:PSS channel although the same value of gate voltage was applied. Afterwards, a massive amount of the negatively charged PSS group will be compensated, which results in a significant change in the electrical conductivity of PEDOT:PSS and then the transfer characteristics of the OECTs.

As described in section 4.1.1, transistors with various channel configurations and geometries were designed on the wafer, while the W/L ratio of each geometry was calculated and displayed in Table 4.1. The same microfabrication technique was conducted to manufacture chips with identical PEDOT:PSS film thicknesses. The transfer characteristics of these transistors were measured using the Keithley 4200 parameter analyzer when 1 mM of the buffer solution was applied. V_{GS} was swept between the source and gate electrodes with a range of -0.6 V to 0.2 V, while V_{DS} ranging from -0.4 V to -0.1 V with a step of -0.1 V was applied between the source and drain electrodes. The same Ag/AgCl reference electrode was

used as the gate electrode. As displayed in figure 5.16, the transfer characteristics (solid lines) of these chips were obtained and compared at V_{DS} of -0.2 V. Meanwhile, the corresponding g_m (dotted lines) was extracted from the first derivative of the transfer curve.

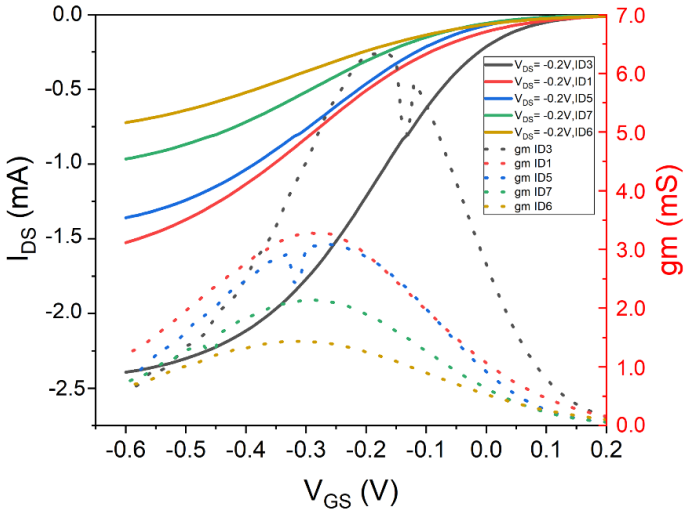

Figure 5.16: *With the application of 1 mM of buffer solution, transfer characteristics (solid lines) and transconductance (dotted lines) of PEDOT:PSS OECTs of Au contact material with different channel geometries was obtained at V_{DS} of -0.2 V.*

Table 5.1: *Maximum g_m value with different channel geometries at V_{DS} of -0.2V.*

ID	W/L ratio	Max g_m (mS)
3	180	6.34
1	116.67	3.27
5	15	3.08
7	10	2.14
6	5	1.44

In figure 5.16, the transfer characteristics of all the chips exhibit a depletion-mode performance. The black solid and dotted curves represent the transfer characteristics and g_m of the chip with the W/L ratio of 180. In contrast, the red solid and dotted curves show the transfer curve and g_m from the chip fabricated with the W/L ratio of 116.67, while the blue solid and dotted curves refer to the transfer curve and g_m for the chip with the W/L ratio of 15. The green solid and dotted curves display the transfer characteristics and extracted g_m of the OECT containing the W/L ratio of 7. The yellow solid and dotted curves represent the transfer characteristics and the corresponding g_m of the transistors with a W/L ratio of 5. As seen in figure 5.16, the measured negative I_{DS} value increases with the increase of the W/L ratio from 5 to 180. Meanwhile, the steepness of the curve behaves the same way, which results in the higher g_m values obtained for the devices with the bigger W/L ratio. A short overview of the maximum g_m value for different channel geometries at V_{DS} of -0.2 V is displayed in Table 5.1. Increasing the W/L ratio from 5 to 180 leads to a sixfold enhancement in the maximum g_m value. Based on

equations (2.2) and (2.3), the measured I_{DS} and g_m are proportional to the W/L ratio. These results proved that the PEDOT:PSS OECTs with various channel geometries have a promising transistor performance, aligning with the theoretical framework.

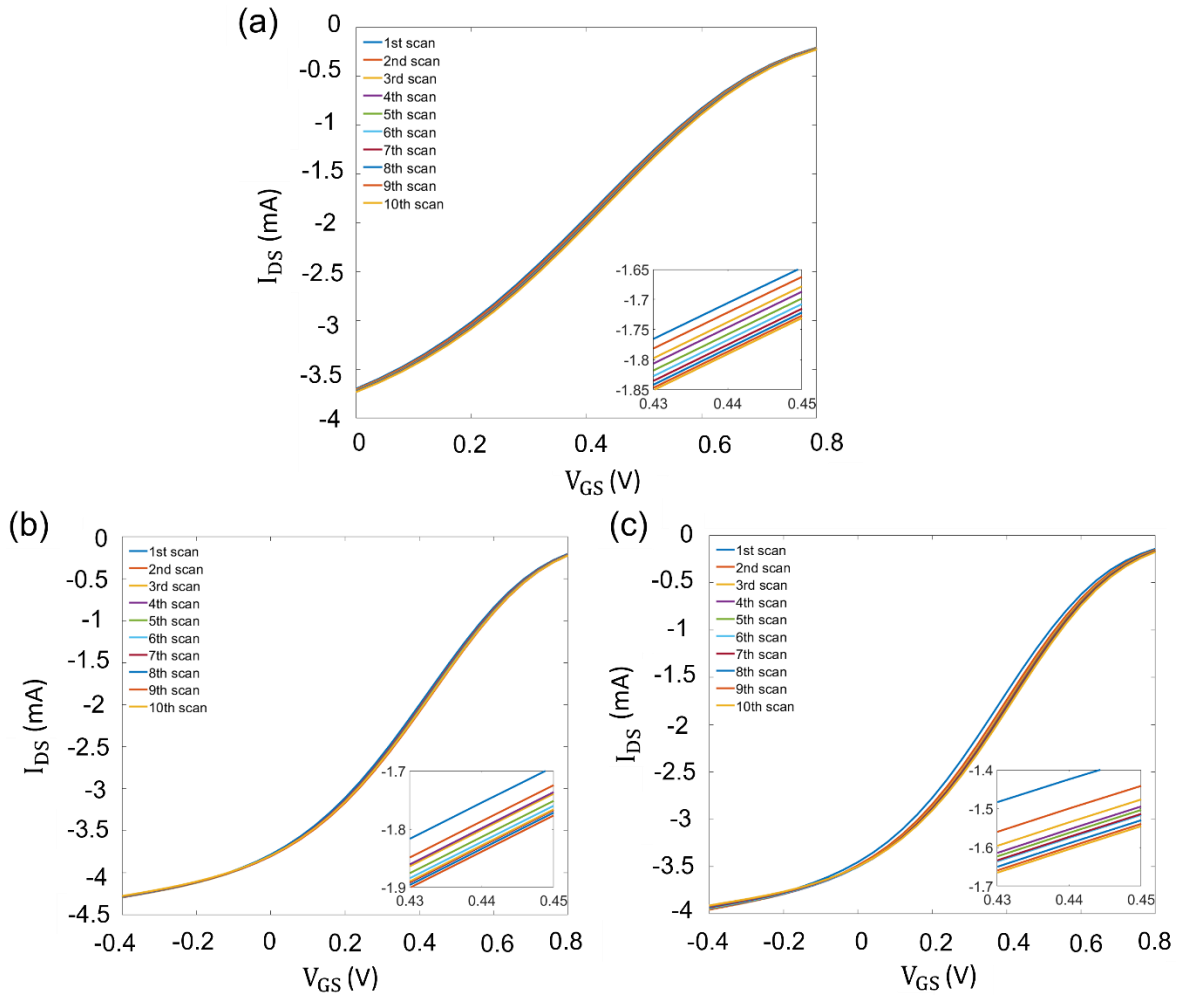

Figure 5.17: *Transfer characteristics of an OECT were obtained using a Pt electrode as the gate electrode by scanning the gate voltage 10 times consecutively at intervals of 1 minute. The measurement was conducted in (a) PBS solution with the voltage range from 0 to 0.8 V, (b) PBS solution with the voltage ranging from -0.4 to 0.8 V, (c) 100 mM buffer solution with application of the voltage from -0.4 to 0.8 V.*

The stability of the fabricated OECTs in the PBS solution and 100 mM buffer solution was investigated using a Pt electrode as the gate electrode. The transfer characteristics of the OECTs were studied using the Keithley 4200 parameter analyzer by scanning the gate voltage 10 times consecutively at intervals of 1 minute. Additionally, various V_{GS} were applied between the gate and source electrodes, while the V_{DS} of -0.3 V was set between the drain and source electrodes. Figure 5.17 (a) and (b) shows the transfer characteristics of the devices in the PBS solution after applying V_{GS} with the range of 0 V to 0.8 V and the range of -0.4 V to 0.8 V, respectively. As presented in figure 5.17 (c), the transfer curves of the OECTs were measured in 100 mM buffer solution with the gate voltage applied from -0.4 V to 0.8 V. The results in figure 5.17 display that the OECTs exhibit the depletion-mode performance, indicating that the

measured drain current decreases with the increase of the positive gate voltage. The transfer curves of these 10 scans are almost overlapping with each other, demonstrating that the OECTs maintain their stable performance during the measurements. Additionally, the stable performance of the transistors is independent from the measured analyte solutions and the applied gate voltage range.

5.2.4 Effect of contact materials on the electrical characteristics of OECTs

Au has been commonly used as the contact material for the PEDOT:PSS film in the OECTs due to its process availability, biocompatibility and electrical properties [1-2]. However, these PEDOT:PSS OECTs show a high contact resistance, limiting their electrical performance. Therefore, it is necessary to further investigate the effect of different contact materials on the electrical characteristics of PEDOT:PSS OECTs, and these materials include Pt, TiN, IrO_x and ITO. TiN is one of the commonly used materials for the realization of electrodes and gates in complementary metal-oxide-semiconductor (CMOS) devices. IrO_x exhibits some redox transitions with the application of various potentials and these electron transitions can facilitate the oxidation or reduction reactions of various substances of interest. Owing to its properties, including high conductivity, excellent stability and robust electrochemical performance, IrO_x has been utilized in several applications such as neural stimulation, energy storage and optoelectronics. ITO, one of the most widely utilized transparent conductive oxide materials, is used in the development of different applications such as biosensors, flat-panels and photovoltaics due to its two main properties: good electrical conductivity and optical transparency.

The two-probe resistance measurement technique using the Keithley 4200 parameter analyzer was used to characterize the resistance between the two contact pads of the source electrode on the OECTs in air. As shown in figure 5.18 (a), the two probes connect to S1 and S2 on the chip. The voltage range from -0.1 V to 0.1 V was systematically applied to the two contact pads of the source electrode and the current value was measured. The resulting resistance was determined by calculating the slope of the linear IV curve using the formula R = V/I, where V and I are the applied voltage and the obtained current value, respectively. Figure 5.18 (b) presents the IV characteristics between two contact pads of the source electrode on the PEDOT:PSS OECTs which were fabricated with different contact materials. Each IV characteristic exhibits the linear relationship between applied voltage and measured current. After calculating the resistance using the IV curve, Au material was found to have the lowest resistance of 40 Ω, while ITO had the highest resistance of 1890 Ω.

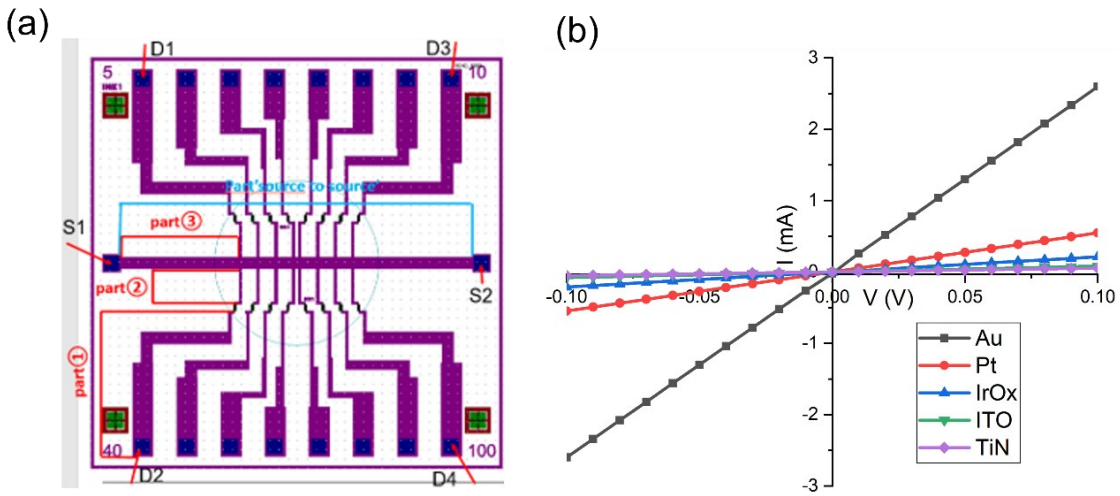

Figure 5.18: *(a) Schematic of chip design (b) IV characteristics of different contact materials.*

The efficiency of the current flow across the metal-semiconductor junction is influenced by contact resistance (R_c). To operate devices efficiently, it is crucial to minimize the contact resistance to allow for smooth injection or extraction of charge carriers (electrons or holes) between the metal and semiconductor regions. Therefore, the analysis of the contact resistance between different contact materials and PEDOT:PSS plays an important role in investigating the overall device performance and function.

Transfer length method (TLM) is commonly used to determine the specific contact resistance of the metal-semiconductor interface. The current voltage measurements are conducted between two contacts with variable or same spacing *d*. Afterwards, the total resistance (R_t) is calculated by the IV measurement and then plotted as a function of the contact spacing *d*. The y-intercept of the linearly fitted curve is twice the contact resistance.

In this work, TLM was utilized to determine the specific contact resistance between the contact material and the PEDOT:PSS film. The four-point measurement structures with the same spacing *d* in figure 4.2 (b) were employed for the IV measurement. The voltage sweeps ranging from -0.05 V to 0.05 V were systematically applied to the two contact pads of the test structures. Then, the total resistance was plotted relative to the contact spacing *d* and the contact resistance was extracted from the plotted curve. Figure 5.19 presents the relationship between the measured total resistance and the spacing *d* of 100 µm on the test structure which was fabricated by Au contact material. As the y-intercept value on the plotted resistance curve is twice the contact resistance value, it can be concluded that the contact resistance between Au and the PEDOT:PSS film is 865.5 Ω. The TLM technique with an identical experiment procedure was performed to investigate the contact resistance between the other contact materials and the PEDOT:PSS film. As shown in figure S3 in Appendix C, the dependence between the total resistance and spacing *d* was plotted and the contact resistance was extracted.

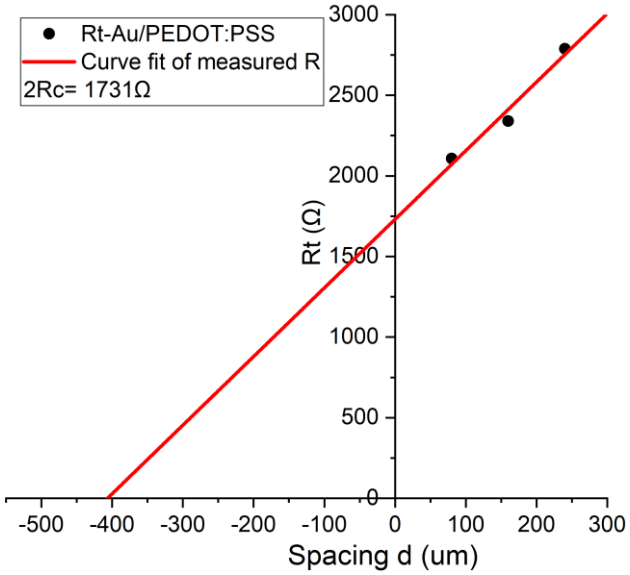

Figure 5.19: *Transfer length method for measuring contact resistance between Au and the PEDOT:PSS film.*

After performing and calculating the contact resistance between different contact materials and the PEDOT:PSS film, all the data was compared. In addition, the resistance between two ends of the source electrode and the contact line resistance for all five contact materials was normalized to their respective thicknesses. Table 5.2 gives an overview of these results. Among these five contact materials, Au has the lowest contact line resistance and IrO_x exhibits the lowest contact resistance with the PEDOT:PSS film. In contrast, ITO and TiN materials have relatively high contact line resistance and contact resistance.

Table 5.2: *Resistance of PEDOT:PSS OECTs with different contact materials.*

(SS means source and source)

Contact material	Resistance of SS (Ω)	Resistance of SS/Thickness (Ω/nm)	Resistance of contact line (Ω)	Resistance of contact line/Thickness (Ω/nm)	Contact resistance (Ω)
Au (50nm)	40	0.8	62	1.55	865.5
Pt (100nm)	158	1.58	245	2.45	3250
IrO_x (150nm)	464	3.09	720	4.8	43.5
ITO (150nm)	1890	12.6	2940	19.6	2517
TiN (150nm)	1234	8.23	1916	12.77	10226.5

The transfer characteristics of PEDOT:PSS OECTs with other contact materials (Pt, TiN, IrO_x and ITO) were investigated in the buffer solution using the Keithley 4200 parameter analyzer. V_{GS} with the range of -0.6 V to 0.2 V was systematically applied to source and drain electrodes, while V_{DS} ranging from -0.4 V to -0.1 V with a step of -0.1 V was employed between the source and drain electrodes. The commercial Ag/AgCl reference electrode was used as the gate electrode. Figure 5.20 (a) shows the transfer characteristics of PEDOT:PSS OECTs fabricated

with Pt contact material with the W/L ratio of 180, while figure 5.20 (b) presents the transfer characteristics of PEDOT:PSS OECTs with IrO_x contact material with the W/L ratio of 116.67. Likewise, these transistors exhibit the depletion-mode performance, indicating that the drain current decreases with the increase of the positive V_{GS} value. Unfortunately, it was not possible to measure the transfer characteristics of PEDOT:PSS OECTs with ITO and TiN contact materials. This may contribute to the high contact line resistance and contact resistance, as illustrated in Table 5.2.

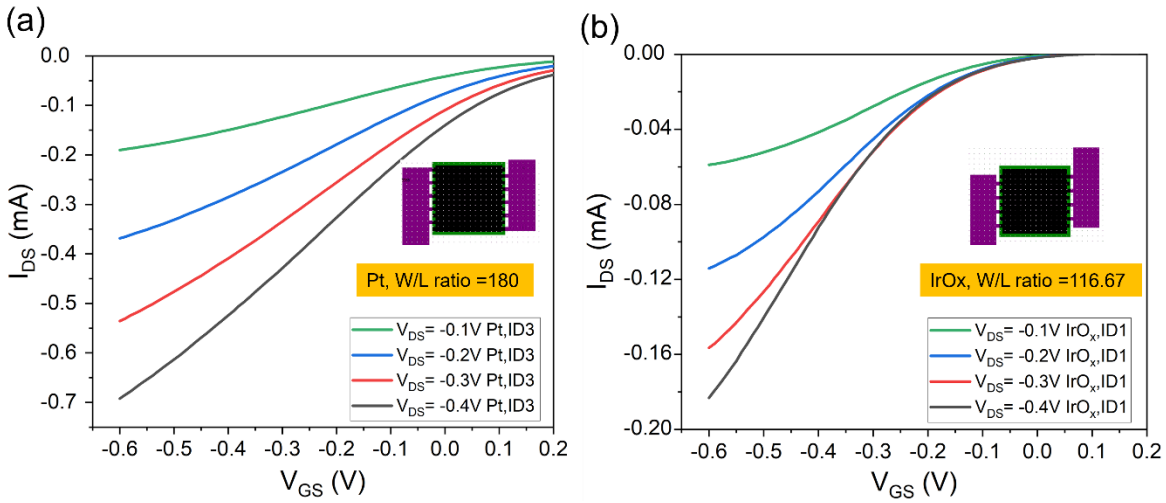

Figure 5.20: *Transfer characteristics of PEDOT:PSS OECTs with Pt contact material (a) and IrO_x contact material (b).*

From Table 5.2, Au exhibits the lowest contact line resistance and IrO_x has the lowest contact resistance of all the contact materials. Therefore, a novel chip design has been carried out, which combines the advantages of Au and IrO_x contact materials. In the new chip design, IrO_x material was used for the IDE structure and Au was used for the contact lines. For the fabrication of these new chips, laser lithography was utilized to pattern the IDE structure with IrO_x and the detailed fabrication process can be seen in figure 4.7.

After completing the fabrication process, the transfer characteristics of the new chip were studied using the Keithley 4200 parameter analyzer and the 10 mM of sodium buffer solution was applied. V_{GS} swept from -0.6 V to 0.6 V and the V_{DS} was set from -0.1 V to -0.4 V with -0.1 V as a step. The transfer curves of the PEDOT:PSS OECTs using Au as contact line and IrO_x as IDE structure are displayed in figure 5.21 (a) and the W/L ratio is 180. The new chip exhibits a good p-type depletion-mode performance, meaning the increase in the positive V_{GS} leads to the reduction of I_{DS}. These results provide evidence that the microfabrication process for the PEDOT:PSS OECTs using Au as the contact line material and IrO_x as the IDE structure was successful. In contrast, the transfer characteristics of the transistors using only IrO_x as contact material with the W/L ratio of 180 are shown in figure 5.21 (b). As shown in figure 5.21, the drain current of both transfer characteristics exhibits the range of mA. Meanwhile, OECTs with Au as contact line and IrO_x as IDE structure perform a fivefold increase in I_{DS} compared to those with only IrO_x contact materials.

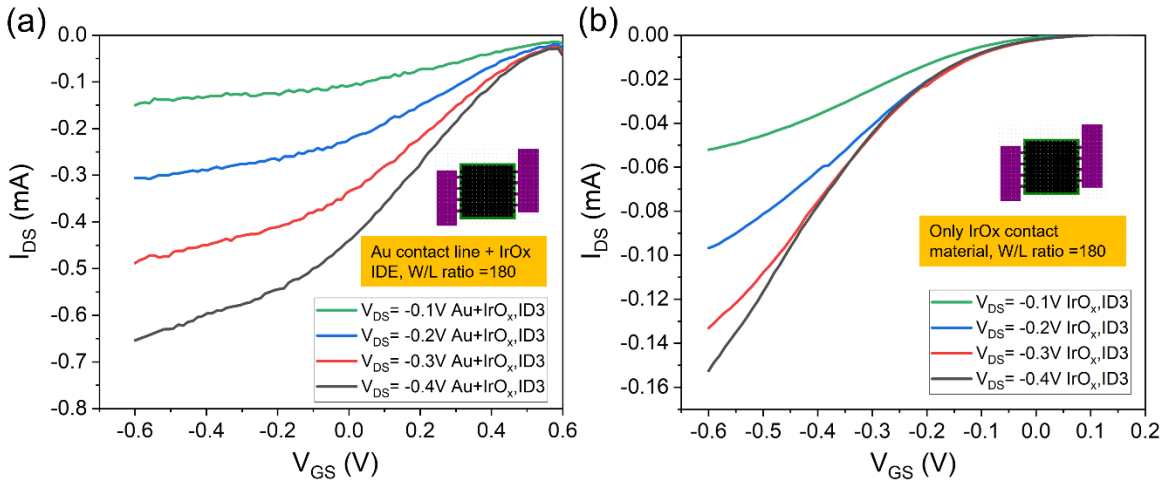

Figure 5.21: *Transfer characteristics of (a) the chips using Au as contact line and IrO_x as IDE structures (b) the chip with IrO_x contact material.*

5.2.5 Effect of PEDOT:PSS film thicknesses on the electrical characteristics of OECTs

Firstly, the effect of different thicknesses of PEDOT:PSS films on the electrical characteristics of the transistors was investigated by modifying their thicknesses using the spin-coating technique. PEDOT:PSS solutions were prepared using the experimental protocol described in section 4.1.3. After depositing the PEDOT:PSS film with solution A on the chips, the thickness was determined by measuring the step height with a stylus profilometer on multiple channels distributed on the chip. The variation of PEDOT:PSS film thickness was obtained using the following spin-coating speeds: 2000 rpm, 3000 rpm, 4000 rpm and 5000 rpm. The relationship between the PEDOT:PSS film thickness and spin-coating speeds is displayed in figure 5.22. After the deposition of PEDOT:PSS film on the transistors, the resistance between the source and drain electrodes was measured using the two-probe resistance measurement technique. The resistance measurement was carried out using the Keithley 4200 parameter analyzer and a voltage ranging from -0.1 V to 0.1 V was systematically applied to source and drain electrodes. The resulting resistance value was obtained by calculating the slope of the linear IV curve via the formula R = V/I, where V and I represent the applied voltage and the measured current value, respectively. Figure 5.22 also shows the impact of the spin-coating speeds on the resistance between the source and drain electrodes. An increase in speed from 2000 rpm to 5000 rpm results in the reduction of PEDOT:PSS thickness from 212 ± 7 nm to 130 ± 4 nm (n = 16), while the obtained resistance value increases from 36 ± 3 Ω to 51 ± 7 Ω (n = 5).

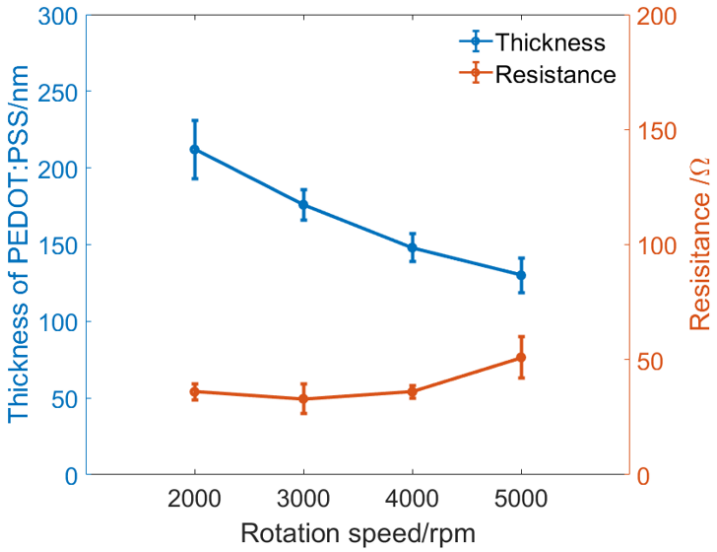

Figure 5.22: *PEDOT:PSS film thickness and resistance change after varying the spin-coating speed (n≥5).*

PEDOT:PSS mixture solutions A, B, C and D were prepared as described in section 4.1.3. Then, the deposition of the PEDOT:PSS film on the OECTs using the identical experimental protocol at the spin-coating speed of 5000 rpm was performed with these PEDOT:PSS mixture solutions. Furthermore, the thickness of the PEDOT:PSS film on the transistors was determined with the stylus profilometer. Figure 5.23 (a) illustrates the relationship between the different PEDOT:PSS solutions and the resulting film thickness. The results indicate that PEDOT:PSS mixture solutions A, B, C and D yielded film thicknesses of 108 ± 7 nm, 78 ± 4 nm, 45 ± 7 nm, 14 ± 8 nm, respectively. Afterwards, measurements were carried out to obtain the resistance between the source and drain electrodes with the application of the voltage range between -0.1 V and 0.1 V. As displayed in figure 5.23 (b), the PEDOT:PSS mixture solutions A, B and C resulted in the resistance values of 33 ± 2 Ω, 188 ± 66 Ω and 512 ± 200 Ω, respectively. Only two channels exhibited the linear IV curve and the resistance of these channels was significantly different after depositing PEDOT:PSS mixture solution D on the OECTs. Therefore, PEDOT:PSS film thicknesses of 108 ± 7 nm, 78 ± 4 nm and 45 ± 7 nm were utilized to study the electrical characteristics of transistors and their applications. The results in figure 5.23 indicate that a more diluted PEDOT:PSS mixture solution leads to a thinner film and higher resistance.

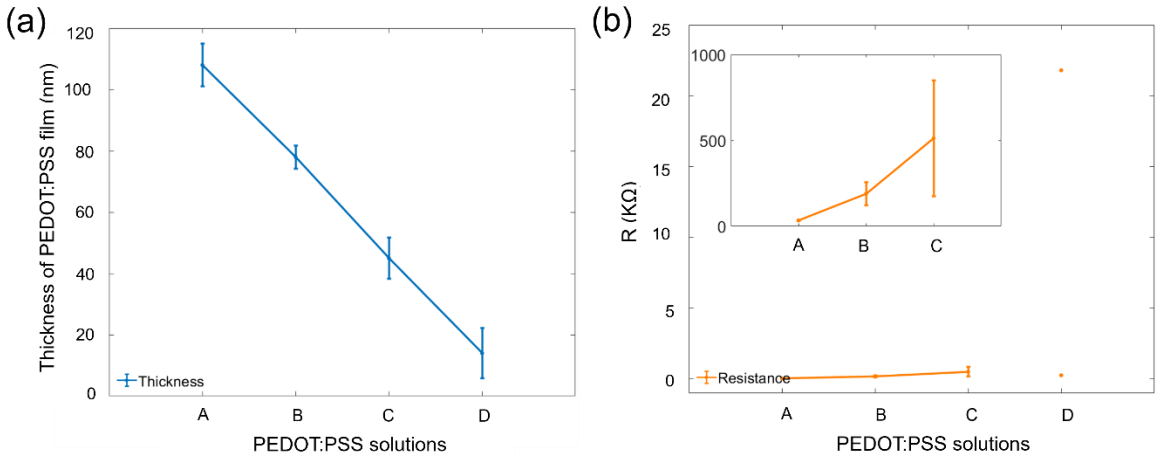

Figure 5.23: *After depositing PEDOT:PSS mixture solutions A, B, C and D on OECTs, (a) Thicknesses of PEDOT:PSS film (n≥3), (b) Resistance between source and drain electrodes (n≥3).*

The morphology of PEDOT:PSS film was investigated by using the SEM image analysis technique. First, PEDOT:PSS mixture solutions A, B, C and D was spin-coated and annealed on the SiO_2 substrate to obtain the PEDOT:PSS films A, B, C and D, respectively. After that, the films were scratched using a knife to distinguish them from the substrate. Figure 5.24 (a), (b), (c) and (d) present SEM images of PEDOT:PSS films A, B, C and D, respectively. The darker areas represent the PEDOT:PSS films, while the slightly brighter areas refer to the SiO_2 substrate. The homogenous dark grey color indicates that each PEDOT:PSS film is uniformly distributed on the substrate.

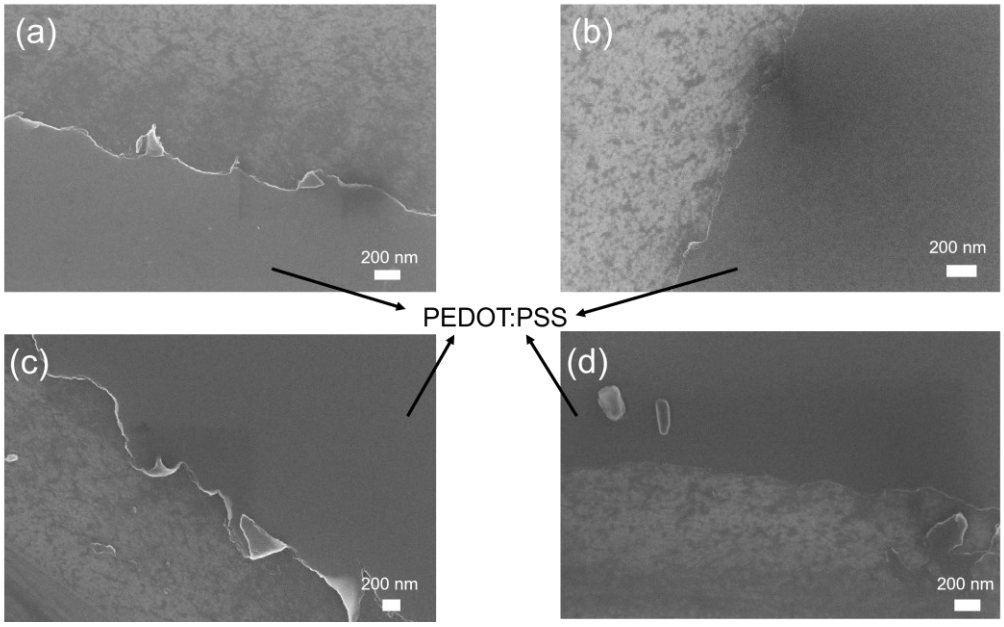

Figure 5.24: *SEM images of PEDOT:PSS films after depositing PEDOT:PSS mixture solutions A (a), B (b), C (c) and D (d) on the SiO_2 substrate.*

Furthermore, the transfer characteristics of the PEDOT:PSS OECTs with different film thicknesses were measured after applying PBS solution onto the transistors. The measurement was carried out using the Keithley 4200 parameter analyzer and an Ag/AgCl

reference electrode was immersed in the PBS solution as a gate electrode. V_{GS} sweeps ranging from -0.4 V and 0.8 V were systematically applied between source and gate electrodes, while a constant V_{DS} of -0.4 V was employed between source and drain electrodes. The transfer characteristics of these transistors are illustrated in figure 5.25. The black curve presents the transfer characteristics of the transistor with 108 nm of PEDOT:PSS film, while the red curve shows the transfer characteristics of the OECTs with 78 nm of PEDOT:PSS film. Lastly, the blue curve refers to the transfer characteristics of the chips after depositing PEDOT:PSS film with 45 nm thickness. All the transistors exhibit the depletion-mode performance, showing the drain current decreases with the application of more positive V_{GS}. Furthermore, the results indicate that the reduction of PEDOT:PSS film thickness leads to a decrease in the drain current value. Since the decrease of the film thickness results in an increase of the ratio of gate capacitance (C_{gate}) to channel capacitance ($C_{channel}$), the gating of the transistors becomes more efficient [200]. When the gate voltage was applied, cations were injected from the PBS solution into the PEDOT:PSS films, and these cations then compensated the anionic sulfonate groups on the PSS chains. Compared to the OECTs with the thicker film, the amount of the available charge carriers in PEDOT:PSS decreases more for the OECTs with thinner PEDOT:PSS film. The electrical conductivity of the PEDOT:PSS film was also significantly reduced in the thinner film, resulting in a dramatic decrease in its drain current.

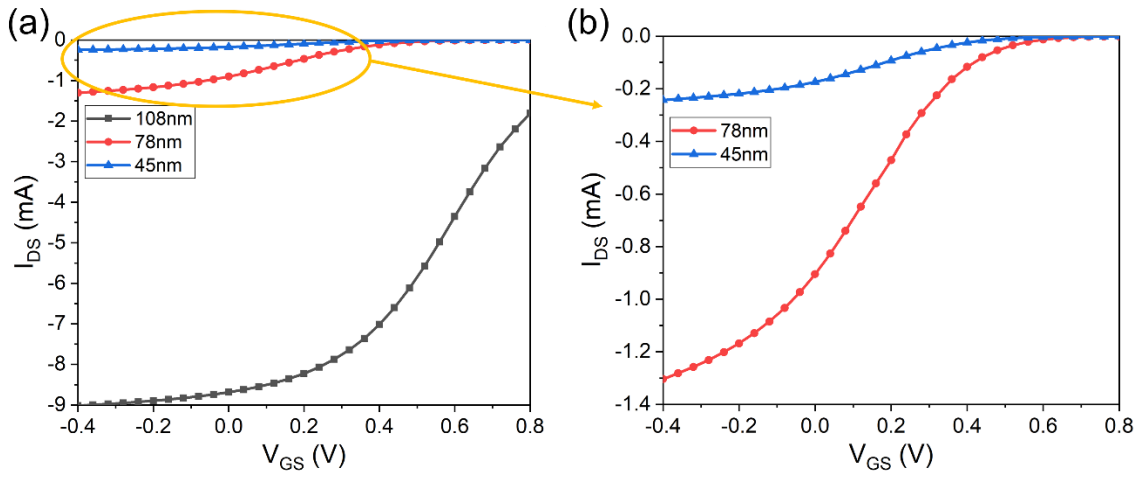

Figure 5.25: *After applying the PBS solution, the transfer characteristics of PEDOT:PSS OECTs with Au contact material was measured when different thicknesses of the PEDOT:PSS films were deposited on the transistors.*

5.3 Ion detection using ion-selective membrane integrated OECTs

5.3.1 Electrical characteristics of OECTs

The transfer characterization of the fabricated PEDOT:PSS OECTs without ISM and with different Na^+ ISMs was performed using the TTF amplifier system when 100 mM of the buffer solution was applied on the chips. V_{GS} sweep ranged from -0.8 V to 0 V, while V_{DS} was kept constant at -0.4 V. Figure 5.26 displays the transfer characteristics of these OECTs without ISM and with Na^+ ISMs containing various membrane compositions and thicknesses. The

black curve refers to the transfer characteristics of the PEDOT:PSS OECTs without ISM, while the red curve presents the transfer characteristics of the PEDOT:PSS OECTs with composition 0 and 1300 nm thickness of Na^+ ISM. The blue curve shows the transfer characteristics of the PEDOT:PSS OECTs with composition 1 and 600 nm of Na^+ ISM. Lastly, the green curve demonstrates the transfer characteristics of the PEDOT:PSS OECTs with composition 2 and 80 nm of Na^+ ISM. As shown in figure 5.26, every transfer characterization curve exhibits the depletion-mode performance. Moreover, the transistors with Na^+ ISMs show a smaller drain current value than those without ISMs. The results indicate that Na^+ ions first permeated through the ISMs and then diffused into the PEDOT:PSS channel. As a result, this diffusion caused the de-doping process of the PEDOT:PSS to occur, as can be explained by the following equation (5.2):

$$PEDOT^+:PSS^- + M+ + e^- \leftrightarrow PEDOT + M^+:PSS^- \quad (5.2)$$

where M^+ represents the cations. After the de-doping process occurred, the available charge carriers in PEDOT decreased. This led to a reduction in the electrical conductivity of the PEDOT:PSS film and a change in the electrical characterization of the OECTs.

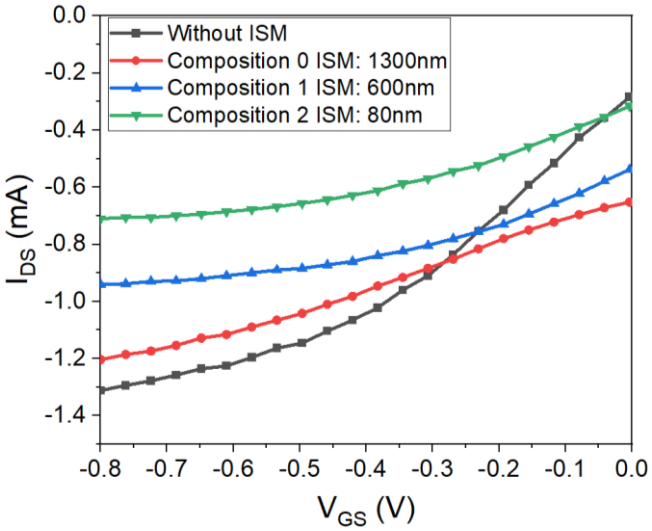

Figure 5.26: *Transfer characteristics of PEDOT:PSS OECTs without ISM, with different compositions and thicknesses of Na^+ ISM after applying 100 mM of Na^+ buffer solution. V_{GS} swept from -0.8 V to 0 V and V_{DS} was constant at -0.4 V.*

5.3.2 Sensitivity of ISM-OECT microarrays for detection of Na^+ and K^+ ions

The real-time measurement was carried out to monitor the Na^+ and K^+ ion concentrations by obtaining the drain current of the ISMs based PEDOT:PSS OECTs when the buffer solutions (pH = 7) with various concentrations (1 mM, 5 mM, 10 mM, 50 mM and 100 mM) flowed through the transistors. V_{DS} had a constant value of -0.4 V and V_{GS} was set to the value when the maximum g_m was reached. Initially, the measurement of the drain current of PEDOT:PSS OECTs was performed in DI water and this drain current value served as a reference data point for the analysis of the drain current change in different buffer solutions. Following that, PEDOT:PSS OECTs were continuously measured in buffer solutions with concentrations ranging from low to high (1 mM to 100 mM) to obtain the drain current. Figure 5.27 (a) shows

the typical change in drain current (ΔI_{DS}) of the exemplary PEDOT:PSS OECTs: without ISM (black), with composition 0 of Na^+ ISM (blue) and composition 0 of K^+ ISM (yellow). The membrane thickness integrated on the transistors was 1300 nm. The formula $\Delta I_{DS} = I_{DS} - I_{DS0}$ was utilized for the calculation, where I_{DS} and I_{DS0} were the drain current values obtained in the buffer solutions and DI water, respectively. As shown in figure 5.27 (a), a noticeable increase in ΔI_{DS} was observed when the buffer concentrations increased, which was expected from the electrochemical characteristics of the PEDOT:PSS. Compared to the buffer solutions with lower concentrations, those with higher concentrations contained more cations. Upon the application of the gate voltage, these cations were able to permeate the ISMs and then reach the PEDOT:PSS channel. This resulted in a larger change in conductivity of the PEDOT:PSS and then a larger change in the drain current of the transistors. The real-time recording of OECTs with other ISM compositions and thicknesses is shown in figure S4 in Appendix C. Likewise, the change in the drain current of these OECTs was greater when the concentrations of the buffer solution were increased.

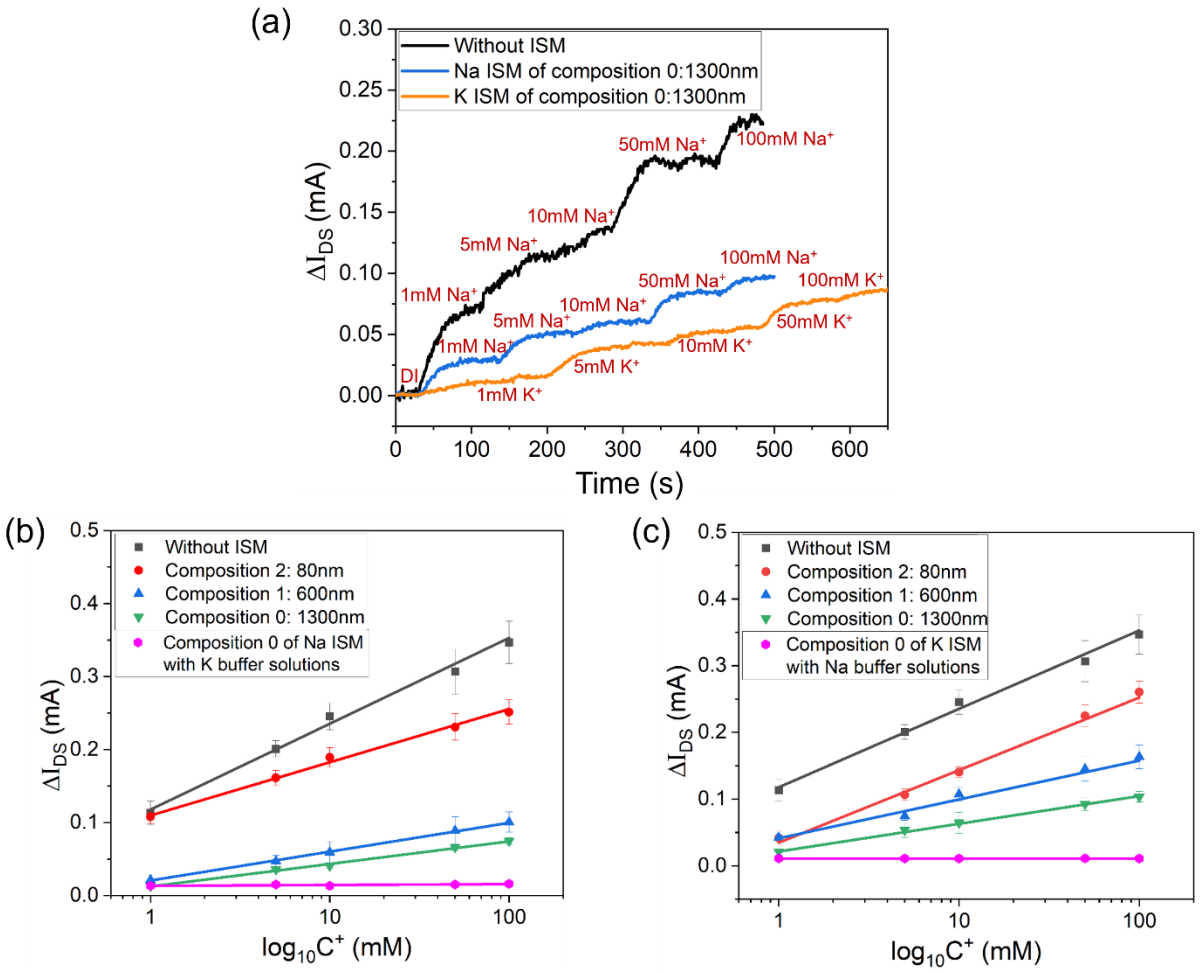

Figure 5.27: *(a) The real-time recorded drain current for the OECTs without ISM, with Na^+ ISM composition 0 and with K^+ ISM composition 0. The thickness of ISM is 1300nm. (b) Sensitivity of Na^+ ISM based PEDOT:PSS OECTs and (c) Sensitivity of K^+ ISM based PEDOT:PSS OECTs with three different ISM compositions and thicknesses.*

The correlation between the ΔI_{DS} and buffer concentrations was obtained from the real-time measurement of the OECTs, presented in figure 5.27 (b). The changes in the drain current of the OECTs exhibit a linear relationship with the buffer concentrations on a logarithmic scale within the measured concentration range. This result indicates the detection of ions using the Na^+ ISM based OECTs. The black curve in figure 5.27 (b) represents the drain current change of OECTs without ISM as various concentrations of Na^+ buffer solution flow through the transistors. In contrast, the red curve displays the change in drain current of Na^+ ISM based OECTs with membrane composition 2 and thickness of 80 nm when varying concentrations of Na^+ buffer solution flowed through the OECTs. Additionally, the blue curve presents the drain current change of Na^+ ISM based OECTs with membrane composition 1 and thickness of 600 nm as various concentrations of Na^+ buffer solution flowed through the OECTs. Comparably, the green curve shows the drain current change of the Na^+ ISM based OECTs covered with composition 0 and thickness of 1300 nm when different Na^+ buffer solutions flowed through the OECTs. Lastly, the pink curve demonstrates the drain current change of the OECTs integrated with the Na^+ ISM containing membrane composition 0 and thickness of 1300 nm when the various concentrations of K^+ buffer solution flowed through the transistors. Furthermore, the dependency of the resulted ΔI_{DS} values with minimal error bar (n=3) on the buffer solutions exhibits a linear fit. The sensitivity of the Na^+ ISM based OECTs towards ions was extracted from the slope of the linear fit, and these sensitivity values are presented in Table 5.3.

Table 5.3: *Sensitivity values for OECTs without ISM, Na^+ ISM and K^+ ISM.*

	Without ISM	Na^+ sensor			K^+ sensor		
		Composition 0 (1300nm)	Composition 1 (600nm)	Composition 2 (80nm)	Composition 0 (1300nm)	Composition 1 (600nm)	Composition 2 (80nm)
Sensitivity (mA/log (mM))	0.115	0.031	0.039	0.073	0.041	0.058	0.108
R-Quadrat	0.99229	0.99393	0.99859	0.99503	0.9988	0.98005	0.99322
Pearson R	0.99614	0.99696	0.9993	0.99751	0.9994	0.98997	0.99661

As indicated by the red curve in figure 5.27 (b) and the sensitivity value in Table 5.3, the Na^+ ISM based OECTs with membrane composition 2 and thickness of 80 nm exhibited a high sensitivity (0.073 mA/log (mM)) towards Na^+ ions over a concentration range from 1 mM to 100 mM. The Na^+ ISM based OECTs with membrane composition 1 and 600 nm thickness showed sensitivity (0.039 mA/log (mM)) towards the Na^+ ion concentration ranging from 1 mM to 100 mM, while the OECTs integrated with Na^+ ISM of membrane composition 0 and thickness of 1300 nm exhibited sensitivity (0.031 mA/log (mM)) towards the Na^+ ion detection. In contrast to the OECTs without ISM, the transistors integrated with Na^+ ISM continued to demonstrate a high sensitivity towards the Na^+ ion detection. The results indicated that enough Na^+ ions permeated through the ISM onto the PEDOT:PSS, even in the presence of the Na^+ ISM. As a result, the conductivity of PEDOT:PSS showed strong variations, leading to a change in the drain current of OECTs. As demonstrated in figure 5.27 (b), the decrease of the Na^+ membrane composition and thickness results in an increase in sensitivity of OECTs towards Na^+ ion detection over a concentration range from 1 mM to 100 mM. The reduced

composition and thickness of ISMs exhibited higher membrane permeability, allowing for the easier passage of the Na^+ ions and increased penetration into the PEDOT:PSS channel. Subsequently, the drain current change of the OECTs with reduced composition and thickness of ISMs was increased, resulting in enhanced sensitivity. Furthermore, the PEDOT:PSS OECTs covered with Na^+ ISM demonstrated a minimal change in drain current when the different K^+ buffer solutions flowed through the transistors. Therefore, these results proved that the OECTs exhibited high selectivity against K^+ ions.

As shown in figure 5.27 (c) and Table 5.3, the drain current change of OECTs covered with K^+ ISM shows their strong ability for ion detection. When various concentrations of K^+ buffer solution flowed through the OECTs, the drain current change of the OECTs without ISM is represented by the black curve in figure 5.27 (c). In contrast, the red curve displays the change in the drain current of OECTs covered with K^+ ISM of membrane composition 2 and thickness of 80 nm as varying concentrations of K^+ buffer solution flowed through the OECTs, where the sensitivity of these OECTs for K^+ ion detection is 0.108 mA/log (mM). The blue curve refers to the drain current change and sensitivity (0.058 mA/log (mM)) of K^+ ISM based OECTs with membrane composition 1 and thickness of 600 nm as various concentrations of K^+ buffer solution flowed through the OECTs. Comparably, the green curve demonstrates the drain current change and sensitivity (0.041 mA/log (mM)) of the K^+ ISM based OECTs with a membrane composition of 0 and thickness of 1300 nm when different K^+ buffer solutions flowed through the OECTs. Lastly, the pink curve shows the change in drain current of the OECTs integrated with K^+ ISM containing membrane composition 0 and 1300 nm thickness when various concentrations of Na^+ buffer solution flowed through the OECTs. These K^+ ISM based OECTs also exhibited a high sensitivity towards K^+ ions within the concentration range of 1 mM to 100 mM. Additionally, only a slight change in drain current in the Na^+ buffer solutions was observed when using the transistors covered with membrane composition 0 and 1300 nm thickness of K^+ ISM. The result indicated the highly selective detection of these OECTs to Na^+ ions. As displayed in figure 5.27 and Table 5.3, PEDOT:PSS OECTs integrated with ISMs can be utilized as highly sensitive sensors for detecting the desired ions within the concentration range of 1 mM to 100 mM.

The effect of the varied spin-coating speeds on detecting the Na^+ and K^+ concentrations was performed using the PEDOT:PSS OECTs based on Na^+ and K^+ ISM with composition 0, respectively. When the buffer solutions with different concentrations flowed through the OECTs, the real-time measurement was carried out by obtaining the drain current to acquire the relationship between ΔI_{DS} and buffer concentrations. Figure 5.28 (a) shows the relationship between ΔI_{DS} and Na^+ buffer solutions using the OECTs based on Na^+ ISM, while figure 5.28 (b) displays the relationship between ΔI_{DS} and K^+ buffer solutions with the OECTs coated with K^+ ISM. The drain current change of these OECTs shows a linear relationship with the buffer concentrations on a logarithmic scale over the measured concentration range of 1 mM to 100 mM. The black line refers to the drain current change of the OECTs integrated without ISM, while the red curve refers to the relationship between the drain current change and buffer

concentrations when using the OECTs integrated with 1600 nm thickness of ISM. Moreover, the blue line represents the change in drain current of the transistors integrated with 1500 nm thickness of ISM. Lastly, the green curve shows the relationship between ΔI_{DS} and buffer concentrations when employing the OECTs integrated with 1300 nm of ISM. As displayed in Table 5.4, the sensitivity values of ISM based OECTs were extracted from the linear curves in figure 5.28. The results indicate that an increase of the spin-coating speeds results in the reduction of membrane thickness, and thus the enhanced sensitivity value of OECTs towards the detection of desired ions.

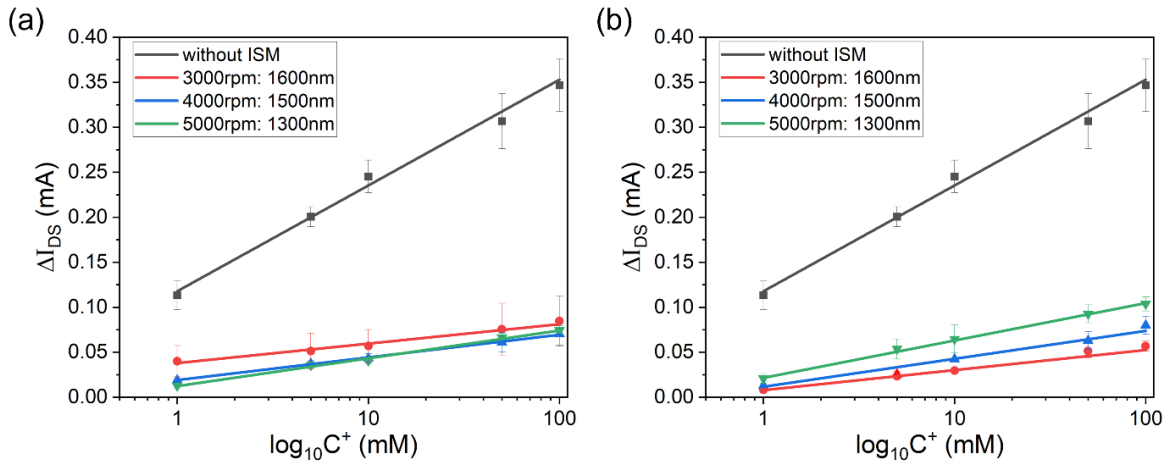

Figure 5.28: *(a) Sensitivity of Na^+ membrane PEDOT:PSS OECTs and (b) Sensitivity of K^+ membrane PEDOT:PSS OECTs with different spin-coating speeds.*

Table 5.4: *Sensitivity value of OECTs without ISM, Na^+ ISM and K^+ ISM using different spin-coating speeds.*

	Without ISM	Na^+ sensor			K^+ sensor		
		3000 rpm (1600nm)	4000 rpm (1500nm)	5000 rpm (1300nm)	3000 rpm (1600nm)	4000 rpm (1500nm)	5000 rpm (1300nm)
Sensitivity (mA/log (mM))	0.11755	0.02094	0.02518	0.03087	0.02233	0.03104	0.04154
R-Quadrat	0.99229	0.96618	0.99817	0.99393	0.98077	0.99044	0.9988
Pearson R	0.99614	0.98285	0.99908	0.99696	0.99034	0.99521	0.9994

5.3.3 Selectivity of ISM-OECT microarrays for detection of Na^+ and K^+ ions

Real-time monitoring of the concentration of Na^+ and K^+ ions was measured by the change in the drain current of OECTs integrated with ISMs when the buffer solutions (pH = 7) with varying concentrations (1 mM, 5 mM, 10 mM, 50 mM and 100 mM) flowed through the transistor. V_{DS} had a constant value of -0.4 V and V_{GS} was set to the value when the maximum g_m was reached. The drain current of PEDOT:PSS OECTs was first measured in DI water, which served as a reference data point for the analysis of the drain current change in different buffer solutions. Figure 5.29 (a) presents the real-time recording of Na^+ ISM based PEDOT:PSS OECTs with composition 0 and thickness of 1300 nm. After the first measurement of the drain current using DI water, PEDOT:PSS OECTs were then measured in the Na^+ buffer solution (pH = 7) with a concentration of 1 mM. Subsequently, K^+ buffer solutions (pH = 7) were

introduced with concentrations ranging from 1 mM to 100 mM, followed by the Na^+ buffer solutions (pH = 7) with concentrations ranging from 1 mM to 100 mM. After 1 mM of Na^+ buffer solution flowed through the transistors, the drain current displayed a significant change, indicating OECTs integrated with 1300 nm of Na^+ ISM were functional. Then, only a slight change in drain current was presented in the real-time measurement when various K^+ buffer solutions flowed through the chips, even at a concentration of 100 mM. This suggests that the chips are highly selective towards K^+ ion detection. Additionally, the transistors persisted in the change in drain current when various Na^+ buffer solutions flowed through the chips. The selectivity measurements of Na^+ ISM based PEDOT: PSS OECTs with other membrane compositions and thickness were carried out using the same experimental procedure. The results are displayed in figure 5.29 (b) and (c). However, the Na^+ ISM based PEDOT:PSS OECTs with composition 2 and 80 nm of thickness exhibited a noticeable change in drain current when different K^+ buffer solutions flowed through the chips, indicating that the selectivity of transistors was compromised.

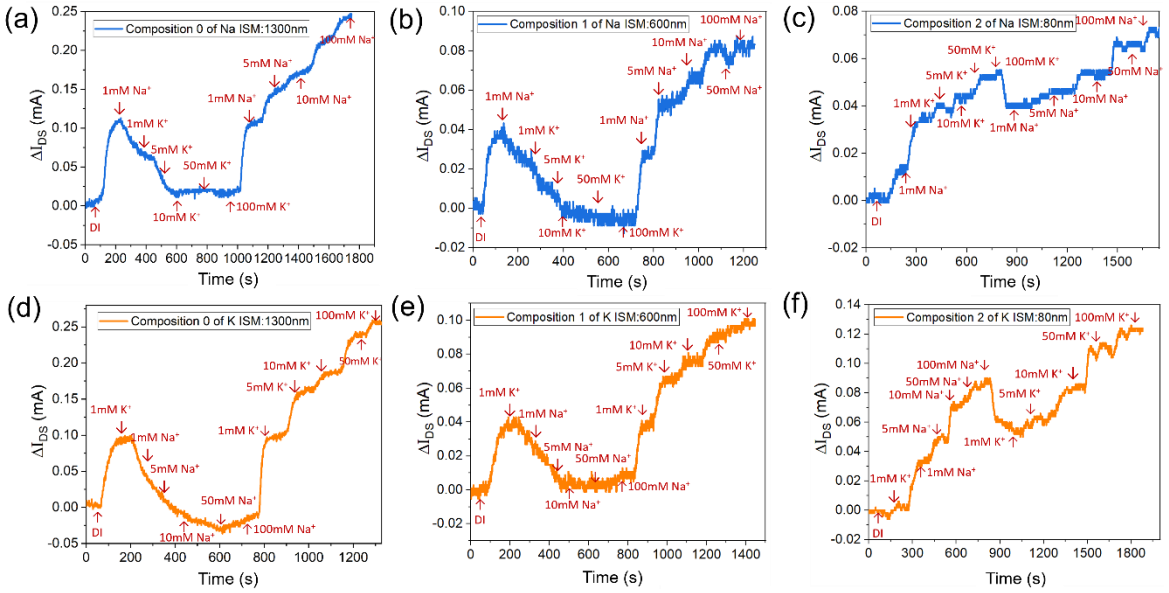

Figure 5.29: *Selectivity of Na^+ ISM OECTs with membrane thicknesses of 1300 nm (a), 600 nm (b) and 80 nm (c). Selectivity of K^+ ISM OECTs with membrane thicknesses of 1300 nm (d), 600 nm (e) and 80 nm (f).*

Figure 5.29 (d) presents the real-time measurement of PEDOT:PSS OECTs covered with K^+ ISM with composition 0 and thickness of 1300 nm. The process began with the DI water flowing though the microfluidic system, followed by the introduction of 1 mM of K^+ buffer solution. The significant change of drain current can be observed when this solution flowed through the chips, showing the chips were functional. Then, Na^+ ions were introduced into the chips via the buffer solution with concentrations ranging from 1 mM to 100 mM. The OECTs exhibited minimal variation in drain current as the Na^+ buffer solutions flowed through, even at a concentration as high as 100 mM. Lastly, the K^+ buffer solution with concentrations ranging from 1 mM to 100 mM flowed through the transistors and the drain current was also displayed in real-time measurement. Figure 5.29 (e) and (f) presents the selectivity measurement of K^+ ISM based PEDOT:PSS OECTs with other membrane compositions and thicknesses. The K^+

ISM based PEDOT:PSS OECTs with composition 2 and thickness of 80 nm showed a significant drain current change when Na^+ buffer solutions were introduced, suggesting that the selectivity of these OECTs towards Na^+ ion detection was compromised.

5.3.4 Reversibility of ISM-OECT microarrays for detection of Na^+ and K^+ ions

Figure 5.30 displays the reversibility of OECTs integrated with ISMs for ion detection. Real-time measurement was carried out by obtaining the drain current as the buffer solutions (pH = 7) with varying concentrations (1 mM, 5 mM, 10 mM, 50 mM and 100 mM) flowed through the transistor. V_{DS} had a constant value of -0.4 V and V_{GS} was set to the value when the maximum g_m was reached. The reversibility of OECTs covered with 1300 nm of Na^+ ISM is shown in figure 5.30 (a). In this measurement, DI water was initially introduced into the microfluidic system and the measured current served as a reference data point. Subsequently, the Na^+ buffer solutions flowed through the chip from low to high concentration (1 mM to 100 mM). The concentration of the Na^+ buffer solutions gradually decreased from high to low (100 mM to 1 mM) until DI water was introduced again in the microfluidic system. The transistors displayed a distinctive drain current change when the concentration of the buffer solutions increased from low to high. When the buffer solutions with concentrations from high to low flowed through the OECTs, a noticeable change in drain current was also observed. The drain current returned to baseline level after the OECTs were rinsed once or twice with DI water. The results indicated that the OECTs integrated with 1300 nm of Na^+ ISM exhibit excellent reversibility towards Na^+ ion detection. The same experimental procedure was carried out on the transistors covered with 600 nm and 80 nm of Na^+ ISM, with these results demonstrated in figure 5.30 (b) and (c).

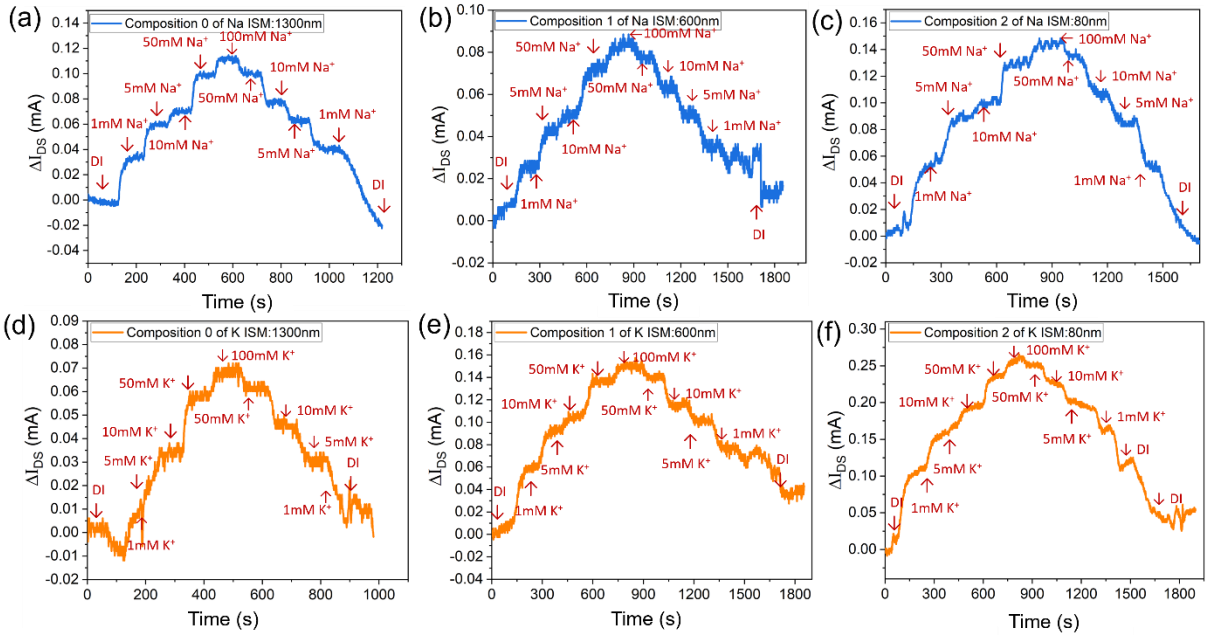

Figure 5.30: *Reversibility of Na^+ ISM OECTs with membrane thicknesses of 1300 nm (a), 600 nm (b) and 80 nm (c). Reversibility of K^+ ISM OECTs with membrane thicknesses of 1300 nm (d), 600 nm (e) and 80 nm (f).*

Figure 5.30 (d) presents the reversibility of the OECTs based on 1300 nm K^+ ISM for detecting the K^+ ions. The real-time measurement started with withdrawing DI water into the microfluidic system and then the K^+ buffer solutions with concentrations ranging from low to high (1 mM to 100 mM) were introduced to the system. Following that, the transistors were measured when the concentration of the K^+ buffer solutions reduced from high to low (100 mM to 1 mM), then the measurement was completed with DI water. The 1300 nm of K^+ ISM based OECTs exhibited a good reversibility response towards the detection of K^+ ions. Furthermore, an identical experimental process was performed with the transistors integrated with 600 nm and 80 nm of K^+ ISM, and the reversibility responses are presented in figure 5.30 (e) and (f). The real-time measurement of the reversibility behavior of the OECTs for detecting Na^+ and K^+ ions exhibited their reliability and repeatability for allowing the measurement of various OECTs multiple times.

5.3.5 Multiplexed sensing of Na^+ and K^+ ions with OECT microarrays

After completing the systematic and statistical investigation into the influence of the membrane on the sensitivity and selectivity of ion detection using PEDOT:PSS OECTs, the intermediate membrane with composition 1 and thickness of 600 nm was chosen for multiplexed sensing of Na^+ and K^+ ions. This choice compromises the sensitivity and selectivity of OECTs for Na^+ and K^+ ion detection.

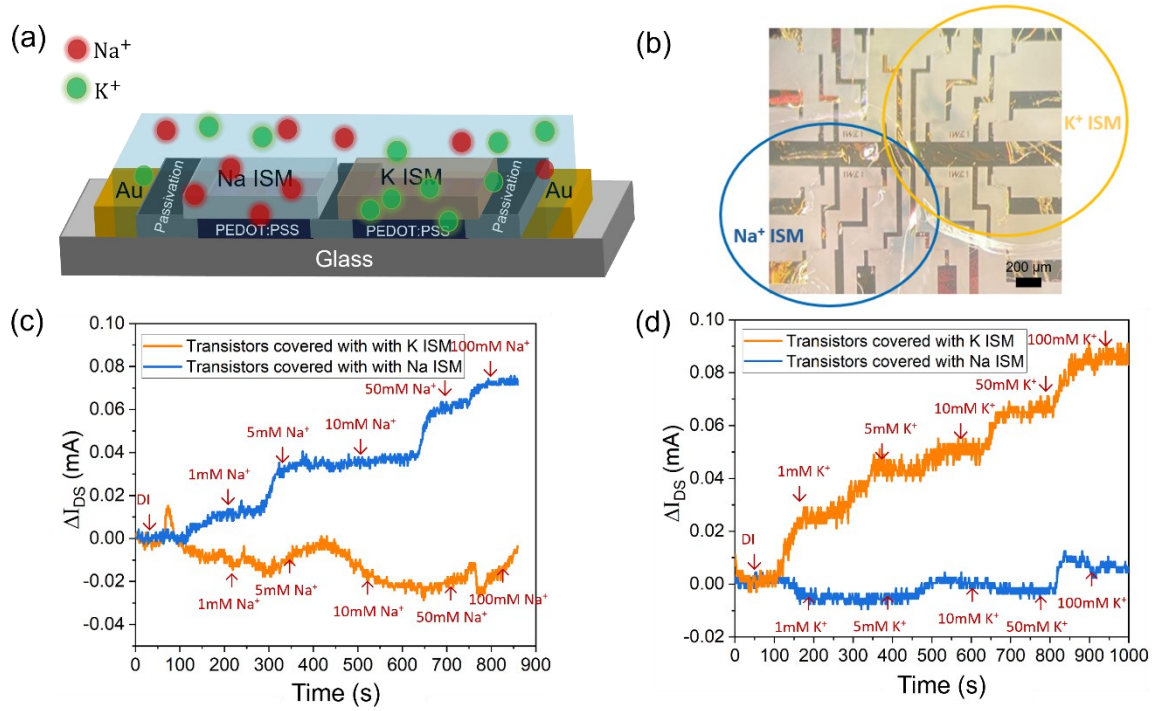

Figure 5.31: *(a) Schematic representation of multiplexed detection of Na^+ and K^+ ions using the same PEDOT:PSS OECT microarray, (b) The microscope image of OECT microarray covered with Na^+ and K^+ ISM, (c) Real-time monitoring of Na^+ ions and (d) Real-time recording of K^+ ions using this OECT.*

Figure 5.31 (a) presents a schematic of multiplexed detection for Na^+ and K^+ ions using a PEDOT:PSS OECT microarray. Different areas of the same chip were covered with the Na^+

ISM and K^+ ISM with composition 1 and thickness of 600 nm using the spin-coating technique in a sequential manner. Figure 5.31 (b) shows the microscope image of an OECT microarray integrated with the Na^+ and K^+ ISM. The upper right corner (yellow circle) displays a uniform and distinctive yellow color, resulting from the incorporation of the K^+ ISM on the chip. The lower left corner (blue circle) of this microarray appears uniformly transparent, attributed to the cover of the transistor with the transparent color of Na^+ ISM.

Real-time measurement was performed for the multiplexed sensing of Na^+ and K^+ ions by obtaining the change in drain current of the PEDOT:PSS OECT microarray when the buffer solutions with varying concentrations (1 mM, 5 mM, 10 mM, 50 mM and 100 mM) flowed through the transistor. V_{DS} had a constant value of -0.4 V and V_{GS} was set to the value when the maximum g_m was reached. The drain current of Na^+ and K^+ ISM based PEDOT:PSS OECTs was first measured using DI water, which served as a reference data point to analyze the drain current change in different buffer solutions. Figure 5.31 (c) displays the real-time monitoring of Na^+ ions using the PEDOT:PSS OECTs covered with Na^+ and K^+ ISMs. After DI water flowed through the microfluidic system, the measurement was continuously carried out to obtain the drain current of the OECT microarray in the Na^+ buffer solutions with the concentrations increasing from low to high (1 mM to 100 mM). As presented in figure 5.31 (c), a noticeable change in drain current can be observed in the transistors integrated with Na^+ ISMs when the Na^+ buffer solutions flowed through. However, the transistors coated with K^+ ISMs demonstrated no response towards the Na^+ buffer solutions. Figure 5.31 (d) displays the real-time measurement for sensing the K^+ ions using the chip integrated with Na^+ and K^+ ISM. The drain current of the chip was first measured in DI water, and used as the reference data point. Subsequently, the drain current was obtained in the K^+ buffer solutions with concentrations ranging from 1 mM to 100 mM. The results indicated that the transistors covered with K^+ ISM exhibited a significant drain current change when sensing the K^+ ions, while only a minimal response on the drain current was obtained from the transistors coated with Na^+ ISM. It can be concluded that the multiplexed sensing for Na^+ and K^+ ions with high sensitivity and selectivity can be realized by utilizing a single chip of PEDOT:PSS OECT microarray integrated with Na^+ and K^+ ISM.

5.4 Dopamine detection using the OECT microarrays

5.4.1 Cyclic voltammetry characterization

CV characterization for DA detection was carried out using two different measurement setups which are described in section 4.5.2. Both setups used a three-electrodes configuration consisting of a WE, CE and RE. These three electrodes were all immersed in the electrolyte solution. A potentiostat was used to linearly sweep the potential between the RE and WE. The potentiostat swept back in the opposite direction when the potential reached the pre-set limit and repeated this process multiple times, while recording the changing current between the WE and CE. The parameters for the CV characterization are also presented in section 4.5.2. Figure 5.32 displays the CV characterization for DA detection using the first measurement setup shown in figure 4.18 (a) and (c). Figure 5.32 (a) shows a continuous CV sequence of 5

scans obtained after applying 1 mM of the DA solution into the system. A voltage sweep ranging linearly from -0.2 V to 0.7 V with a scan rate of 0.05 V/s was applied between the WE and RE. Then, the voltage reversed from 0.7 V to -0.2 V once it reached 0.7 V. This procedure was repeated 5 times, and the changing current between WE and CE was recorded. As the voltage increased from -0.2 V to 0.7 V, the measured current initially increased rapidly until it reached its peak. At this current peak position, which was observed between 0.2 V and 0.4 V, DA underwent electro-oxidation at the Pt working electrode. After reaching its oxidation peak, the current rose slowly or remained constant, then accelerated again until the high voltage limit of 0.7 V was reached. As the voltage was swept reversely from 0.7 V to -0.2 V, the current first decreased dramatically until a reduction current peak was reached at a voltage between 0 V to 0.2 V. The results indicated that the electro-reduction of the DA occurred at this reduction current peak. As shown in figure 5.32 (a), when the number of scans increased, the measured currents gradually decreased until the stable currents were recorded after the 4th scan. This phenomenon demonstrates a reduction in DA concentrations which are needed for electro-reoxidation during characterization, indicating a gradual consumption of DA after each successive scan. The identical experimental procedure was performed for CV characteristics when various concentrations of DA solutions (10 µM, 100 µM and 250 µM) were applied to the measurement setup. Five sequence CV scans were carried out for each DA concentration, and the fourth scan was extracted and compared for each concentration. Figure 5.32 (b) shows the CV characteristics of DA solutions with varied concentrations ranging from 10 µM to 250 µM. For the DA solution with concentrations of 100 µM and 250 µM, the CV current gradually increased until reaching its oxidation peak within the voltage range of 0.2 to 0.4 V when the voltage swept from the -0.2 V to 0.7 V. However, the oxidation peak was not observed for the 10 µM of DA solution, indicating that the first CV measurement setup exhibited no significant current response until 100 µM of DA concentration was added.

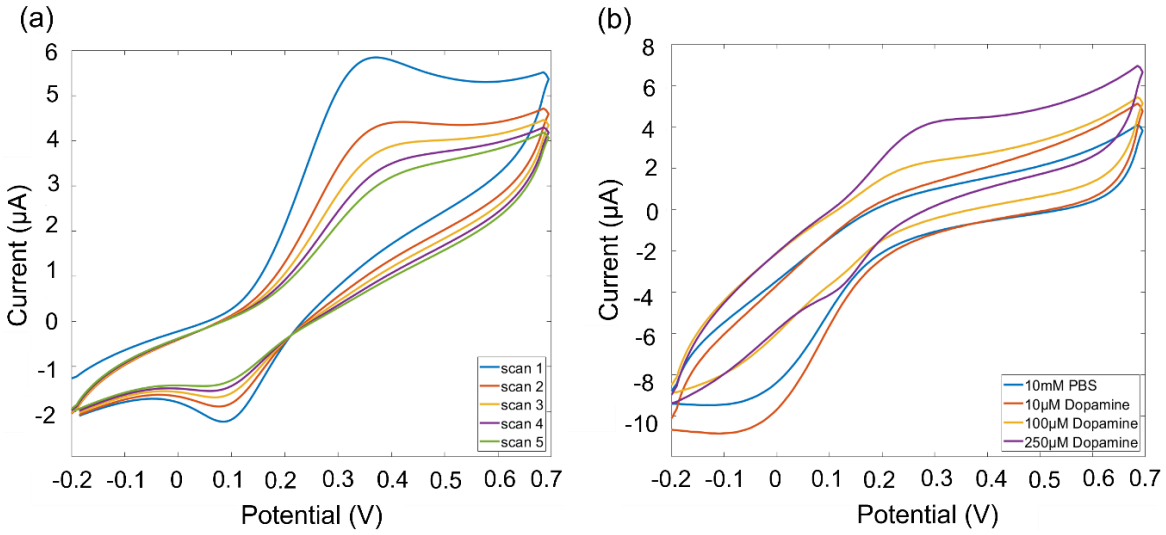

Figure 5.32: *Cyclic voltammetry (CV) characterization of the first measurement setup (WE and CE: Pt electrode, RE: Ag/AgCl reference electrode). The voltage was swept from -0.2 to 0.7 V with the scan rate of 0.05 V/s then reversed. (a) CV curves using a continuous sequence of 5 scans with application of 1 mM of DA solution. (b) The fourth scan of the CV curves were extracted and compared when DA solutions with various concentrations were added.*

Figure 5.33 displays the CV characteristics of DA detection using the second measurement setup described in figure 4.18 (b) and (d). Figure 5.33 (a) presents the continuous series of five CV scans with the DA concentration of 1 mM. When the voltage was swept from -0.2 V to 0.7 V, a current peak was observed between the voltage of 0.2 V and 0.4 V in various scans, indicating the occurrence of the electro-oxidation of DA. The peak current value gradually decreased as the scanning process progressed, showing that the DA concentration was gradually consumed after each scan. Afterwards, CV characterization with the application of different DA concentrations was carried out and the fourth CV scan of each concentration was compared. The concentrations of DA ranged from 1 µM to 1 mM and the results are shown in figure 5.33 (b). When the voltage swept from -0.2 V to 0.1 V, the current maintained a steady state of 0 µA. Then, the current exhibited a significant increase as the voltage increased until the current reached a peak. Oxidation for each DA concentration occurred at this peak position within the voltage range of 0.2 V to 0.4 V. As the voltage continuously increased, the current underwent a sudden drop after the oxidation peak and stabilized at a constant current value. When the voltage swept from 0.7 V to -0.2 V, the reduction peak of DA solution was observed. As the DA concentration increased from 1 µM to 1 mM, the oxidation peak also increased. The results show that the second measurement setup for CV characterization enables a wider range of DA concentration detection, ranging from 1 µM to 1 mM.

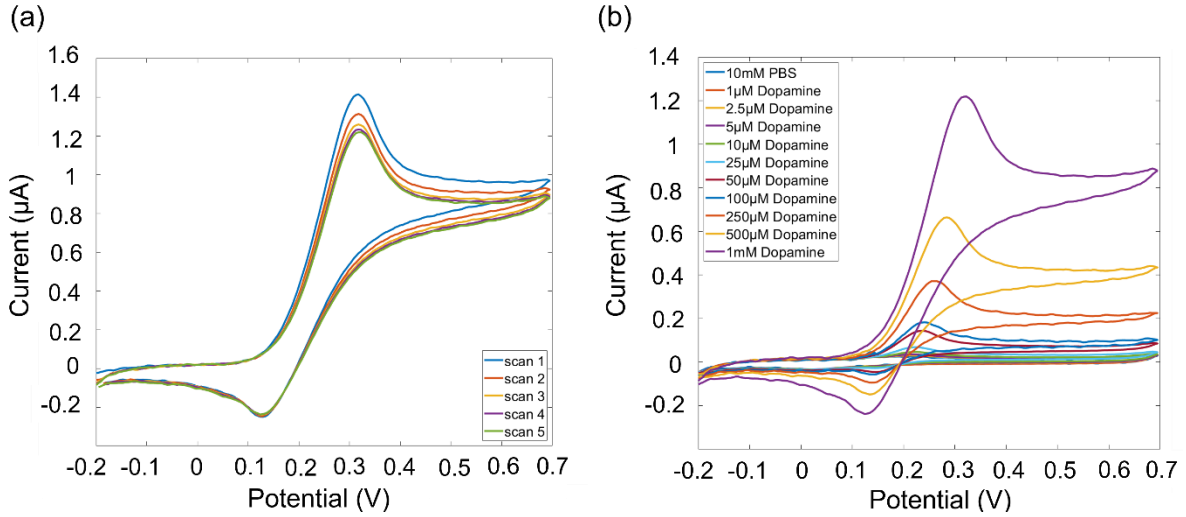

Figure 5.33: *CV characteristic curves of an OECT for the second measurement setup (WE: connected source and drain electrode; CE: Pt electrode; RE: Ag/AgCl reference electrode). The voltage swept from -0.2 to 0.7 V then reversed, (a) CV curves using a continuous sequence of 5 scans with 1 mM of dopamine solution, (b) CV curves of the fourth scan with varying DA concentrations.*

5.4.2 Transfer characteristics of the OECTs with PBS and dopamine solutions

The transfer characteristics of the OECTs were evaluated in PBS solution and 250 µM of DA solution, as presented in figure 5.34 (a). The measurement was performed using the Keithley 4200 parameter analyzer and a Pt electrode was used as a pseudo-reference electrode. V_{GS} sweeps ranging from -0.5 V to 0.8 V were applied between the source and gate electrodes, while a constant V_{DS} value of -0.3 V was applied between the source and drain electrodes.

For each transfer curve, the transistors were measured continuously three times. Results are displayed as mean values with small error bars, indicating the high reliability and repeatability of the measurements. The transfer characteristics obtained from the PBS solution serve as reference data and each transfer curve exhibits the depletion-mode of transistor performance. The drain current acquired from 250 µM DA solution exhibits a notable reduction in comparison to the current obtained from the PBS solution. Additionally, the results demonstrate that an increase in DA concentration leads to a shift of the transfer curve at the oxidation potential of DA (between 0.3 V to 0.4 V) towards more negative voltages. As the electro-oxidation of DA occurred at the Pt electrode, a Faradic current was created, increasing the effectively applied gate voltage and resulting in a change in the transfer curves of the transistors.

Furthermore, the transfer characteristics of the OECTs were studied in DA solutions with various concentrations using the Pt electrode as the gate electrode. V_{DS} was kept constant at -0.3 V and V_{GS} swept from -0.4 V to 0.8 V. Likewise, the transistors were continuously measured three times in each DA solution. Figure 5.34 (b) illustrates the transfer characteristics of the OECTs based on 108 nm of PEDOT:PSS film after applying the PBS solution and DA solutions ranging from 1 nM to 3 mM. As expected, when the concentration of the applied DA solution increases from low to high (1nM to 3 mM), the transfer characteristics of the OECTs shift towards more negative voltages, and the measured drain current reduces.

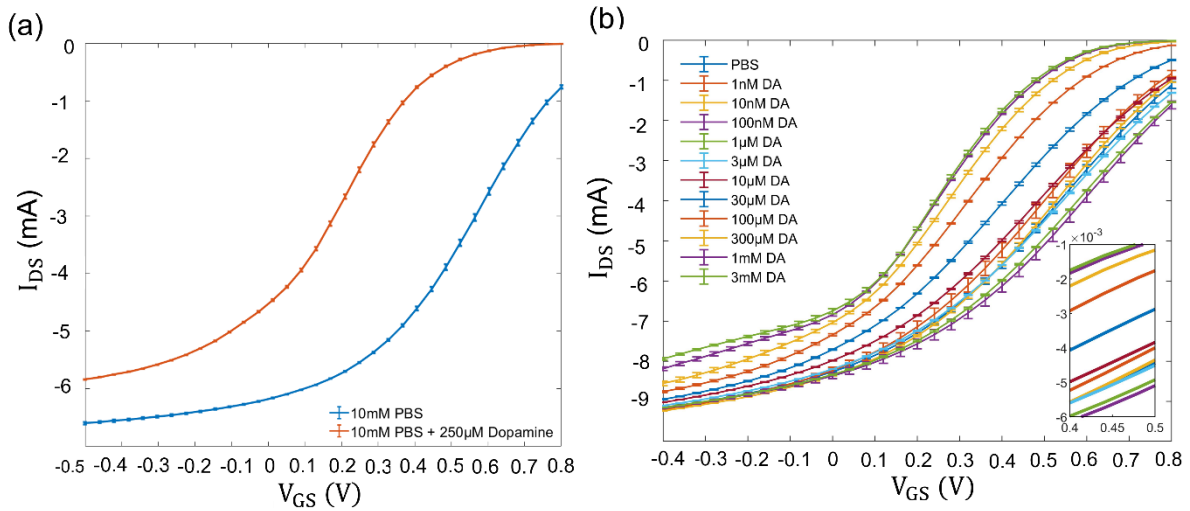

Figure 5.34: *(a)Transfer characteristics using an OECT with Pt gate electrode in PBS and 250 µM DA solutions at the V_{DS} of -0.3 V and V_{GS} swept from -0.5 V to 0.8 V, (b) Transfer characteristics of the transistors with 108 nm of PEDOT:PSS film when DA solutions with various concentrations were applied at the at the V_{DS} of -0.3 V and the V_{GS} swept from -0.4 V to 0.8 V.*

Furthermore, the transfer characteristics are utilized for the analysis of sensitivity, selectivity, and limit of detection (LoD) of DA detection. The normalized response of the source-drain current (NCR) is extracted from the transfer characteristics and employed for the comparisons. In this analysis, DA concentration and NCR were used as x-axis and y-axis, respectively.

Normalization is typically performed with respect to the zero-concentration limit and can be calculated using the following equation (5.3):

$$\text{NCR} = \frac{I_{DS}^{con=0} - I_{DS}}{I_{DS}^{con=0}} \tag{5.3}$$

where $I_{DS}^{con=0}$ represents the drain current obtained at zero concentration (without DA analyte), and I_{DS} is the drain current acquired by the DA solutions with specific concentrations. By calculating the slope of the NCR curve, the sensitivity of analyte detection over the analyte concentrations in a logarithmic scale is determined, allowing for comparison between different OECTs.

The influence of the different scanning rates and directions of gate voltage on the transfer characteristics of the OECTs was performed in PBS solutions using a Pt electrode as the gate electrode. V_{GS} sweeps ranging from -0.4 V to 0.8 V were applied between the source and drain electrodes, while V_{DS} was kept constant at -0.3 V. All the transfer characteristics of the OECTs are presented in figure 5.35.

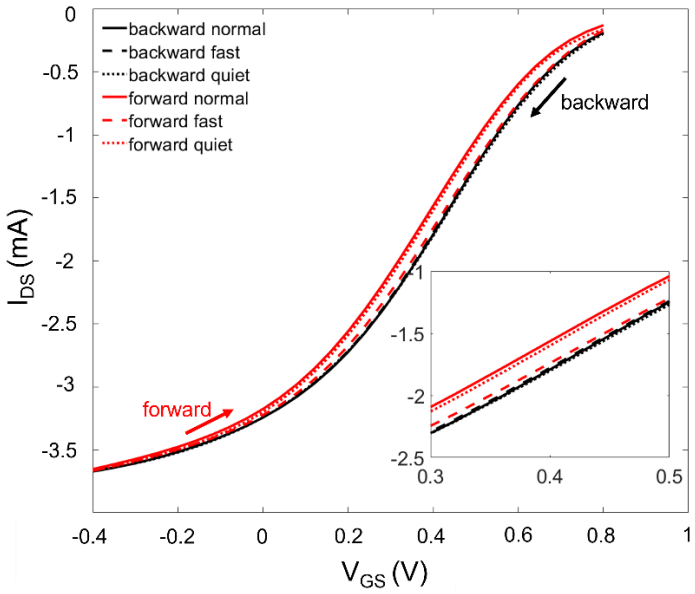

Figure 5.35: *Transfer characteristics of OECTs were measured in PBS solution at different scanning rates and directions using the Pt electrode as the gate electrode. V_{GS} swept between -0.4 V and 0.8 V, while V_{DS} was -0.3 V. The gate voltage of forward scanning (red curves) swept from lower to higher value (-0.4~0.8 V) and the backward scanning mode (black curves) swept the gate voltage from higher to lower value (0.8~-0.4 V). Solid, dashed and dotted lines represent normal rate, fast rate and quiet rate respectively.*

The process of forward scanning is the sweeping of gate voltage from lower to higher voltage, whereas backward scanning refers to the sweeping of gate voltage from higher to lower values. The scanning rates include normal, fast and quiet rates. As shown in figure 5.35, the transfer characteristics of the backward scanning with three different scanning rates show considerable overlap, indicating that the scanning rates in backward scanning will not impact the transfer characteristics of OECTs. The transfer characteristics of the forward scanning with

various scanning rates cause a difference in the drain current. Fast scanning resulted in a lower reduction of the drain current when the forward scanning with gate voltage sweeping from lower to higher value was used. This may be due to the insufficient response time of the device to the changes in gate voltage. The transfer characteristics of quiet and normal scanning rates during the forward scanning overlap, suggesting that these two scanning rates yield nearly identical transfer characteristics for OECTs. Based on the DA detection principle, the electro-oxidation process of DA will lead to electron transfer and a corresponding change in effective gate voltage, which results in changes in the drain current. Therefore, it is essential for the characterization methods to detect these changes promptly and effectively. Forward scanning with normal scanning rate was thus chosen for the following electrochemical characterizations and DA detection.

5.4.3 Transfer characteristics of OECTs for DA detection with different gate electrodes

The effect of different gate electrodes on the transfer characteristics of DA detection was investigated using a Pt electrode and an Ag/AgCl reference electrode. For these transfer characteristics, V_{DS} was kept constant at -0.3 V. For the transfer curve obtained by the Pt electrode, V_{GS} swept from -0.4 V to 0.8 V between source and gate electrodes. V_{GS} sweeps ranging from -0.8 V to 0.4 V were applied to acquire the transfer curve using the Ag/AgCl reference electrode. First, the transfer curve of OECTs was performed in PBS solution, serving as a reference data point to analyze the change of the transfer characteristics in different DA solutions. Subsequently, OECTs were measured in DA solutions with concentrations ranging from low to high (1 nM to 3 mM) to obtain the transfer curves. Figure 5.36 (a) shows the transfer characteristics of OECTs with 108 nm of PEDOT:PSS film using a Pt electrode after applying the PBS and different DA solutions to the chips. Each transfer curve was measured continuously three times. The results exhibit the mean values with small error bars, demonstrating reliable and repeatable measurements. Additionally, every transfer curve shows the depletion-mode of transistor performance. As shown in figure 5.36 (a), increasing DA concentrations results in an evident shift of the curve towards more negative voltages. At the oxidation potential of DA between 0.3 V and 0.4 V, the most significant decrease in the drain current is observed when DA concentrations increase. Due to electro-oxidation of DA occurring at the Pt gate electrode, a Faradic current was generated and thus the effectively applied gate voltage increased, leading to the change in the transfer curves of the OECTs.

Figure 5.36 (b) displays the transfer curves of OECTs based on 108 nm of PEDOT:PSS film with an Ag/AgCl reference electrode after the application of different concentrations of DA solutions. However, the drain current acquired from the PBS solution and DA solutions with different concentrations exhibited minimal change when the Ag/AgCl reference electrode was used as the gate electrode. The results indicate that the Ag/AgCl reference electrode cannot effectively facilitate DA detection. Typically, a gate electrode that can accommodate potential variations is utilized to detect DA concentrations, allowing for the necessary potential changes caused by the electro-oxidation process of the DA solution. An Ag/AgCl reference electrode is unsuitable for the transistors in detecting DA concentrations as it provides a stable gate

voltage when immersed in the solutions, which means the electro-oxidate process of DA concentrations cannot easily be initiated.

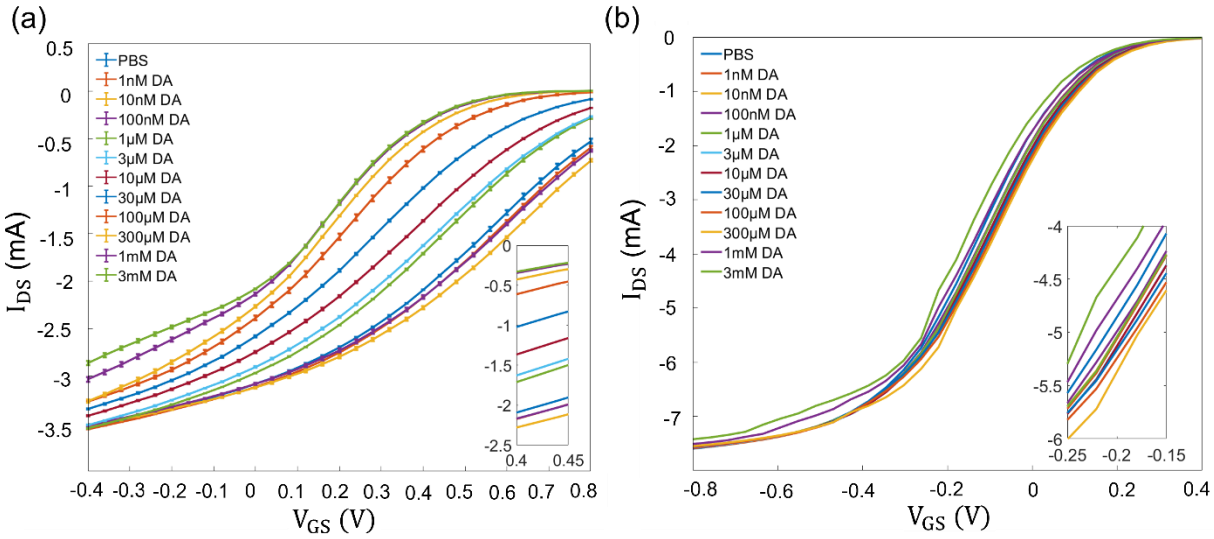

Figure 5.36: *(a) Transfer characteristics of OECTs based on 108 nm of PEDOT:PSS film for DA detection with Pt electrode (n=3), and (b) Ag/AgCl reference electrode when V_{DS} was maintained constant at -0.3 V.*

5.4.4 Effect of the PEDOT:PSS thickness on DA detection

The transfer characteristics were evaluated to investigate the influence of the PEDOT:PSS film thicknesses (108 nm, 78 nm and 45 nm) on the sensitive detection of DA concentrations using the fabricated transistors. A Pt electrode was utilized as the pseudo reference electrode and the concentrations of DA solutions ranged from 1 nM to 100 μM. V_{GS} sweeps ranging from -0.4 V to 0.8 V were applied between the gate and source electrodes, while the V_{DS} kept the constant value of -0.3 V throughout the whole measurement. Figure 5.37 shows the transfer characteristics of the OECTs for detecting the DA concentrations with the PEDOT:PSS film thicknesses of 108 nm (a), 78 nm (b) and 45 nm (c). The transfer curves with each PEDOT:PSS thickness exhibit the depletion-mode of transistor performance, meaning an increase in the positive gate voltage leads to the reduction of the measured drain current. Additionally, for each PEDOT:PSS film thickness, its transfer curves shift towards more negative voltages with the increase of the DA concentrations.

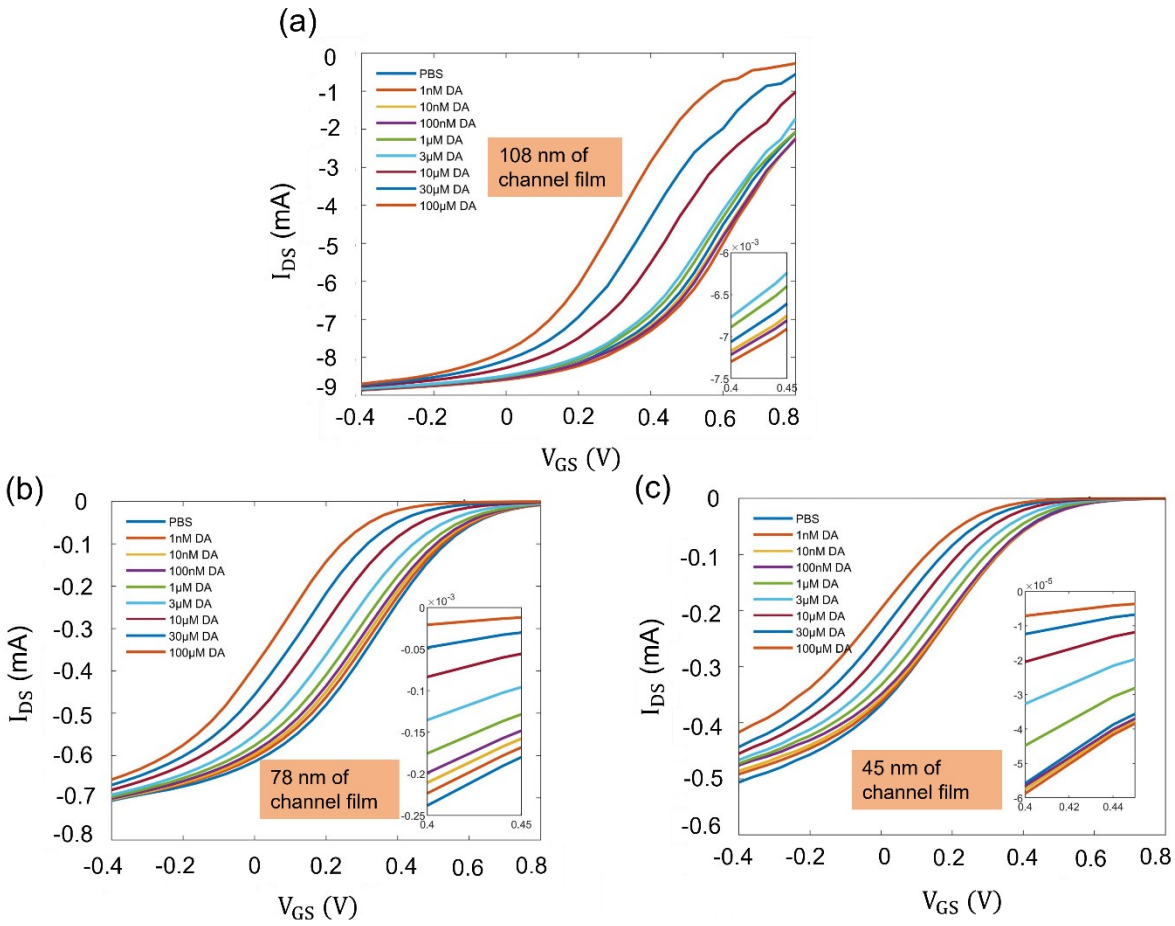

Figure 5.37: *Transfer characteristics of the OECTs for DA detection with PEDOT:PSS film thicknesses of 108 nm (a), 78 nm (b) and 45 nm (c). V_{GS} swept from -0.4 V to 0.8 V and V_{DS} was kept constant at -0.3 V.*

Afterwards, the NCR value of the OECTs with different PEDOT:PSS film thicknesses was calculated and compared based on the transfer curves. Figure 5.38 displays the relationship between NCR and DA concentrations in the logarithmic scale with the range from 1 nM to 100 μM when V_{GS} is 0.4 V and V_{DS} is -0.3 V. The black curve shows the relationship between NCR values and DA concentrations using the transistors based on 108 nm of PEDOT:PSS film. A linear correlation between NCR values and DA concentrations is displayed in the range from 3 μM to 100 μM, exhibiting the sensitivity value of 0.358/log (M). In contrast, the red curve presents the relationship between NCR and DA concentrations using the OECTs with the PEDOT:PSS film thickness of 78 nm. It shows linear fitting when the DA concentrations ranging from 1 μM to 30 μM with the sensitivity of 0.369/log (M). Lastly, the blue curve shows the correlation between NCR and DA concentrations when 45 nm of PEDOT:PSS film was deposited on the OECTs. The NCR changes of the transistors exhibit a linear relationship with the DA concentrations from 1 μM to 30 μM with the sensitivity of 0.424/log (M). As displayed in figure 5.38, the decrease in the PEDOT:PSS film thickness resulted in an increase in the sensitivity of the transistors for DA detection within concentrations ranging from 1 μM to 30 μM. The channel capacitance ($C_{channel}$) decreases with the reduction of PEDOT:PSS film thicknesses. Then, the ratio of gate capacitance (C_{gate}) to channel capacitance ($C_{channel}$)

increases, leading to more efficient gating and better sensitivity of OECTs [200]. As can be seen in figure 5.38, the devices with PEDOT:PSS film thicknesses of 45 nm and 108 nm perform LoD of 100 nM and 3 µM, respectively. Notably, the OECTs deposited with 78 nm of PEDOT:PSS film exhibit LoD as low as 1 nM. A linear relationship between NCR and DA concentrations ranging from 1 nM to 1 µM with the sensitivity value of 0.068/log (M) can also be obtained from these OECTs with 78 nm thickness of PEDOT:PSS film. Therefore, the optimal PEDOT:PSS thickness has been established to be 78 nm for sensitive detection.

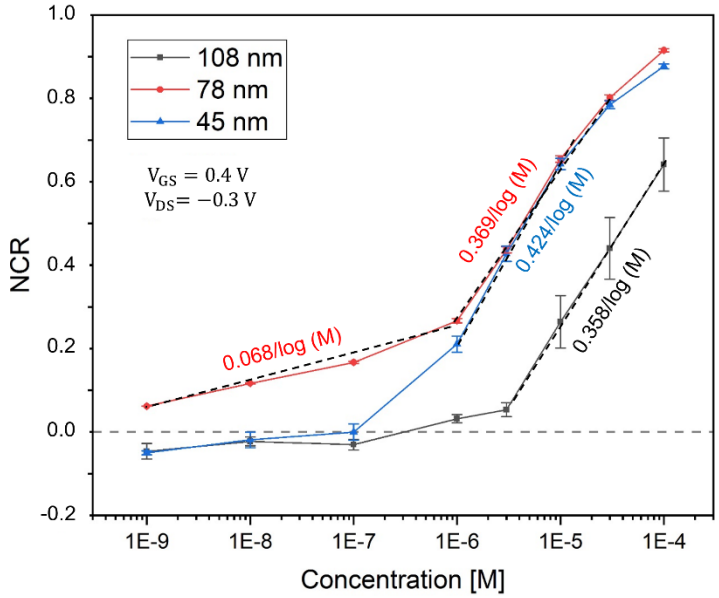

Figure 5.38: *NCR comparison of DA detection using the OECTs with 108, 78 and 45 nm of PEDOT:PSS thicknesses when V_{DS} is -0.3 V and V_{GS} is 0.4 V.*

5.4.5 Transfer characteristics of OECTs for detection of ascorbic acid and uric acid

Transfer characteristics of AA and UA detection using OECTs with 108 nm of PEDOT:PSS film were investigated. The detection was performed using the Keithley 4200 parameter analyzer with a Pt electrode as the pseudo-reference electrode. A voltage range from -0.4 V to 0.8 V was applied between the source and gate electrode, while a constant voltage of -0.3 V was applied between the source and drain electrode. The concentration range for AA detection was from 1 nM to 3mM, while the concentration range from 1 nM to 1 mM was used for UA detection. For each concentration, the OECTs were measured continuously three times to obtain the transfer curve. Figure 5.39 (a) and (b) display the transfer characteristics of the OECTs measured in various concentrations of AA and UA solution, respectively. The transfer curves are given by the mean values with small error bars, indicating the highly repeatable and reliable properties of the measurements. All the transfer curves of AA and UA detection exhibit the depletion-mode of transistor behavior. The transfer characteristics of AA and UA detection present a minimal shift at the voltage between 0.3 V and 0.4 V towards more negative voltages, even with the application of the higher concentrations of solutions. Compared to the transfer curves of DA detection in figure 5.36 (a), the transfer characteristics of OECTs for AA and UA detection display a relatively small shift. The transfer characteristics of OECTs with 78 nm of PEDOT:PSS film for AA and UA detection is shown in figure S5 in

Appendix C, while the transfer curve of OECTs with 45 nm of film thickness for AA and UA detection is displayed in figure S6 in Appendix C.

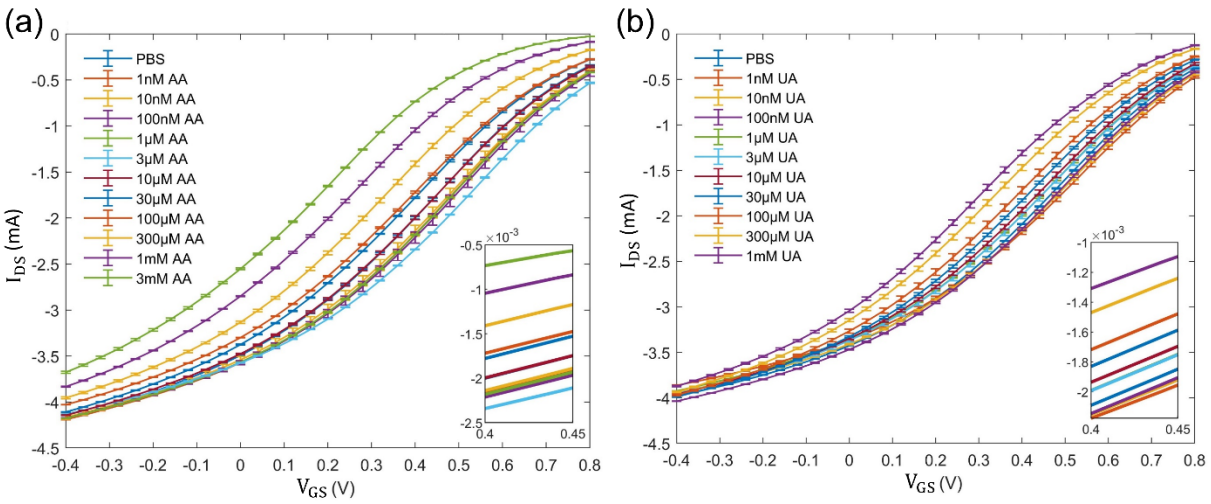

Figure 5.39: *Transfer characteristics of AA (a) and UA (b) detection using OECT with 108 nm of PEDOT:PSS film. V_{GS} swept from -0.4 V to 0.8 V and V_{DS} was kept constant at -0.3 V (n=3).*

5.4.6 Selectivity of OECT microarrays for detection of ascorbic acid and uric acid

After obtaining the transfer characteristics of OECTs with various thicknesses of the PEDOT:PSS film for DA, AA and UA detection, NCR values were calculated and compared for evaluating the selectivity of the devices. Figure 5.40 presents the function of NCR for OECTs with three different PEDOT:PSS film thicknesses, to various concentrations of analyte and to different gate voltages when V_{DS} was kept constant at -0.3 V. The yellow plane represents the NCR value of 0. As shown in figure 5.40 (a), NCR results for OECTs with 108 nm of PEDOT:PSS film exhibit changes for detecting analytes with the concentration range from low to high, especially for detecting DA molecules at the higher gate voltage. Additionally, the transistors with 108 nm of PEDOT:PSS film evidently show a different NCR value for DA detection compared to AA and UA detection at the higher concentration ranges and bigger gate voltages, indicating that these OECTs have highly selective detection for DA molecules compared to AA and UA molecules. However, NCR values of OECTs with 108 nm film for DA detection stay above 0 only at higher concentration ranges, demonstrating that the transistors have a limited ability to detect the DA molecules at lower concentration ranges. Figure 5.40 (b) displays the NCR values of the device with 78 nm of film for detecting the three different analytes. Compared to the NCR values for AA and UA detection, the OECTs for DA detection have much higher NCR values, especially at lower concentration ranges and smaller gate voltages. Figure 5.40 (c) presents the NCR values of the transistors with 45 nm of PEDOT:PSS film for detecting these different analytes. The devices present greater NCR values for DA detection than for AA and UA detection in the lower concentration range and the smaller gate voltage.

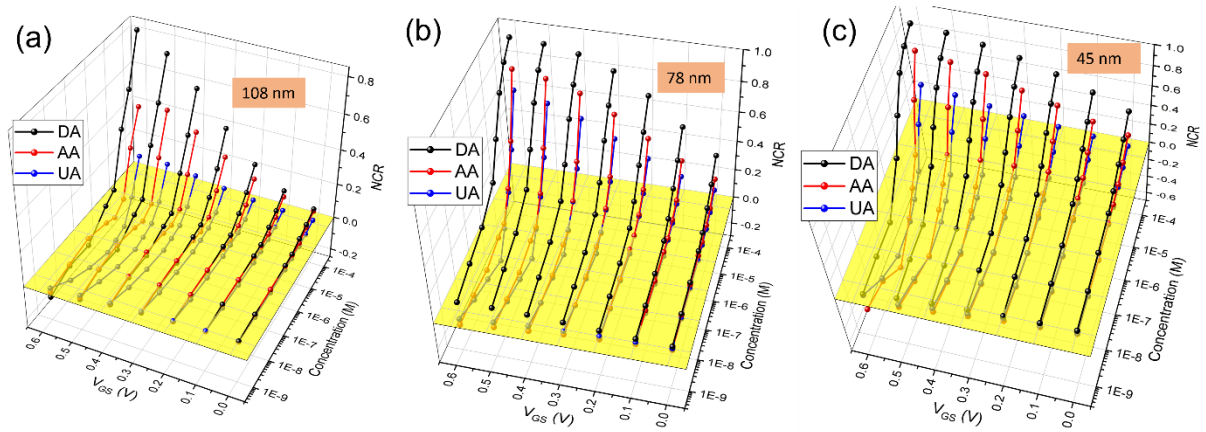

Figure 5.40: *3D diagram of DA, AA and UA detection using the OECTs based on PEDOT:PSS film thicknesses of (a) 108 nm, (b) 78 nm and (c) 45 nm. The results were obtained when V_{DS} was maintained constant at -0.3 V and V_{GS} stayed at 0, 0.1, 0.2, 0.3, 0.4, 0.5, 0.6 V. Yellow plane means the NCR value of 0.*

Figure 5.41 shows the relationship between the NCR values and analyte concentrations for the OECTs with three different thicknesses of PEDOT:PSS film. The NCR values are calculated when V_{GS} is 0.4 V and V_{DS} is -0.3 V. The black curve represents the relationship between NCR and DA concentrations, while the red curve shows the dependence of NCR on AA concentrations. Lastly, the blue curve displays the correlation between NCR and UA concentrations. 108 nm PEDOT:PSS film based OECTs have a LoD of 1 µM for DA detection and limited selectivity against AA and UA from 1 µM to 10 µM. In contrast, The LoD for DA detection using the OECTs with 45 nm PEDOT:PSS film is 100 nM and the concentration range of selective detection is from 100 nm to 10 µM. The transistors with 78 nm of PEDOT:PSS show an excellent LoD of 1 nM for DA detection, and exhibit their selectivity against AA and UA analytes in the concentration range of 1 nm to 10 µM. These results highlight their importance in selective detection of DA analyte at low concentration ranges. Therefore, 78 nm of PEDOT:PSS film was found to be the optimal thickness for the OECTs to selectively detect DA concentrations and maintain a satisfactory LoD.

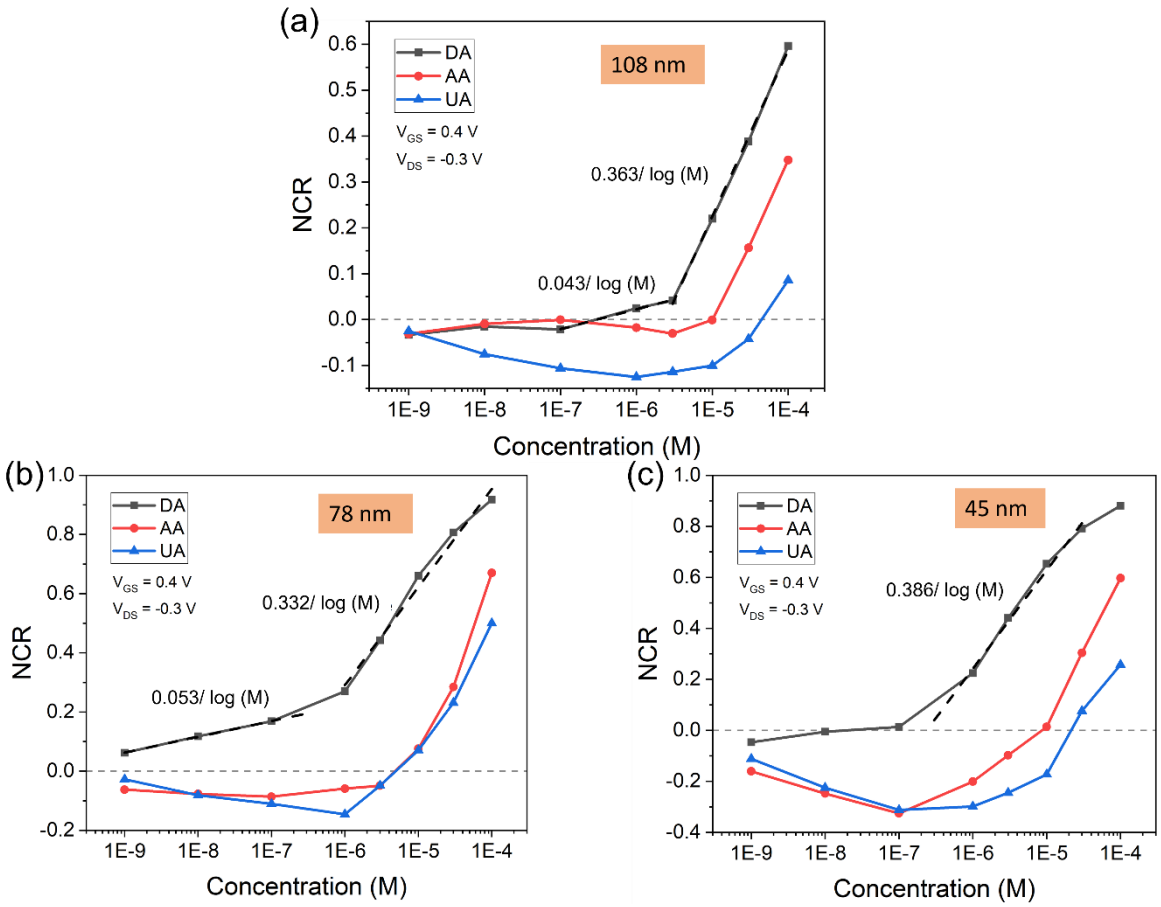

Figure 5.41: *NCR comparison of DA, AA, UA detection by OECTs with 108 nm (a), 78 nm (b) and 45 nm (c) channel thickness calculated at V_{DS} = -0.3 V and V_{GS} = 0.4 V.*

5.4.7 Real-time measurement without a microfluidic system

Real-time measurement is crucial for capturing the dynamic variations of DA concentrations. In the absence of a microfluidic system, real-time measurements were conducted by manually adding solutions with a micropipette and the corresponding drain currents were recorded. The measurement was performed using the Keithley 4200 parameter analyzer, while V_{DS} at a constant value of -0.3 V and V_{GS} at 0.3 V were chosen as the working points. Figure 5.42 (a) shows an image of the partial measurement setup with a time interval of 0.5 seconds. To establish a stable baseline control, 50 µL of PBS solution was first added using a micropipette over a period of 300 seconds. Then, 50 µL of DA solution was added at regular intervals of 200 seconds, starting from lower to higher concentrations (1 nM to 3 mM). This sequential process enabled the systematic evaluation of the response under different DA concentrations. Figure 5.42 (b) presents the result of the real-time measurement, showing the responsive behavior of the OECT after each sequential addition of the solution. The inset shows the drain current change when 1 nM of DA solution was added into the system. After each addition of the solution, a distinct bulge first emerges on the current curve. Then, the current curve will have a sudden drop followed by a rapid rise again. At the end of every 200 second interval, the curve trends to constant. It is assumed that the previously added DA was completely exhausted within 200 seconds. A reduction in the drain current was observed when DA

concentrations increased during the real-time measurement. More DA molecules exist in the DA solutions with higher concentrations, facilitating more DA molecules to be electro-oxidated at the Pt gate electrode and generating more Faradic currents. Thus, a more effective gate voltage was generated, leading to a greater decrease in drain current. Moreover, a significant change in I_{DS} was detected when the DA concentration was 1 nM. These results suggested that the transistors using Pt electrode as a pseudo-reference electrode can be utilized as a highly sensitive sensor for DA detection as low as 1 nM. Due to the rapid change of the obtained current, the influence of the artifact cannot be neglected. The utilization of a microfluidic system provides a strategic approach to avoid some of the effects associated with manual operation.

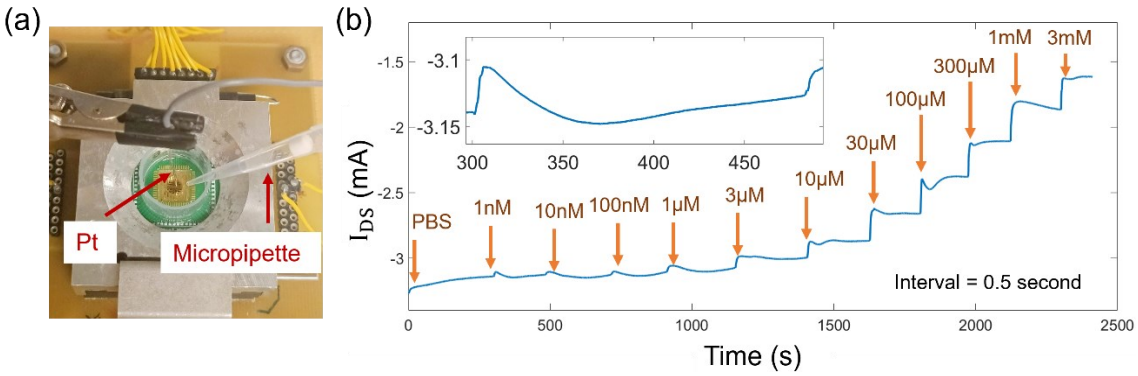

Figure 5.42: *(a) Image of the partial setup for the real-time measurement, (b) Real-time curves of DA detection without microfluidic system using an OECT with 108 nm channel thickness measured at V_{DS} = -0.3 V and V_{GS} = 0.3 V. Drain current was obtained at 0.5 second intervals and the solution was added at 200 second intervals.*

5.4.8 Real-time measurement with a microfluidic system

Real-time measurement with the integration of a microfluidic system is shown in figure 5.43 (a). All the solutions were introduced by using a pump system with a flow rate of 150 µL/min. Additionally, the pump did not stop during the whole measurement. The change in analyte concentration was achieved by changing the inlet pipe to centrifuge tubes containing different solutions. The real-time measurement always began and ended with the introduction of the PBS solution. First, the real-time measurement began with introducing UA solutions from lower to higher concentrations. Then, the measurement for AA detection from lower to higher concentrations was conducted, and finally the measurement for DA detection from lower to higher concentrations was carried out. The characterization was measured on the same channel of an OECT at V_{DS} = -0.3 V and V_{GS} = 0.3 V.

Figure 5.43 (b) presents an evident current change for each molecule detection using the OECTs based on 78 nm of film with a microfluidic system. The blue curve refers to the UA detection with the concentration range from 1 nM to 10 µM, while the red curve represents the detection of AA concentrations ranging from 1 nM to 10 µM. Lastly, the yellow curve shows the drain current change of the transistors for DA detection. As shown in figure 5.43 (b), the drain current value for UA detection does not change significantly during the real-time

measurement, even at the higher UA concentrations. The change in the drain current of OECTs for detecting the AA is more evident only after adding 3 µM concentration of AA solution. The drain currents of the devices for DA detection exhibit a significant change when 3 µM concentrations of DA solution flowed through the microfluidic system. When the PBS solution was introduced again in the microfluidic system at the end of the measurement, the obtained drain curves for DA and AA detection underwent a sudden increase and drop. It is hypothesized that a small volume of the analyte solution might remain within the microfluidic system and initiate electrochemical reactions there. Compared to the results obtained by the transistors without the microfluidic system, the change in the current value was smaller when the real-time measurement was applied to the OECTs with a microfluidic system. There are several reasons for this: first, the volume of analyte solutions within the microfluidic system is decreased, resulting in the decreased quantity of the DA molecules participating in the electro-oxidation reaction. Second, the contact and reaction time between molecules and Pt gate electrode is short as the analyte solutions continuously flow through the electrode and channel. Lastly, the position of the gate electrode may lead to this reduction of current change. In the real-time measurement without the microfluidic system, the Pt gate electrode hung 1-2 mm above the center of the OECTs. In contrast, the Pt gate electrode in the microfluidic system was hung further away from the center of the OECTs at 1 cm above the channel. The latter measurement setup may lead to a weaker electro-oxidation of analyte on the Pt gate electrode and less efficient gating effect of OECTs. Therefore, real-time measurement using the OECTs with the microfluidic system may cause slightly reduced responses in DA, AA and UA detection.

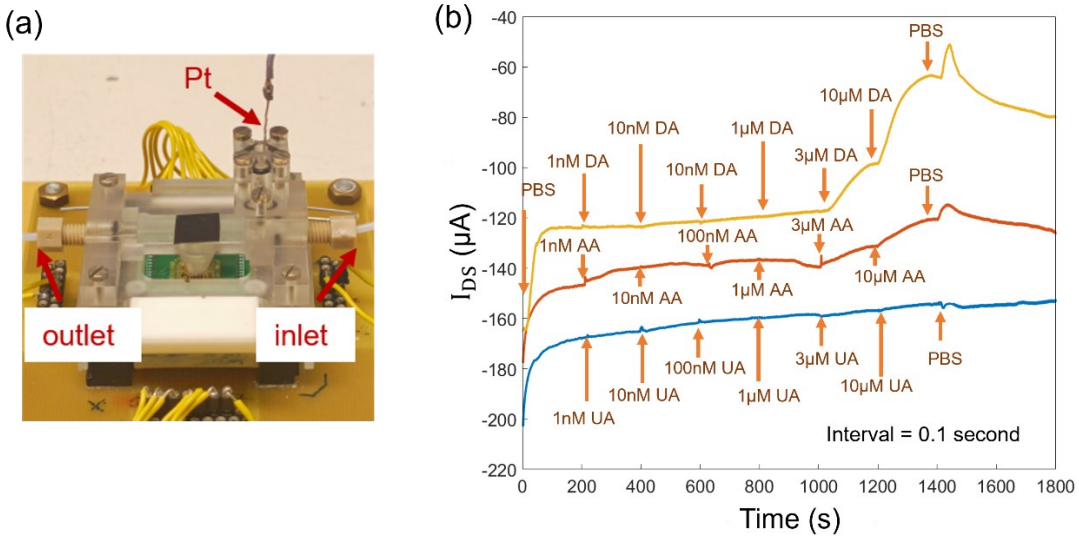

Figure 5.43: *(a) Image of the partial setup for the real-time measurement, (b) Real-time curves of an OECT with 78 nm channel thickness for UA, AA and DA detection with microfluidic system measured at V_{DS} = -0.3 V and V_{GS} = 0.3 V. Drain current was obtained at 0.1 second intervals and the solution was added at 200 second intervals.*

5.4.9 Selectivity improvement by surface modification of the Pt gate electrode

Figure 5.44 shows the experimental procedure for modifying the surface of the Pt gate electrode. First, the chitosan solution was prepared using the experimental protocol which is described in section 4.5.1. The Pt electrode was then submerged into the chitosan solution for

30 seconds to obtain a homogenous coating on its surface. Finally, the Pt electrode coated with chitosan was air-dried at room temperature for 24 hours.

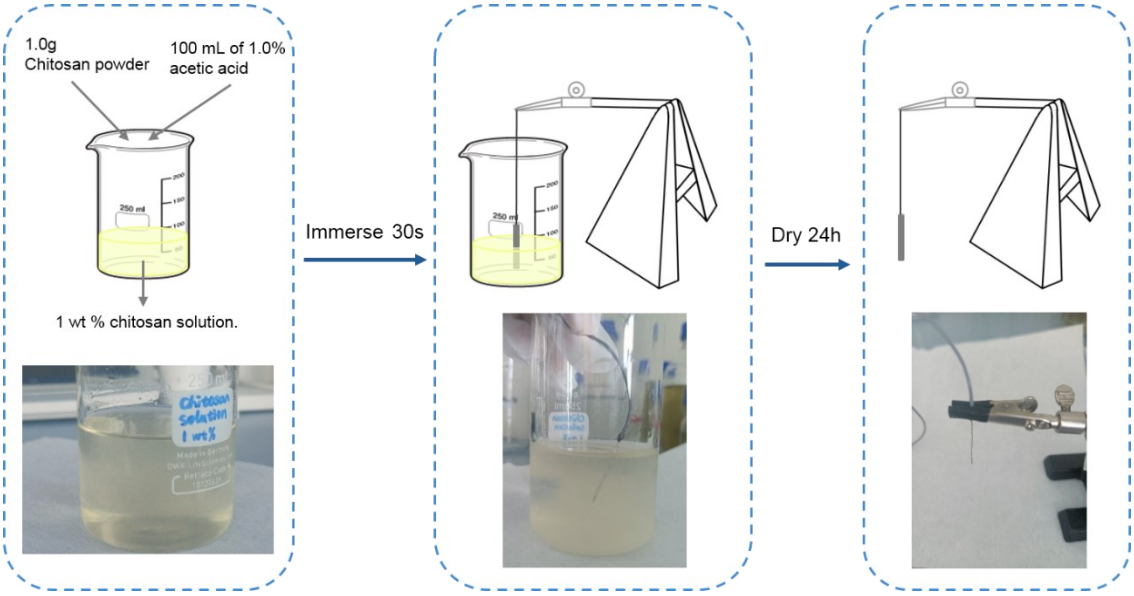

Figure 5.44: *Chitosan modification process on the surface of the Pt gate electrode.*

After the modification on the surface of the Pt gate electrode with 1.0 wt% chitosan solution, the transfer characteristics of the OECTs based on 78 nm of PEDOT:PSS film for detecting three different analytes were evaluated. Likewise, all the transfer curves exhibited the depletion-mode performance, while the transfer characteristics at gate voltage between 0.3 V and 0.4 V shifted towards the negative voltage. Following that, the NCR values were calculated and compared at the V_{GS} of 0.4 V and V_{DS} of -0.3 V, which is depicted in figure 5.45. The black curve presents the correlation between NCR and DA concentrations, while the red curve displays the correlation between NCR and AA concentrations. The blue curve presents the relationship between NCR and UA concentrations. Compared to the NCR curve (black curve in figure 5.41 (b)) obtained using the OECTs with pure Pt gate electrode, the transistors maintained the LoD for detecting DA concentrations as low as 1 nM after modifying the surface of the Pt gate electrode. More importantly, the selective detection of DA molecules over AA and UA molecules in higher concentrations ranging from 10 µM to 100 µM was significantly improved after the surface modification of the Pt electrode with chitosan. In a PBS solution with pH value of 7.4, a chitosan layer usually has the pK_a of 6.4 and exhibits an anionic state, while AA molecules with pK_a of 4.2 and UA molecules with pK_a of 5.4 are negatively charged. Therefore, there was electrostatic repulsion between the AA/UA and chitosan layer, preventing the diffusion of AA/UA through the chitosan layer to the Pt gate electrode [177]. These electrostatic effects may lead to improved selectivity for OECTs to detect DA molecules over AA and UA molecules.

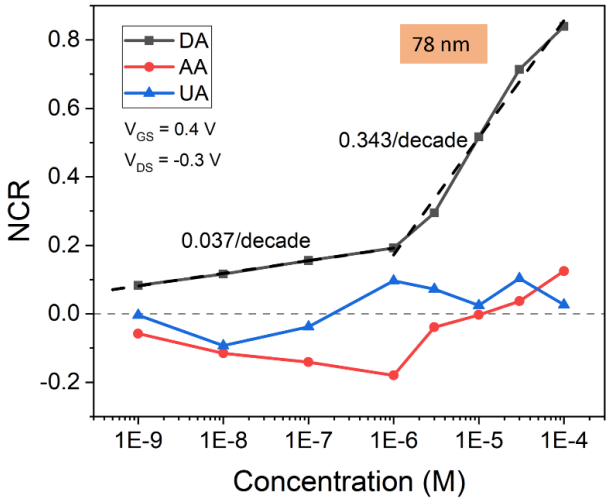

Figure 5.45: *NCR comparison of DA, AA, UA detection using an OECT with 78 nm of PEDOT:PSS film after the surface modification of Pt gate electrode. The data was obtained at V_{DS} of -0.3 V and V_{GS} of 0.4 V.*

5.5 Ion-selective textile sensors realized with PEDOT:PSS for ion detection

5.5.1 Microscopic characteristics of textile sensors integrated with ISMs

As shown in figure 5.46 (a), a microscopic examination of the structure of cotton yarn was conducted before immersing it in the PEDOT:PSS solution. The cotton yarn consists of textile fibers and maintains a uniform diameter of 0.6 mm. Figure 5.46 (b) presents a microscope image of the cotton yarn integrated with PEDOT:PSS. After submerging in the PEDOT:PSS solution for 4 seconds, the cotton yarn displays a homogenous dark blue color. This change in coloration is clear and can be attributed to the uniform integration of the PEDOT:PSS into the yarn.

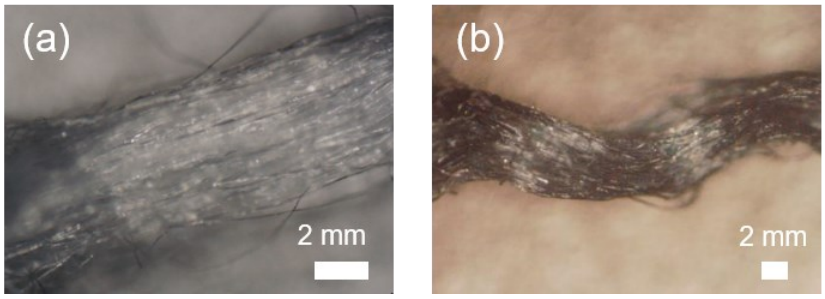

Figure 5.46: *Microscope image of the cotton yarn before (a) and after (b) coating with PEDOT:PSS solution for 4 seconds.*

Na^+ and K^+ ISMs were integrated into the PEDOT:PSS coated yarn for fabricating the ISM based textile sensors to detect Na^+ and K^+ ions, respectively. As can be seen in figure 5.47 (a), the cotton yarn integrated with PEDOT:PSS is roughly 10 mm long and the two ends of the yarn and the metal wires were connected together using silver glue. To provide effective insulation in the buffer solutions for the connection points between the cotton yarn and the metal wire, these two connection points were completely covered by the silicon adhesive. This configuration ensures that the textile sensors will function in a reliable and stable manner for the electrical characterization, electrochemical characterization and ion detection.

The sensors were integrated with the ISMs by submerging the PEDOT:PSS coated cotton yarn into the membrane solution for 10 seconds and then air-drying it at room temperature. As depicted in figure 5.47 (b), a textile sensor was integrated with a membrane for detecting K^+ ions. Due to the incorporation of yellow-colored K^+ ISM solution, the resulting cotton yarn displays a uniform and distinctive yellow color. Likewise, the textile sensors covered with Na^+ ISMs were manufactured using this experimental procedure. These two images shown in figure 5.47 highlight that the fabrication process integrating textile sensors with ISMs is straightforward and easily reproducible.

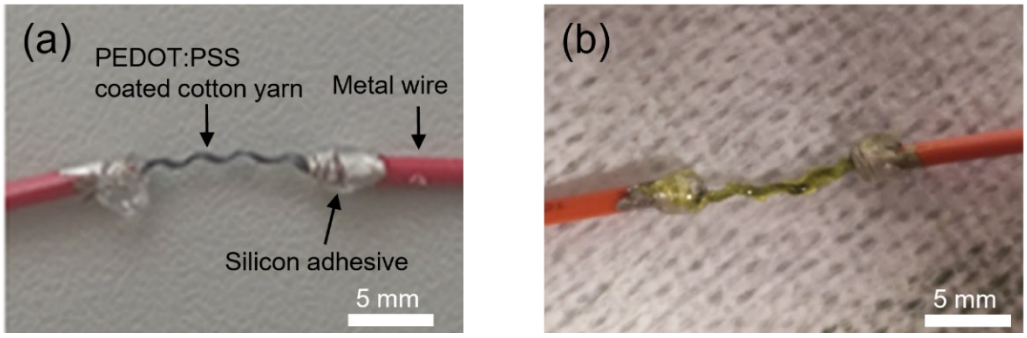

Figure 5.47: *Images of textile sensor before (a) and after (b) integrating with K^+ ion selective membrane.*

5.5.2 Electrical characteristics of the PEDOT:PSS based textile sensors

The electrical characteristics for the fabricated textile sensors in air were investigated. The IV characteristics of the prepared textile sensors were evaluated utilizing the voltage sweep from -0.1 V to 0.1 V. As shown in figure 5.48 (a), the IV characteristic curves of the textile sensors are linear, and the resistance of each sensor can be extracted. Figure 5.48 (b) displays the resistance of the textile sensors using the cotton yarn coated with PEDOT:PSS for durations of time ranging from 2 seconds to 12 seconds. For each different immersion time, three textile sensors were manufactured and utilized to obtain the resistance. The mean values and small error bars are displayed in figure 5.48 (b), indicating that the manufacture process for the textile sensors is highly reproducible. Additionally, the results present that an increase in the immersion time leads to a decrease in the resistance of these textile sensors. An exponential relationship is also exhibited between the immersion time and the reduction of resistance. A combination of the liquid diffusion [201] and wetting effect [202, 203] theories can be used to explain this relationship.

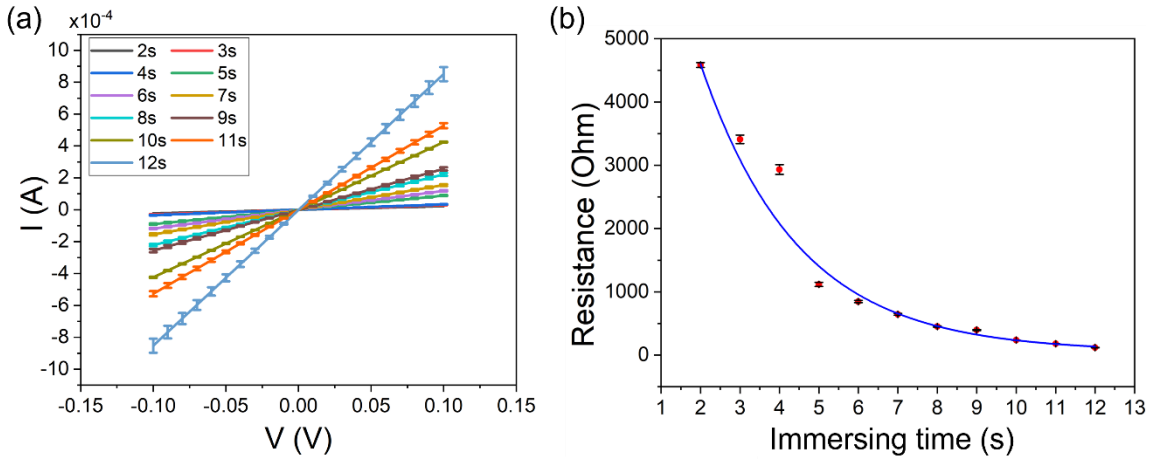

Figure 5.48: *(a) IV characteristics of the textile sensors fabricated by immersing in PEDOT:PSS solution for different times ranging from 2 seconds to 12 seconds (n=3), (b) Resistance of textile sensors with different immersion times in PEDOT:PSS solution (n=3).*

5.5.3 Electrochemical characteristics of the PEDOT:PSS based textile sensors

The electrochemical characteristics of the textile sensors were investigated by analyzing the resistance changes in the Na^+ buffer solutions with various concentrations (1 mM, 5 mM, 10 mM and 50 mM). Three textile sensors were prepared and utilized for the measurement in each buffer solution. The IV characteristics of the textile sensors were measured in DI water, serving as a reference data point to analyze the resistance change in the different buffer solutions. Following this, the textile sensors were immersed in Na^+ buffer solutions with pH of 7 and concentrations ranging from low to high (1 mM to 50 mM). The measurements of each IV curve were carried out after submerging the textile sensors in each buffer solution for 10 seconds.

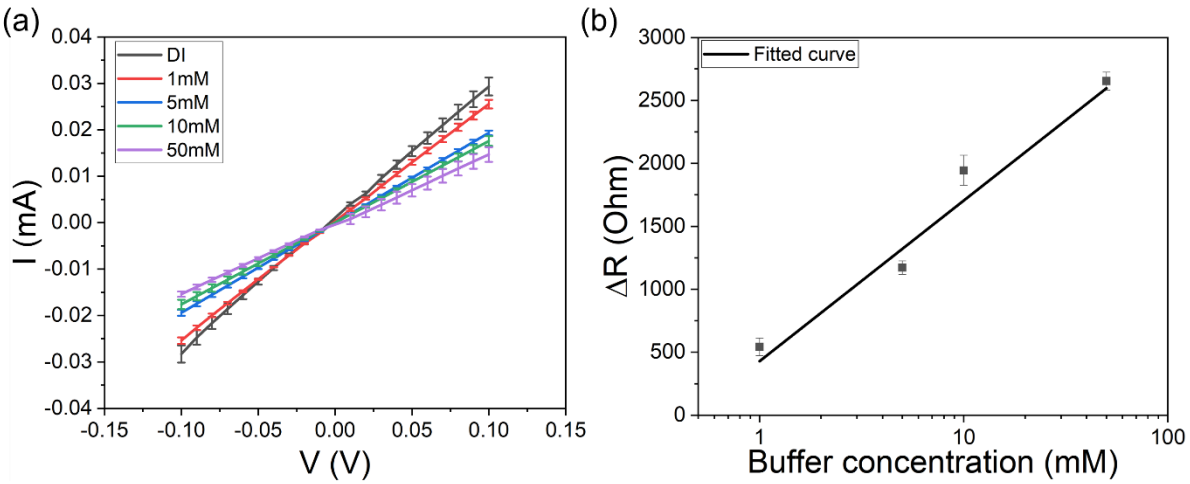

Figure 5.49: *After fabricating the textile sensors using an immersion time of 4 seconds in PEDOT:PSS solution, IV curves (a) of the textile sensors when submerged in Na^+ buffer solution with different concentrations (n=3) and resistance change (ΔR) (b) of these textile sensors was calculated when varied buffer solutions were applied (n=3).*

Figure 5.49 (a) displays the IV characteristics of the textile sensors after coating with PEDOT:PSS with an immersion time of 4 seconds and each IV curve displays linear behavior. The mean values and a minimal error bar appear in each curve, indicating a high repeatability and reproducibility of the measurement. Figure 5.49 (b) presents the calculated resistance change (ΔR) of the textile sensors which were manufactured with immersion time of 4 seconds in the PEDOT:PSS solution. The formula for the calculation is $\Delta R = R - R_0$, where R and R_0 were the resistance values obtained in the buffer solutions and DI water, respectively. Based on the electrochemical properties of the PEDOT:PSS, increasing the buffer concentrations results in an increase in the resistance. Furthermore, a linear relationship is displayed between the resistance changes and the buffer concentrations on a logarithmic scale within the measured concentration range. When the textile sensors were immersed in the buffer solution, the diffusion of the cations into the PEDOT:PSS coated cotton yarn led to the de-doping process of the PEDOT:PSS, according to equation (5.2). This process results in a decrease in available charge carriers in PEDOT, leading to a reduction in the electrical conductivity of the PEDOT:PSS and an increase in the resistance of the textile sensors. Therefore, the electrochemical characteristics of the PEDOT:PSS textile sensors provide evidence that they can function as electrochemical sensors.

5.5.4 Stability and flexibility of the textile sensors

The long-term stability of the fabricated textile sensors was tested by measuring the resistance on consecutive days after the fabrication was completed (Day 0). On Day 1, the IV characteristics of the textile sensors in air were evaluated and their resistance was extracted. Subsequently, these textile sensors were left to air-dry until the end of Day 5. Following this, the resistance of the textile sensors was measured daily from Day 1 to Day 5 and compared with the resistance measured on Day 0. Three textile sensors were measured and the average resistance with small error bars was displayed for each data point. Figure 5.50 (a) presents the long-term stability of the textile sensors which were prepared by immersing the cotton yarn in PEDOT:PSS solution for 2 seconds (black curve), 3 seconds (red curve) and 4 seconds (blue curve). All the curves exhibit constant resistance values with negligible fluctuations during the measurement period. The results indicate that these textile sensors remain stable in the air for 5 days.

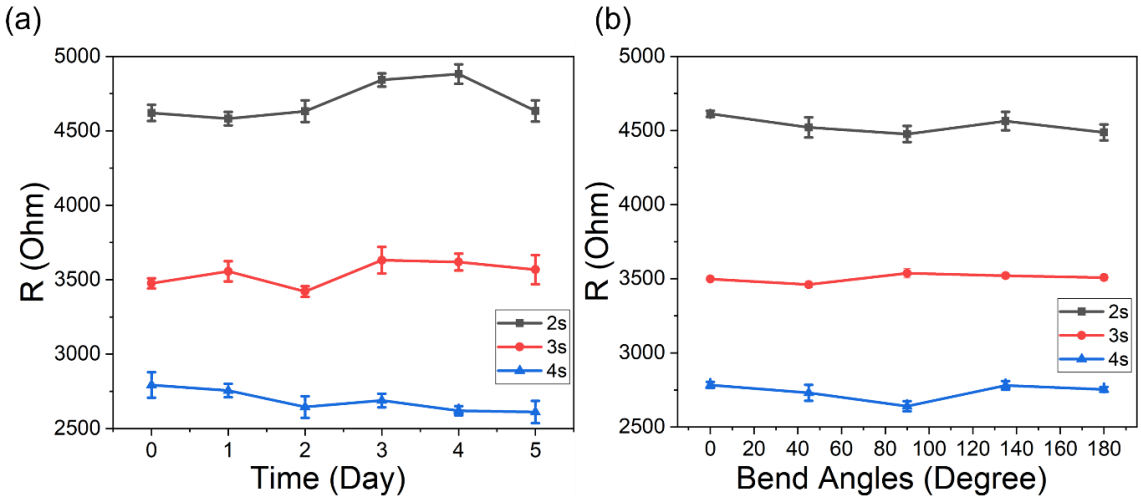

Figure 5.50: *(a) Resistance of the textile sensors on different days with 2 seconds (black), 3 seconds (red) and 4 seconds (blue) of immersion time (n=3), (b) Resistance of textile sensors bent at various angles with different immersion times (n=3).*

Furthermore, the flexibility of the textile sensors in the air was assessed by evaluating the resistance changes when they were bent at 5 different angles (0°, 45°, 90°, 135° and 180°). At each angle, the resistance value of the textile sensors was measured three times. For each data point, an average resistance with a minimal error bar was obtained. Figure 5.50 (b) presents the flexibility of the textile sensors when the cotton yarn was submerged in PEDOT:PSS solution for 2 seconds (black curve), 3 seconds (red curve) and 4 seconds (blue curve). The resistance values of these textile sensors were remarkably stable when undergoing various degrees of bending. These observed results are consistent, proving that the PEDOT:PSS coating on the cotton yarn retained its intact structure despite being bent at distinct angles, indicating the robust performance of these textile sensors and demonstrating their potential in flexible and wearable applications.

5.5.5 Ion detection using the textile sensors

Na^+ ISMs and K^+ ISMs were integrated into the textile sensors to facilitate ion detection. The schematic of the measurement process for detecting the ions using ISMs based textile sensors is shown in figure 5.51 (a). ISMs based textile sensor was connected to the Keithley 4200 parameter analyzer to perform IV characterization while the sensor was immersed in different solutions.

After immersing the ISMs based textile sensors in the solution for 10 seconds, a voltage ranging from -0.1 V to 0.1 V was applied to the measurement setup to obtain the resistance value. Firstly, the IV curve of the ISM-based textile sensors was obtained in DI water, and the resistance was calculated. This resistance value served as a reference data point to analyze the change in resistance of the textile sensors when measured in various buffer solutions (1 mM, 5 mM, 10 mM and 50 mM). Following this, the resistance of the textile sensors integrated with ISMs was measured and calculated after submerging them in the buffer solutions (pH = 7) with concentrations ranging from low to high (1 mM to 50 mM).

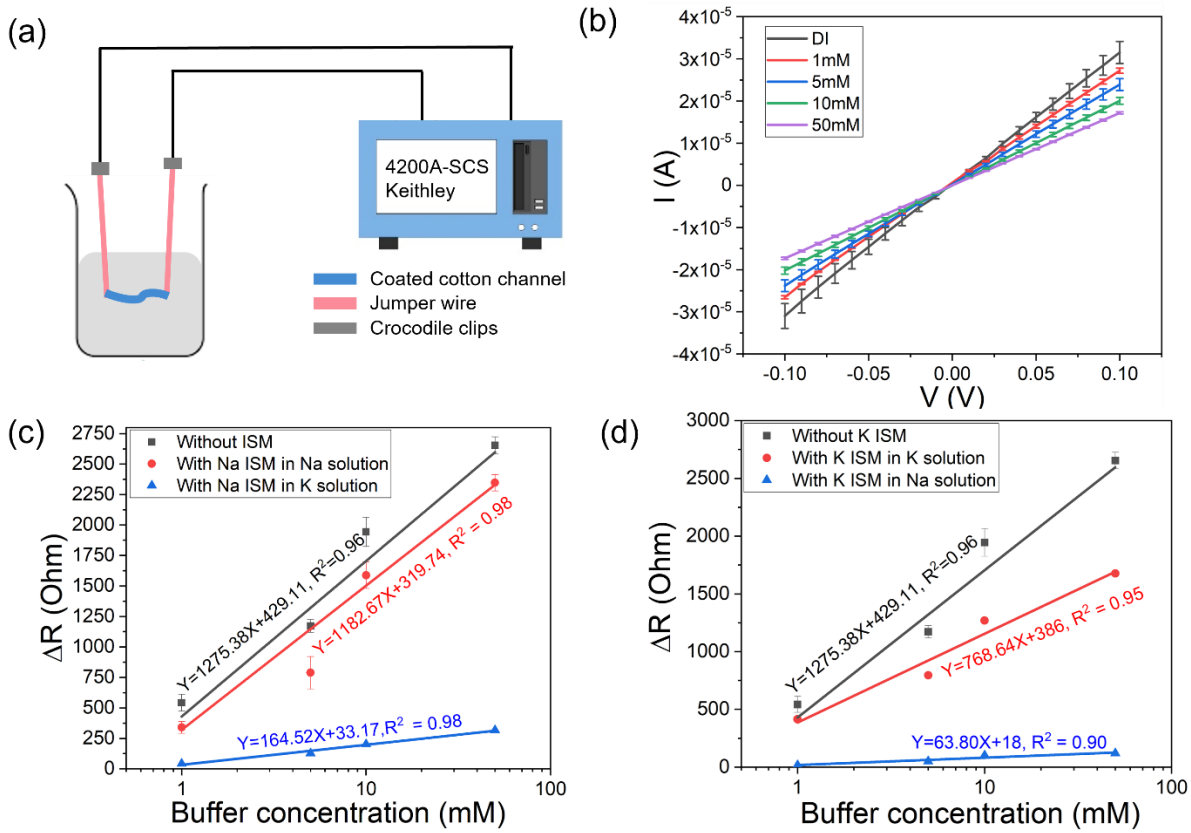

Figure 5.51: *(a) Schematic of the measurement procedure for ion detection using ISM-based textile sensors, (b) IV characterization for detecting the Na^+ ions in various Na^+ buffer solutions using the Na^+ ISM based textile sensor with 4 seconds of immersion time (n=3), (c) Resistance change of Na^+ ISM textile sensor and (d) K^+ ISM textile sensor in different buffer solutions.*

The IV characteristics of the Na^+ ISM textile sensors were obtained when the sensors were immersed in different Na^+ buffer solutions for 10 seconds, as shown in figure 5.51 (b). The IV characteristics were measured three times for each buffer solution, and a linear relationship between the current and voltage with minimal error bars (n=3) is displayed in all IV curves. Figure 5.51 (c) presents the ability of the Na^+ ISM textile sensors for ion detection. First, the IV characteristics were acquired in different buffer solutions using the measurement procedure shown in figure 5.51 (a), and the change in the resistance was then extracted from the IV curve. The black curve shows the change in the resistance of textile sensors without ISMs which were submerged in Na^+ buffer solutions with different concentrations. In contrast, when submerging the Na^+ ISM textile sensors in varying concentrations of Na^+ buffer solutions, the resistance changes of these sensors are displayed with the red curve. Lastly, the blue curve represents the change in the resistance of the Na^+ ISM textile sensors immersed in the K^+ buffer solutions with different concentrations. Furthermore, the sensitivity of the red curve in figure 5.51 (c) is as high as 1182.67 Ohm/log (mM) for the detection of the Na^+ ions within the concentration range from 1 mM to 50 mM. Compared to the textile sensors without ISMs, the Na^+ ISM textile sensors still exhibit a high sensitivity for detecting the Na^+ ions. The results demonstrate that a significant amount of the Na^+ ions permeate through the Na^+ ISM into the PEDOT:PSS, although the cotton yarn of the textile sensors was covered with the Na^+ ISM.

Therefore, the electrical conductivity of the PEDOT:PSS changed, resulting in resistance change in the textile sensors. Moreover, the resistance of the Na^+ ISM textile sensors displayed a minimal change when they were submerged in K^+ buffer solutions with various concentrations. This result proved that the textile sensors integrated with Na^+ ISM have a high selectivity against K^+ ions.

Figure 5.51 (d) presents the resistance change obtained from the IV curve, indicating the detection of ions using the K^+ ISM based textile sensors. When submerged in K^+ buffer solutions with varying concentrations, K^+ ISM textile sensors exhibited the resistance change and the result is presented by the red curve. Likewise, these K^+ ISM textile sensors had high sensitivity of 768.64 Ohm/log (mM) towards the detection of K^+ ions within the concentration range of 1 mM to 50 mM. Additionally, the blue curve displays the change in the resistance of K^+ ISM textile sensors when submerged in Na^+ buffer solutions with various concentrations. K^+ ISM textile sensors displayed a small resistance change when Na^+ buffer solutions were applied, indicating their high selectivity against the detection of the Na^+ ions. All the results in figure 5.51 provide evidence that PEDOT:PSS based textile sensors with integrated ISMs can be utilized to detect desired ions with high sensitivity, while also maintaining high selectivity against undesired ions.

6 Conclusion

Over the past few decades, chemical sensors and biosensors have been extensively explored and developed for application in a wide range of fields such as environment monitoring, food quality control and healthcare monitoring. With the rapid progress in interdisciplinary research, technology and materials science, the future of chemical sensors and biosensors appears to be promising. Since its first ever reported successful synthesis, PEDOT:PSS has displayed outstanding benefits such as flexibility, biocompatibility, high conductivity, optical transparency and ease of fabrication. Therefore, it has been widely studied and utilized in various applications, particularly in the fields of chemical sensors and biosensors. PEDOT:PSS has also been commonly utilized in OECTs as a channel material where the electrical conductivity can be changed through the doping or de-doping process. However, despite the widespread use of PEDOT:PSS, there is an increasing need for further research to enhance the functionality and performance of such OECTs. This thesis has two main objectives: the first is to improve the reliability and stability of the PEDOT:PSS OECTs and to enhance their electrochemical performance for chemical and biosensing applications. The second objective is to develop highly sensitive and selective sensors for ion and DA detection for utilization in sweat and environment monitoring. To achieve these goals, the following tasks were carried out and several key findings were discovered:

The microscale PEDOT:PSS OECTs at wafer scale were successfully fabricated using reliable, reproducible, optimized and high-throughput microfabrication techniques in the clean room, including lithography, lift-off and RIE processes. Using an optimized PECVD process, a 300 nm silicon oxide layer was successfully deposited as a passivation layer on the contact lines to achieve stable and reliable operation in the solution. The thickness of the PEDOT:PSS film was adjusted to 30 nm by controlling the spin-coating and subsequent lift-off processes. Compared to the pristine PEDOT:PSS film, the electrical conductivity of the PEDOT:PSS/EG/GOPS film, created by optimizing the pristine solution with EG and GOPS, increased tenfold. The established wire-bonding and encapsulation protocols have been proved to be reliable in facilitating the OECTs to operate in various liquid solutions. Among five different contact materials (Au, Pt, TiN, ITO and IrO_x), IrO_x was found to have the lowest contact resistance with PEDOT:PSS film on the IDEs. All these fabricated OECTs exhibited typical p-type depletion-mode performance. The transistor was in the “ON” state at the zero-gate voltage and the current response decreased with the increase of positive gate voltage. The achievement of the reliable electrical characteristics in the liquid solution demonstrated the reliable and successful microfabrication process. With the integration of the fabricated microfluidic system, these OECTs were facilitated for the real-time and multiplexed detection of analytes.

Since PEDOT:PSS OECTs are sensitive to the ionic strength in buffer solutions, the establishment and optimization of the detection of specific ions with high sensitivity and selectivity is challenging. The ion detection was achieved by directly integrating ISMs onto PEDOT:PSS channels using the spin-coating technique. The minimal variation in resistance

values between source and drain electrodes on the OECTs during the integration process can be disregarded, indicating that this direct integration of ISM on OECTs was reliable. Two different methods were utilized to optimize the thicknesses of ISMs: adjusting the spin-coating rotational speeds and controlling the compositions of the membrane solutions. Moreover, the results indicated that a reduction in membrane thickness led to an increase in sensitivity and a decrease in selectivity for detecting the ion concentrations. Therefore, the optimal membrane thickness of 600 nm was found to have high sensitivity towards the desired ions while maintaining a good selectivity against the undesired ions. Integrating with the microfluidic system, the OECTs enabled the multiplexed, reversible and real-time detection for Na^+ and K^+ ions in an applicable concentration range from 1 to 100 mM in different electrolytes.

In addition to the wafer-scale fabrication, a simple fabrication method integrating PEDOT:PSS into cotton yarn to be used as textile sensors for ion detection was successfully developed. This fabrication technique shows the possibility of producing large quantities of textile sensors. The electrochemical characterization proved that the resistance changes in the textile sensors were achieved by ion diffusion into the PEDOT:PSS, even without a third electrode as was required in the OECTs. These fabricated textile sensors maintained their stability over 5 days and exhibited excellent flexibility. After the integration of Na^+ or K^+ ISMs, the textile sensors were able to detect the desired ion concentration range of 1 mM to 50 mM with high sensitivity, while maintaining highly selective detection against undesired ions. This proof-of-concept emphasized the potential of using a two-terminal electrode configuration for the achievement of the electrical response and ion detection. Furthermore, this sensor configuration also simplifies the read-out process for the sensors.

Due to the low concentration of DA and the high concentration of interference, the detection of DA with high sensitivity and selectivity is challenging. The detection principle for DA molecules was explored using an OECT microarray in combination with a Pt gate electrode. After conducting the CV characterization with the same Pt electrode, the electro-oxidation peak for DA detection within the voltage range between 0.2 V and 0.4 V was achieved, however the detection limit could only reach 1 µM. Due to its high amplification property, PEDOT:PSS-based OECTs exhibited remarkable capabilities in detecting varied DA concentrations. The results demonstrated that an increase in DA concentration led to a shift of the transfer curve at the oxidation potential of DA towards more negative voltages. The electrochemical reaction occurred at the Pt electrode and the effective gate voltage increased, resulting in the decrease of drain current and the changes in the electrical characterization of the OECTs. The real-time measurement of DA concentrations through the signal readouts from the OECT realized DA detection as low as 1 nM, which established a platform for rapid and non-invasive DA monitoring. Furthermore, the reduction of the PEDOT:PSS film thicknesses resulted in an enhanced sensitivity within the range of 1 µM to 30 µM. The channel capacitance ($C_{channel}$) decreased as the thickness of the PEDOT:PSS films decreased. As a result, the ratio of gate capacitance (C_{gate}) to channel capacitance ($C_{channel}$) increased, leading to more efficient gating and better sensitivity of the OECTs. The study explored the detection

of interferents such as UA and AA using identical experimental protocols. The results demonstrated that PEDOT:PSS OECT microarrays exhibited good selectivity against AA and UA in the concentration range of 1 nM to 10 μM. Subsequent modifications to the surface of the Pt electrode with chitosan achieved an improved selective detection of DA over AA and UA at the concentration range of 10 μM to 100 μM. In PBS solutions, the negatively charged AA and UA molecules were prevented from diffusing onto the Pt electrode due to the electrostatic repulsion between AA/UA and the anionic state of the chitosan layer.

In this dissertation, PEDOT:PSS OECTs with reliable properties and enhanced electrical characteristics have been achieved using the developed microfabrication process. Additionally, PEDOT:PSS coated cotton yarn has been utilized as sensitive textile sensors for ion detection within an applicable concentration range. After successfully integrating the optimal ISMs on the transistor, detection for different ions with high sensitivity and selectivity has been realized. Multiplexed, real-time and reversible detection for ions in different electrolytes has been achieved using the fabricated microfluidic system. A novel platform by combining the OECTs with a Pt gate electrode for DA detection has been developed, and this combination shows high sensitivity to DA while maintaining good selectivity against AA and UA. This developed sensor platform offers much potential to be applied in various fields such as environmental monitoring, modern healthcare, clinical diagnostics, and flexible and wearable electronics.

7 Outlook

Firstly, further research could be undertaken to optimize the ISM composition of ionophores and ion exchangers for ion detection using the fabricated PEDOT:PSS OECT microarrays. Secondly, other types of ISMs such as Ca^{2+} and NH^{4+} for detecting different ions should be explored. These OECTs can be utilized to monitor the varied ions in complex liquid solutions such as tap water and rain. Furthermore, there is the possibility of conducting further research into the integration of OECTs with advanced microfluidic technologies and other flexible substrates, which could result in the development of portable sensors for a wide range of chemical and biosensing applications.

In this thesis, the PEDOT:PSS OECTs achieved DA detection with high sensitivity while maintaining good selectivity against UA and AA. Nevertheless, additional research can be carried out to enhance their sensitivity and selectivity. The thickness of PEDOT:PSS film can be further optimized to study their influence on the sensitive and selective detection of DA concentrations. For example, the mixture ratio between PEDOT:PSS solution and DI water can be expanded, producing a greater range of film thicknesses on the OECTs to be investigated. Subsequently, further attention can be given to optimizing the dimensions of the gate electrode and the distance between it and the channel to increase sensitivity for accurate detection. The selective detection of PEDOT:PSS OECTs of other interfering molecules such as tyramine and tryptamine can be tested. This novel detection platform can be redesigned into a planar configuration, in which an external gate electrode is not needed. Real-time monitoring for DA detection can be performed by the combination of OECTs with wireless communication or powerful smart data analysis techniques, thus expanding their applications as portable sensors. Furthermore, the multiplexed detection of various analytes simultaneously can be further developed by modifying the channel or the gate electrode, providing the potential capability to access a range of biological information using a single platform. This novel transistor configuration exhibits great potential in the development of wearable and flexible OECTs for DA detection. First, to withstand stretching and bending situations, the glass substrate needs to be replaced with other materials which contain highly flexible and durable properties. Next, the PEDOT:PSS OECTs need to be further tested in more complicated physiological and pathological environments to ensure their high sensitivity and selectivity for DA detection remains, to guarantee the reliability and performance of these transistors in real-world situations. These micro-scaled OECTs based on PEDOT:PSS have the potential to be used in a variety of applications, such as neurological research, diagnostic tools and in vivo real-time monitoring of diseases.

In this thesis, the ISMs were successfully integrated into the PEDOT:PSS coated cotton yarn as textile sensors for detection of various ions. In the future, the fabrication method for ISM textile sensors could be improved by immersing them in membrane solutions for varying times, ensuring more precise control over the fabrication parameters. Moreover, further optimization of the ISMs can be conducted and studied to improve the sensitivity and selectivity of ion detection, starting with the adjustment of the membrane compositions and thicknesses.

Likewise, other types of ISMs can be integrated into the textile sensors for detecting a great range of ions including Ca^{2+} ions and Cl^- ions. The whole textile-based sensor platform can be utilized as wearable and flexible sensors. However, several aspects should be considered: first, it must be possible for any alternative materials used for the textile sensor to be easily integrated into smart electric textile (e-textile) by using weaving or sewing processes. Second, it is essential to investigate the textile sensors in complicated environments with varying temperatures, stress and humidity to ensure stable and reliable transistor performance in these situations. Third, it is crucial to put effort into enhancing the inherent properties of the textile sensors. For example, their flexibility must accommodate all body movements, while their electrical and electrochemical stability should withstand multiple washing cycles. Ultimately, these textile sensors have demonstrated their potential for applications in a variety of fields in the near future, including environmental sensing, sweat monitoring and the development of smart clothing.

References

1. Banica, F.G., *Chemical sensors and biosensors: fundamentals and applications*. 2012: John Wiley & Sons.
2. Taylor, R.F. and Schultz, J.S., *Handbook of chemical and biological sensors*. 1996: CRC Press.
3. Spichiger-Keller, U.E., *Chemical sensors and biosensors for medical and biological applications*. 2008: John Wiley & Sons.
4. Göpel, W., et al., *Sensors, chemical and biochemical sensors*. Vol. 2. 2008: John Wiley & Sons.
5. Chen, X., Yao, C., and Li, Z., *Microarray-based chemical sensors and biosensors: Fundamentals and food safety applications.* TrAC Trends in Analytical Chemistry, 2023. **158**: p. 116785.
6. Mohanty, S.P. and Kougianos, E., *Biosensors: A tutorial review.* Ieee Potentials, 2006. **25**(2): p. 35-40.
7. Gründler, P., *Chemical sensors: an introduction for scientists and engineers*. 2007: Springer Science & Business Media.
8. Mohd Said, N.A., *Electrochemical biosensor based on microfabricated electrode arrays for life sciences applications.* 2014.
9. Sørensen, S., *Enzyme studies-note II-the measurement and the significance of hydrogenic concentrate in enzymatic processes.* Biochem. Z., 1909. **21**: p. 131-304.
10. McKee, C., *The determination of hydrogen ions.* Canadian Medical Association Journal, 1928. **19**(6): p. 758.
11. Qlark Jr, L.C., *Monitor and control of blood and tissue oxygen tensions.* Asaio Journal, 1956. **2**(1): p. 41-48.
12. Clark Jr, L.C. and Lyons, C., *Electrode systems for continuous monitoring in cardiovascular surgery.* Annals of the New York Academy of sciences, 1962. **102**(1): p. 29-45.
13. Heineman, W.R. and Jensen, W.B., *Leland c. clark jr.(1918–2005).* Biosensors and Bioelectronics, 2006. **21**(8): p. 1403-1404.
14. Mikhelson, K.N., *Ion-selective electrodes*. Vol. 81. 2013: Springer.
15. Arnold, M.A. and Meyerhoff, M.E., *Ion-selective electrodes.* Analytical Chemistry, 1984. **56**(5): p. 20-48.
16. Schultz, J.S., Mansouri, S., and Goldstein, I.J., *Affinity sensor: a new technique for developing implantable sensors for glucose and other metabolites.* Diabetes Care, 1982. **5**(3): p. 245-253.
17. Peterson, J.I., et al., *Fiber optic pH probe for physiological use.* Analytical Chemistry, 1980. **52**(6): p. 864-869.
18. Belli, S. and Rechnitz, G., *Prototype potentiometric biosensor using intact chemoreceptor structures.* Analytical Letters, 1986. **19**(3-4): p. 403-416.
19. Bobacka, J. and Ivaska, A., *Chemical sensors based on conducting polymers.* Electropolymerization: Concepts, Materials and Applications, 2010: p. 173-187.
20. Zamani, F.G., et al., *Current trends in the development of conducting polymers-based biosensors.* TrAC Trends in Analytical Chemistry, 2019. **118**: p. 264-276.
21. Chadha, U., et al., *Recent progress and growth in biosensors technology: A critical review.* Journal of Industrial and Engineering Chemistry, 2022. **109**: p. 21-51.
22. Malhotra, B.D., Chaubey, A., and Singh, S., *Prospects of conducting polymers in biosensors.* Analytica Chimica Acta, 2006. **578**(1): p. 59-74.
23. Dahlin, A.B., *Size matters: problems and advantages associated with highly miniaturized sensors.* Sensors, 2012. **12**(3): p. 3018-3036.
24. Derkus, B., *Applying the miniaturization technologies for biosensor design.* Biosensors and Bioelectronics, 2016. **79**: p. 901-913.
25. Li, G., et al., *Wearable fluid capture devices for electrochemical sensing of sweat.* ACS Appl Mater Interfaces, 2019. **11**(1): p. 238-243.

26. Xu, H., et al., *A multifunctional wearable sensor based on a graphene/inverse opal cellulose film for simultaneous, in situ monitoring of human motion and sweat.* Nanoscale, 2018. **10**(4): p. 2090-2098.
27. Steinberg, M.D., et al., *A wireless potentiostat for mobile chemical sensing and biosensing.* Talanta, 2015. **143**: p. 178-183.
28. Kassal, P., Steinberg, M.D., and Steinberg, I.M., *Wireless chemical sensors and biosensors: A review.* Sensors and Actuators B: Chemical, 2018. **266**: p. 228-245.
29. Tsekenis, G., et al., *Heavy metal ion detection using a capacitive micromechanical biosensor array for environmental monitoring.* Sensors and Actuators B: Chemical, 2015. **208**: p. 628–635.
30. Jarczewska, M., Górski, Ł., and Malinowska, E., *Electrochemical aptamer-based biosensors as potential tools for clinical diagnostics.* Analytical Methods, 2016. **8**(19): p. 3861-3877.
31. Sun, H., et al., *Construction of a water-soluble fluorescent probe for copper (II) ion detection in live cells and food products.* Food Chemistry, 2023. **418**: p. 135994.
32. Gao, W., et al., *Fully integrated wearable sensor arrays for multiplexed in situ perspiration analysis.* Nature, 2016. **529**(7587): p. 509-514.
33. Arakawa, T., Dao, D.V., and Mitsubayashi, K., *Biosensors and chemical sensors for healthcare monitoring: a review.* IEEJ Transactions on Electrical and Electronic Engineering, 2022. **17**(5): p. 626-636.
34. Wen, Y.P. and Xu, J.K., *Scientific importance of water-processable PEDOT-PSS and preparation, challenge and new application in sensors of its film electrode: a review.* Journal of Polymer Science Part a-Polymer Chemistry, 2017. **55**(7): p. 1121-1150.
35. Chandrasekhar, P., *Conducting polymers, fundamentals and applications: a practical approach*. 2013: Springer Science & Business Media.
36. Shirakawa, H., et al., *Synthesis of electrically conducting organic polymers: halogen derivatives of polyacetylene,(CH) x.* Journal of the Chemical Society, Chemical Communications, 1977(16): p. 578-580.
37. Naarmann, H. and Theophilou, N., *New process for the production of metal-like, stable polyacetylene.* Synthetic Metals, 1987. **22**(1): p. 1-8.
38. Skotheim, T.A. and Reynolds, J., *Conjugated polymers: theory, synthesis, properties, and characterization*. 2006: CRC press.
39. Groenendaal, L., et al., *Poly(3,4-ethylenedioxythiophene) and its derivatives: past, present, and future.* Advanced Materials, 2000. **12**(7): p. 481-494.
40. Hempel, F., et al., *PEDOT: PSS organic electrochemical transistors for electrical cell-substrate impedance sensing down to single cells.* Biosensors and Bioelectronics, 2021. **180**: p. 113101.
41. Liang, Y., et al., *Tuning channel architecture of interdigitated organic electrochemical transistors for recording the action potentials of electrogenic cells.* Advanced Functional Materials, 2019. **29**(29).
42. Tintelott, M., et al., *Realization of a PEDOT:PSS/Graphene oxide on-chip pseudo-reference electrode for integrated ISFETs.* Sensors, 2022. **22**(8): p. 2999.
43. Liao, C., et al., *Flexible organic electrochemical transistors for highly selective enzyme biosensors and used for saliva testing.* Adv Mater, 2015. **27**(4): p. 676-81.
44. Campana, A., et al., *Electrocardiographic recording with conformable organic electrochemical transistor fabricated on resorbable bioscaffold.* Adv Mater, 2014. **26**(23): p. 3874-8.
45. Khodagholy, D., et al., *NeuroGrid: recording action potentials from the surface of the brain.* Nat Neurosci, 2015. **18**(2): p. 310-5.
46. Wen, Y. and Xu, J., *Scientific importance of water‐processable PEDOT:PSS and preparation, challenge and new application in sensors of its film electrode: a review.* Journal of Polymer Science Part A: Polymer Chemistry, 2017. **55**(7): p. 1121-1150.
47. Zhang, X., et al., *PEDOT: PSS: From conductive polymers to sensors.* Nanotechnology and Precision Engineering (NPE), 2021. **4**(4).

48. Hokazono, M., Anno, H., and Toshima, N., *Thermoelectric properties and thermal stability of PEDOT:PSS films on a polyimide substrate and application in flexible energy conversion devices.* Journal of Electronic Materials, 2014. **43**(6): p. 2196-2201.
49. Keene, S.T., et al., *Wearable organic electrochemical transistor patch for multiplexed sensing of calcium and ammonium ions from human perspiration.* Adv Healthc Mater, 2019. **8**(24): p. e1901321.
50. Liao, J., et al., *Functional sensing interfaces of PEDOT:PSS organic electrochemical transistors for chemical and biological sensors: a mini review.* Sensors (Basel), 2019. **19**(2).
51. Hempel, F., et al., *PEDOT: PSS organic electrochemical transistor arrays for extracellular electrophysiological sensing of cardiac cells.* Biosensors and Bioelectronics, 2017. **93**: p. 132-138.
52. Alshabouna, F., et al., *PEDOT: PSS-modified cotton conductive thread for mass manufacturing of textile-based electrical wearable sensors by computerized embroidery.* Materials Today, 2021. **59**: p. 56-67.
53. Beniwal, A., John, D.A., and Dahiya, R., *PEDOT: PSS-based disposable humidity sensor for skin moisture monitoring.* IEEE Sensors Letters, 2023. **7**(3): p. 1-4.
54. Sanchez-Sanchez, A., et al., *Conductive poly (3, 4-ethylenedioxythiophene)(PEDOT)-based polymers and their applications in bioelectronics*. *Smart Polymers and Their Applications*. 2019, Elsevier. p. 191-218.
55. Rivnay, J., et al., *Organic electrochemical transistors.* Nature Reviews Materials, 2018. **3**(2): p. 1-14.
56. Friedlein, J.T., McLeod, R.R., and Rivnay, J., *Device physics of organic electrochemical transistors.* Organic Electronics, 2018. **63**: p. 398-414.
57. Rivnay, J., et al., *Structural control of mixed ionic and electronic transport in conducting polymers.* Nat Commun, 2016. **7**: p. 11287.
58. Rivnay, J., et al., *High-performance transistors for bioelectronics through tuning of channel thickness.* Science Advances, 2015. **1**(4): p. e1400251.
59. Kim, Y., et al., *A glucose sensor based on an organic electrochemical transistor structure using a vapor polymerized poly(3,4-ethylenedioxythiophene) layer.* Japanese Journal of Applied Physics, 2010. **49**(1).
60. Tang, H., et al., *Highly sensitive glucose biosensors based on organic electrochemical transistors using platinum gate electrodes modified with enzyme and nanomaterials.* Advanced Functional Materials, 2011. **21**(12): p. 2264-2272.
61. Fan, J., Pico, A.A.F and Gupta, M., *A functionalization study of aerosol jet printed organic electrochemical transistors (OECTs) for glucose detection.* Materials Advances, 2021. **2**(22): p. 7445-7455.
62. Khodagholy, D., et al., *In vivo recordings of brain activity using organic transistors.* Nat Commun, 2013. **4**: p. 1575.
63. Williamson, A., et al., *Controlling epileptiform activity with organic electronic ion pumps.* Adv Mater, 2015. **27**(20): p. 3138-44.
64. Liang, Y., et al., *High performance flexible organic electrochemical transistors for monitoring cardiac action potential.* Adv Healthc Mater, 2018. **7**(19): p. e1800304.
65. Yang, Y.R. and Gao, W., *Wearable and flexible electronics for continuous molecular monitoring.* Chemical Society Reviews, 2019. **48**(6): p. 1465-1491.
66. Jones, A.P., Webb, L.M., Anderson, A.O., Leonard, E.J. and Rot, A., *Normal human sweat contains interleukin-8.* J. Leukoc. Biol., 1995. **57**(3): p. 434-437.
67. Choi, D.H., et al., *Wearable potentiometric chloride sweat sensor: The Critical Role of the Salt Bridge.* Analytical Chemistry, 2016. **88**(24): p. 12241-12247.
68. Chung, M., Fortunato, G., and Radacsi, N., *Wearable flexible sweat sensors for healthcare monitoring: a review.* Journal of the Royal Society Interface, 2019. **16**(159): p. 20190217.
69. Bandodkar, A.J., et al., *Wearable sensors for biochemical sweat analysis.* Annu Rev Anal Chem (Palo Alto Calif), 2019. **12**(1): p. 1-22.

70. Schazmann, B., et al., *A wearable electrochemical sensor for the real-time measurement of sweat sodium concentration.* Analytical Methods, 2010. **2**(4): p. 342-348.
71. Bandodkar, A.J., et al., *Epidermal tattoo potentiometric sodium sensors with wireless signal transduction for continuous non-invasive sweat monitoring.* Biosensors & Bioelectronics, 2014. **54**: p. 603-609.
72. Speedy, D.B., Noakes, T.D., and Schneider, C., *Exercise-associated hyponatremia: a review.* Emerg Med (Fremantle), 2001. **13**(1): p. 17-27.
73. Gao, W., et al. *Wearable sweat biosensors*. *2016 IEEE International Electron Devices Meeting (IEDM)*. 2016. IEEE.
74. Kinnamon, D., et al., *Portable biosensor for monitoring cortisol in low-volume perspired human sweat.* Scientific Reports, 2017. **7**(1): p. 13312.
75. Kim, J., Campbell, A.S., and Wang J., *Wearable non-invasive epidermal glucose sensors: A review.* Talanta, 2018. **177**: p. 163-170.
76. Beauchamp, M. and Lands, L.C., *Sweat-testing: a review of current technical requirements.* Pediatr Pulmonol, 2005. **39**(6): p. 507-11.
77. Abellan-Llobregat, A., et al., *A stretchable and screen-printed electrochemical sensor for glucose determination in human perspiration.* Biosens Bioelectron, 2017. **91**: p. 885-891.
78. Lin, P., Yan, F., and Chan, H.L., *Ion-sensitive properties of organic electrochemical transistors.* ACS Appl Mater Interfaces, 2010. **2**(6): p. 1637-41.
79. Tintelott, M., et al., *Physical interpretation of mixed ionic‐electronic conductive polymer‐coated electrodes by a simple universal impedance model.* Electroanalysis, 2023. **35**(4): p. e202200332.
80. Li, Y., et al., *Ion-selective organic electrochemical transistors: recent progress and challenges.* Small, 2022. **18**(19): p. e2107413.
81. Ghittorelli, M., et al., *High-sensitivity ion detection at low voltages with current-driven organic electrochemical transistors.* Nat Commun, 2018. **9**(1): p. 1441.
82. Cadogan, A., et al., *All-solid-state sodium-selective electrode based on a calixarene ionophore in a poly (vinyl chloride) membrane with a polypyrrole solid contact.* Analytical Chemistry, 1992. **64**(21): p. 2496-2501.
83. Sessolo, M., et al., *Ion-selective organic electrochemical transistors.* Adv Mater, 2014. **26**(28): p. 4803-7.
84. Han, S., et al., *Microfabricated ion-selective transistors with fast and super-nernstian response.* Adv Mater, 2020: p. e2004790.
85. Eddin, F.B.K. and Fen, Y.W., *Recent advances in electrochemical and optical sensing of dopamine.* Sensors (Basel, Switzerland), 2020. **20**(4).
86. Liu, X. and Liu, J., *Biosensors and sensors for dopamine detection.* View, 2020. **2**(1): p. 20200102.
87. Matt, S.M. and Gaskill, P.J., *Where is dopamine and how do immune cells see it?: dopamine-mediated immune cell function in health and disease.* J Neuroimmune Pharmacol, 2020. **15**(1): p. 114-164.
88. Steckl, A.J. and Ray, P., *Stress biomarkers in biological fluids and their point-of-use detection.* Acs Sensors, 2018. **3**(10): p. 2025-2044.
89. Bucolo, C., et al., *Dopamine outside the brain: The eye, cardiovascular system and endocrine pancreas.* Pharmacol Ther, 2019. **203**: p. 107392.
90. Klein, M.O., et al., *Dopamine: functions, signaling, and association with neurological diseases.* Cell Mol Neurobiol, 2019. **39**(1): p. 31-59.
91. Tang, H., et al., *Highly sensitive dopamine biosensors based on organic electrochemical transistors.* Biosens Bioelectron, 2011. **26**(11): p. 4559-63.
92. Liu, K.K., Wu, R.G., Chuang, Y.J., Khoo, H.S, Huang, S.H. and Tseng, F.G., *Microfluidic systems for biosensing.* Sensors 2010. **10**: p. 6623-6661.
93. Lapizco-Encinas, B.H. and Zhang, Y.V., *Microfluidic systems in clinical diagnosis.* Electrophoresis, 2023. **44**: p. 217–245.

94. Rivet, C., Lee, H., Hirsch, A., Hamilton, S. and Lu, H., *Microfluidics for medical diagnostics and biosensors.* Chemical Engineering Science 2011. **66**: p. 1490–1507.
95. Pol, R., Céspedes, F., Gabriel, D. and Baeza, M., *Microfluidic lab-on-a-chip platforms for environmental monitoring.* Trends in Analytical Chemistry, 2017. **95**: p. 62-68.
96. Delattre, C., Allier, C.P., Fouillet, Y., Jary, D., Bottausci, F., Bouvier, D., Delapierre, G., Quinaud, M., Rival, A., Davoust, L. and Peponnet, C., *Macro to microfluidics system for biological environmental monitoring.* Biosensors and Bioelectronics, 2012. **36**: p. 230-235.
97. Kim, D., Wu, X., Young, A.T. and Haynes, C.L., *Microfluidics-based in vivo mimetic systems for the study of cellular biology.* Acc. Chem. Res. , 2014. **47**: p. 1165−1173.
98. Young, E.W. and Simmons, C.A., *Macro- and microscale fluid flow systems for endothelial cell biology.* Lab on a Chip, 2010. **10**: p. 143–160.
99. Islam, M.R., et al., *Smart electronic textile-based wearable supercapacitors.* Adv Sci (Weinh), 2022. **9**(31): p. e2203856.
100. Cho, S., et al., *Smart electronic textiles for wearable sensing and display.* Biosensors (Basel), 2022. **12**(4): p. 222.
101. Coppede, N., et al., *Human stress monitoring through an organic cotton-fiber biosensor.* J Mater Chem B, 2014. **2**(34): p. 5620-5626.
102. Zhao, Y., et al., *Highly stretchable and strain-insensitive fiber-based wearable electrochemical biosensor to monitor glucose in the sweat.* Anal Chem, 2019. **91**(10): p. 6569-6576.
103. Piper, A., et al., *A disposable, wearable, flexible, stitched textile electrochemical biosensing platform.* Biosens Bioelectron, 2021. **194**: p. 113604.
104. Ortiz-Conde, A., et al., *A review of recent MOSFET threshold voltage extraction methods.* Microelectronics Reliability, 2002. **42**(4-5): p. 583-596.
105. Possanzini, L., et al., *Textile sensors platform for the selective and simultaneous detection of chloride ion and pH in sweat.* Sci Rep, 2020. **10**(1): p. 17180.
106. Coppedè, N., et al., *Ion selective textile organic electrochemical transistor for wearable sweat monitoring.* Organic Electronics, 2020. **78**: p. 105579.
107. Manjakkal, L., et al., *Textile-based potentiometric electrochemical pH sensor for wearable applications.* Biosensors, 2019. **9**(1): p. 14.
108. Han, S., et al., *A multiparameter pressure–temperature–humidity sensor based on mixed ionic–electronic cellulose aerogels.* Advanced Science, 2019. **6**(8): p. 1802128.
109. Serafini, M., et al., *A wearable electrochemical gas sensor for ammonia detection.* Sensors, 2021. **21**(23): p. 7905.
110. Fan, X., et al., *PEDOT:PSS for flexible and stretchable electronics: modifications, strategies, and applications.* Advanced Science, 2019. **6**(19): p. 1900813.
111. Lang, U., et al., *Microscopical investigations of PEDOT:PSS thin films.* Advanced Functional Materials, 2009. **19**(8): p. 1215-1220.
112. Dkhissi, A., et al., *Theoretical investigation of the nature of the ground state in the low-bandgap conjugated polymer, poly(3,4-ethylenedioxythiophene).* Chemical Physics Letters, 2002. **359**(5-6): p. 466-472.
113. Ouyang, J., et al., *High‐conductivity poly (3, 4‐ethylenedioxythiophene): poly (styrene sulfonate) film and its application in polymer optoelectronic devices.* Advanced Functional Materials, 2005. **15**(2): p. 203-208.
114. Park, J.K., et al., *Real-time humidity sensor based on microwave resonator coupled with PEDOT: PSS conducting polymer film.* Scientific Reports, 2018. **8**(1): p. 439.
115. Ouyang, J., *"Secondary doping" methods to significantly enhance the conductivity of PEDOT:PSS for its application as transparent electrode of optoelectronic devices.* Displays, 2013. **34**(5): p. 423-436.
116. Moujoud, A., et al., *On the mechanism of conductivity enhancement and work function control in PEDOT:PSS film through UV-light treatment.* Physica Status Solidi a-Applications and Materials Science, 2010. **207**(7): p. 1704-1707.

117. Benor, A., et al., *Dramatic efficiency improvement in phosphorescent organic light-emitting diodes with ultraviolet-ozone treated poly(3,4-ethylenedioxythiophene):poly(styrenesulfonate).* Applied Physics Letters, 2009. **94**(19).
118. Huang, J., et al., *Influence of thermal treatment on the conductivity and morphology of PEDOT/PSS films.* Synthetic Metals, 2003. **139**(3): p. 569-572.
119. Shi, H., et al., *Effective approaches to improve the electrical conductivity of PEDOT:PSS: a review.* Advanced Electronic Materials, 2015. **1**(4): p. 1500017.
120. Kim, J., et al., *Enhancement of electrical conductivity of poly (3, 4-ethylenedioxythiophene)/poly (4-styrenesulfonate) by a change of solvents.* Synthetic Metals, 2002. **126**(2-3): p. 311-316.
121. Wei, Q., et al., *Morphological change and mobility enhancement in PEDOT:PSS by adding co-solvents.* Adv Mater, 2013. **25**(20): p. 2831-6.
122. Döbbelin, M., et al., *Influence of ionic liquids on the electrical conductivity and morphology of PEDOT: PSS films.* Chemistry of Materials, 2007. **19**(9): p. 2147-2149.
123. Xia, Y. and Ouyang, J., *Salt-induced charge screening and significant conductivity enhancement of conducting poly(3,4-ethylenedioxythiophene):poly(styrenesulfonate).* Macromolecules, 2009. **42**(12): p. 4141-4147.
124. Xia, Y. and Ouyang, J., *Anion effect on salt-induced conductivity enhancement of poly(3,4-ethylenedioxythiophene):poly(styrenesulfonate) films.* Organic Electronics, 2010. **11**(6): p. 1129-1135.
125. Kim, N., et al., *Highly conductive PEDOT: PSS nanofibrils induced by solution-processed crystallization.* Advanced Materials, 2014. **26**(14): p. 2268-2272.
126. Yan, H., Jo, T. and Okuzaki, H., *Highly conductive and transparent poly (3, 4-ethylenedioxythiophene)/poly (4-styrenesulfonate)(PEDOT/PSS) thin films.* Polymer Journal, 2009. **41**(12): p. 1028–1029.
127. Sankir, N.D., *Selective deposition of PEDOT/PSS on to flexible substrates and tailoring the electrical resistivity by post treatment.* Circuit World, 2008. **34**: p. 37-37.
128. Xia, Y., Sun, K., and Ouyang, J., *Highly conductive poly(3,4-ethylenedioxythiophene):poly(styrene sulfonate) films treated with an amphiphilic fluoro compound as the transparent electrode of polymer solar cells.* Energy Environ. Sci., 2012. **5**(1): p. 5325-5332.
129. Alemu, D., Wei, H.Y., Ho, K.C. and Chu, C.W., *Highly conductive PEDOT:PSS electrode by simple film treatment with methanol for ITO-free polymer solar cells.* Energy & Environmental Science, 2012. **5**: p. 9662.
130. Xia, Y., Sun, K., and Ouyang, J., *Solution-processed metallic conducting polymer films as transparent electrode of optoelectronic devices.* Adv Mater, 2012. **24**(18): p. 2436-40.
131. Palumbiny, C.M., et al., *The crystallization of PEDOT: PSS polymeric electrodes probed in situ during printing.* Advanced Materials, 2015. **22**(27): p. 3391-3397.
132. Zheng, W., et al., *Effect of organic vapors on the molecular conformation of non-doped polyaniline.* Synthetic Metals, 1997. **84**(1-3): p. 63-64.
133. Ohayon, D., Druet, V. and Inal, S., *A guide for the characterization of organic electrochemical transistors and channel materials.* Chem. Soc. Rev., 2023. **52**: p. 1001–1023.
134. Blom, P.W.M., *Polymer electronics: to be or not to be?* Adv. Mater. Technol., 2020. **5**: p. 2000144.
135. Ortiz-Conde, A., et al., *Revisiting MOSFET threshold voltage extraction methods.* Microelectronics Reliability, 2013. **53**(1): p. 90-104.
136. Zeglio, E. and Inganäs, O., *Active Materials for Organic Electrochemical Transistors.* Advanced Materials, 2018. **30**: p. 1800941.
137. Bernards, D.A. and Malliaras, G.G., *Steady-state and transient behavior of organic electrochemical transistors.* Advanced Functional Materials, 2007. **17**(17): p. 3538-3544.

138. Inal, S., Malliaras, G.G., and Rivnay, J., *Benchmarking organic mixed conductors for transistors.* Nat Commun, 2017. **8**(1): p. 1767.
139. Koutsouras, D.A., et al., *Impedance spectroscopy of spin-cast and electrochemically deposited PEDOT:PSS films on microfabricated electrodes with various areas.* ChemElectroChem, 2017. **4**(9): p. 2321-2327.
140. Tanguy, J., et al., *Study of the redox mechanism of poly-3-methylthiophene by impedance spectroscopy.* Electrochimica Acta, 1992. **37**(8): p. 1417-1428.
141. Sheliakina, M., Mostert, A., and Meredith, P., *An all-solid-state biocompatible ion-to-electron transducer for bioelectronics.* Materials Horizons, 2018. **5**(2): p. 256-263.
142. Tarabella, G., et al., *A single cotton fiber organic electrochemical transistor for liquid electrolyte saline sensing.* Journal of Materials Chemistry, 2012. **22**(45): p. 23830.
143. Demuru, S., Kunnel, B.P., and Briand, D., *Real‐time multi‐ion detection in the sweat concentration range enabled by flexible, printed, and microfluidics‐integrated organic transistor arrays.* Advanced Materials Technologies, 2020. **5**(10): p. 2000328.
144. Macaya, D.J., et al., *Simple glucose sensors with micromolar sensitivity based on organic electrochemical transistors.* Sensors and Actuators B: Chemical, 2007. **123** (1): p. 374-378.
145. Tarabella, G., et al., *Effect of the gate electrode on the response of organic electrochemical transistors.* Applied Physics Letters, 2010. **97**(12): p. 123304.
146. Pappa, A.M., et al., *Organic transistor arrays integrated with finger-powered microfluidics for multianalyte saliva testing.* Advanced Healthcare Materials, 2016. **5**(17): p. 2295-302.
147. Gualandi, I., et al., *Selective detection of dopamine with an all PEDOT:PSS organic electrochemical transistor.* Scientific Reports, 2016. **6**: p. 35419.
148. Ji, W., et al., *Carbonized silk fabric-based flexible organic electrochemical transistors for highly sensitive and selective dopamine detection.* Sensors and Actuators B: Chemical, 2020. **304**: p. 127414.
149. Butt, H.J., Graf, K., and Kappl, M., *Physics and chemistry of interfaces*. 2023: John Wiley & Sons.
150. Du, H., et al., *Electric double-layer transistors: a review of recent progress.* Journal of Materials Science, 2015 **50**: p. 5641–5673.
151. Prickril, B., Rasooly, A. and Prickril, *Biosensors and biodetection.* Springer, 2017.
152. Armstrong, R. and Todd, M., *The role of PVC in ion selective electrode membranes.* Journal of Electroanalytical Chemistry and Interfacial Electrochemistry, 1987. **237**(2): p. 181-185.
153. Özbek, O., *Potentiometric PVC membrane ion–selective electrode for the determination of Sr(II) ions.* Sensors International, 2022. **3**: p. 100185.
154. Mihali, C. and Vaum, N., *Use of plasticizers for electrochemical sensors.* Recent Advances in Plasticizers, 2012. **125**.
155. Hussain, R., Khan, M.Q., and Khan, A.A., *Tetrahydrofuran vapour sensing by electrically conductive silver nanoparticle doped Poly-1-napthylamine-titanium(IV) sulphosalicylophosphate ion exchange nanocomposite.* Journal of Industrial and Engineering Chemistry 2019. **70**: p. 186–195.
156. Müller, H., *Tetrahydrofuran.* Wiley-VCH, Weinheim, 2005.
157. Jackson, D.T. and Nelson, P.N., *Preparation and properties of some ion selective membranes: a review.* Journal of Molecular Structure, 2019. **1182**: p. 241-259.
158. Papp, S., Jagerszki, G., and Gyurcsanyi, R.E., *Ion-selective electrodes based on hydrophilic ionophore-modified nanopores.* Angewandte Chemie-International Edition, 2018. **57**(17): p. 4752-4755.
159. Bobacka, J., Ivaska, A., and Lewenstam, A., *Potentiometric ion sensors.* Chemical Reviews, 2008. **108**(2): p. 329-351.
160. Lindner, E., Gyurcsányi, R.E., and Buck, R.P., *Tailored transport through ion‐selective membranes for improved detection limits and selectivity coefficients.* Electroanalysis:

An International Journal Devoted to Fundamental and Practical Aspects of Electroanalysis, 1999. **11**(10-11): p. 695-702.
161. Xiong, C., Qu, H., Chen, W., Zhang, L., Qiu, L., Zheng, L. and Xia, F., *Real-time detection of Cu(II) with PEDOT:PSS based organic electrochemical transistors.* Science China Chemistry, 2017. **60**: p. 1205–1211.
162. Meng, X., Zou, T., Chan, M.H., Chan, D.T.M., Tsang, A.C.O., Leung, G.K.K., Zhang, S. and Chan, P.K.L., *Selective ion sensing organic electrochemical transistors suitable for blood analysis.* Advanced Sensor Research 2024. **3**(1): p. 2300097.
163. Yoshitake, T., et al., *High-sensitive liquid chromatographic method for determination of neuronal release of serotonin, noradrenaline and dopamine monitored by microdialysis in the rat prefrontal cortex.* J Neurosci Methods, 2004. **140**(1-2): p. 163-8.
164. Woolley, A.T., et al., *Capillary electrophoresis chips with integrated electrochemical detection.* Analytical Chemistry, 1998. **70**(4): p. 684-688.
165. Hows, M.E., et al., *High-performance liquid chromatography/tandem mass spectrometric assay for the simultaneous measurement of dopamine, norepinephrine, 5-hydroxytryptamine and cocaine in biological samples.* J Neurosci Methods, 2004. **138**(1-2): p. 123-32.
166. Barreto, W.J., et al., *Raman, IR, UV-vis and EPR characterization of two copper dioxolene complexes derived from L-dopa and dopamine.* Spectrochim Acta A Mol Biomol Spectrosc, 2008. **71**(4): p. 1419-24.
167. Wang, H.Y., Sun, Y., and Tang, B., *Study on fluorescence property of dopamine and determination of dopamine by fluorimetry.* Talanta, 2002. **57**(5): p. 899-907.
168. Jamal, M., et al., *Ethanol and acetaldehyde differentially alter extracellular dopamine and serotonin in Aldh2-knockout mouse dorsal striatum: a reverse microdialysis study.* Neurotoxicology, 2016. **52**: p. 204-9.
169. Fritzen-Garcia, M.B., et al., *Characterization of horseradish peroxidase immobilized on PEGylated polyurethane nanoparticles and its application for dopamine detection.* Sensors and Actuators B: Chemical, 2013. **182**: p. 264-272.
170. Sajid, M., et al., *Chemically modified electrodes for electrochemical detection of dopamine in the presence of uric acid and ascorbic acid: a review.* TrAC Trends in Analytical Chemistry, 2016. **76**: p. 15-29.
171. Shin, J.W., et al., *Silver nanoparticle modified electrode covered by graphene oxide for the enhanced electrochemical detection of dopamine.* Sensors 2017. **17**(12): p. 2771.
172. Liu, S.Q., Sun, W.H. and Hu, F.T., *Graphene nano sheet-fabricated electrochemical sensor for the determination of dopamine in the presence of ascorbic acid using cetyltrimethylammonium bromide as the discriminating agent.* Sensors and Actuators B: Chemical, 2012. **173**: p. 497-504.
173. Si, B. and Song, E., *Recent advances in the detection of neurotransmitters.* Chemosensors, 2018. **6**(1): p. 1.
174. Kim, D.S., et al., *Electrochemical detection of dopamine using periodic cylindrical gold nanoelectrode arrays.* Sci Rep, 2018. **8**(1): p. 14049.
175. Manbohi, A. and Ahmadi, S.H., *Sensitive and selective detection of dopamine using electrochemical microfluidic paper-based analytical nanosensor.* Sensing and Bio-Sensing Research, 2019. **23**: p. 100270.
176. Lakard, S., Pavel, I.A., and Lakard, B., *Electrochemical biosensing of dopamine neurotransmitter: a review.* Biosensors 2021. **11**(6): p. 179.
177. Liao, C., et al., *Organic electrochemical transistors with graphene-modified gate electrodes for highly sensitive and selective dopamine sensors.* J Mater Chem B, 2014. **2**(2): p. 191-200.
178. Xie, K., et al., *Organic electrochemical transistor arrays for real-time mapping of evoked neurotransmitter release in vivo.* Elife, 2020. **9**: p. e50345.
179. Mariani, F., et al., *Needle-type organic electrochemical transistor for spatially resolved detection of dopamine.* Mikrochim Acta, 2020. **187**(7): p. 378.

180. Liang, Y., et al., *Label-free split aptamer sensor for femtomolar detection of dopamine by means of flexible organic electrochemical transistors.* Materials, 2020. **13**(11): p. 2577.
181. Tang, K., et al., *Organic electrochemical transistor with molecularly imprinted polymer-modified gate for the real-time selective detection of dopamine.* ACS Applied Polymer Materials, 2022. **4**(4): p. 2337-2345.
182. Li, W., et al., *Fast-scanning potential-gated organic electrochemical transistors for highly sensitive sensing of dopamine in living rat brain.* Angew Chem Int Ed Engl, 2022. **61**(31): p. e202204134.
183. Bernards, D.A., et al., *Enzymatic sensing with organic electrochemical transistors.* J. Mater. Chem., 2008. **18**(1): p. 116-120.
184. Madou, M.J., *Fundamentals of microfabrication: the science of miniaturization*. 2018: CRC press.
185. Depla, D., Mahieu, S. and Greene, J., *Sputtering deposition processes*, in *Handbook of deposition technologies for films and coatings*. 2010, Elsevier. p. 253-296.
186. Bortolotti, A., et al., *Optical lithography.* Silicon Sensors and Actuators: The Feynman Roadmap, 2022, Springer. p. 169-201.
187. Oehrlein, G.S., *Reactive‐ion etching.* Physics Today, 1986. **39**(10): p. 26-33.
188. Pauw, L.J.v.d., *A method of measuring specific resistivity and Hall effect of discs of arbitrary shape.* Philips Research Reports, 1958. **13**: p. 1-9.
189. *Making van der Pauw resistivity and Hall voltage measurements using the 4200A-SCS Parameter Analyzer*. Online Database.
190. Bhuvanendran, N., et al., *A quick guide to the assessment of key electrochemical performance indicators for the oxygen reduction reaction: a comprehensive review.* International Journal of Hydrogen Energy, 2022. **47**(11): p. 7113-7138.
191. Marken, F., Neudeck, A., and Bond, A.M., *Cyclic voltammetry.* Electroanalytical methods: guide to experiments and applications, 2010: p. 57-106.
192. Elgrishi, N., et al., *A practical beginner's guide to cyclic voltammetry.* Journal of Chemical Education, 2018. **95**(2): p. 197-206.
193. Taherpour, A.A. and Mousavi, F., *Carbon nanomaterials for electroanalysis in pharmaceutical applications*. Fullerens, Graphenes and Nanotubes. 2018, Elsevier. p. 169-225.
194. Kupper, H., *Surface modified PEDOT:PSS organic electrochemical transistor for biosensing*. 2019.
195. Nguyen, T.C., et al., *PSPICE model for silicon nanowire field-effect transistor biosensors in impedimetric measurement mode.* Physica Status Solidi (a), 2013. **210**(5): p. 870-876.
196. Schwartz, M., et al., *Impedimetric sensing of DNA with silicon nanowire transistors as alternative transducer principle.* Physica Status Solidi (a), 2018. **215**(15): p. 1700740.
197. Nguyen, T.D.D., *Development of a sensor platform for leukemia detection using field-effect transistor arrays*. 2022.
198. Bandodkar, A.J., et al., *Epidermal tattoo potentiometric sodium sensors with wireless signal transduction for continuous non-invasive sweat monitoring.* Biosens Bioelectron, 2014. **54**: p. 603-9.
199. Yang, M., et al., *Amperometric glucose biosensor based on chitosan with improved selectivity and stability.* Sensors and Actuators B: Chemical, 2004. **101**(3): p. 269-276.
200. Yaghmazadeh, O., Cicoira, F., Bernards, D.A., Yang, S.Y., Bonnassieux, Y. and Malliaras, G.G., *Optimization of organic electrochemical transistors for sensor applications.* Plolymer Science 2010. **49**: p. 34-39.
201. Fick, A., *On liquid diffusion.* Journal of Membrane Science, 1995. **100**(1): p. 33-38.
202. Nyoni, A.B. and Brook, D., *Wicking mechanisms in yarns—the key to fabric wicking performance.* Journal of the Textile Institute, 2006. **97**(2): p. 119-128.

203. Wang, F., Kumari, S., and Schiller, U.D., *Computational characterization of nonwoven fibrous media. II. Analysis of microstructure effects on permeability and tortuosity.* Physical Review Materials, 2020. **4**(8): p. 083804.

Acknowledgements

I would like to express my deepest gratitude to all those who supported and helped me during my PhD journey. The accomplishments of this dissertation would not be possible without your kind support.

First of all, I would like to thank my supervisor Univ. -Prof. Dr. rer. nat. Sven Ingebrandt who gave me the opportunity to work in the institute. His constructive criticism and guidance were always available for me during my time at the institute.

My thanks will also go to Univ. -Prof. Dr. rer. nat. Partick Wagner for agreeing to be the second examiner of my thesis work. Additionally, many thanks for his corrections and reviews of my thesis work. I appreciate his contribution.

I would like to express my gratitude to my direct supervisor, Dr. Xuan Thang Vu, for the many fruitful discussions about my topic. His kind encouragement, patience and support during these years were meaningful for me, while his critical scientific attitude will influence and benefit me in my future career.

I thank all the ZMNT staff in IWE1 for their technical support and good cooperation. Special thanks go to Jochen Heiss for his answers and help for many technical questions and discussions. I would also like to thank the staff from the secretary office for their support and profound conversations.

I would like to thank all the colleagues in IWE1 who accompanied and supported me during these years, which gave me a beautiful memory working in the institute. I would like to specifically thank my officemate and friend, Felix. His friendship and support have been invaluable throughout my time at the institute. I am especially thankful for the many insightful scientific discussions we shared. Furthermore, I appreciate Dr. Divagar Murugan for his scientific discussions about my work and critical reviews for my thesis, which inspired me a lot every time. Additionally, I would like to thank Eashika who would always find a way to encourage and cheer me up. I express my thanks to all my students who helped me so much during their time in the institute and I wish every of them a bright future.

A heartfelt thanks to my family for their endless love and support throughout my PhD journey and my life, which gives me so much energy and makes me a better person. Moreover, special thanks for their trust and understanding that I could not visit them and witnessed many milestones in their lives during these years. Warm thanks to all my friends who offered me help, especially in difficult times with good advice and encouragement. All the great time that we spent together gave me a good chance to recharge myself and bring me back to the right way. I would like to express my deep appreciation to my friend Suzanna for her time and invaluable support. I would also like to extend my heartfelt thanks to my friend Onno for his commitment and keen attention to detail.

Acknowledgements

Last but not least, I would like to extend my heart gratitude to my husband, Marcel, who provided me his unwavering support, love and encouragement during my PhD journey as well as the time in Germany. Thanks for always being my sounding board, for listening to my ideas and for giving me thoughtful feedback. His insights have enriched my work and helped me overcome numerous challenges, and I could not have reached this milestone without him by my side.

I would like to express my appreciation to my baby boy, Emmanuel Lee, for choosing me as his mother at the end of my PhD and treating me nicely during my writing time. Thanks for all the exciting and happy moments that he brought me, which gave me so much inner strength.

Table of Figures

Figure 1.1: The basic elements of a chemical sensor or a biosensor. Figure is adapted from reference [8]. 1
Figure 1.2: Representative applications of PEDOT:PSS. Figure is adapted from reference [54]. It shows the schematics of OECTs (a), thermoelectric device (b), organic-electronic ion pump (c) and electronic textile (d). 3
Figure 1.3: A synaptic transmission process. Figure is adapted from reference [85]. 5
Figure 2.1: (a) Chemical structure of PEDOT:PSS, (b) The described microstructure of the conducting polymer system. Part a shows the synthesis onto the PSS template, part b displays colloidal gel particles formed in dispersion, part c is the resulting film containing PEDOT:PSS-rich (blue) and PSS-rich (grey) phases, where crystallites (part d) support enhanced electronic transport. Figure is adapted from reference [57]. 9
Figure 2.2: Two distinct PEDOT structures: (a) Benzoid structure and (b) Quinoid structure. Figure is adapted from reference [114]. 10
Figure 2.3: Timeline of conductivity values for PEDOT:PSS. Figure is adapted from reference [119]. 11
Figure 2.4: (a) The schematic of an OECT, (b) Working principle of PEDOT:PSS OECTs. Figure is adapted from reference [55]. 12
Figure 2.5: (a) Output characteristics, (b) Transfer characteristics (green curve) and (c) Transconductance of an OECT. Figure is adapted from reference [133]. 13
Figure 2.6: (a) The relationship between the transconductance (gm) and the channel geometry (Wd/L) for microscale OECTs with various materials, (b) The relationship between channel capacitance (C_{CH}) and channel geometry (WdL) of OECTs. Figure is adapted from reference [56]. 15
Figure 2.7: (a) Schematic configuration of an PEDOT:PSS based OECT. Figure is adapted from reference [78], (b) Schematic of the OECT integrated with an ISM. Figure is adapted from reference [83]. 16
Figure 2.8: (a) The schematic of the flexible OECTs integrated into the microfluidic system. Figure is adapted from reference [143], (b) Schematic presentation of the wearable OECTs based on ISMs for multiplexed detection of ammonium and calcium ions. Figure is adapted from reference [49]. 17
Figure 2.9: (a) The schematic presentation of PEDOT:PSS OECTs for glucose detection. Figure is adapted from reference [60], (b) Schematic of the biosensing multiplatform using “finger-powered” PDMS microfluidics. Figure is adapted from reference [146]. 18
Figure 2.10: Schematic of electrical double layer at the interface between PEDOT:PSS channel and electrolyte using the Gouy-Chapman-Stern model when a positive gate voltage is applied. Figure is adapted from reference [149-151]. 20
Figure 2.11: Chemical structures of K^+ (a), NH_4^+ (b), Na^+ (c) and Ca^{2+} (d) ionophores. Figure is adapted from reference [80]. 22
Figure 2.12: Structural composition and working mechanism of a K^+ ion-selective membrane. Figure is adapted from references [80, 159, 160]. 23

Table of Figures

Figure 2.13: (a) Model of OECTs consisting of an electronic circuit and ionic circuit. Figure is adapted from reference [74], (b) The distribution of potential in the ionic circuit with capacitances at the gate/electrolyte (C_g) and channel/electrolyte (C_{ch}) interfaces, respectively. Figure is adapted from reference [55]. 24
Figure 2.14: (a) The chemical structure of DA and its several analogues, (b) two interferents of DA. Figure is adapted from reference [86]. 26
Figure 2.15: (a) Working principle of dopamine detection using PEDOT:PSS OECTs, (b) Potential changes of the OECT in the absence of dopamine (solid line), the presence of dopamine (dashed line) and the effective gate voltage (dotted line). Figure is adapted from reference [183]. 28
Figure 3.1: Image of exterior (a) and interior (b) of the evaporation system of Leybold A700QE. This machine is located in Room 007, ZMNT, RWTH university, and the photos were provided by Jochen Heiss. 31
Figure 3.2: Schematic of an electron-beam evaporation system. Figure is adapted from reference [184]. 32
Figure 3.3: Image of exterior (a) and interior (b) of the Nordiko NS2550 sputtering system. This machine is in Room 007, ZMNT, RWTH university, and the photos were provided by Jochen Heiss. 33
Figure 3.4: Schematic of lift-off process. Figure is adapted from reference [186]. 34
Figure 3.5: Image of PECVD equipment. 35
Figure 3.6: Image of RIE machine. 36
Figure 3.7: Schematics of reactive ion etching process. Figure is adapted from references [184, 187]. 37
Figure 3.8: (a) Van der Pauw configuration on a square sample, (b) Van der Pauw sheet resistance value measurement configuration. Figure is adapted from reference [189]. 38
Figure 3.9: (a) The potential versus time waveform showing the forward and reversed linear potential sweep, (b) Cyclic voltammogram of the measured current-potential curve. Figure is adapted from reference [193]. 39
Figure 4.1: Chip design of IDE structures with 10 fingers. 41
Figure 4.2: (a) Test structures on the test chip, (b) A four-point measurement structure. 43
Figure 4.3: (a) IDE structures (light blue) are placed between the source and drain contact line, (b) PEDOT:PSS area is designed on the IDE structures to be slightly bigger than the channel opening area. 43
Figure 4.4: Wafer layout for Van der Pauw structures (a) mask 1 for patterning the contact path, (b) mask 2 for opening the contact pads, (c) mask 3 for opening the PEDOT:PSS area. 44
Figure 4.5: Preparation procedure for four different PEDOT:PSS mixture solutions. 46
Figure 4.6: Fabrication process for OECT microarrays with gold (Au) contact material using the mask layout shown in figure S1 in Appendix C. 47
Figure 4.7: Fabrication process for OECTs with Au as contact lines and IrO_x as IDEs. 48
Figure 4.8: HANNA instrument with pH, conductivity, and temperature electrodes. 50
Figure 4.9: A commercial Keithley 4200A-SCS semiconductor characterization system. 50

Figure 4.10: (a) An image of the transistor transfer function (TTF) amplifier system, (b) The schematic of working principle of the real-out system. 51
Figure 4.11: (a) A fabricated flow cell made of PMMA, (b) The center area of the flow cell. 52
Figure 4.12: (a) Schematic of the microfluidic channel mold (top view), (b) The cover plate of the fabricated microfluidic channel mold, (c) Fabricated mold form for PDMS channels, (d) Two fabricated PDMS channels. 53
Figure 4.13: Schematic representation of electrical characteristics of OECTs integrating with the microfluidic system. 54
Figure 4.14: (a) Na^+ ion-selective membrane (ISM) mixture solution, (b) K^+ ion-selective membrane (ISM) mixture solution. 54
Figure 4.15: (a) Schematic representation of integrating the ion-selective membranes (ISMs) onto OECTs, (b) Resistance between source and drain electrodes during the fabrication process of ISM-based PEDOT:PSS OECTs. Step 1 means after depositing the PEDOT:PSS on OECTs, step 2 refers to after integrating ISMs on PEDOT:PSS OECTs, step 3 means after chip encapsulation process (n=3). 56
Figure 4.16: Fresh dopamine solutions with concentrations ranging from 1 nM to 3 mM. ... 58
Figure 4.17: Image of 1.0% chitosan solution. 58
Figure 4.18: Schematic (a) and image (c) of the first setup for CV characterization, schematic (b) and image (d) of the second setup for CV characterization. 59
Figure 4.19: (a) Schematic presentation of the fabrication process for textile sensors integrated with ion-selective membrane (ISM), (b) Schematic of coating the cotton yarn with the PEDOT:PSS mixture solution. 60
Figure 5.1: Microscope image of glass wafer after the development process. (a) The patterned contact lines and IDE structures, (b) The patterned test structure for four-point measurements. 62
Figure 5.2: (a) 50 nm of evaporated Au contact material, (b) 100 nm of sputtered Pt material, (c) 150 nm of sputtered TiN material, (d) 150 nm of sputtered ITO material, (e) 150 nm of sputtered IrO_x contact material. 62
Figure 5.3: (a) Microscope image of glass wafer after etching the silicon oxide layer using the reactive ion etching (RIE) process, (b) Microscope image of one IDE structure after patterning the PEDOT:PSS area. 63
Figure 5.4: Microscope image of an OECT structure with Au material after depositing PEDOT:PSS solution on the transistor. 64
Figure 5.5: (a) Microscope image of the patterned contact lines after optical lithography, and (b) after lift-off process for Au contact material. 64
Figure 5.6: (a) Microscope image of the IDE structure after the laser writing process, and (b) the IDE structures with IrO_x after sputtering and the lift-off process. 65
Figure 5.7: (a) Microscope image of the opening on the IDE structure and (b) the openings of the contact pads after silicon oxide passivation layer was completely etched away. 65
Figure 5.8: Microscope image of the IDE after patterning the PEDOT:PSS area using laser lithography. 66

Figure 5.9: (a) Wire bonding plan for connecting the chip and its carrier, (b) Boned aluminum (Al) wire on the contact pads of chip and carrier. 67
Figure 5.10: (a) Prepared PDMS hoppers, (b) Schematic of an encapsulated chip, (c) Image of an encapsulated chip. 67
Figure 5.11: (a) The schematic of electrical characterization using Van der Pauw (VDP) measurement technique, (b) The electrical conductivity of the pristine PEDOT:PSS films and the PEDOT:PSS/EG/GOPS films (n≥3). 69
Figure 5.12: Transfer characteristics of a transistor measured in 10 mM buffer solution with an Ag/AgCl reference electrode when V_{GS} swept from -0.6 V to 0.3 V and V_{DS} is -0.1 V (blue), -0.2 V (red), -0.3 V (yellow), -0.4 V (purple). 70
Figure 5.13: Output characteristics of an OECT with an Ag/AgCl reference electrode immersed in 10 mM buffer solution when V_{DS} swept from -0.8 V to -0.1 V and V_{GS} is 0 V (purple), 0.1 V (yellow), 0.2 V (red), 0.3 V (blue). 71
Figure 5.14: Transconductance of a transistor measured in 10 mM buffer solution with an Ag/AgCl reference electrode when V_{GS} swept from -0.6 V to 0.2 V and V_{DS} was -0.1 V (blue), -0.2 V (red), -0.3 V (yellow), -0.4 V (purple). 72
Figure 5.15: (a) Transfer characteristics of the PEDOT:PSS OECTs with Au contact material after applying 1 mM of buffer solution (n>3), (b) Transfer characteristics of PEDOT:PSS OECTs with Au contact material when different buffer solutions were applied. 73
Figure 5.16: With the application of 1 mM of buffer solution, transfer characteristics (solid lines) and transconductance (dotted lines) of PEDOT:PSS OECTs of Au contact material with different channel geometries was obtained at V_{DS} of -0.2 V. 74
Figure 5.17: Transfer characteristics of an OECT were obtained using a Pt electrode as the gate electrode by scanning the gate voltage 10 times consecutively at intervals of 1 minute. The measurement was conducted in (a) PBS solution with the voltage range from 0 to 0.8 V, (b) PBS solution with the voltage ranging from -0.4 to 0.8 V, (c) 100 mM buffer solution with application of the voltage from -0.4 to 0.8 V. 75
Figure 5.18: (a) Schematic of chip design (b) IV characteristics of different contact materials. 77
Figure 5.19: Transfer length method for measuring contact resistance between Au and the PEDOT:PSS film. 78
Figure 5.20: Transfer characteristics of PEDOT:PSS OECTs with Pt contact material (a) and IrO_x contact material (b). 79
Figure 5.21: Transfer characteristics of (a) the chips using Au as contact line and IrO_x as IDE structures (b) the chip with IrO_x contact material. 80
Figure 5.22: PEDOT:PSS film thickness and resistance change after varying the spin-coating speed (n≥5). 81
Figure 5.23: After depositing PEDOT:PSS mixture solutions A, B, C and D on OECTs, (a) Thicknesses of PEDOT:PSS film (n≥3), (b) Resistance between source and drain electrodes (n≥3). 82
Figure 5.24: SEM images of PEDOT:PSS films after depositing PEDOT:PSS mixture solutions A (a), B (b), C (c) and D (d) on the SiO_2 substrate. 82

Figure 5.25: After applying the PBS solution, the transfer characteristics of PEDOT:PSS OECTs with Au contact material was measured when different thicknesses of the PEDOT:PSS films were deposited on the transistors. 83
Figure 5.26: Transfer characteristics of PEDOT:PSS OECTs without ISM, with different compositions and thicknesses of Na^+ ISM after applying 100 mM of Na^+ buffer solution. V_{GS} swept from -0.8 V to 0 V and V_{DS} was constant at -0.4 V. 84
Figure 5.27: (a) The real-time recorded drain current for the OECTs without ISM, with Na^+ ISM composition 0 and with K^+ ISM composition 0. The thickness of ISM is 1300nm. (b) Sensitivity of Na^+ ISM based PEDOT:PSS OECTs and (c) Sensitivity of K^+ ISM based PEDOT:PSS OECTs with three different ISM compositions and thicknesses..... 85
Figure 5.28: (a) Sensitivity of Na^+ membrane PEDOT:PSS OECTs and (b) Sensitivity of K^+ membrane PEDOT:PSS OECTs with different spin-coating speeds. 88
Figure 5.29: Selectivity of Na^+ ISM OECTs with membrane thicknesses of 1300 nm (a), 600 nm (b) and 80 nm (c). Selectivity of K^+ ISM OECTs with membrane thicknesses of 1300 nm (d), 600 nm (e) and 80 nm (f). 89
Figure 5.30: Reversibility of Na^+ ISM OECTs with membrane thicknesses of 1300 nm (a), 600 nm (b) and 80 nm (c). Reversibility of K^+ ISM OECTs with membrane thicknesses of 1300 nm (d), 600 nm (e) and 80 nm (f). 90
Figure 5.31: (a) Schematic representation of multiplexed detection of Na^+ and K^+ ions using the same PEDOT:PSS OECT microarray, (b) The microscope image of OECT microarray covered with Na^+ and K^+ ISM, (c) Real-time monitoring of Na^+ ions and (d) Real-time recording of K^+ ions using this OECT. 91
Figure 5.32: Cyclic voltammetry (CV) characterization of the first measurement setup (WE and CE: Pt electrode, RE: Ag/AgCl reference electrode). The voltage was swept from -0.2 to 0.7 V with the scan rate of 0.05 V/s then reversed. (a) CV curves using a continuous sequence of 5 scans with application of 1 mM of DA solution. (b) The fourth scan of the CV curves were extracted and compared when DA solutions with various concentrations were added..... 93
Figure 5.33: CV characteristic curves of an OECT for the second measurement setup (WE: connected source and drain electrode; CE: Pt electrode; RE: Ag/AgCl reference electrode). The voltage swept from -0.2 to 0.7 V then reversed, (a) CV curves using a continuous sequence of 5 scans with 1 mM of dopamine solution, (b) CV curves of the fourth scan with varying DA concentrations..... 94
Figure 5.34: (a)Transfer characteristics using an OECT with Pt gate electrode in PBS and 250 µM DA solutions at the V_{DS} of -0.3 V and V_{GS} swept from -0.5 V to 0.8 V, (b) Transfer characteristics of the transistors with 108 nm of PEDOT:PSS film when DA solutions with various concentrations were applied at the at the V_{DS} of -0.3 V and the V_{GS} swept from -0.4 V to 0.8 V..... 95
Figure 5.35: Transfer characteristics of OECTs were measured in PBS solution at different scanning rates and directions using the Pt electrode as the gate electrode. V_{GS} swept between -0.4 V and 0.8 V, while V_{DS} was -0.3 V. The gate voltage of forward scanning (red curves) swept from lower to higher value (-0.4~0.8 V) and the backward scanning mode (black curves)

swept the gate voltage from higher to lower value (0.8~-0.4 V). Solid, dashed and dotted lines represent normal rate, fast rate and quiet rate respectively. 96
Figure 5.36: (a) Transfer characteristics of OECTs based on 108 nm of PEDOT:PSS film for DA detection with Pt electrode (n=3), and (b) Ag/AgCl reference electrode when V_{DS} was maintained constant at -0.3 V. 98
Figure 5.37: Transfer characteristics of the OECTs for DA detection with PEDOT:PSS film thicknesses of 108 nm (a), 78 nm (b) and 45 nm (c). V_{GS} swept from -0.4 V to 0.8 V and V_{DS} was kept constant at -0.3 V. 99
Figure 5.38: NCR comparison of DA detection using the OECTs with 108, 78 and 45 nm of PEDOT:PSS thicknesses when V_{DS} is -0.3 V and V_{GS} is 0.4 V. 100
Figure 5.39: Transfer characteristics of AA (a) and UA (b) detection using OECT with 108 nm of PEDOT:PSS film. V_{GS} swept from -0.4 V to 0.8 V and V_{DS} was kept constant at -0.3 V (n=3). 101
Figure 5.40: 3D diagram of DA, AA and UA detection using the OECTs based on PEDOT:PSS film thicknesses of (a) 108 nm, (b) 78 nm and (c) 45 nm. The results were obtained when V_{DS} was maintained constant at -0.3 V and V_{GS} stayed at 0, 0.1, 0.2, 0.3, 0.4, 0.5, 0.6 V. Yellow plane means the NCR value of 0. 102
Figure 5.41: NCR comparison of DA, AA, UA detection by OECTs with 108 nm (a), 78 nm (b) and 45 nm (c) channel thickness calculated at V_{DS} = -0.3 V and V_{GS} = 0.4 V. 103
Figure 5.42: (a) Image of the partial setup for the real-time measurement, (b) Real-time curves of DA detection without microfluidic system using an OECT with 108 nm channel thickness measured at V_{DS} = -0.3 V and V_{GS} = 0.3 V. Drain current was obtained at 0.5 second intervals and the solution was added at 200 second intervals. 104
Figure 5.43: (a) Image of the partial setup for the real-time measurement, (b) Real-time curves of an OECT with 78 nm channel thickness for UA, AA and DA detection with microfluidic system measured at V_{DS} = -0.3 V and V_{GS} = 0.3 V. Drain current was obtained at 0.1 second intervals and the solution was added at 200 second intervals. 105
Figure 5.44: Chitosan modification process on the surface of the Pt gate electrode. 106
Figure 5.45: NCR comparison of DA, AA, UA detection using an OECT with 78 nm of PEDOT:PSS film after the surface modification of Pt gate electrode. The data was obtained at V_{DS} of -0.3 V and V_{GS} of 0.4 V. 107
Figure 5.46: Microscope image of the cotton yarn before (a) and after (b) coating with PEDOT:PSS solution for 4 seconds. 107
Figure 5.47: Images of textile sensor before (a) and after (b) integrating with K^+ ion selective membrane. 108
Figure 5.48: (a) IV characteristics of the textile sensors fabricated by immersing in PEDOT:PSS solution for different times ranging from 2 seconds to 12 seconds (n=3), (b) Resistance of textile sensors with different immersion times in PEDOT:PSS solution (n=3). 109
Figure 5.49: After fabricating the textile sensors using an immersion time of 4 seconds in PEDOT:PSS solution, IV curves (a) of the textile sensors when submerged in Na^+ buffer

solution with different concentrations (n=3) and resistance change (ΔR) (b) of these textile sensors was calculated when varied buffer solutions were applied (n=3). 109
Figure 5.50: (a) Resistance of the textile sensors on different days with 2 seconds (black), 3 seconds (red) and 4 seconds (blue) of immersion time (n=3), (b) Resistance of textile sensors bent at various angles with different immersion times (n=3). 111
Figure 5.51: (a) Schematic of the measurement procedure for ion detection using ISM-based textile sensors, (b) IV characterization for detecting the Na^+ ions in various Na^+ buffer solutions using the Na^+ ISM based textile sensor with 4 seconds of immersion time (n=3), (c) Resistance change of Na^+ ISM textile sensor and (d) K^+ ISM textile sensor in different buffer solutions. 112

Table of Tables

Table 2.1: The state-of-art research in PEDOT:PSS-based OECTs for dopamine detection. 27
Table 3.1: Main parameters for evaporating 5 nm of Ti and 50 nm of Au. 32
Table 3.2: Main parameters for sputtering Pt, TiN, IrO_x and ITO. 34
Table 3.3: Main parameters of PECVD process for depositing a 300 nm silicon oxide layer. 36
Table 3.4: Parameters of the RIE process for etching a 300 nm silicon oxide layer 37
Table 4.1: Different chip geometries on the wafer. 42
Table 4.2: Three different compositions of Na^+ ion-selective membrane (ISM) solutions. ... 55
Table 4.3: Three different compositions of K^+ ion-selective membrane (ISM) solutions..... 55
Table 5.1: Maximum g_m value with different channel geometries at V_{DS} of -0.2V. 74
Table 5.2: Resistance of PEDOT:PSS OECTs with different contact materials. 78
Table 5.3: Sensitivity values for OECTs without ISM, Na^+ ISM and K^+ ISM. 86
Table 5.4: Sensitivity value of OECTs without ISM, Na^+ ISM and K^+ ISM using different spin-coating speeds. 88

Appendix A: Abbreviations

OECTs: Organic Electrochemical Transistors

PEDOT:PSS: Poly(3,4-ethylenedioxythiophene):poly(4-styrenesulfonate)

GOPS: 3-glycidoxypropyltrimethoxysilane

EG: ethylene glycol

CPs: conductive polymers

DMSO: dimethyl sulfoxide

Glucose oxidase: GO_x

Hydrogen peroxide: H_2O_2

EDL: electric double layer

IHP: inner Helmholtz plane

OHP: outer Helmholtz plane

PMMA: polymethyl methacrylate

PDMS: polydimethylsiloxane

Au: gold

Pt: platinum

TiN: titanium nitride

IrO_x: iridium oxide

ITO: indium tin oxide

ISMs: ion selective membranes

Na^+: sodium ion

K^+: potassium ion

Na-TFPB: natrium-tetrakis-[3,5-bis-(trifluormethyl)-phenyl]-borat

KTB: kalium-tetrakis-(4-chlorphenyl)-borat

PVC: polyvinyl chloride

DOS: dioctyl sebacate

THF: tetrahydrofuran

NTs: neurotransmitters

CNS: central nervous system

DA: dopamine

UA: uric acid

Appendix A: Abbreviations

AA: ascorbic acid

DI water: deionized water

Na_2HPO_4: sodium phosphate dibasic

NaH_2PO_4: sodium phosphate monobasic

K_2HPO_4: potassium phosphate dibasic

KH_2PO_4: potassium phosphate monobasic

TTF: transistor transfer function

CV: cyclic voltammetry

LoD: limit of detection

NCR: normalized current response

MEMS: micro-electro-mechanical system

HMDS: hexamethyldisilane

IDEs: interdigitated electrodes

DC: direct current

RF: radio frequency

CVD: chemical vapor deposition

PECVD: plasma enhanced chemical vapor deposition

RIE: reactive ion etching

F_2: fluorine

Cl_2: chlorine

SF_6: sulfur hexafluoride

VDP: Van der Pauw

TLM: transfer length method

R_{sh}: sheet resistance

R_c: contact resistance

R_t: total resistance

SNR: signal-to-noise

RE: reference electrode

WE: working electrode

CE: counter electrode

SEM: scanning electron microscope

Appendix A: Abbreviations

V_{DS}: drain-source voltage

I_{DS}: drain-source current

V_{GS}: gate-source voltage

g_m: transconductance

q: electron charge

μ: hole mobility

C^*: volumetric capacitance

V_T: threshold voltage

W: width of channel film

d: thickness of channel film

L: length of channel film

C_g: gate/electrolyte capacitance

C_{ch}: channel/electrolyte capacitance

V_g^{eff}: effective gate voltage

V_p: pinch-off voltage

V_{offset}: offset voltage

Appendix B: Details of reagents and equipment

Agents		
Name	**Company**	**Country**
Clevios PH1000 (PEDOT:PSS)	Heraeus Clevios	Germany
Ethlene glycol (EG)	Sigma-Aldrich	Germany
3-Glycidyloxypropyl-triethoxysilan (GOPS)	Sigma-Aldrich	Germany
Sodium phosphate dibasic (Na_2HPO_4)	Sigma-Aldrich	Germany
Sodium phosphate monobasic (NaH_2PO_4)	Sigma-Aldrich	Germany
Potassium phosphate dibasic (K_2HPO_4)	Sigma-Aldrich	Germany
Potassium phosphate monobasic (KH_2PO_4)	Sigma-Aldrich	Germany
Sodium-ionophore X	Sigma-Aldrich	Germany
Sodium tetrakis [3, 5 bis (trifluoromethyl) phenyl] borate (Na-TFPB)	Sigma-Aldrich	Germany
Polyvinyl chloride (PVC)	Sigma-Aldrich	Germany
Bis (2-ethylhexyl) sebacate (DOS)	Sigma-Aldrich	Germany
Tetrahydrofuran (THF)	Sigma-Aldrich	Germany
Potassium-ionophore III (valinomycin)	Sigma-Aldrich	Germany
Kalium-tetrakis-(4-chlorphenyl)-borat (KTB)	Sigma-Aldrich	Germany
AZ5214 photoresist	Microchemicals	Germany
AZ726MIF developer	Microchemicals	Germany
Acetone	Microchemicals	Germany
Isopropanol	Microchemicals	Germany
DMSO	Microchemicals	Germany
PDMS	Distrelec	Germany
Ag/AgCl reference electrode	Word precision instruments	USA
4-inch borosilicate glass wafer	Microchemicals	Germany
Chitosan	Sigma-Aldrich	Germany
Dopamine hydrochloride (DA)	Sigma-Aldrich	Germany
Ascorbic acid (AA)	Sigma-Aldrich	Germany
Uric acid (UA)	Sigma-Aldrich	Germany
Phosphate buffered saline (PBS) solution (pH=7.4)	Sigma-Aldrich	Germany
Acetic acid (100%)	Merk KGaA	Germany
Adhesive silver glue	Kemo Electronic	Germany
Silicone adhesive	Dow Silica	Germany

Appendix B: Details of reagents and equipment

Equipment		
Name	**Company**	**Country**
Photolithography System	SÜSS MicroTec	Germany
Electron-Beam Evaporation System	Leybold	Germany
Sputtering System	Nordiko (Duisburg)	Germany
Spin coater	Sawatec AG	Switzerland
LaserWriter	Microteach	Germany
PECVD	Oxford instruments	Germany
RIE etching	Oxford instruments	Germany
Keithley(4200A-SCS)	Keithley instruments	USA
DektakXT	Bruker	Germany

Appendix C: Supporting images for results

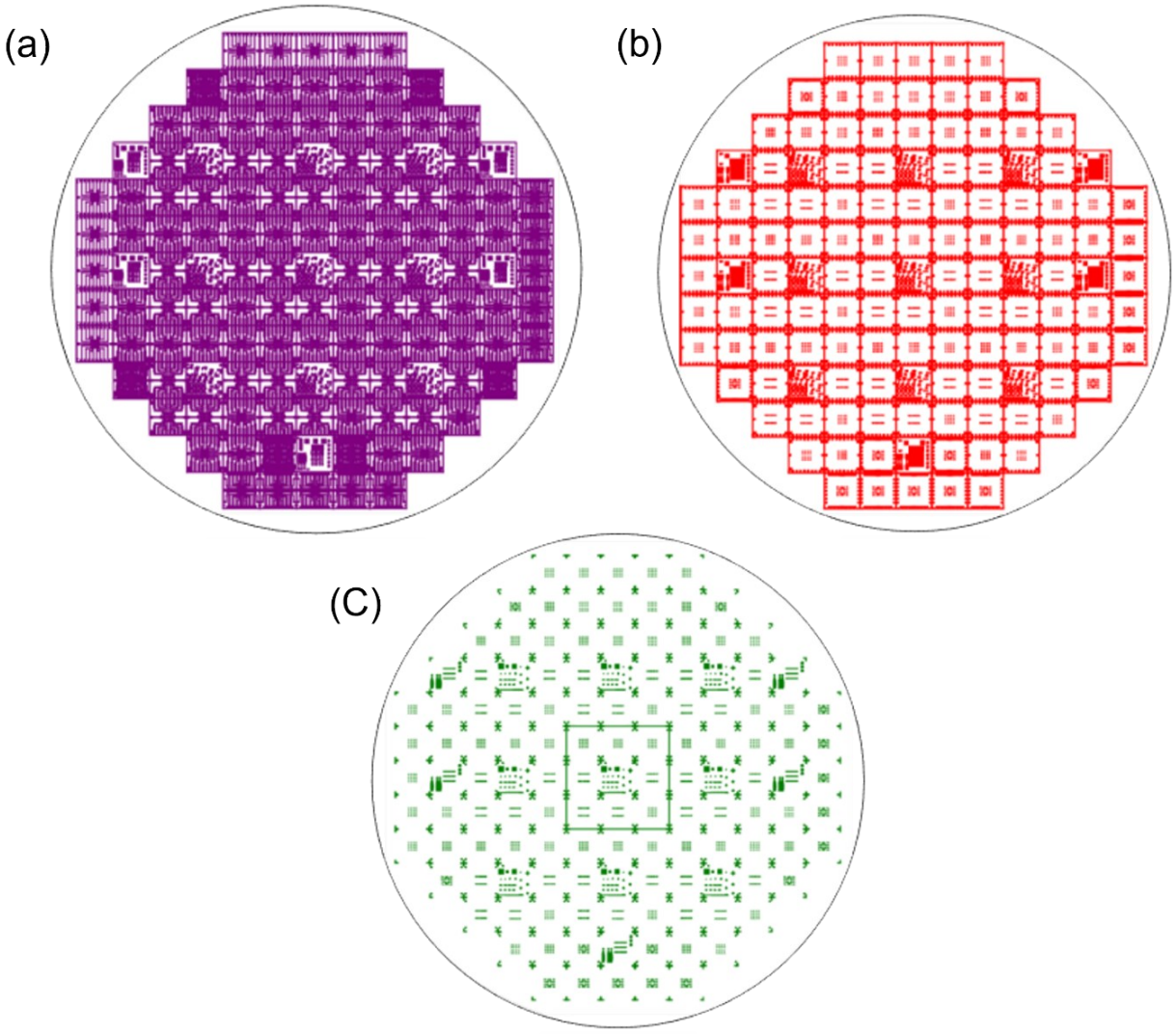

Figure S1: *Whole wafer layout with all masks (a) Mask 1 (purple color) for patterning the metal path, (b) Mask 2 (red color) for gate and contact pads opening, (c) Mask 3 (green color) for structuring the channel materials opening.*

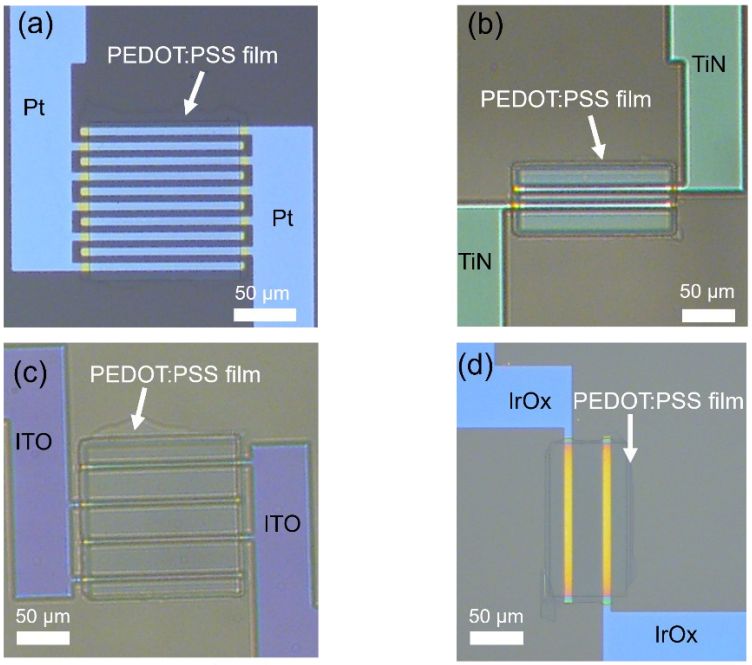

Figure S2: *After depositing PEDOT:PSS on the transistor, microscope images of an OECT structure with Pt (a), TiN (b), ITO (c) and IrO_x (d).*

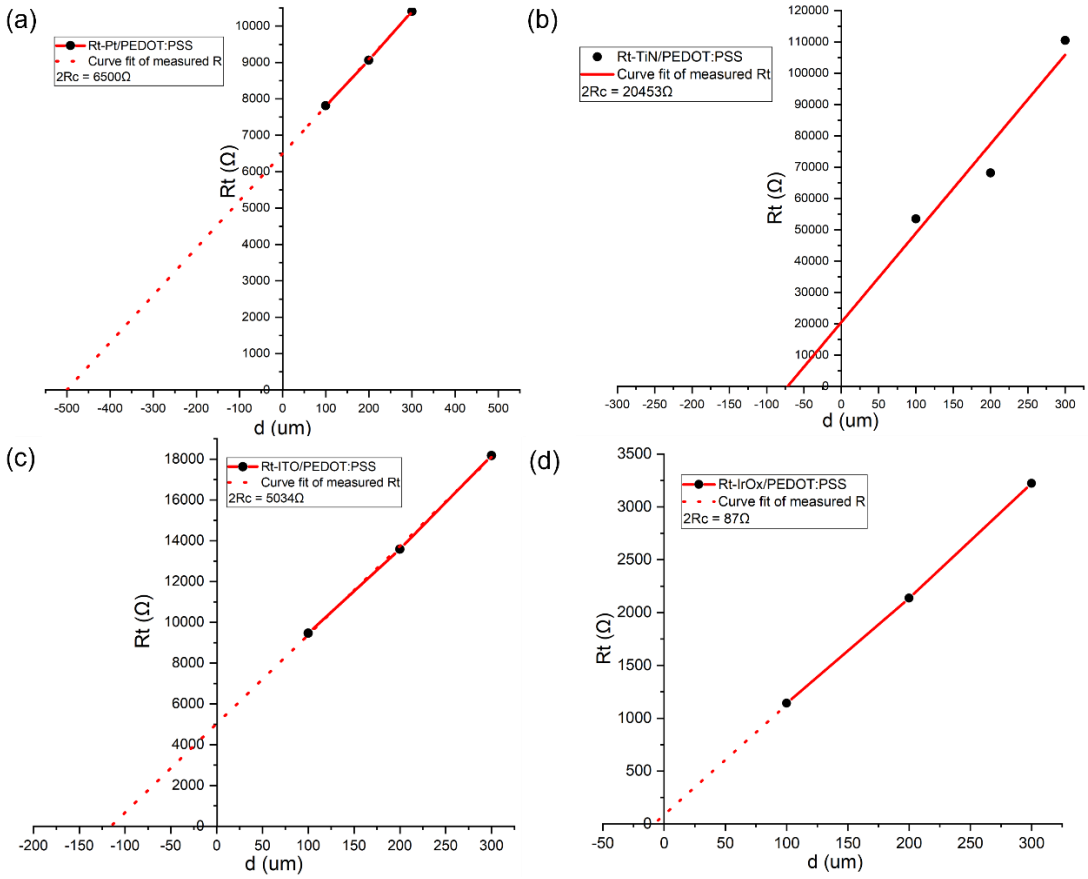

Figure S3: *Transfer length method for measuring contact resistance between PEDOT:PSS film and metal materials with Pt (a), TiN (b), ITO (c) and IrO_x (d).*

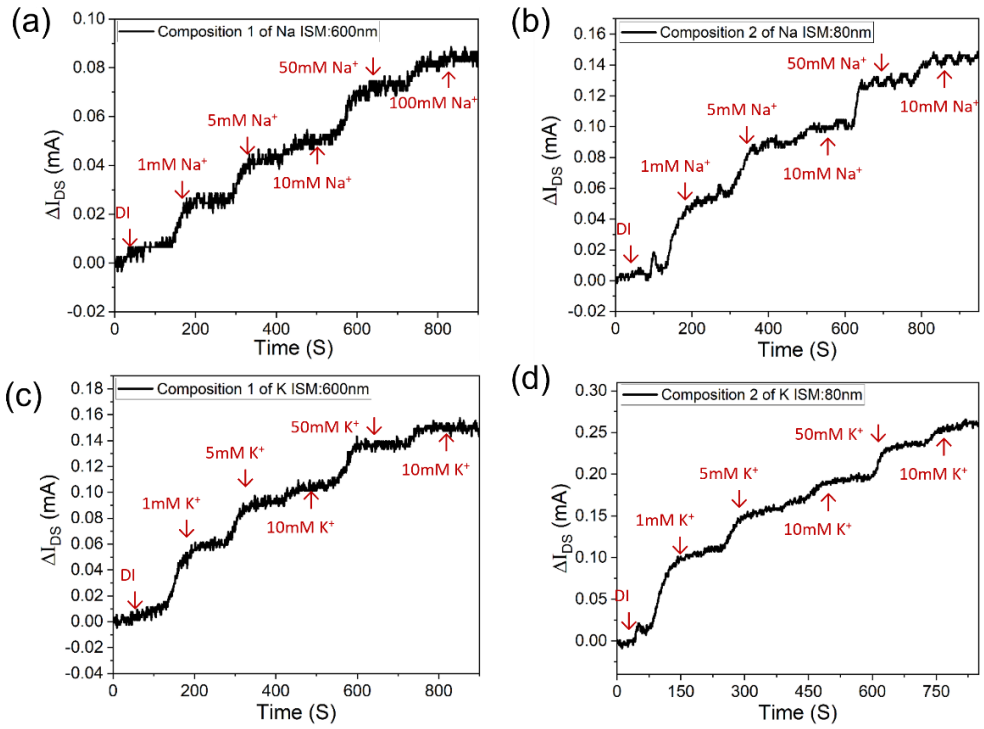

Figure S4: *Real-time recording of Na^+ ISM OECT with composition 1 (a) and composition 2 (b). Real-time recording of K^+ ISM OECT with composition 1 (c) and composition 2 (d).*

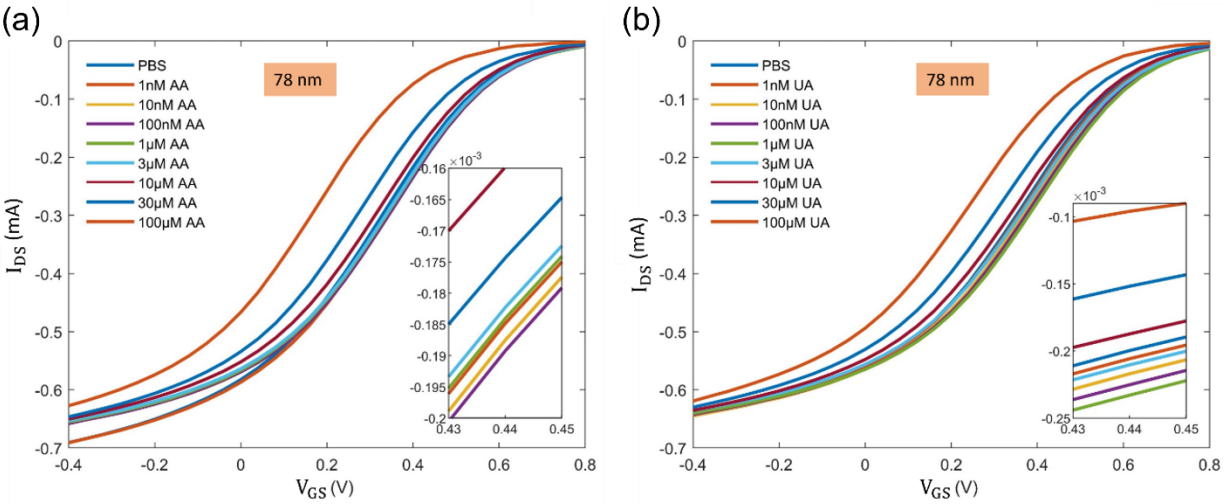

Figure S5: *Transfer characteristics of AA (a) and UA (b) detection using OECT with 78 nm of PEDOT:PSS film. V_{GS} swept from -0.4 V to 0.8 V and V_{DS} kept constantly at -0.3 V.*

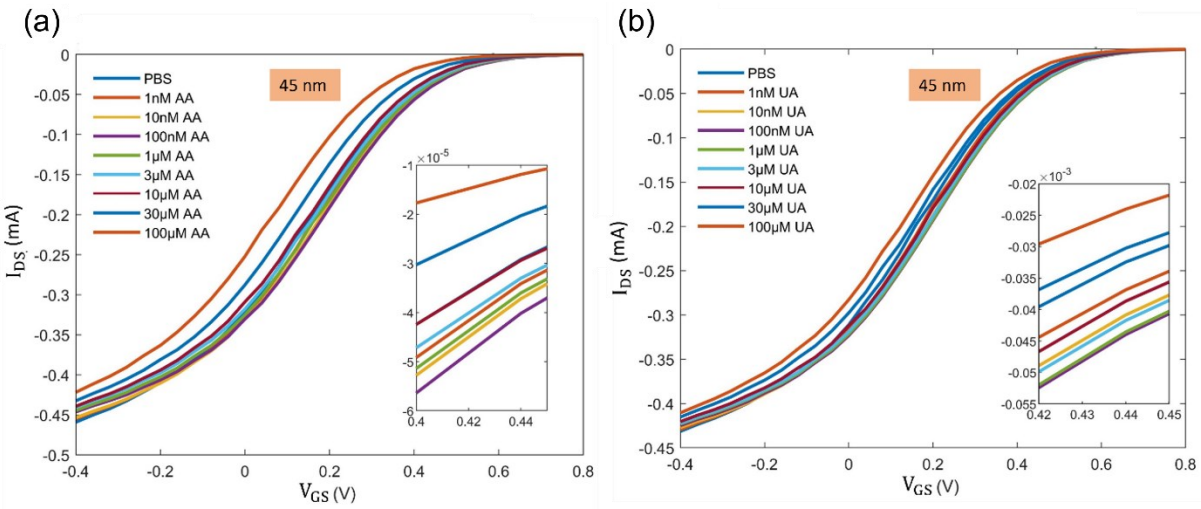

Figure S6: *Transfer characteristics of AA (a) and UA (b) detection using OECT with 45 nm of PEDOT:PSS film. V_{GS} swept from -0.4 V to 0.8 V and V_{DS} kept constantly at -0.3 V.*

Appendix D: Publications and conferences

1. **Chunling Li**, Ni Zhang, Sven Ingebrandt, Xuan Thang Vu*

Integration of PEDOT:PSS into cotton yarn as ion selective sensors for smart clothing applications. Phys. Status Solidi A, 2024, 2400086.

2. **Chunling Li**, Zhiyun Li, Thanh Do Dylan Nguyen, Sven Ingebrandt, Xuan Thang Vu*

Real-time and multiplexed detection of sodium and potassium ions using PEDOT:PSS OECT microarrays integrated with ion-selective membranes. Electrochimica Acta (2024): 145111.

3. **Chunling Li**, Yingying He, Sven Ingebrandt, Xuan Thang Vu*

Microscale sensor arrays for the detection of dopamine using PEDOT:PSS organic electrochemical transistors. Sensors, 24(16), 5244.

4. **The 3rd European Biosensor Symposium 2021**

Chunling Li, Hendrik Kupper, Vivek Pachauri, Sven Ingebrandt, Xuan Thang Vu

Investigating the effects of the contact metal to the characteristics of PEDOT:PSS based organic electrochemical transistors, Online conference, Abstract and Poster.

5. **13rd Engineering of Functional Interfaces 2022**

Chunling Li, Baichen Liu, Vivek Pachauri, Sven Ingebrandt, Xuan Thang Vu

Effect of ZnO nanoparticles to the electrical characteristics of PEDOT:PSS based organic electrochemical transistors, Maastricht, Netherlands, Abstract and Poster.

6. **14th Engineering of Functional Interfaces 2023**

Chunling Li, Yingying He, Sven Ingebrandt, Xuan Thang Vu

Development of a novel dopamine biosensor using PEDOT:PSS OECTs for healthcare applications, Brussels, Belgium, Abstract and Poster.

7. **European Biosensor Symposium 2023**

Chunling Li, Zhiyun Li, Thanh Do Dylan Nguyen, Sven Ingebrandt, Xuan Thang Vu

Optimization of ion-selective membranes on PEDOT:PSS OECT microarrays for real-time and multiplexed sensing of sodium and potassium ions, Aachen, Germany, Abstract and Poster.

8. **5th conference on impedance-based cellular assays 2023**

Lea Baumann, **Chunling Li**, Xuan Thang Vu, Sven Ingebrandt

Cell-substrate adhesion measurements using PEDOT:PSS organic electrochemical transistors, Aachen, Germany, Abstract and Poster.

Recognition

Conference Travel Grant, RWTH Materials Science & Engineering (MatSE) profile area, 2023

Supervised student works

1. Ni Zhang, Bachelor thesis, Textile chemical sensors based on PEDOT:PSS for the analysis of sweat.
2. Baichen Liu, Master project work, Impact of ZnO nanoparticles on the electrical characteristics of PEDOT:PSS organic electrochemical transistors.
3. Zhiyun Li, Bachelor thesis, Optimization of ion selective membranes on PEDOT:PSS transistor arrays for the detection of sodium and potassium ions.
4. Baichen Liu, Master thesis, Study of the influence of pH on electrical characteristics of organic electrochemical transistors based on PEDOT:PSS/ZnO nanoparticles.
5. YingYing He, Master thesis, Development of a novel dopamine biosensor using PEDOT:PSS organic electrochemical transistor for healthcare applications.

Curriculum Vitae

18.11.2024	Doctoral Examination for Dr.-Ing.
2020-2024	Research Assistant and Doctoral Candidate
	Institute of Materials in Electrical Engineering 1 (IWE1)
	RWTH Aachen University, Germany
2016-2019	Master of Science, Xi’an Jiaotong University, China
2011-2015	Bachelor of Science, Xi’an Polytechnic University, China
2007-2011	Dali high school, Weinan, China
1992	Born in Shaanxi Province, China